“Everything is vague to a degree you do not realize till you have tried to make it precise”

Bertrand Russel

UNIVERSITÀ DEGLI STUDI DI MILANO

DIPARTIMENTO DI CHIMICA

Doctorate School in Chemical Sciences and Technologies

XXV Cycle

PhD Course in Chemical Sciences

CHIM/02 – Chimica Fisica

Tunable features of TiO_2 nanoparticles for photocatalytic and photovoltaic applications: a fundamental study of electronic and structural aspects

PhD Candidate

Francesca Spadavecchia

Tutor: Dr. Giuseppe Cappelletti

Director of the School: Prof. Silvia Ardizzone

A. A. 2011-2012

Table of Contents

Extended Abstract

Nanosized titanium dioxide has been widely explored as both pristine and doped semiconductor. TiO_2 nanocrystals were successfully synthesized by three different procedures. Two of them are based on a controlled sol–gel reaction, implemented either by doping or by a hydrothermal growth step with the use of surfactants, exploiting three-dimensional micelles. The latter one is a microemulsion-mediate route, to accurately control the growth of Ti precursor in nanoreactors by the confinement in aqueous droplets. As for the doping, both metal and non-metal elements have been chosen, namely praseodymium, silver and nitrogen. In this latter case, both organic and inorganic sources, in turn, were used to modulate the N content of doped-titania.

All samples were characterized from the morphological, structural, optical, and electronic points of view. Moreover, for selected N-TiO_2 samples, the role of the aging time after the calcinations of the powders (from "freshly prepared" to "old" samples) both on the intensity of the optical features and on the bulk paramagnetic nitrogen concentration was also considered.

Two main fields of applications for titania powders and films were investigated: photocatalysis and photovoltaics. Thus, the photocatalytic activity of several samples was tested using either UV or visible light irradiation with regard to different pollutants, ranging from ethanol (both in aqueous and gaseous media) to the more complex methylene blue molecule (deposited onto the oxide film). Besides, advanced oxidation processes were successfully applied to the degradation and final mineralization of bisphenol A and 4-cumylphenol. The use of TiO_2 immobilized in thin films is of paramount importance for the plant-scale applicability of the process, especially if a low intensity irradiation source, such as solar light, is to be exploited. Then, photocatalytic reduction of hexavalent chromium was conducted with the use of electrodeposited TiO_2 layers.

Even though (doped) titanium dioxide is one of the most commonly adopted semiconductors in photocatalysis, it suffers from a relatively high bandgap – hence the doping to increase visible light absorption – and from recombination of photogenerated charge carriers. Furthermore, univocal conclusions on the Fermi energy levels, chemical nature and location of the doping centers, and related charge transfer processes versus dopant

concentration are absent in the literature. Therefore, electronic effects induced by the presence of the heteroatom in the TiO_2 nanocrystals were investigated by a synergistic combination of electrochemical experiments (Mott-Schottky plots, photovoltage and photocurrent measurements) and theoretical DFT calculations. Results on the doped materials point towards a reduced tendency to charge carriers' recombination and different effects on the (quasi-)Fermi energy location of the final material.

Recombination is a central issue also in solar cell devices, resulting in possible low efficiencies. The ability of spin-coated and spray-pyrolyzed TiO^2 blocking layers in preventing or reducing losses arising from electron transfer via the transparent conductive substrate has been examined in bilayer hybrid dye-sensitized solar cell (DSC) devices. Then, different types of both solid-state dye-sensitized solar cells and DSCs with a liquid electrolyte were tested making use of the more effective spray-pyrolyzed TiO_2 as "blocking layer" and optimizing home-made nanostructured titania pastes.

Introduction

In recent years, with the rapid development of semiconductor-based photocatalytic and photovoltaic devices, studies of surface and bulk processes on nano-sized titanium dioxide, as well as its deep characterization, have gained significant importance. Much attention is devoted to its wide potential applications in clean solar energy conversion and environmental purification. Despite the numerous papers published since the discovery of photoinduced decomposition of water on TiO_2 electrodes in 1972, many fundamental questions remain unsolved.

This thesis deals with several aspects related to nanocrystalline TiO_2, both pristine and doped, ranging from its chemical synthesis to its characterizations and applications.
As a general fact, the photocatalytic performance of titania should be further enhanced from the viewpoint of practical application and commercial benefit. To achieve this purpose, academic research has drawn the attention to various modifying methods, such as doping, metal deposition, surface sensitization, coupling of semiconductors, and so forth, in order to optimize different properties of TiO_2, thus enhancing its photocatalytic activity.
In the present work, three different synthetic routes have been adopted to obtain titania with the above mentioned desired features. A classical sol-gel synthesis has been integrated on one side by doping with either metal (Pr, Ag) or non-metal elements (N) – codoped samples have been considered too – and on the other side by an hydrothermal growth step using monomeric (dodecylpyridinium chloride, DPC) or dimeric gemini-like (GS3) surfactants as template directing agents. Furthermore, a microemulsion-mediated route has been employed to accurately control the synthesis of bare titanium dioxide nanocrystals grown in nanoreactors by the confinement in aqueous droplets.
The first mentioned synthetic procedure has been derived by the awareness that, in a context of photocatalytic applications, it is desirable to move over the well-established photoactivity of TiO_2 in ultraviolet region. This is due to the fact that only a small fraction of solar light (3-5 %) can be utilized by the photocatalyst because of its wide band gap (3.0-3.2 eV). As a matter of fact, the success in nitrogen doping provides good opportunities for extensive applications but needs more exhaustive and comprehensive enlightenments, such as what concerns the not striking coincidence between absorption into the visible light and better photocatalytic results with visible irradiation.

Different starting N/Ti molar ratio, as well as dissimilar N precursors, appeared to affect some peculiar features and properties of the final material. Some of them have been already described in the literature for N-doped samples, while some others, such as unexpected effects upon aging the samples, were not previously reported.

Moving from nitrogen dopant, also Pr and Ag were exploited, thus exploring other promising heteroatoms which are either very scantily taken into account in the literature, as in the case of rare-earth elements, or show outstanding characteristics such as suitable reaction with chemicals, environmental friendliness, reasonable price, and antimicrobial activity, as in the case of Ag.

This part of the work has been driven by the fact that, in addition to the main drawback of titanium dioxide consisting in its quite large intrinsic bandgap, a second important issue to be controlled and optimized is the low quantum photoefficiency due to the high recombination rate of photogenerated electron–hole pairs. If, on the one hand, the presence of metal centers in TiO_2 leads to a considerable absorption of light into the visible region, on the other hand both Pr and Ag - in the metallic state - reduce the electron-hole recombination rate in doped titania.

Composite oxides and doped semiconductors are both well exploited categories which include titanium dioxide as one of the most studied material. Even though literature studies on applications and basic characterizations of TiO_2 are probably prevailing, some authors also focus on the principles of band bending, surface states, charge transport (*etc.*) and their effect on photochemistry and photocatalysis. This may be helpful to chemists and material scientists in understanding the photoexcitation process and the development of highly efficient photoactive materials and processes. To gain insight into these electronic aspects of doped and undoped nano-TiO_2, optical measurements have been combined with direct electrochemical characterizations, such as chronoamperometry, impedance, and photovoltage measurements. Starting from an introduction to the physical principles of semiconductors and theory of the measurements performed, going through experimental details and results, the effects of electronic features on other semiconductor properties are considered. Chronoamperometry, in terms of photocurrent developed by the samples under irradiation, could give a reliable insight into charge carrier recombination rate, whereas the other two techniques have been adopted to evaluate the (quasi-)Fermi level of the oxide

or the absolute scale of conduction/valence band location. Both impedance analysis in the form of Mott-Schottky plot and photovoltage measurements as a function of the pH of the TiO_2 suspension can shed light on band bending occurring in titanium dioxide when in contact with an electrolyte. Therefore, the flatband potential representing the lower edge of the conduction band for an n-type semiconductor, which is approximately the value of the Fermi energy on an electrochemical scale, could be determined when using a Mott-Schottky plot. On the other hand, photovoltage analysis gives access to the quasi-Fermi level of electrons, thus enabling a direct measure of the lower edge of the TiO_2 conduction band under illumination, which can be compared with the information achieved by Mott-Schottky analysis performed in the dark. In this way it is possible to capture a picture of two different physical situations for the same oxide, both meaningful when dealing with both heterogeneous photocatalysis and all other possible titania studies and applications.
Electrochemical methods were chosen for their inherently sensitivity to the electronic structure and for the need to tackle the above mentioned still unsolved issues. Besides this, also morphological and structural features of the synthesized metal oxide powders were explored by several techniques, extended to the less routinely used EXAFS (extended X-ray absorption fine structure) and EPR (electron paramagnetic resonance) measurements. In this context, a multidisciplinary approach involving surface, interphases and synthetic knowledge by my group has been performed with the help of Dr. L. Falciola (Electroanalytical Chemistry Working Group, Università degli Studi di Milano) for the electrochemistry involved and in partnership with a theoretical chemistry group (Dr. M. Ceotto, Università degli Studi di Milano). Indeed, by placing theory and experiment side by side, the aim was that of systematically and fully explore these systems to gain novel insights into the interplay among structural and electronic degrees of freedom that underlie the observed photochemical properties of TiO_2.

Another worldwide exploitation of titanium dioxide is in dye-sensitized solar cells as the preferred inorganic wide-bandgap semiconductor. The main reasons of its success can be summarized in the following: it is easy to synthesize, it acts as an n-type semiconductor due to the donor-like oxygen vacancies, and molecular sensitizers (dye molecules) attached to the its

surface can be finely used to collect a greater portion of the electromagnetic spectrum. Basically, a photon absorbed by a dye-sensitizer molecule layer induces electron injection into the conduction band of titania, resulting in current flow. However, short diffusion length in titania dye-sensitized solar cells decreases the solar-to-energy conversion efficiency. Thus, to enhance diffusion length or carrier lifetime, a variety of organic materials are tuned to be attached to titania.

Ensuing the enormously growth in research interest on different types of solar cells, herein the third generation devices belonging to the group of thin film photovoltaics, namely dye-sensitized solar cells, have been studied with the perspective of analyzing the role of home-made titanium dioxide. This has been done during a research period at the Department of Physical and Analytical Chemistry (Uppsala, Sweden), in the group held by Professor A. Hagfeldt.

A first goal was to investigate the performance of different types of titanium dioxide pastes made from previously obtained TiO_2 nanopowders or sol in hybrid solar cells, solid state dye-sensitized solar cells or liquid electrolyte dye-sensitized solar cells. The first class of devices encompasses a wide range of solar cells with different assembling materials, both organic and inorganic, which have recently revealed to be highly challenging. Eventually, the hybrid devices investigated herein can be considered as well solid state dye-sensitized solar cells with the traditional “transparent” hole conductor replaced by a hole transporting dye.

In bilayer hybrid solar cells the device performance depends critically on the nanoscale morphology of the interface between the inorganic and organic semiconducting components. Therefore, a second goal was to display the differences between two types of commonly used “flat” titanium dioxide films, prepared by either spray-pyrolysis or spin-casting, to be adopted as acceptor layer in bilayer hybrid solar cells. This part of the thesis includes work in close collaboration with Dr. E.L. Unger (ex PhD student at Uppsala University). In addition to playing this inescapable role, such TiO_2 films should also prevent recombination losses to the fluorine-doped tin oxide substrate, thus avoiding one of the major reasons of reduced efficiency of the device.

In the following chapters, first an overview on titanium dioxide and its applications at a glance will be given (chapter 1). Then, the different synthetic

procedures are described (chapter 2). Basic characterizations, ranging from morphological to optical and structural ones, are exposed in chapter 3 along with the obtained results. The background for understanding the electronic features of the oxide besides the techniques used to investigate those intrinsic material properties will be presented in chapter 4, together with references to theoretical calculations. Chapter 5 is devoted to photocatalytic experiments, whereas chapters 6 and 7 deal with solar cells from the perspective of the inorganic semiconductor component, namely titanium dioxide. Whereas in chapter 6 two types of TiO_2 films as "underlayers" for hybrid (dye-sensitized) solar cells are deeply characterized, in chapter 7 three classes of dye-sensitized solar cells are investigated making use of the best of the two TiO_2 previously discussed films and different other TiO_2 nanostructured materials.
All experimental details are reported together with results - in appropriate sections - for syntheses, electrochemical characterizations, and photocatalytic tests (chapters 2, 4, and 5, respectively), while an appendix is dedicated to "instrument, method, and accessories" in which experimental details relative to all other material or device characterization (chapters 3, and partly 6, 7) are reported.

1.
TiO_2,
General Aspects

1.1. Abundance and polymorphs

Titanium dioxide occurs in nature as different mineral polymorphs: rutile, anatase, brookite and two recently found high pressure forms, namely monoclinic baddeleyite-like and orthorhombic α-PbO_2-like. The first three are the most abundant and, therefore, most studied modifications. Their crystal structures are shown in Figure 1.1.

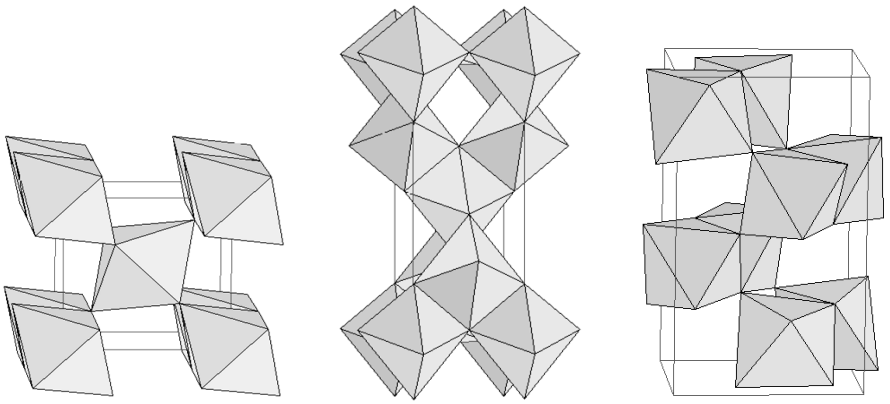

Figure 1.1. Rutile (left), anatase (middle) and brookite (right) structures described in terms of TiO_6 octahedrons**.**

Rutile is stated to be the thermodynamically most stable form of TiO_2 at all temperatures and pressures up to 60 kbar (6 GPa). There are only small differences in Gibbs free energy between anatase, brookite and rutile (4-20 kJ mol^{-1}) meaning that the metastable polymorphs are almost as stable as rutile at normal pressures and temperatures.

As the differences in Gibbs free energy are so small, the relative phase stability may be reversed as a function of particle dimensions. At decreasing the particle size the specific surface area increases, thus affecting surface free energy and surface stress.

Anatase has lower surface energy than rutile, therefore if the particle sizes of the three crystalline phases are equal, anatase is most thermodynamically stable at sizes less than 11 nm, brookite is most stable between 11 and 35 nm, and rutile is most stable at sizes larger than 35 nm.[1]

Kinetically, anatase is stable, thus its transformation into rutile at room temperature is so slow that the transformation practically does not occur.

Such transformation, achieved by increased temperature or pressure, reaches a measurable rate for bulk TiO_2 at T >600 °C and is influenced by several factors, such as the concentration of surface and bulk defects and the particle size.

Rutile

Rutile is the most common natural TiO_2 polymorph: it is present in high-pressure and high-temperature metamorphic and igneous rocks since it has the lowest molecular volume among the three polymorphs. Natural rutile may contain up to 10 % Fe (it often has a red color) and significant amounts of other impurities. Rutile is a mineral with a very high refractive index (n = 2.55-2.65 or 2.83-2.95 depending on the light polarization), thus it is largely used as white pigment. It has a hardness between 6 and 6.5 on the Mohs scale and a specific weight of 4.3×10^3 kg m^{-3}.

Rutile crystallizes in the tetragonal system ($P4_2/mmm$ space group) with cell constants $a = b = 4.593$ Å and $c = 2.959$ Å. Its structure is a distorted *hcp* lattice of O^{2-} ions, with Ti^{4+} cations occupying only half of the octahedral holes. Each Ti atom is surrounded by a slightly distorted octahedron of O^{2-} ions (Ti^{4+} coordination number = 6, O^{2-} coordination number = 3). The rutile structure can be equivalently described in terms of a chain of octahedral TiO_6 units. Each octahedron shares two opposite edges with neighbors, giving rows of octahedrons parallel to the [001] direction. Rows are connected along the [110] direction through the vertex of the octahedron. Channels are created along [001] direction.

Anatase

Anatase is usually found in nature in very small crystals with variable colour (from blue to yellow), depending on the type of impurities. Its hardness is around 6 on the Mohs scale and its specific weight is 3.85×10^3 kg m^{-3}.

Anatase crystallizes in the tetragonal system ($I4_1/amd$ space group) with cell constants $a = b = 3.785$ Å, $c = 9.514$ Å (values obtained by theoretical calculations performed by Dr. M. Ceotto will be given in chapter 3). The unit cell contains 4 formula units instead of 2. In the anatase structure, TiO_6 octahedrons are still present, even if they are much more distorted: each octahedron shares 4 edges and 4 corners with neighbors. This increases Ti-Ti distances and reduces O-O distances with respect to rutile. The anatase

structure is rich in channels. These cavities are large enough to host either cations or anions that can be included in the structure at the synthesis stage.

Brookite

Brookite forms small tubular to platy crystals, with a colour that varies from pink to brown. Its hardness is around 5.5 - 6 in the Mohs scale and its specific weight is of 4.1 x 10^3 kg m^{-3}.

Brookite is the TiO_2 polymorph with the highest structural complexity. It crystallizes in the orthorhombic system (*Pbca* space group) with cell constants: *a* = 9.184 Å, *b* = 5.447 Å, *c* = 5.145 Å. The unit cell contains 8 formula units. The TO_6 octahedrons are remarkably distorted: all distances between the atoms are different. Each TiO_6 octahedron shares three edges with the others. Small ions, for example H and Li, can be guests in the channels formed along the *c* axis ([001]) direction.

Polymorphs' stability

The anatase polymorph is the dominant outcome of the vast majority of liquid-solid and gas-solid transformation-based preparation methods.[2] This is a consequence of being a stable polymorph at working temperatures for sizes (*e.g.*, primary particle size) below *ca*. 15 nm.[3] However, as in most of the cases presented in this thesis, samples often contain some brookite or, alternatively, mixtures of anatase and rutile, owing to the different preparation conditions (temperature, precursor concentration, etc.).[1,4]

Upon heating, amorphous Ti-containing materials would generically transform on anatase.[1,5] Exarhos *et al.* were the first to study the kinetics of the corresponding transition of amorphous films supported on silica substrates.[5] Under hydrothermal conditions, several authors gave evidence of the media influence (pH, presence of ions) on the crystallization mechanism and pointed out that the rate-determining step can be related to the incorporation of new building units at the surface of the growing anatase crystal (solid-type step) and/or the dissolution of small anatase particles (Ostwald ripening; liquid-type step).[6,7] In other studies, using sol-gel[8,9] or microemulsion[10] procedures, details of the solid-state transformation mechanism leading to the anatase phase have been reported. Quantitative knowledge of the key kinetic parameters controlling the amorphous titania to anatase transformation has been achieved in liquid media under hydrothermal conditions[11] and for solid-

solid transformations concerning titania films,[5] powders,[9] or mesostructured systems.[12] The physical characteristics of the transformation (*e.g.*, onset and reaction rate-energy of activation) in air should be different from those in liquid media as, obviously, dissolution steps are critically involved in the latter. The broad range of temperatures where amorphous titania transform into anatase (see below) also tells of a wide range of situations within the air-assisted transformation occurring in solid materials, as it happens during the calcination step. To this end, crystallization has been considered to be controlled by either surface[10] or interface[9] nucleation processes. As a first approach to the rationalization of the nucleation mechanism, one may expect that interface nucleation can work at low temperature, starting from the lowest onset published (*ca*. 350 °C), while the surface dominated mechanism may get primacy above a certain temperature, *ca.* 600 °C.[13] However, a point to stress is that all the above analyses are mainly of kinetic nature and always involve several assumptions to establish the kinetic mechanism, which should be ultimately validated by a multi-parameter fitting procedure of the experimental data. On the contrary, Fernandez-Garcia and co-workers[14] examined the crystallization of anatase from amorphous titania powders using an essentially assumption-free experimental approach. Indeed, using bulk and surface structural characterization techniques sensitive to both local and long range order, they eventually proved that the anatase nucleation onset is exclusively dependent on amorphous intraparticle structural characteristics and then that anatase crystallization is essentially free of interface interferences. This was said to be valid for samples crystallizing in the 400 to 600 °C temperature interval, indicating the invariance of the mechanism with temperature. No doubts on the fact that the structural characteristics of the initial amorphous powders determine the final morphology of the nanoparticles, inferring in this manner the main parameters of the growth step.

1.2. Nanosize effect

In the nanosize regime (<10 nm), a new class of materials has emerged where quantum confinement and surface phenomena based on particle size dominate materials properties. It is well known that nanoparticles of a certain material exhibit very different behaviors compared to their bulk counterpart.

A vast number of fields, ranging from magnetism and luminescence to sensors and renewable/alternative energy as well as photocatalysis, continuously benefit from this new class of materials. The common theme in all these fields is the alteration and possible enhancement of physical properties based on control of the electronic energy levels via quantum size and surface effects.

The principal benefit of decreasing the particle size of TiO_2 is the increased surface to volume ratio. Usually a blue shift in the absorption spectra is recorded for nanosized particles. Concomitantly, the small Bohr radius of this material ensures that only a minor effect on the electronic properties and the absorption onset occurs.

Of course different materials have different critical sizes. With the broadening of the band gap, electrons at the bottom edge of the conduction band and holes at the top edge of the valence band acquire more negative and positive potentials, respectively, which means that they have stronger redox powers in such nanoparticles. A TiO_2 crystal already has a relatively large band gap (3.2 eV), with quite energetic holes and so the efforts to increase the gap by decreasing the size below the value of the Bohr radius is almost unnecessary. However, by decreasing the particle size from bulk TiO_2 to $\sim$ 20–30 nm, the ratio of surface/volume atoms increases by $\sim$ 10 %. Also, the distance the photogenerated carriers have to travel to reach the surface is significantly decreased leading to possible enhancement in charge separation and increased carrier lifetime. This has been shown to be effective for materials such as the well-known P25 (Evonik) TiO_2 photocatalyst with a primary particle size of $\sim$ 20–30 nm and a popcorn-ball like aggregate structure of 2–3 µm.[15]

Larger surface area also provides more active sites for reactant adsorption and decomposition, and light harvest. A shorter distance for the charge carrier transfer is provided, thus largely avoiding the bulk recombination.

These effects provide a multitude of possibilities in the fields of photocatalytic degradation of waste and H_2 production. For example, cluster surface modification can enhance the efficiency of charge transfer and charge separation. Materials systems that are not viable for these applications in bulk form due to insufficiently energetic holes or electrons can be utilized on the nanoscale.

There are also several potential disadvantages if the size becomes too small. First of all, not always the best crystal structure for photocatalysis can be guaranteed. Normally, too small particles (or quantum dots) are apt to have

amorphous structure. Then, too small particles easily aggregate and may result in increased surface electron-hole recombination, which offsets the benefits of high surface area.

Furthermore, porous materials have high surface area and good adsorption ability, and can concentrate reactants around active sites. Selective photocatalysis can be achieved by adjusting the pore size.

In the field of nanomaterials, low-dimensional samples have shown their outstanding properties in catalysis and photocatalysis. One-dimensional (1D) nanostructures (*i.e.,* nanowires, nanorods, nanotubes and nanofibers) have higher surface areas and can normally provide fast charge transportation, especially in the case of single crystalline 1D nanostructures. Two-dimensional (2D) structured materials (*i.e.,* nanosheets, nanoscrolls and nanolayers) can expose a certain facet with high photocatalytic activity (or high selectivity), and provide fast charge transfer.

Due to the nanosize effect, surface related defects play an important role in determining the electronic energy levels of an electrode composed of metal oxide nanoparticles.[16] Surface states originate from the breakdown of the lattice periodicity in the semiconductor, resulting in the formation of dangling bonds and/or the rearrangement of the surface atoms. They are critical in the case of carrier trapping, since they retard the recombination rate under optimum conditions. This will be discussed in more details in chapter 4.

Eventually, it should be mentioned that nanosize materials are small enough to easily escape undetected into the environment. Even though they are claimed to be useful in solving some of the environmental problems facing the nowadays society, their possible adverse effects have to be seriously considered. It is responsibility of researchers in the field of nanotechnology to take these issues into account, providing the foresight to avoid many potential problems.

1.3. TiO_2 crystal lattice and defects

During last decades, it has been realized that several properties of solid materials are mostly controlled by faults or defects in the structure, more than by their pure geometric and electronic structure.[17] Defects in solids, especially if nanosized, should be carefully distinguished between bulk and surface defects. In ionic compounds, the complexity of defects is at least one

order of magnitude higher than in metals because of the presence of anions and cations, which, in some cases, can assume different charged states. This situation is particularly pronounced in metal oxides.

The problem is that defects are often elusive species, highly diluted, and therefore difficult to detect.[18] Very often the proofs of their existence are indirect, based on the change of a property or of a spectroscopic response as a function of the number of defects present in the sample; sometimes, a more direct detection can be provided, as in the case of electron paramagnetic spectroscopy for oxygen vacancies in titania or Ti^{3+} centers.[19-22] Along with oxygen vacancies, reduced titanium species (Ti^{3+}) formation is indeed expected.

In titanium dioxide, the octahedral site occupied by the Ti-ions in anatase is slightly distorted as to have a square base (best defined by the diagonal of 0.378 nm which is identical to the lattice constant *a*) and a long axis (0.398 nm), according to calculations previously performed by the theoretical group held by Dr. M. Ceotto. The anatase structure involves the presence of interstitial sites, which can be described by a strongly distorted octahedron or a square bi-pyramid with the same square base as the TiO_6 octahedrons (diagonal = 0.378 nm) but have a long axis of 0.555 nm. As a result, these square bi-pyramids have a larger volume but still the same square base.

As a matter of fact, foreign atoms - as dopants in titania - are associated with defect formation in the original crystal lattice. Therefore, larger cations can be expected to occupy the larger interstitial site but will most likely cause a distortion of the square base of the bipyramid. Cations smaller than or similar in size to Ti^{4+} can occupy the cation lattice site. Some cations can take both positions due to their intermediate size. Dopant anions normally only occupy the O^{2-} positions. If the anion is reported to go interstitial it is normally not introduced as anion but as oxo-anion (*i.e.*, as cation with bonding to nearby O). An example is the introduction of NO^-, which can occur when doping TiO_2 with N.

One of the easiest way to determine which lattice position could be occupied by the cation is to consider its size. However, not only many exceptions can occur, but one should also take into account that ion sizes are not constant for a given ion. They depend on the coordination environment defined by the site the ion occupies in the crystal lattice, on the type and number of the

neighboring atoms as well as the nature of the bonding between them. This means that the ion adjusts its size to the lattice position it occupies.

According to its valence and its occupation site, vacancies or charge carriers must be created for charge balance. Then, in the case of 'acceptor doping', doping is associated with hole formation,[23] whereas for 'donor doping', extra-electrons are generated. This occurs under loss of oxygen. Additionally, since the electron can be associated with Ti^{4+}, a Ti^{3+} state should be created. It is worthy to highlight that in both acceptor and donor doping, normally, not only a charge defect is associated with the foreign ion, but also a size defect, since the ionic radii of dopant ion and lattice ion deviate to some extent. If a cation is substituted interstitially its charge will always be higher than the lattice site (which is equivalent to zero), so that the result is always donor doping. In this case there is a lattice distortion associated with the defect. If an ion of the same valence is introduced in the lattice site (substitutional doping), there is no nominal charge defect, but a lattice distortion will usually be formed due to the size difference.

From the electronic point of view, any lattice defect introduces an energy state in the band gap: a donor introduces a state (just) below the conduction band, while an acceptor introduces a state (just) above the valence band. There is no total agreement on the exact depth of the defect state in the band gap. The states in the band gap may facilitate the formation of an electron-hole pair and increase the number of charge carriers, but they also may act as trap sites, decreasing the number of charge carriers, especially when they are deep in the band gap. Carp *et al.* [24] argued that the charge carrier trapping out-weighs any positive benefits.

Since the nature of the individual dopant as well as its concentration and distribution determine the defect structure of the crystal, it will also influence the electronic and optical properties of the resulting TiO_2 crystal.

1.4. Doping

Titania doping with various metal and non-metal ions is one of the strategies that has been more extensively used to enhance the semiconductor photocatalytic efficiency. Dopants can substitute lattice ions (a cation X^+ replacing Ti^{4+}, an anion X^- replacing O^{2-}) or occupy an interstitial position, or even form mixed oxides.

It has to be stressed in advance that “doping” is here used in a broad sense meaning modification of the material by foreign atoms. The amount of foreign atoms is considerably higher than traditionally used for doping for applications in electronics.

The effect of doping on titania photocatalytic activity is a complex issue, as the dopant addition may produce manifold effects. Indeed, it essentially modifies the catalyst spectral absorption, the number of charge carriers, the adsorption capacity at the catalyst surface, the interfacial charge transfer rate. These two latter effects are direct consequences of the possible preferential occupancy of surface sites by the dopant ions and the role of trapping sites for charge carriers that the dopant itself may play.

According to the literature, the main aim of doping is to induce a bathochromic shift, *i.e.*, a shift of the absorption edge of TiO_2 to longer wavelengths. Indeed, one of the main drawback of titanium dioxide is its large band gap (3.2 eV for anatase and 3.0 eV for rutile) that corresponds to an absorption in the UV (λ <390 nm for anatase, λ <410 nm for rutile). This definitely limits TiO_2 photocatalytic activity under solar irradiation, which is composed of UV rays by less than 5 %.

One of the first strategies that has been explored to enhance titania visible absorption was doping with metal ions. Substitution of Ti^{4+} by d^n metallic ions in the TiO_2 lattice creates allowed energy states in the band gap of TiO_2 which may induce photoactive transitions in the visible light, due to the excitation of an electron from these energy levels into the TiO_2 conduction band.

However, the doped materials suffer from thermal instability and increase of the charge carrier recombination rates. In fact, p-type dopants (*i.e.*, heterocations of valency lower than that of Ti^{4+}, like Al^{3+}, Cr^{3+} or Ga^{3+}) act as acceptor centers, which trap photoelectrons and, once negatively charged, attract holes, thus forming recombination centers. On the opposite, n-type metal dopants (heterocations of valency higher than +4 , like Nb^{5+}, Ta^{5+}, Sb^{5+}) act as donor centers.

To overcome this point, anion non-metal species such as C,[25,26] S,[27] B,[28] F[29,30] and N,[31-34] have been considered to improve the photocatalytic efficiency of TiO_2 under visible light. Among the anion dopants, nitrogen has proved to be one of the most promising. However, the mechanism of the visible light response in N-doped TiO_2 has not yet been clarified. One of the main debated questions concerns the electronic structure of these systems, once

established that the enhanced visible-light absorbance is due to the narrowing of the apparent band gap, and more precisely to the introduction of localized impurity states in the gap (intra-gap or mid-gap states). Further questions regard the actual localization of N species in the TiO_2 lattice and their interactions with oxygen vacancies. Depending on the material, the nature and properties of oxygen vacancies can vary substantially. As affirmed by Pacchioni,[18] one could say that the oxygen vacancy is a fingerprint of the electronic structure of the oxide.

A second important issue to be controlled and optimized since it constitutes a downside of TiO_2 is the low quantum photoefficiency due to the high recombination rate of photogenerated electron−hole pairs.[35] This is a recurring problem during photoelectrochemical and photocatalytic processes, and it is often considered to some extent to be the major limitation for TiO_2 widespread applications.[36] Unfortunately, the recombination of photogenerated charge carriers most often results to be an undesired effect of the modifications made on titania to overcome the wide bandgap issue and the related visible-light inactivity. Many authors have studied the influence of the dopant on the electron-hole recombination processes which take place in the doped oxide.[37,38] Choi *et al.*[35] widely explored the role of different metal ion dopants on photoreactivity and charge carrier recombination dynamics concluding that these processes are deeply affected by both the nature and the amount of the dopant. In fact, on one hand a small dopant content (<1 %) can introduce traps for electrons and holes, thus increasing the recombination time;[38] on the other hand, such a low concentration could be not enough to significantly increase the absorption of the material in the visible range. A rather high amount of the dopant (5-10 %) definitely leads to an effective narrowing of the semiconductor band gap, but at the same time introduces new recombination centres for the photogenerated charge carriers so that recombination processes could be more numerous and probable.[39]

As for the preparation of doped-TiO_2 materials, a brief overview will be given in the following chapter. In the present thesis, all kinds of material have the peculiarity to possess a basic shape and are very easily obtainable, so that an accurate study on the electronic and structural features could be reasonably straightforward, if not really applicable to other titania samples of different habit and shape. Therefore, a one-pot facile synthesis of doped-TiO_2

nanoparticles is presented in the following chapter. The focus will be on the dopant selected to be investigated in this study: N, Pr, Ag.

1.4.1. N-doped TiO_2

At present, N-doped TiO_2 has been prepared by various methods such as mechanochemical reaction, sputtering, ion implantation, chemical vapor deposition, spray pyrolysis, sol-gel, and oxidation of TiN.[40,41] Then, various methods for preparing thin films of N-doped TiO_2 by gas condensation techniques have also been reported in recent years.[42,43] Most of the above methods need a higher temperature or complicated and expensive equipment; therefore, it is important to insist on simple and lower temperature method to extend the application of the nitrogen-doped TiO_2 photocatalyst, not using more lengthy and complex doping approaches at elevated temperature.

Charge carriers lifetime is a relevant parameter to evaluate the photocatalytic efficiency of a catalyst; however it is important to bear in mind that metal ion-doping might affect the efficiency of the material altering several other parameters (such as changes in surface hydrophilicity and adsorption ability towards reactant species, shifts of Fermi levels or other physical properties) that can be relevant in determining the reactivity of the particles. In the literature it is reported that doping with nitrogen may lead to a decrease in charge carrier recombination, as proved by photoluminescence spectra.[44] This effect can be attributed to both electrons trapping by oxygen vacancies and holes trapping by N atoms.[44] On the other hand, one can argue that excited electrons might be transferred back from the conduction band to the N-induced states in the gap and more easily reach photogenerated holes, thus decreasing recombination efficiency. This is a debated aspect and depends on different side parameters. Indeed, at high levels of nitrogen doping the introduction of a significant number of defects, would serve as recombination centers for holes and electrons and would, therefore, decrease the quantum yield of photocatalytic reactions.[45]

As far as the electronic effects on the oxide bandgap are concerned, Asahi *et al.*[46] proposed that the substitutional doping of nitrogen into the TiO_2 lattice causes a significant red-shift of the absorption edge of TiO_2 by narrowing the titania band gap. Their calculation predicted that N 2p states contribute to the

band gap narrowing through mixing with O 2p states in the valence band. The same authors investigated interstitial doping of N and a combination of substitutional and interstitial doping of N, which might correspond to the introduction of molecular NO or N_2. Such molecularly existing dopants give rise to bonding states below the O 2p valence band and antibonding states deep in the band gap: both are well screened and not interacting with the band states of TiO_2, thus they are unlikely to be active for photocatalysis.

Irie *et al.*[41] proposed that an isolated narrow band formed above the valence band in N-doped titania is responsible for the visible light response. In addition, they found that an increase in the nitrogen concentration lowered the quantum yield under UV irradiation, indicating that the doping sites could also work as recombination centers. Lindgren *et al.*[42] used photoelectrochemical measurements to confirm that the nitrogen created states were located close to the valence band edge and that the conduction band edge remains unchanged by nitrogen doping.

Ihara and coworkers[40] synthesized N-doped TiO_2 with oxygen deficient stoichiometry active in the visible; they proposed that oxygen deficient sites formed in the grain boundaries were responsible for the visible light response, while the presence of nitrogen only improved the stabilization of these oxygen vacancies by preventing re-oxidation during heat treatments. Serpone[47] argued that the visible light activation of the anion doped TiO_2 was the result of the formation of color centers associated with the oxygen vacancies created during the doping.

Since the pioneering work of Asahi and coworkers,[43] there has been an astounding number of publications describing N-doped TiO_2 and its related photochemistry. However, the debate on the fundamental understanding of the electronic and structural aspects of these materials is still open. A general agreement has been reached on the fact that for N-TiO_2 the visible absorption involves the occupied hybridized O 2p–N 2p states in the proximity of the valence band: transitions of electrons occur from the impurity states to the conduction band states. It is here anticipated that the case of undoped TiO_2, the valence band has mainly a 2p–O character whereas the conduction band has mainly a 3d–Ti character.

Reported experimental results also show considerable diversity. As already mentioned, several different methods have been presented in literature to incorporate nitrogen in titanium dioxide, and different sources of N have been

adopted (NH_3/NH_4^+, amines, nitrides, *etc*.).[31,47,48-50] Characterization analyses proved that the predominant type of N dopant species depends on the experimental synthetic conditions. Di Valentin's calculations[51] suggested that substitutional N-doping can be stabilized by the presence of oxygen vacancies under oxygen-poor experimental conditions, whereas under oxygen-rich conditions interstitial N species become favored.

Absorption spectra of N-doped samples invariably exhibit a shift to the visible region, regardless of the preparative method employed and of the nature of the dopant. Nevertheless, visible-light photoactivity of N-doped TiO_2 appears to be highly sensitive to the preparative routes: although these materials absorb visible light, they are nonetheless frequently inactive in photo-oxidation and photocatalysis in general, probably because of charge recombination effects.

1.4.2. Pr-doped TiO_2

While the number of papers on p-block non-metal dopants (especially B, C, N) has undergone an exponential increase, some other promising heteroatoms are very scantily taken into account.[52-54] In this respect, rare-earth (RE) metals have started to show a tremendous potential improvement of several TiO_2 features, becoming interesting sources for new advanced materials and receiving quite much attention as dopants too. It is reported that doping TiO_2 with such metal ions can slow the recombination rate of photogenerated charge pairs by shallowly trapping electrons and enhance the interfacial charge transfer efficiency due to the ability of the metal to form complexes with a Lewis base (*e.g.*, amines, aldehydes, alcohols, thiols, etc.) *via* interactions of functional groups of the base with the metal empty f-orbitals.[53] Secondly, the RE dopant can retard the transformation from anatase to rutile phase[55] and also inhibit the increase of the crystallite size.[52] Most importantly, Pr doping could slow the radiative recombination of photogenerated electrons and holes in TiO_2.[53] Once again, it is the case that doping not only alters the charge-transfer properties but also affects the crystallinity and optical characteristics of the material.

Consequently, Pr-TiO_2 systems may find successful applications in photocatalysis, as already pointed out by several authors both recently and in the past.[52,56,57]

Notwithstanding all these findings, no complementary experimental and theoretical studies have been found in the literature focusing on the above mentioned aspects, except Chen *et al*. who analyzed the electronic structures of the different lanthanide-doped systems by using a DFT + U (Density Functional Theory with Hubbard U correction) approach.[58]

Thus, in this thesis theoretical calculations are employed to corroborate the electronic and structural experimental results. A similar combined approach has been used when studying the location of nitrogen dopant species in TiO_2 matrix by EXAFS measurements[59] (see chapter 3).

In this work, the aim has been to focus on a synergic and deep experimental and theoretical characterization of Pr-doped TiO_2 with – Pr as a representative RE element - from both electronic and structural points of view, while keeping the synthetic strategies as simple, quick and effortless as possible.

1.4.3. Ag-doped TiO_2

It is generally believed that modification on TiO_2 with transition metal ions could influence the light absorption and photoactivity of TiO_2 since the metal should act as electron (or hole) trap, which could decrease the electron-hole pair recombination rate and subsequently increase the lifetime of charge carriers.[35,60] In a photocatalytic context, transition metals deposited on semiconductors increase the charge transfer rate between reactants and photocatalyst as the intermediary in electron pathway.[61,62]

Moreover, noble metals are said to extend the light absorption into the visible range, besides, in some cases, modifying the surface properties of the photocatalyst.[63,64]

Among all kinds of metal-semiconductor heterostructures, Ag-TiO_2 nanocomposites especially attract much more attentions because silver has the most efficient plasmon resonance in the visible region, which can be attributed to the favorable frequency dependence of the real and imaginary parts of the dielectric function.[65] Therefore, many Ag-TiO_2 composite materials with different morphology have been synthesized through a variety of methods.[66-68] However, the photocatalysis efficiency of these photocatalysts is sometimes still low. Indeed, there are still some voices in the literature claiming that, except for a few favorable cases, the photocatalytic activity of a cation-doped TiO_2 decrease, because of thermal instability or an

increase in charge carriers recombination (due to recombination centers introduced by the dopants' localized d-states deep in the band gap of titania).[69]

Silver is known for its antibacterial properties. Indeed, enhanced photocatalytic disinfection of different types of bacteria even under visible light illumination was achieved by several authors.[70,71]

Ag/TiO_2 nanocomposite films have been known for few years to exhibit multicolor photochromism,[72] thus being very interesting for many applications like rewritable color copy paper, smart glass, multiwavelength optical memory, holographic data storage, or writable and rewritable data carriers.[73,74] Several methods have been implemented for their fabrication such as the photocatalytic or electrochemical growth of silver nanoparticles (NP) in porous[75-77] or on bulk crystal[78,79] TiO_2 films, or the deposition by magnetron sputtering.[80] In all cases, the reversible change of color under illumination relies on the modification of the nanoparticles size distribution through photo-activated redox reactions occurring specifically with the titania matrix. UV light excites electrons in the conduction band of titania, which reduce Ag(I) species and lead to the formation of Ag NP. Visible light oxidizes silver NP via the photoexcitation of electrons on Ag and their stabilization by adsorbed oxygen molecules in the titania matrix.[79,81]

As shown in chapter 2, home-made $Ag\text{-}TiO_2$ materials have been studied by varying synthetic parameters. Moreover, the concept of Ag-doping has been taken further and Ag,N-codoped TiO_2 samples have been also synthesize. As stated by Sun *et al.*, it could be expected that the transition metal ion modification on anion-doped TiO_2 could be helpful to address what is said by some authors to be the intrinsic problem of charge carrier recombination from anion doping.[70] Accordingly, a facile and simple synthesis of a conceptually novel $Ag/TiO2_{2-x}N_x$ under mild experimental conditions was also reported by Virkutyte and Varma to produce a remarkably efficient, stable and recyclable nano-photocatalyst that is functional under visible light.[82]

1.5. Applications

Chemical stability, non-toxicity and cheapness are always invoked as the main qualities of TiO_2 that motivate the choice of such material among other inorganic semiconductors. Nevertheless, it has received special attention due

to other properties such as high refractive index, high dielectric constant, biocompatibility, superhydrophilicity (under UV light), and superior photocatalytic properties. Thus, depending on the type of application, it can be used as bulk, powder, thick/thin film or granulate as photocatalyst, bone substituent, reinforcing mechanical support, white pigment (paints, cosmetics, etc.), and also in optical interference coating, capacitors, self-cleaning, anti-fogging, gas-sensing and photovoltaics.
These features have brought about a great interest not only in the investigation of fundamental aspects of titania but also in the manifold applications it can be involved into.

In this thesis, different types of TiO_2 commercial and home-made samples have been explored in the field of photocatalysis and photovoltaics.

Different powders or films have been tested towards the degradation of pollutants in the gaseous, liquid or dry state. Whereas these experiments have been carried out in the NIG group held by Professor Silvia Ardizzone at the Università degli Studi di Milano, the studies on solar cells (specifically, dye-sensitized solar cells, DSCs) have been conducted in the Department of Analytical and Physical Chemistry at Ångström, Uppsala (Sweden).

1.5.1. Photocatalysis

In the very broad area of chemical reactions, electron transfer reactions between two species (redox reactions) which have to go through a transition state are said to be catalyzed when the activation energy of the process is lowered and, as a result, the reaction rate is enhanced.

Ideally, the catalyst is returned to its original state after the reaction is completed: the catalyst participates without being consumed. In reality, its lifetime is limited due to alteration of its state, referred to as ‘catalyst poisoning’. Therefore, usually a ‘turn-over number’ is defined, which gives the number of reaction cycles that can be catalyzed before the catalyst becomes inactive.

If the catalyst is in a different phase than that of the reactants, as in the case of photocatalysis, the process is heterogeneous. Here the reaction takes place at the surface of the catalysts, to which the reactants are absorbed.

Thus, heterogeneous semiconductor photocatalysis describes a process where a semiconductor particulate (TiO_2, ZnO, WO_3, CdS, ZnS, ZrO_2, *etc.*) is activated by illumination with light suitable to its band gap energy (*i.e.*, equal or higher than the semiconductor band gap) to catalyze a redox reaction at its surface. Among all, TiO_2 is the most studied photocatalyst in both bulk and nanosized form.

The light irradiation causes excitation of the system, which is followed by an energetic and/or electronic transfer. Due to their band structure, semiconductors with appropriate bandgap show photocatalytic activity: after the generation of an electron-hole (e^--h^+) pair in the semiconductor caused by the light-induced promotion of an electron from the valence band (VB) to the conduction band (CB), such e^--h^+ pair has a sufficient lifetime (in the order of nanoseconds) to allow the transfer of the photoexcited electron or hole to a reagent adsorbed at the catalyst surface. However, the e^--h^+ generation is followed by e^--h^+ recombination, which, to some extent, is an unavoidable process. Indeed, different fates exist for the excited-state conduction band electrons which can recombine with the holes and dissipate the input energy, get trapped in surface states, or react with electron donors and electron acceptors adsorbed on the semiconductor surface. To successfully compete with electron-hole recombination and trap effectively the conduction band electrons or the valence band holes, the respective electron acceptor or donor should be confined to the semiconductor surface

One of the most important prospective technologies for all types of photocatalysts resides in the field of environmental remediation.[15] Issues directly related to human health and the health of the environment such as water and air purity can be effectively addressed through photocatalysis. Photooxidation of organics and toxic biological organisms in water by ozone, a strong oxidant, using UV light, as for instance, is widely used. The use of semiconductor nanoclusters in photocatalysis enables the photooxidation of a large range of toxic chemicals by more effective alignment of valence (holes) bands with the necessary redox potentials of the contaminant. In addition, the correct choice of semiconductor material can allow the oxidation to occur using sunlight, reducing energy costs.

1.5.2. Photovoltaics

The increasing demand for clean energy and the largely untapped potential of the sun as an energy source is making solar energy conversion technology increasingly important.

Generally speaking, photovoltaics (PV) is a method of generating electrical power by converting solar radiation into direct current electricity; this is indeed possible using semiconductors that exhibit the photovoltaic effect.

Photovoltaic power generation employs solar panels composed of a number of solar cells containing a photovoltaic material. Nowadays, the most used materials on the market include silicon (either single-crystalline or multicrystalline or amorophous), cadmium telluride, copper indium selenide or sulfide, gallium arsenide, and others. Although silicon wafer solar cells are still the most commercially widespread as well as the oldest type (first generation of solar cells), the so called second, third and fourth generation solar cells are attracting researchers' attention. They respectively involve thinner, more flexible and more inexpensive amorphous silicon, cadmium telluride and copper-indium-gallium-selenide (main materials for the second generation); plastic (polymer) solar cells, photoelectrochemical solar cells and organic dye-sensitized cells (third generation); while fourth generation solar cells are considered the future of solar technology. Still years off, this category includes such cutting edge technology as quantum dots and nanowires.

Eventually, each material has unique strength and characteristics that influence its suitability for specific applications. For example, PV cell materials may differ according to their crystallinity, band gap, absorption, and manufacturing complexity.

In the case of dye-sensitized solar cells (DSCs), in contrast with the conventional systems where the semiconductor assume both the task of light absorption and charge carrier transport, the two functions are separated. Light is absorbed by a sensitizer, which is anchored to the surface of a wide-band-gap semiconductor. Although other inorganic semiconductors are emerging as promising components in DSCs, TiO_2 is still the preferred inorganic material since it is easy to synthesize and acts as a n-type semiconductor due to the donor-like oxygen vacancies.

Charge separation takes place at the interface via photo-induced electron injection from the dye into the conduction band of the oxide. Carriers are then

transported to the charge collector. The use of sensitizers having a broad absorption band in conjunction with oxide films of nanocrystalline morphology permits to harvest a large fraction of sunlight. Nearly quantitative conversion of incident photon into electric current (IPCE) is achieved over a large spectral range extending from the UV to the near IR region. Solar (standard AM 1.5) to current conversion efficiencies over 12 % have been recently reached.[83] Increasing the module efficiencies of DSCs to more than 14 % would relax the ultralow-cost constraints, thus providing substantial incentive to create laboratory-scale devices with efficiencies greater than 15 %.[84] The relatively slow increase in record values for DSCs over the past ten years could give the impression of a performance ceiling, which is partially justified since conventional iodide- and ruthenium-based DSCs are said to have a realistic maximum possible efficiency of little more than 13 %.[85]
However, to make the big step towards full commercialization of the technology, DSCs have first to demonstrate, as a main priority, significantly enhanced efficiencies, without neglecting other important parameters such as their operating lifetime, the total cost for their integration, as well as their complete life-cycle assessment.[86] Additionally, there are good opportunities and new prospects to produce these cells at lower cost than conventional devices, making dye-sensitized solar cells viable and competitive alternative to traditional silicon solar cells and other new expensive devices. Since DSCs can be produced from low-cost materials using simple manufacturing processes (such as coating and printing), overall manufacturing expenditures are expected to be comparatively low. Other benefits over silicon-based solar cells include the ability to use a variety of designs and colors and achieve high performance under indoor and low light settings. Additionally, changes in the angle at which light hits the surface of the cells have minimal effect on performance. Such advantages are expected to expand the range of use for solar cells, which are ideal for a variety of consumer-related applications in which even conventional solar cells are unsuitable.

1.6. Thin films deposition

The application of thin films in modern technology is widespread, ranging from the above mentioned photovoltaics and photocatalysis to optoelectronics and sensors. "Thin" is a relative term, but

nowadays deposition techniques control layer thickness from fractions of a nanometer (monolayer) to several micrometers.

"Thin film deposition" refers to a technique for applying a thin film of material onto a surface, either previously deposited layers or a different substrate. Deposition techniques fall into two broad categories, depending on whether the process is primarily chemical or physical. The physical methods involve mechanical, electromechanical or thermodynamic means to produce the film. They include sputtering, physical vapor deposition, laser ablation, cathodic arc deposition, electrohydrodynamic deposition, molecular beam epitaxy, and so on. The chemical methods comprise gas-phase deposition methods and solution techniques, in both cases involving a fluid precursor which undergoes a chemical change at a solid surface. Among the former types are chemical vapor deposition[86,87] and atomic layer epitaxy,[89] while spray pyrolysis,[90] sol-gel,[91] spin-[92] and dip-coating[93] methods employ precursor solutions.

In this thesis four methods (drop-casting, spin-coating, spray-pyrolysis, and screen-printing) have been used to deposit TiO_2 for different purposes (characterization, photocatalysis, solar cell devices) on different substrates, ranging from aluminum rough foil to optically transparent electrodes. In this latter case commercial glasses covered with indium-doped tin oxide (ITO) were used for some preliminary experiments. However, a similar high-performance material is fluorine-doped tin oxide (FTO), which provides the following advantages: it is less expensive than ITO, it has lower sensitivity to surface cleaning methods, and, most importantly, more light is obtained at a given voltage. One drawback is that the leakage current is on the order of 1 mA cm^{-2}, which could cause cross talking problems among pixels in certain display applications, but it should not constitute a problem in configurations employed .

Except for the very simple and intuitive drop-casting method, in the following a brief description of the three other methods employed for titania deposition is given.

Spin- coating

Spin coating is a process in which a solution is spread evenly over a surface using centripetal force, resulting in a relatively uniform thin film of a specific thickness. During the spin coating process the solvent evaporates, thus leading to increasing concentration and viscosity, which change the rheology

of the solution. Indeed, the flow of the liquid is governed by a balance between centrifugal driving force and viscous resisting force. Spin coating involves four main processing steps:[94]: i) the material dissolved in a volatile solvent is poured by dripping on the centre of a rotating substrate initially at rest (solution pouring); ii) while the substrate spins, the liquid flows radially driven by the centrifugal force (spin-up); iii) the liquid which reaches the substrate edge is expelled in drops, with viscosity increasing as the film thins down (spin-off); iv) though evaporation occurs at all times from the beginning of the spin-coating process, when spin-off is slow and for less volatile solvents, the evaporation becomes the main mechanism of solvent removal and thinning of the film. To get homogeneous films, several different factors have to be considered, such as the evaporation rate of the solvent, the viscosity of the fluid and concentration of the solution, the angular velocity (rotating speed), the spinning time, the substrate roughness and the air surrounding (temperature and humidity).

Spray pyrolysis

The spray pyrolysis thin film deposition is a simple, cheap and versatile method of preparing thin films for studying and manufacturing DSCs, as precursors can be directly deposited on various substrates in ambient atmosphere.

The typical equipment consists of an atomizer, precursor solution, substrate (FTO) heater, and temperature controller, and the technique involves spraying a solution containing the precursor onto the heated substrate.[95] A crucial role is played by the substrate surface temperature: sprayed droplets or residual particles reaching the hot surface undergo pyrolytic decomposition and form the crystalline film.

The main atomization variables are: droplet size, atomization rate, droplet velocity (affecting residence time) and size dispersion, in term of homogeneity of the final products.

As for the phenomena which take place in a spray pyrolysis deposition, the first step is the evaporation of the solvent from the surface, which accounts for the diffusion of solvent vapor away from droplet, a change in droplet temperature, the diffusion of the solute toward the center of the droplet, and a change in droplet size. Then, precipitation/drying involves volume precipitation or surface precipitation of the solute, followed by the

evaporation of the solvent through the nanoporous crust. The thermal decomposition (pyrolysis) usually forms the nanoporous structure. Finally, the sintering step results in the solidification and adhesion of the crystallites.
Undesired hollow particles are formed when the droplets are large and the droplet number concentration is low. Smaller droplets produce solid particles because the diffusion distance for the solute is shorter, leading to a more uniform concentration distribution within the droplet. Increasing the number of droplets results in a larger solvent vapor concentration in the carrier gas. Consequently, the evaporation rate decreases and precipitation is delayed.[96] Chen *et al.* investigated the correlations between film morphologies and deposition parameters.[97]

Screen printing

This approach is more versatile than traditional printing techniques. Indeed, the surface does not have to be printed under pressure, unlike etching or lithography, and it does not have to be planar. Different inks or pastes can be used to work with a variety of materials, such as textiles, ceramics, wood, paper, glass, metal, and plastic. Screen printing has become increasingly popular recently for the fabrication of electrodes and complete cells for a number of diagnostic and other applications.
The printing apparatus consists of a frame with fabric stretched across it. Parts of the fabric are masked so that the printing areas remain open and permeable to the material that has to be printed. Pastes are then applied and forced by means of a semi-flexible squeegee blade through the masking screen onto the substrate to create the film electrode assembly. The downward pressure closes the gap between the substrate and screen. Finally, the drying and curing steps of the process are also crucial and depends on the desired application.

1.7. References

1. M. Fernández-García, A. Martínez-Arias, J. C. Hanson, J. A. Rodriguez *Chem. Rev.* 104 (**2004**) 4063.
2. J. A. Rodriguez, M. Fernandez-Garcia, Synthesis, Properties and Applications of Solid Oxides. Eds. John Wiley, New York, **2007**; Chapters 4, 5.
3. H. Zhang and J. F. Bandfield *J. Mater. Chem.* 8 (**1998**) 2073.
4. M. Fernandez-Garcia, A. Martinez-Arias, J. C. Hanson, J. A. Rodriguez *Chem. Rev*. 104 (**2004**) 4063.
5. G. J. Exarhos and M. Aloi *Thin Solid Films* 193 (**1990**) 42.
6. K. Yanagisawa and J. Ovenstone *J. Phys. Chem. B* 103 (**1999**) 7781.
7. A. Testino, I. R. Bellobono, V. Buscaglia, C. Canevali, M. D'Arienzo, S. Polizzi, R. Scotti, F. Morazzoni *J. Am. Chem. Soc.* 129 (**2007**) 3564.
8. B. Ohtani, Y. Ogawa, S. Wishimoto *J. Phys. Chem. B* 101 (**1997**) 3746.
9. H. Zhang and J. F. Banfield *Chem. Mater*. 14 (**2002**) 4145.
10. M. Fernandez-Garcia, X. Wang, C. Belver, J. C. Hanson, J. A. Rodriguez *J. Phys. Chem. C* 111 (**2007**) 674.
11. Y. Inoue, S. Yin, S. Uchida, Y. Fujishiro, M. Ishitsura, E. Min, T. Sato, T. *Br. Ceram. Trans*. 97 (**1998**) 222.
12. B. L. Kirsch, E. K. Richman, A. E. Riley, S. H. Tolbert, *J. Phys. Chem. B* 108 (**2004**) 12698.
13. H. Zhang and J. F. Bandfield *J. Phys. Chem. C* 111 (**2007**) 6621.
14. M. Fernandez-Garcia, C. Belver, J. C. Hanson, X. Wang, J. A. Rodriguez *J. Am. Chem. Soc.* 129 (**2007**) 13604.
15. B. L. Abrams and J. P. Wilcoxon *Crit. Rev. Solid State Mater. Sci*. 30 (**2005**) 153.
16. S. H. Kang, J.-Y. Kim, Y.-E. Sung *Electrochimica Acta* 52 (**2007**) 5242.
17. A. M. Stoneham, Theory of defects in solids, Oxford University Press, Oxford, **1975**.
18. G. Pacchioni *Chem. Phys. Chem*. 4 (**2003**) 1041.
19. R. F. Howe and M. Grätzel *J. Phys. Chem*. 89 (**1985**) 4495.
20. X. Zhou, F. Peng, H. Wang, H. Yu, J. Yang *J. Solid State Chem*. 184 (**2011**) 134.
21. S. Livraghi, M. Chiesa, M. C. Paganini, E. Giamello *J. Phys. Chem. C* 115 (**2011**) 25413.
22. G. Barolo, S. Livraghi, M. Chiesa, M. C. Paganini, E. Giamello *J. Phys. Chem. C* 116 (**2012**) 20887.
23. J. I. Pankove, Optical processes in semiconductors. Dover Publications, Inc., New York, **1971**.

24. O. Carp, C. L. Huisman, A. Reller *Progr. Solid State Chem.* 32 (**2004**) 33.
25. S. Sakthivel and H. Kisch *Angew. Chem*. 51 (**2003**) 577.
26. S. Sakthivel and H. Kisch *Angew. Chem. Int. Ed*. 42 (**2003**) 4908.
27. T. Umebayashi, T. Yamaki, H. Itoh, K. Asai *Appl. Phys. Lett*. 81 (**2002**) 454.
28. V. M. Zainullina, V. P. Zhukov, M. A. Korotin, E. V. Polyakov *Phys. Solid State* 53 (**2011**) 1353.
29. S. Tosoni, D. Fernandez Hevia, G. O. Diaz, F. Illas J. *Phys. Chem. Lett.* 3 (**2012**) 2269.
30. D. Li, H. Haneda, S. Hishita, N. Ohashi *Chem. Mater*. 17 (**2005**) 2588.
31. S. Livraghi, M. C. Paganini, E. Giamello, A. Selloni, C. Di Valentin, G. Pacchioni *J. Am. Chem. Soc*. 128 (**2006**) 15666.
32. R. Kun, S. Tarjan, A. Oszko, T. Seemann, V. Zoellmer, M. Bussed, I. Dekany *J. Solid State Chem*. 182 (**2009**) 3076.
33. S. Hoang, S. P. Berglund, N. T. Hahn, A. J. Bard, C. Buddie Mullins *J. Am. Chem. Soc.* 134 (**2012**) 3659.
34. F. Spadavecchia, G. Cappelletti, S. Ardizzone, C. L. Bianchi, S. Cappelli, C. Oliva, P. Scardi, M. Leoni, P. Fermo *Appl. Catal. B: Environ.* 96 (**2010**) 314.
35. W. Choi, A. Termin, M. R. Hoffmann *J. Phys. Chem*. 98 (**1994**) 13669.
36. Y. L. Su, X. W. Zhang, M. H. Zhou, S. Han, L. C. Lei *J. Photochem. Photobio. A: Chem.* 194 (**2008**) 152.
37. M. Ni, M. K. H. Leung, D. Y. C. Leung, K. Sumathy *Renew. Sustain Energy Rev.* 11 (**2007**) 401.
38. M.I. Litter, J. A. Navi, *J. Photochem. Photobio. A: Chem* 98 (**1996**) 171.
39. M. Radecka, M. Rekas, A. Trenczek-Zajac, K. Zarrzewska *J. Power Sources* 181 (**2008**) 46.
40. T. Ihara, M. Miyoshi, Y. Iriyama, O. Matsumoto, S. Sugihara *Appl. Catal. B: Environ*. 42 (**2003**) 403.
41. H. Irie, Y. Watanabe, K. Hashimoto *J. Phys. Chem*. B 107 (**2003**) 5483.
42. T. Lindgren, J. M. Mwabora, E. Avendano, J. Jonsson, A. Hoel, C.-G. Granqvist, S.-E. Lindquist *J. Phys. Chem. B* 107 (**2003**) 5709.
43. R. Asahi, T. Morikawa *Chem. Phys*. 339 (**2007**) 57.
44. Y. Cong, J. Zhang, F. Chen , M. Anpo *J. Phys. Chem. C* 111 (**2007**) 6976.
45. Z. Lin, A. Orlov, R. M. Lambert, M. C. Payne *J. Phys. Chem. B* 109 (**2005**) 20948.
46. R. Asahi, T. Morikawa, T. Ohwaki, K. Aoki, Y. Taga *Science* 293 (**2001**) 269.
47. N. Serpone *J. Phys. Chem. B* 110 (**2006**) 24287.
48. A. V. Emeline, V. N. Kuznetsov, V. K. Rybchuk, N. Serpone *Int. J. Photoen.* 2008 (**2008**) 1.

49. M. Bellardita, M. Addamo, A. Di Paola, L. Palmisano, A. M. Venezia *Phys. Chem. Chem. Phys*. 11 (**2009**) 4084.
50. S. Sato, R. Nakamura, S. Abe, *Appl. Catal. A: Gen.* 284 (**2005**) 131.
51. E. Finazzi, C. Di Valentin, A. Selloni, G. Pacchioni *J. Phys. Chem. C* 111 (**2007**) 9275.
52. C. Liang, C. Liu, F. Li, F. Wu *Chem. Eng. J.* 147 (**2009)** 219.
53. J. Yang, J. Dai, J. Li *Appl. Surf. Sci.* 257 (**2011**) 8965.
54. S. Bingham, W. A. Daoud *J. Mater. Chem.* 21 (**2011**) 2041.
55. H. X. Zhang, Y. X. Xu, Y. G. Wang *J. Solid State Chem.* 177 (**2004)** 3490.
56. W. A. Daoud *J. Mater. Chem.* 21 (**2011)** 2041.
57. Y. Gao, H.-Q. Liu *J. Catal.* 207 (**2002)** 151.
58. W. Chen, P. Yuan, S. Zhang, Q. Sun, E. Liang, Y. Jia *Physica B: Cond. Mat.* 407 (**2012)** 1038.
59. M. Ceotto, L. Lo Presti, G. Cappelletti, D. Meroni, F. Spadavecchia, R. Zecca, M. Leoni, P. Scardi, C. L. Bianchi, S. Ardizzone *J. Phys. Chem. C* 116 (**2012)** 1764.
60. A. K. Ghosh and H. P. Maruska *J. Electrochem. Soc*. 124 (**1977**) 1516.
61. X. X. Slamet, H. W. Nasution, E. Purnama, S. Kosela, J. Gunlazuardi *Catal. Commun*. 6 (**2005**) 313.
62. A.V. Rupa, D. Manikandan, D. Divakar, T. Skvakumar *J. Hazard. Mater*. 147 (**2007**) 906.
63. H. J. Yun, Hyunjoo Lee, N. D. Kim, Y. Jongheop *Electrochem. Commun*. 11 (**2009**) 363.
64. H. M. Sung-Suh, J. R. Choi, H. J. Hah, S. M. Koo, Y. C. Bae *J. Photochem. Photobio. A: Chem*. 163 (**2004**) 37.
65. Z. C. Wang and G. Chumanov *Adv. Mater*. 15 (**2003**) 1285.
66. P. Christopher, D. B. Ingram, S. Linic *J. Phys. Chem. C* 114 (**2010**) 9173.
67. T. Hirakawa and P. V. Kamat *J. Am. Chem. Soc*. 127 (**2005**) 3928.
68. H. Li, X. Duan, G. Liu, X. Liu *J. Mater. Sci*. 43 (**2008**) 1669.
69. H. Wang and J. P. Lewis *J. Phys.: Condens. Matter* 18 (**2006**) 421.
70. C. Sun, Q. Li, S. Gao, L. Cao, J. K. Shang *J. Am. Ceram. Soc*. 93 (**2010**) 3880.
71. K. Kowal, K. Wysocka-Król, M. Kopaczynska, E. Dworniczek, R. Franiczek, M. Wawrzynska, M. Vargová, M. Zahoran, E. Rakovsky, P. Kuš, G. Plesch, A. Plecenik, F. Laffir, S. A.M. Tofail, H. Podbielska *J. Colloid Interf. Sci*. 362 (**2011**) 50.
72. Y. Ohko, T. Tatsuma, T. Fujii, K. Naoi, C. Niwa, Y. Kubotas, A. Fujishima *Nat. Mater*. 2 (**2003**) 29.
73. Q. Qiao, X. Zhang, Z. Lu, L. Wang, Y. Liu, X. Zhu, J. Li *Appl. Phys. Lett.* 94 (**2009**) 074104.
74. N. Crespo-Monteiro, N. Destouches, L. Bois, F. Chassagneux, S.

Reynaud, T. Fournel *Adv. Mater*. 22 (**2010**) 3166.
75. K. Naoi, Y. Ohko, T. Tatsuma *Chem. Commun*. 10 (**2005**) 1288.
76. J. Preclikova, F. Trojanek, P. Nemec, P. Maly *Phys. Status Solidi (C)* 5 (**2008**) 3496.
77. L. Bois, F. Chassagneux, Y. Battie, F. Bessueille, L. Mollet, S. Parola, N. Destouches, N. Toulhoat, N. Moncoffre *Langmuir* 26 (**2010**) 1199.
78. K. Matsubara and T. Tatsuma *Adv. Mater*. 19 (**2007**) 2802.
79. K. Matsubara, K. L. Kelly, N. Sakai, T. Tatsuma *Phys. Chem. Chem. Phys*. 10 (**2008**) 2263.
80. C. Dahmen, A. N. Sprafke, H. Dieker, M. Wuttig, G. von Plessen *Appl. Phys. Lett*. 88 (**2006**) 011923.
81. J. Okumu, C. Dahmen, A. N. Sprafke, M. Luysberg, G. von Plessen, M. Wuttig *J. Appl. Phys*. 97 (**2005**) 094305.
82. J. Virkutyte and R. S. Varma *New J. Chem*. 34 (**2010**) 1094.
83. A. Yella, H.-W. Lee, H. N. Tsao, C. Yi, A. K. Chandiran, M. K. Nazeeruddin, E. W.-G Diau, C.-Y. Yeh, S. M. Zakeeruddin, M. Grätzel *Science* 334 (**2011**) 629.
84. B. E. Hardin, H. J. Snaith, M. D. McGehee *Nat. Photon*. 6 (**2012**) 162.
85. H. J. Snaith *Adv. Funct. Mater.* 20 (**2010**) 13.
86. R. E. Blankenship, D. M. Tiede, J. Barber, G. W. Brudvig, G. Fleming, M. Ghirardi, M. R. Gunner, W. Junge, D. M. Kramer, A. Melis, T. A. Moore, C. C. Moser, D. G. Nocera, A. J. Nozik, D. R. Ort, W. W. Parson, R. C. Prince, R. T. Sayre *Science* 332 (**2011**) 805.
87. W. A. Bryant *J. Mater. Sci*. 12 (**1977**) 1285.
88. R. N. Ghoshtagore *J. Electrochem. Soc*. 125 (**1978**) 110.
89. T. Suntola *Thin Solid Films* 216 (**1992**) 84.
90. R. R. Chamberlin and J.S. Skarman *J. Electrochem. Soc*. 113 (**1966**) 86.
91. C. J. Brinker, A. J. Hurd, G. C. Frye, K. J. Ward, C. S. Ashley *J. Non-Cryst. Solids* 121 (**1990**) 294.
92. C. C. Chen, M. M. Nasrallah, H. U. Anderson *J. Electrochem. Soc*. 140 (**1993**) 3555.
93. C. J. Brinker, G. C. Frye, A. J. Hurd, C. S. Ashley *Thin Solid Films* 201 (**1991**) 97.
94. R. G. Aguilar, J. O. López *Lat. Am. J. Phys. Educ*. 5 (**2011**) 368.
95. D. Perednis and L.J. Gauckler J. *Electroceramics* 14 (**2005**) 103.
96. H. F. Yu and W. H. Liao *Int. J. Heat and Mass Transfer* 41 (**1998**) 993.
97. C. H. Chen, E. M. Kelder, P. J. J. M. van der Put, J. Schoonman *J. Mater. Chem.* 6 (**1996**) 765.

2.
Synthesis

An astounding number of studies can be found in the literature not only about modified TiO_2 but also related to titania synthesized in various sizes and shapes. Indeed, a variety of preparation methods have been investigated for both undoped and doped TiO_2 powders, ranging from the chemical synthesis (*e.g.*, sol-gel,[1,2] chemical treatment of TiO_2[3] or of TiN[4] reverse microemulsions[5,6]) to sophisticated physical methods (*e.g.*, ion implantation[7]). All of these different procedures could lead, in principle, to materials quite different from one another.
Quite often, titania is hydrothermally treated in order to form a crystalline sample at relatively low temperature[8] or even at room temperature.[9]
Furthermore, many of these studies have also included evaluations of the photocatalytic activity of the home-made synthesized materials.[5,10-12] The type of reaction (reduction or oxidation) as well as the reaction conditions seem to play a major role in the outcome of the photoinduced process.

In the present thesis, both home-made (mostly) and commercial (as reference) titania powders were considered. Home-made samples were prepared by three different synthetic procedures: a classic sol-gel method from an alkoxide precursor, a template synthesis and a microemulsion mediated route.
Home-made samples were compared with two commercial titania samples: P25 (Evonik), widely accepted in literature as the benchmark for photocatalytic tests, and Hombikat UV-100 (Sachtleben), a large surface area pure anatase sample.

2.1. Sol-gel synthesis

Sol-gel synthesis is a general synthetic method that allows to obtain high purity metal oxides. The general mechanism is the hydrolysis and polycondensation of the metal alkoxide $M(OR)_x$, which leads to the formation of a hydrated gel, formed by a 3D network of M-O bonds, finally ending with the solvent elimination.

Without presenting operative difficulties, it can be performed in controlled and reproducible conditions. Moreover, the final oxide features may be tailored by varying selected experimental parameters, such as the molar ratio of the components, the duration of hydrolysis and polycondensation steps,

the catalyst type and concentration, the reaction temperature, the technique to remove the solvent and the addition of salts or surfactants to the reaction environment.
Since the obtained product is generally amorphous, further thermal treatments (*i.e*., final calcination step) are needed to improve the crystallinity of the sample and also to remove water, organic residuals and other impurities. However, high temperature treatments cause sintering processes which decrease the surface area, may induce phase transformation from anatase to rutile and provoke the removal of physi-chemisorbed water.

2.1.1. Experimental details (undoped and doped TiO_2)

All reactants employed in this thesis were purchased by Sigma-Aldrich and used without any other purification treatment; doubly distilled water passed through a Milli-Q apparatus (Millipore Corporation) was used as reagent itself and to prepare solutions and suspensions.

In the following, the synthetic procedures for nitrogen-doped TiO_2 (N-TiO_2), praseodymium-doped TiO_2 (Pr-TiO_2), silver-doped (Ag-TiO_2) and nitrogen-, silver-codoped TiO_2 (N,Ag-TiO_2) are described. Undoped reference samples are always produced.

Undoped TiO_2
Undoped titania samples were synthesized by sol–gel route with the following procedure. Titanium (IV) isopropoxide (30.7 mL) (MM = 284.26 g mol^{-1}, d = 0.955 g cm^{-3}, 97%) was used as precursor and put into a 500 mL reactor with 2-propanol (37.6 mL) (MM = 60 g mol^{-1}, d = 0.786 g cm^{-3}). The mixture was kept stirring (300 rpm) for about 10 min to form a solution. A KOH aqueous solution (180 mL) was added dropwise. The molarity of this basic solution was adjusted to fix the pH around 9. It should be noted that the hydrolysis process depends on the pH. Then the possible addition of a base could catalyze the reaction. The gel prepared at basic pH is usually formed in shorter time and at lower temperature than at acidic conditions.[13] The water/alkoxide molar ratio was 100 and the water/2-propanol molar ratio was 20, on the grounds of optimization studies performed by the group.[14] Temperature was kept constant at 25 °C by means of a water/ethylene glycol bath. A white gel was immediately obtained. The same stirring continued for 90 min after the

completion of addition of the alkaline solution. Then, the wet precursor was dried in oven as a xerogel (80 °C overnight) and subsequently calcined for 6 h under oxygen (nitrogen in the case of microemulsion-mediate route) stream (9 NL h^{-1}).
The usual calcination temperature was set to 400 °C, but in some peculiar cases it has been raised to 500 °C or 600 °C. Unless otherwise specified, all xerogels, even for doped samples, were calcined with the above mentioned standard procedure.

N-TiO_2

TiO_2 samples were synthesized by following a classical sol-gel route. A solution of 0.063 mol of $Ti(OC_3H_7)_4$ in 24 mL of 2-propanol was stirred for 10 min at 300 rpm. An aqueous solution containing the base necessary to obtain a final pH of 9 was prepared separately: KOH was adopted for all the samples except for the case of the NH_3-doped powders, in which a buffer solution containing NH_3 and $(NH_4)_2CO_3$ was employed in order to have an initial N/Ti molar ratio of 0.1. In the case of triethylamine- (TEA) and urea-doped samples, the correspondent N-source was also added to the base solution in the stoichiometric amount to obtain an initial N/Ti molar ratio of 0.1. 114 ml of the alkaline aqueous solution were added dropwise to the alkoxide solution, in order to obtain a water/alkoxide molar ratio of 100 and a water/2-propanol molar ratio of 20. The slurry was stirred for 90 min at 25 °C to complete the hydrolysis. Such precursor was dried to a xerogel. Finally the powders were thermally treated at 400 °C for 6 h under O_2 stream (9 NL h^{-1}).
For different purposes, samples doped with triethylamine and urea were synthesized with different initial N/Ti molar ratio: 0.05-0.1-0.2-0.4-0.5.[15]
Titania samples are named by labelling T or TN in the case of the undoped and N-doped oxides respectively, followed by the name of the nitrogen source (urea, TEA or NH_3). In a context where a series of samples with different nominal dopant amount, the label “TN_x”, with x standing for the nominal N/Ti molar ratio, was used. Otherwise, if no specific molar ratio is expressed, N/Ti = 0.1 is meant.

Pr-TiO_2

Once again the synthetic chemical route has been very quick and simple, as follows. TiO_2 precursor was obtained by acidic hydrolysis (pH 4 by adding HCl)

of titanium(IV) isopropoxide in 2-propanol at room temperature. Except for a reference undoped sample (named "T"), a varied amount of $Pr(NO_3)_3$ (Pr/Ti = 0.2-0.3-0.5-0.7 % molar ratio) was dissolved in the aqueous HCl solution, which was added dropwise to the organic mixture. The colloidal suspension was stirred at 300 rpm for 90 min and then dried in the oven at 80 °C overnight. Finally, the dry powder was calcined at 400 °C under oxygen stream. Doubly distilled Milli-Q (Millipore Corporation) water was used and reagent grade chemicals were supplied by Aldrich.

Thus, the praseodymium dopant was introduced into the titania precursor by a synthesis which is typically a bulk procedure. EDX analyses confirmed the presence of the Pr species and the relative concentration in the titania powders (0.18-0.62 Pr/Ti atomic ratio).

Doped titania samples were named "TPr_x", with x standing for the percentage of initial Pr/Ti molar ratio.

Ag-TiO_2 and N,Ag-TiO_2

Single-doped and codoped samples were obtained by following the same procedure described for N-TiO_2 (urea/triethylamine doped) samples, except for the source of the dopant: for Ag-TiO_2, $AgNO_3$ was used, whereas for N,Ag-TiO_2 both $AgNO_3$ and urea were introduced as precursors in the sol-gel procedure. N/Ti and Ag/Ti initial molar ratio are equal to 0.1 and 0.1-0.5, respectively. Ag content higher than 5 % could be detrimental: a 10 % led to a non-homogeneous sample with a decreased surface area and segregated metal species.

The synthetic route for the samples reduction (to obtain metallic Ag) was realized by suspending the calcined powders in methanol, then adding sodium borohydride and heating the suspension at 60 °C for 6 h. Finally, filtration and washing steps were performed to obtain the nanopowders.

Doped titania samples were named "TAg_x", with x standing for the Ag/Ti molar ratio. In the case of codoped samples, the label "TNAg_x" was adopted. Chemically reduced samples were named "T(N)Ag_x_R".

2.2. Template titania materials

Surfactant templating route for the synthesis of mesoporous inorganic frameworks utilizes aggregated structures formed by surfactant molecules as moulds around which a solid inorganic matrix may subsequently be formed. The effective removal of surfactant molecules from this composite can generate porosity according to the size of the aggregates in that solid material. This soft templating approach for the synthesis of ordered nanoporous materials has been extensively practiced since the first report of the synthesis of ordered mesoporous silica, M41S, by the Mobil researchers in 1992.[16] Besides silica-based materials, mesoporous transition metal containing molecular sieves have huge potential applications in the fields of catalysis,[17,18] electronic,[19] magnetic,[20] and optical[21] materials, as they usually have very high surface area and tunable pore diameters. In contrast to Si, the transition metals have ability to form complex with organic ligands by utilizing their coordination sphere. So different organic ligands can act as co-templates along with surfactants/polymer assemblies. This may play a significant role into two possible directions to be taken at the time of the formation of mesoporous transition metal oxide framework. Indeed, on the one hand, as a template the constituent ligand molecules form complexes with the precursor of transition metal; due to this reason the subsequent hydrolysis and condensation rate to metal oxide may be retarded, which is an important criteria for the formation of ordered porous materials. On the other hand, in the mixed surfactant assembly the ligands/cosurfactant may modify the shape and size of the surfactant assemblies either through hydrophobic interaction or interaction between functional groups of ligands and the head groups of surfactants.

Nevertheless, the use of a single specific surfactant allows to tune the synthesis of the transition metal oxide with the desired features. In this context, sol-gel techniques based on low-temperature synthetic processes are to be preferred because higher temperatures are responsible for undesired particle growth and sintering, which decrease surface areas and increase particle sizes.[22]

It has been demonstrated that crystalline anatase TiO_2 powders with hierarchically macro/mesoporous structures, reasonable phase structures and

composition provide a readily accessible porewall system, high specific surface area for light and reactants, and optimize the transport of matter within materials.[23] As for instance, the presence of such mesoscopic pores in TiO_2 is of great importance for dye-sensitized solar cells.

In general, the control of the bimodal porosity is achieved by combining suitable templates for the required length scale organization; for example, tetraalkylammonium ions are used for directing microporosity (<2 nm), long-chain surfactant or block copolymer micelles for mesoporosity (2-50 nm), and polystyrene latexes or organized bacterial threads for macroporosity (>50 nm).[24] Promising results were obtained by Mitra *et al.*[25] by using self-assembly of surfactant (anionic, like sodium dodecyl sulfate, or cationic ones, as cetyltrimethyl ammonium bromide) and cosurfactant (benzyl alcohol) mixtures as templates.

Recently, several reports have confirmed that ordered macro/mesoporous materials including titania can be obtained by the surfactant templating method.[26] However, post-treatment removal (via dissolution and calcination) of the templates to produce the desired titania powder requires additional processing steps that can be costly, wasteful, and of environmental concern. Several attempts to easily solve these problems have been done by working in the absence of auxiliary organic templates and additives: in literature the coupling of hydrothermal reactions with physical phenomena such as microphase separation, transient hydrodynamic gradients, time dependent diffusion gradients and phase transformation of amorphous TiO_2 are reported.[27] For example, three recent works by Yu *et al.*[28-30] describe a facile and environmentally benign synthetic route which is template-free and leads to enhanced photocatalytic activity of trimodal macro/mesoporous titania obtained at room temperature by simple dropwise addition of tetrabutyl titanate to pure water, and then calcined at various temperatures or hydrothermal treatment. However, the template-free synthesis of high-surface-area materials with precise porous structures still remains a great experimental challenge.

Among several liquid-crystal templating (LCT) techniques which exploit three-dimensional structures of ionic/nonionic surfactants and block copolymers,[31] a simple process implying a sol-gel starting reaction, followed by a growth step with surfactants in solution, has been chosen and performed in the presence

of both monomeric and dimeric "gemini-like" alkylpyridinium surfactants. The former was dodecylpyridinium chloride (DPC) and the latter 1,1'-didodecyl-2,2'-trimethylendipyridinium-dicloride "gemini spacer 3" (GS3). Their structures are shown in Fig. 2.1.

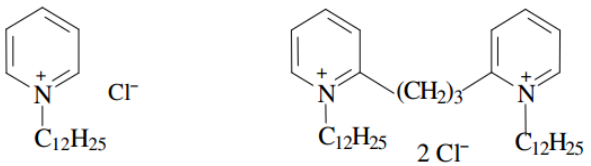

Figure 2.1. Structural formulas of the monomeric dodecylpyridinium chloride (DPC) and dimeric 1,1'-didodecyl-2,2'-trimethylendipyridinium-dicloride "gemini spacer 3" (GS3) surfactants used in the template TiO_2 synthesis.

Together with the surface area/porosity, also the grain size and relative enrichment in the different oxide polymorphs should be controlled through such template routes. In fairly recent times, many studies concerning the practical use of gemini molecules appeared in the literature[32-34] showing that the first speculative interests were followed by practical applications, due to their unusual properties.

2.2.1. Gemini surfactant

Gemini surfactants belong to the family of surfactant molecules possessing more than one hydrophobic tail and hydrophilic head group. Whereas conventional surfactants have a single hydrophobic tail connected to an ionic or polar head group, a gemini has in sequence a long hydrocarbon chain, an ionic group, a spacer spacer (short or long, rigide or flexible, polar or nonpolar), a second ionic group and another hydrocarbon tail. A schematic representation of gemini is given in Figure 2.2.

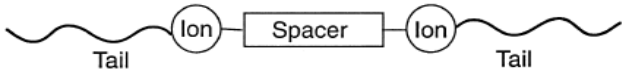

Figure 2.2. Schematic representation of gemini surfactant.

Menger and Littau[35] assigned the name gemini to *bis*-surfactants with rigid spacer (*i.e.*, benzene, stilbene). The name was then extended to other *bis* or double-tailed surfactants, irrespective of the nature of spacers, which can vary

a lot.[36] The great majority of geminis have symmetrical structures with two identical polar groups and two identical chains. A gemini with two Cn (n is the number of alkyl carbon atoms) tails and a Cs (s is the number of alkyl carbon atoms) spacer separating the quaternary nitrogen atoms can be represented as n-s-n.

Gemini can show unique properties, even orders of magnitude more evident than those of comparable conventional surfactants.[37] First of all, these surfactants generally have better surface-active properties than corresponding surfactants of equal chain length. They also have lower critical micellar concentration (CMC) values with respect to their single monomers, and the tendency to form micelles of different shapes and dimensions (*i.e.*, spherical, rodlike, threadlike, vesicles), even at low concentration.

Nowadays, gemini are used as promising surfactants in industrial detergency and have shown efficiency in skin care, antibacterial property, metal-encapped porphyrazine, vesicle formation, construction of high porosity materials, and so on.[38,39]

A detailed review by Hait and Moulik deals with synthesis, structure, critical micellar concentration, surface active properties and uses of gemini surfactant.[34]

CMC for gemini surfactants

Critical micellar concentration (CMC) is the concentration above which monomeric surfactant molecules abruptly aggregate to form micelles. It is determined mostly by tensiometry, conductometry, goniometry, and so on. By using these techniques, not only CMC, but also shape and structure of micelle, surface activity, solubilization, adsorption, wetting and phase behavior of surfactants can be accounted for. As a general rule, the value of CMC decreases with increase in the hydrophobic chain length of the molecule. Hydrophobic interaction opposed by electrostatic repulsion among the ionic head groups drives the process of micellization. A list of CMC data of some gemini tensides with some conventional surfactants determined by static surface tension method is presented by Hait and Moulik.[34] Some general conclusions can be drawn from literature data, starting from the statement that geminis have remarkably low CMC values compared to the corresponding conventional surfactants of equivalent chain length. Furthermore, CMC values are not sensitive to the polarity of short spacers (2–8 atoms). A long

hydrocarbon spacer of 16 methylene groups reduces the CMC almost ten-fold relative to a short spacer of 3–8 methylene groups. Additionally, the long spacer contributes to the overall hydrophobicity of the gemini reducing the monomer solubility and enhancing its tendency to self-assemble. Anionic gemini surfactants have somewhat lower CMC values than their cationic counterparts. Finally, geminis are more responsive to tail length than conventional surfactants. Thus, increasing the tail length by four carbon atoms in a conventional cationic surfactant lowers the CMC 16-fold. A corresponding tail lengthening in the gemini series lowers the CMC by two orders of magnitude.

Thermodynamic parameters for micellization of geminis with varying spacer length (n-s-n; n = 12) obtained by calorimetry are reported by Bai *et al*.,[40] who compared the results with conventional surfactants.

Menger and Littau[35] have reported the use of pinacyanol chloride to investigate micellization of gemini surfactants. Corrin *et al*.[41] had used the method and started a discussion based on the pink–blue color shift. The method is not useful unless it gives a broad range of concentration values as CMC. It is applicable to anionic surfactants as they form a charge transfer complex with the dye rather than the cationic surfactants.

2.2.2. Experimental details

Titania samples' preparation

TiO_2 particles were obtained by following a room-temperature sol-gel reaction starting from $Ti(C_4H_9O)_4$ and adopting a water/alkoxide molar ratio of 81.7 and a water/propanol molar ratio of 8.5. The xerogel powders were purified by centrifugation-resuspension cycles and then powder fractions were aged at 80 °C, at neutral pH, for fixed time-length (5h) with different surfactants concentrations (1-100 mM and 0.1-50 mM for DPC and GS3, respectively). After the ageing step, the suspensions were dried in oven at 80 °C. Finally, the powders were thermally treated at 600 °C for 6 h under oxygen stream (9 NL h^{-1}).

CMC determination

The values of the critical micelle concentration (CMC) of DPC and gemini surfactants were obtained by conductimetric determinations as a function of the temperature. Therefore, using as a guideline an average increasing slope

with the temperature of the CMC of DPC and GS3, obtained from the present results and literature data,[42-44] a concentration range roughly corresponding to a possible CMC at 80 °C was estimated for both surfactants (18-22 mM, for DPC and 2-4 mM in the case of GS3).

Adsorption isotherm measurements

The adsorption isotherm of GS3 at the TiO_2 interface was obtained under the following conditions: T = (25 ± 0.3) °C; pH = 8.0 ± 0.2; equilibration time = 4 h; ionic strength I = 2×10^{-3} M KCl. At the end of the adsorption time the surnatant solution was sampled for the residual surfactant concentration by spectrophotometric characterization at 265 nm for the gemini salt. Data on DPC adsorption on TiO_2, obtained by Koopal et al[42] are elaborated and reported for comparison (T = (21 ± 1) °C; pH = 8.0 ± 0.2; equilibration time = 12 h; ionic strength I = 1×10^{-3} M NaCl). Adsorption isotherms of the two surfactant molecules are reported by plotting the surface excess (Γ) as a function of the final concentration at equilibrium.

2.2.3. Determined features of DPC and GS3 surfactants

Self aggregation features

Due to the formation of colloidal aggregates, many physicochemical properties of a solution show sudden changes when the concentration of a surfactant is exceeded. Usually, such change occurs over a relatively small concentration range which is characteristic of the surfactant. The formation of direct micelles of DPC in water and in aqueous salt solutions has been widely explored by different experimental approaches. By scattering techniques, DPC is reported to form in water, globular micelles with aggregation number of about 20, with a corresponding micellar radius of about 1.9 nm, comparable with the extended length of a C_{12} chain (1.67 nm).[45,46] Spherical DPC micelles are not reported to aggregate in tridimensional structures.[47] The corresponding gemini surfactant (GS3) having short spacer (n = 3) has a particular behavior since it binds its counterions more strongly than the "single" does, as the n-s-n ammonium gemini amphiphiles.[48,49] The lack of conformational freedom could be the result of the sharing of one counterion between the two pyridinium head groups.[43] As a consequence, the short spacer surfactant (GS3) is probably aggregating in non spherical micelles, but

in elongated forms, like rods, as reported in the literature for ammonium gemini surfactants.[50,51] In particular, Manne *et al*.[50] found that simmetric gemini C_{12}-s-C_{12} (s ≤6) surfactants composed by linear hydrocarbon tail with quaternary ammonium headgroups may assemble in hexagonal cylinders in silicate mesophase and parallel cylinders at the mica surface with average spacings of (4.2 ± 0.4) nm. Thus, possibly cylinders in hexagonal arrangement for gemini spacer 3 could also occur at high surfactant concentrations.

Adsorption at TiO_2-solution interface

Figure 2.3 reports the experimental adsorption isotherms, at the TiO_2 solution interface, of both monomeric DPC and dimeric "gemini-like" GS3 surfactants. The shape of the two curves is markedly different. The monomer isotherm (Fig. 2.3a) is S-shaped showing a low adsorbent-adsorbate affinity due to weak interactions between the surfactant and the oxide.[42] Interestingly, it can be proposed that the adsorption leads to the formation of surface ion pairs, $Ti{-}O^{-}Py^{+}$ (the surface charge of TiO_2 at pH 8 is negative), provoking a partial compensation of the surfactant aromatic charge, in accordance with previous XPS results from our group.[31]

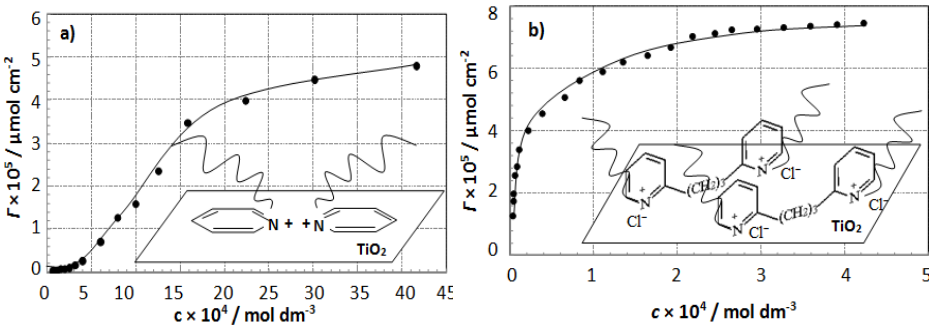

Figure 2.3. Adsorption isotherms (surface excess *vs* equilibrium concentrations) at the TiO_2/solution interface of monomeric DPC (a) and dimeric GS3 (b) surfactants. Inset: sketches of possible disposition/orientations of the adsorbed surfactant at the titania surface; *å* is the adsorbate co-area value, calculated from the maximum coverage (Γ_{max}). Data of DPC are re-elaborated from ref. [42].

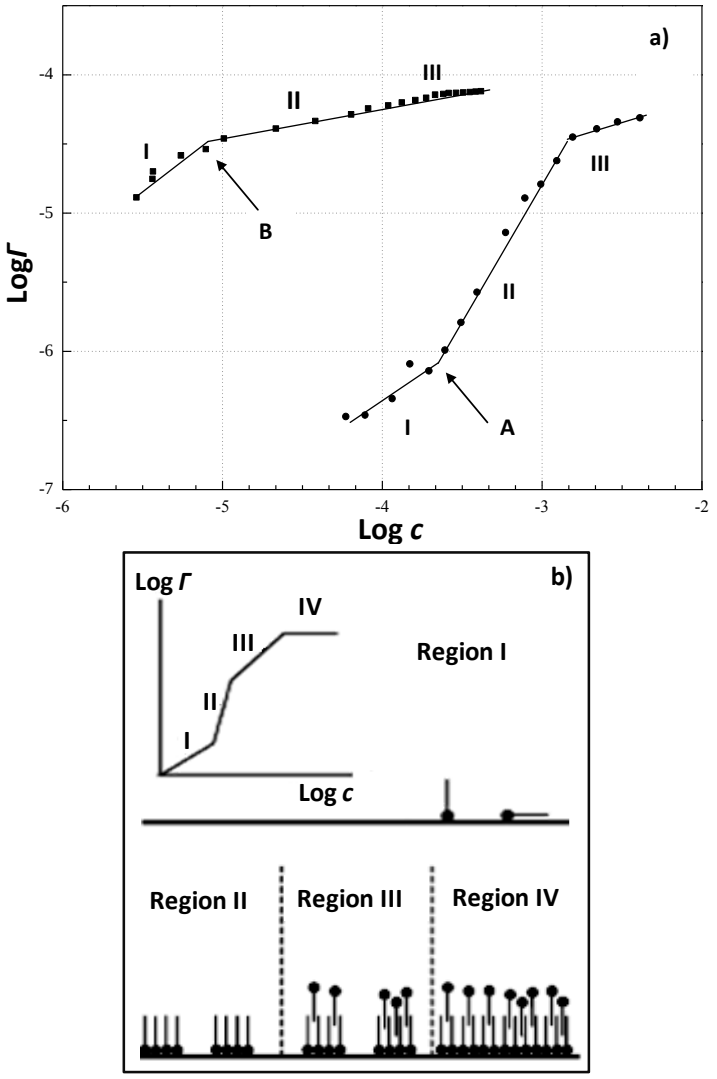

Figure 2.4. Log-log plot of the surface excess (*Γ*) as a function of the equilibrium concentration for DPC and GS3 surfactants (**a**). The general shape of surfactants adsorption isotherms at solid substrates and the proposed four-region model of adsorption (**b**).

The curve pertaining to the gemini (Fig. 2.3b), instead, follows the trend classified in the literature as L-type, which is generally associated with coverage of the solid surface by a monolayer of adsorbate molecules and is characterized by a strong adsorbent-adsorbate interaction. The higher affinity of the gemini GS3 for the solid appears also from the larger adsorbed amounts

(Γ_{max} = 7.7×10^{-5} µmol cm^{-2}) in the quasi-plateau regions with respect to the maximum surface excess (Γ_{max} = 4.8×10^{-5} µmol cm^{-2}) of the monomeric DPC surfactant.

For these reasons, data relative to the DPC and GS3 isotherms were elaborated on the basis of the Langmuir (strong adsorbent-adsorbate interaction, no lateral interactions between adsorbate molecules) and the Frumkin-Fowler-Guggenheim (FFG, weak adsorbent-adsorbate interaction, electrostatic and non-electrostatic lateral interactions[52-54]) model equations, respectively, and the obtained parameters are reported in Table 2.1. The linear correlation (R^2) is good in both cases, justifying the choice of the two different model approaches. The adsorption equilibrium constants (β) and the relative standard adsorption Gibbs energy (ΔG^0) values support the dramatic increase in adsorption at the TiO_2 surface passing from the monomer to the dimer.[55] In the case of the DPC isotherm the lateral interaction parameter (*a*) is positive, *i.e*., it represents electrostatic repulsion interactions between the positive charges of the surfactant headgroups, in agreement with what reported by Mehrian *et al*.[56] in the case of DPC adsorption on clays. They studied the influence of the electrolyte concentration on the adsorption of DPC on Na-kaolinite; an attractive lateral term was obtained only in the case of high ionic strength (100 mM), while repulsion prevailed at lower electrolyte concentrations (5 and 20 mM).

Surfactant	**Isotherm model**	**R^2**	**β**	**ΔG^0 (kJ mol^{-1})**	***a***
DPC	FFG	0.97	160 ± 20	-5.6 ± 0.2	3.2 ± 0.2
GS3	Langmuir	0.997	18000 ± 6000	-27.1 ± 0.3	-

Table 2.1. Data (β, adsorption equilibrium constant; ΔG^0, standard adsorption Gibbs energy; *a*, lateral interaction parameter) from the elaboration of GS3 and DPC isotherms.

The limiting areas (*å*, co-area) for DPC and GS3 – (350 ± 20) and (216 ± 5) Å^{2}mol^{-1}, respectively – at maximum packing (Γ_{max}) calculated from the surface excess at maximum coverage are higher than those present in the literature. Ottewill *et al*.[57] reported two different values of co-area for DPC molecule, obtained by surface tension at the air-water interface, in the case of flat-lying (110 Å^2) and vertical (35 Å^2) orientations. Thus, on the basis these

considerations, the present size of adsorbed DPC molecule could be interpreted as being due to a flat orientation (sketch inset Fig. 2.3), with the formation of a diluted film, characterized by electrostatic repulsion between the charged pyridinium heads. On the contrary, the lower value of *å* for the GS3 surfactant could be ascribable to a vertical orientation (see sketch inset Fig. 2.3) in which, in agreement with our previous results of adsorption of gemini zero-spacer on TiO_2,[55] only one pyridinic group is directly involved in the electrostatic interactions with the oxide, whereas the second one is compensated by its counterion (Cl^-).

As stated above, strong chemi- and physi-interactions with TiO_2, in the absence of lateral interactions, occur for GS3. This feature is amplified by a log-log plot at low surface excess values (Fig. 2.4a). The primary advantage of using a log–log plot is that it amplifies the features of the isotherm at low surface excess values. The general form of isotherms plotted in this manner, and the morphology of adsorbed structures associated with each region are depicted schematically in Fig. 2.4b. Somasundaran *et al*.[58.59] proposed the four-regions model attributed respectively to the adsorption of (I) monomers by electrostatic interactions, (II) surface aggregates (hemimicelles) up to the substratum charge compensation, (III) headout molecules by chain–chain interactions, and (IV) fully formed bilayer. In the case of the examined samples, only three regions are appreciable since the isotherms are limited to monolayer coverage (for both surfactants, c_{SURF} < CMC) without the complete formation of bilayers. The surfactant concentration relative to the beginning of hemimicelle formation is about 1.8×10^{-4} M and 8.0×10^{-6} M, respectively for DPC (A point) and GS3 (B point); these values could be compared with the bulk CMC values (DPC: 1.6×10^{-2} M, GS3: 1.5×10^{-3} M at 25 °C) obtained from conductimetric/tensiometric determinations,[42-46] following the criterion reported by Fuerstenau[60] that hemimicelles may occur about 1/100th of the CMC.

The trend between the two isotherms (the shift along the x-axis, the variation of the slope in the different regions and the distribution of surface excesses) is the expected one due to the presence of a second homologous pyridinic ring in the case of GS3 species. For both surfactants, the slope of the plot in the region I (the Henry region), is unity in the ideal situation (ΔG^0 is constant).[42] The initial slope of the experimental isotherms cannot be determined accurately, but they are, within experimental error, almost equal to unity. The

slope of the DPC curve increases passing from region I to region II, where hemimicelles form, indicating that the adsorption is enhanced by the formation of surface aggregates. This trend is typical for S-shaped isotherms.[42] In the case of the gemini molecules the slope is, instead, depressed in the region of hemimicelles, possibly due to the steric hindrance.

2.3. Microemulsion-mediate titania materials

General aspects

An emulsion is generally defined as a thermodynamically stable, isotropic and transparent mixture composed of at least three components: two immiscible liquids (typically water and oil) and a surfactant, which plays the role of separating the former two by a thin monolayer. It can be either water in oil (see Fig. 2.5, oil in water, or bicontinuous.[61] Such system can be very complicated, containing a great variety of complex structures, such as liquid crystals, gels, vesicles, micelles, *etc*.[62]

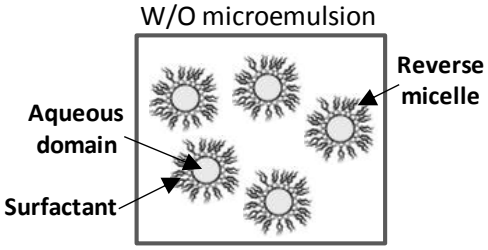

Figure 2.5. A pictorial representation of a water-in-oil microemulsion.

The use of a suitable emulsifier allows to disperse an aqueous solution containing the metal precursor into the oil phase, forming nanosized droplets due to minimization of the surface energy. Chemical reaction or precipitation can take place within each single droplet, giving rise to final products maintaining the main characteristics of the starting nanodroplets in terms of size and shape. Moreover, during the precipitation stage, each particle is coated by a surfactant film preventing the particle agglomeration.[63]

The stability of the microemulsion, which affects the success of the synthesis, depends on several process parameters, in particular the water-to-oil ratio, the type and content of emulsifier, the precursor concentration into the solution and the mixing conditions.

The advantage with the microemulsion route is that the size of the particles can be affected by the ratio of surfactant to water. The size of the water droplets in the reverse microemulsions is approximately the same as that of the produced particles.[64] When water in oil microemulsions are used, water droplets are typically in the size range of a few nanometers to 100 nm, and they can be used as micro/nanoreactors for chemical reactions[5,64] as illustrated by Andersson *et al.* in the sketch reported in Fig. 2.6.[5]

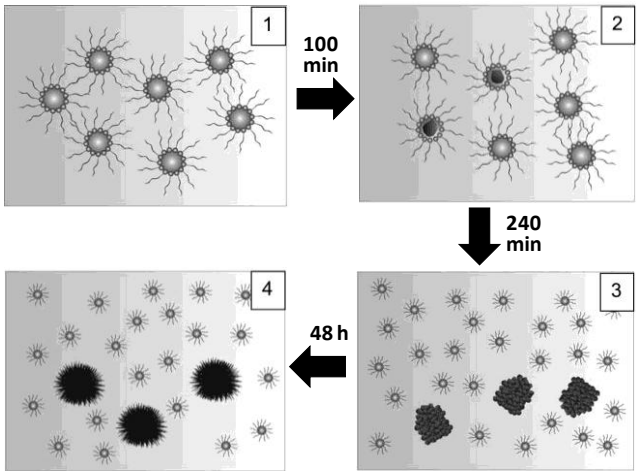

Figure 2.6. Schematic overview of the different stages of titania formation as a function of time using the microemulsion route at room temperature: stable water-in-oil microemulsion to which the Ti precursor (titanium alkoxide) is added, being soluble in the continuous organic phase (1); hydrolysis and formation of water-soluble species within the water droplets (2); aggregation of titania particles (3); crystallization process (4). Re-drawn from ref [5].

By dissolving metal salts in the water pools followed by the addition of a reducing agent, researchers have prepared metals such as Cu, Pt, and Pd in the form of nanoparticles.[65,66] If, instead, two microemulsions containing salts such as $Cd(NO_3)_2$ and Na_2S are used, water insoluble compounds such as CdS can be prepared as nanoparticles.[67,68]

Wu and co-workers showed that nanoparticles of both anatase and rutile TiO_2 can be prepared at 120 °C by hydrothermal treatment of microemulsions.[69] Although their interpretation that the microemulsion templates the TiO_2 particle size at 120 °C was fairly wrong, as shown by Andersson *et al.*[5], their

outcome can be considered of great interest since they yielded the two polymorphs using the same temperature and the same synthetic method. Later on Andersson *et al.* performed a similar synthesis at room temperature, resulting in nanocrystalline rutile with an extremely high specific surface area (*ca.* 300 m^2g^{-1}). Furthermore, Cong *et al.*[70] successfully synthesized nitrogen-doped nanocrystalline titania by a microemulsion-hydrothermal process, avoiding high calcination temperatures and consequently averted the agglomeration and sintering of the TiO_2 particles. Triethylamine, urea, thiourea, and hydrazine hydrate were employed as nitrogen sources. More recently, the reactive microemulsion synthesis has been further studied by Deorsola and coworkers starting from a $TiCl_4$ solution emulsified into the oil phase.[71] The precipitation of spherical and ultrafine titania particles occurred due to the high instability of the Ti precursor and the interactive contact among nanodroplets. This is one of the rare case in which the process parameters were varied in order to investigate their effect on the microemulsion stability and consequently on the structural and morphological characteristics of the particles. As a result, the synthesis parameters were optimized in order to achieve spherical and nanosized titania particles.

The interest of the present work was limited to microemulsions showing a simple structure, namely water-in-oil microemulsions, as the purpose of the method described hereafter was the optimization of the process parameters for the achievement of ultra fine and nanometric particles.

Thus, after having used surfactants to dictate the shape of the final TiO_2 materials (particles and pores) as in the template route, now surfactants are used to stabilize an emulsion, which plays the role of “nano-reactor” for the oxide material.

2.3.1. Surfactants used

In the syntheses *via* microemulsions three different surfactants were employed: LUTENSOL TO389, TWEEN 80, and TRITON X-100. Details are reported in Table 2.2 and their structural formulas are depicted in Fig. 2.7.

Surfactant (short name)	Chemical name	MM (g mol^{-1})	d (g mL^{-1})	cloud point (°C)	CMC (mM)
LUTENSOL TO389	polyoxyethylene saturated iso-C_{13} ether	500	0.99	70	n.d.
TWEEN 80	polyoxyethylene (20) sorbitan monooleate	1310	1.08	65	0.01
TRITON X-100	polyoxyethylene octyl phenyl ether	625	1.07	66	0.50

Table 2.2. Main features of the surfactant employed.

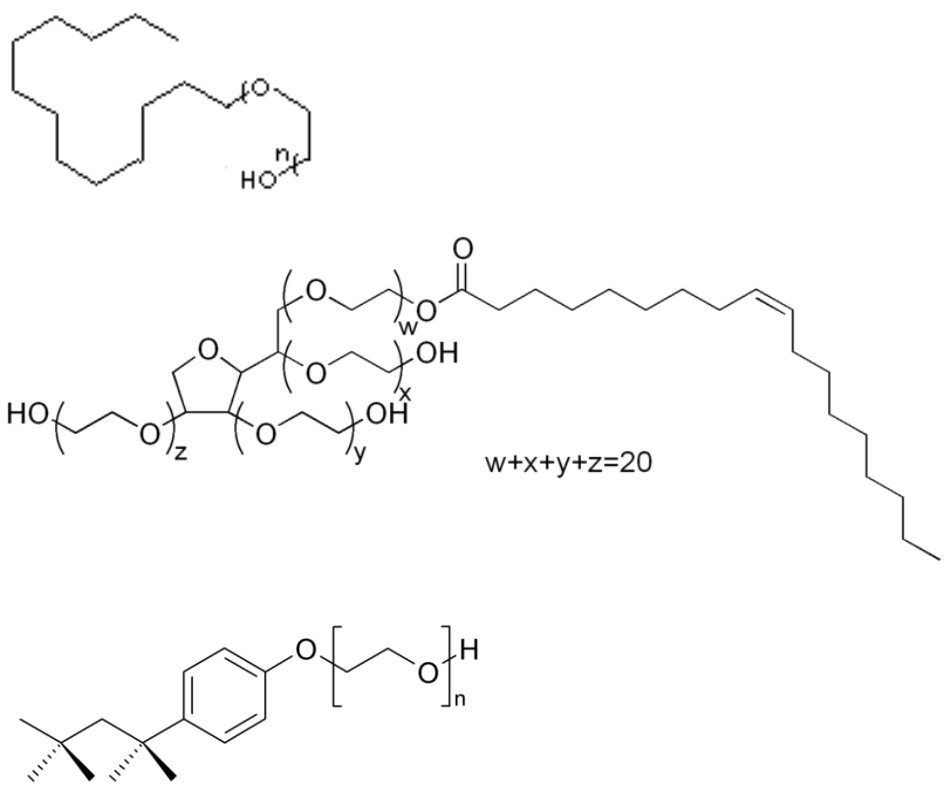

Figure 2.7. Structures of the surfactant employed in the microemulsion synthetic routes: LUTENSOL TO389 (top), TWEEN 80 (center), and TRITON X-100 (bottom).

In the following, thermogravimetric analysis (TGA) performed on the pure surfactants are reported. The purpose of such analyses was to identify the proper calcination temperature according to the degradation of the surfactant Degradation of LUTENSOL TO389 starts at about 224 °C and most of the surfactant is degraded at 276 °C. It is however necessary to go up to 446 °C to complete the process, as shown in Figure 2.8.
This is the reason why the calcinations temperature had been set to 500 °C. Nitrogen was chosen instead of oxygen, since it turned out to be more effective (oxygen led to a final powder not properly white, probably owing to the faster and more complete combustion which leads to carbonaceous residues).

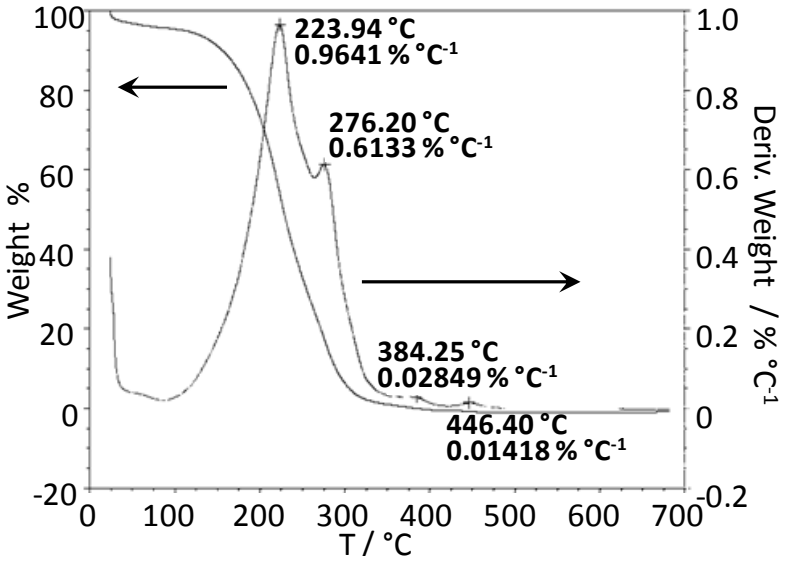

Figure 2.8. Thermogravimetric analysis of LUTENSOL TO389 surfactant.

TGA analysis on TWEEN 80 appears much more simple than the previous case (surfactant LUTENSOL TO389): as shown in Fig. 2.9, degradation occurs in a sole step at a temperature not much higher than 400 °C. Unfortunately, a residue of the surfactant equal to 2.3 % of the total weight is not eliminated even raising the temperature up to 700 °C.

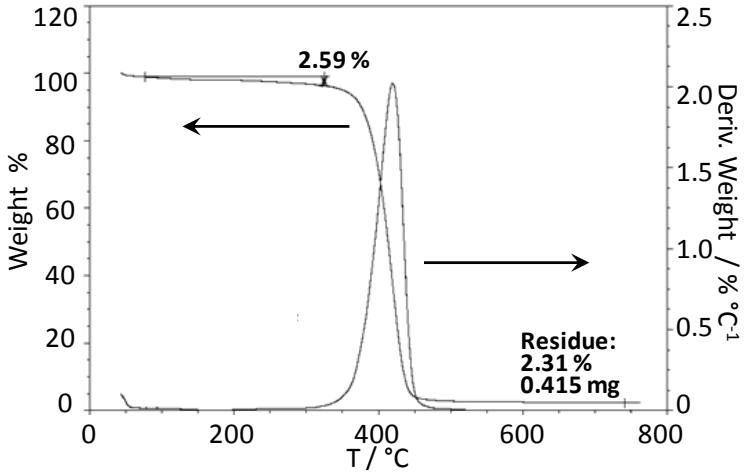

Figure 2.9. Thermogravimetric analysis of TWEEN 80 surfactant.

Degradation of TRITON X-100 occurs at 377 °C and is completed a few degrees above 400 °C (Fig. 2.10). For this reason, in the case of this surfactant, the calcination step has been performed at 400 °C, under nitrogen stream.

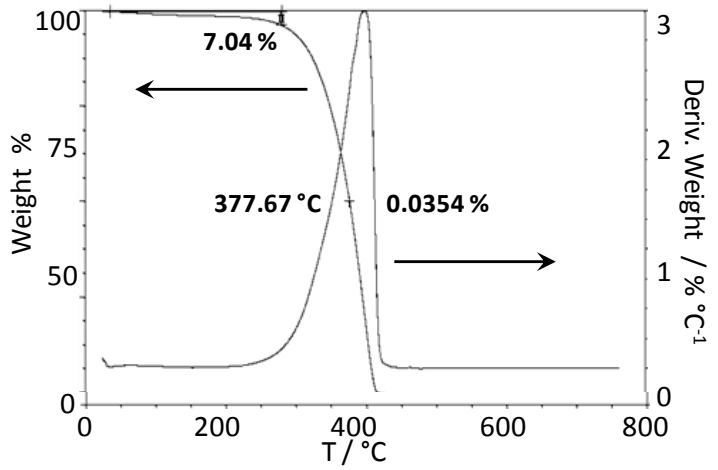

Figure 2.10. Thermogravimetric analysis of TRITON X-100 surfactant.

2.3.2. Experimental details

Microemulsion stabilization and titania samples' preparation

Most of the research on this system has been focused on the choice of the surfactant, on the determination of molar ratios among reagents, which primarily affect the microemulsion stability before and after reaction (Ti

precursor hydrolysis and polycondensation), on the purification of the product (washing and filtration steps) and, related to this latter issue, also on the conditions to be adopted for the final thermal treatment.

The surfactant was dissolved in n-heptane and the solution was stirred for about 30 min. Then, the proper amount of water was slowly added at room temperature, thus forming the quite viscous microemulsion. After 90 min stirring, a solution containing $Ti(OPr)_4$ and i-propanol was added drop-wise. The resulting precursor-containing mixture turned into a milky-white suspension and was kept stirring 10 h. Then, the precipitate was recovered by either centrifugation or filtration and washed several times with deionized water (900 mL) and absolute ethanol (60 mL totally), in order to remove solvents and surfactant. The residual wet solid was dried in oven at 90 °C and subsequently calcined at 500 °C for 6 h under N_2 stream (9 NL h^{-1}). Calcination at 400 °C (sufficient for the complete removal of the surfactant) was maintained only for samples obtained with TRITON X-100: In Table 2.3 the amounts of all components used in the syntheses are reported.

The amount of surfactant was varied in the range 0.3-1.2 surfactant/Ti molar ratio. In some cases, a mixture of two surfactants (LUTENSOL TO389 and TWEEN 80) has been used instead of a single one.

Preliminary experiments were carried out using different amount of the microemulsion components. The final choices were made with aim of keeping the surfactant amount not too high and, at the same time, maintaining the microemulsion stable all over the reaction time. Accordingly, the volume percentages of surfactant and water were varied within the one-phase microemulsion region, detecting the phase boundaries as those compositions where samples became turbid.[72]

In Table 2.4 samples are listed as they are named in the following and details on the amount of surfactant employed are reported.

Reference samples obtained by a traditional sol-gel route (see paragraph 2.1.1) are reported for comparison and labeled as “T_400N” and “T_500N”, according to the different calcination temperatures (suffix “N” refers to the calcination atmosphere, namely nitrogen, always used for samples obtained from microemulsions, instead of oxygen, which is more commonly used throughout this thesis). It should be noted that the only sample obtained *via* microemulsion calcined at 400 °C is the one deriving from TRITON X-100,

because of the complete decomposition of the surfactant at that temperature.

Chemical	MM (g mol^{-1})	m (g)	d (g mL^{-1})	vol (mL)	mol
$Ti(OPr)_4$	284	14.33-7.33	0.955	7.50	0.050-0.025
i-propanol	60	12.50	0.800	15.9	0.417-0.208
n-heptane	100	48.15	0.683	70.5	0.961-0.481
water	18	17.00	1.000	17.0	1.875-0.938
LUTENSOL TO389	500	7.43/14.85 /22.28	0.990	7.5/15.0/23.0	0.015/0.030 /0.045
TWEEN 80	1310	26.74	1.076	24.85	0.021
LUT : TWEEN	-	-	-	-	0.0067:0.0158 /0.002:0.020
TRITON X-100	625	18.90	1.070	17.70	0.030

Table 2.3. Details of all components used for the syntheses *via* microemulsion route.

Sample	Surfactant(s)	Surf/Ti molar ratio
T_L0.3	LUTENSOL TO389	0.3
T_L0.6	LUTENSOL TO389	0.6
T_L0.9	LUTENSOL TO389	0.9
T_TW0.9	TWEEN 80	0.9
T_TW0.6L	TWEEN 80 + LUT. TO389	0.9 (0.6 + 0.3)
T_TW0.8L	TWEEN 80 + LUT. TO389	0.9 (0.81 + 0.09)
T_TW0.09L	TWEEN 80 + LUT. TO389	0.9 (0.09 + 0.81)
T_TX1.2	TRITON X-100	1.2

Table 2.4. Labels used for samples obtained *via* microemulsion route and details on the amount of surfactant employed.

2.4. Samples ID

Throughout all the thesis, the undoped TiO_2 sample, prepared by the simple sol-gel synthesis and calcined at 400 °C was labeled as T. Whenever other calcination temperatures or atmospheres (N_2 instead of O_2) have been used, they are explicitly written after "T" (*e.g.*, T_500N stands for TiO_2 obtained with the basic sol-gel procedure and annealed under nitrogen stream – same conditions as for oxygen).
For all other types of TiO_2, valid samples ID are those explained at the end of each experimental section related to a specific synthesis (see above).

To summarize, besides samples prepared by template and microemulsion routes, different sets of samples were obtained by sol-gel reaction:

- undoped TiO_2 calcined at 400 °C or higher temperatures (**T, T_600, T_400N, T_500N**)
- N-doped TiO_2,: TEA-doped / urea-doped / NH_3-doped titania (**TN_TEA / TN_urea / TN_NH_3**)
  The reason why in some cases no N sources are explicitly written is that the comparison is not meant among different N sources but among different starting dopant/Ti ratios.
- Pr-doped TiO_2 from $Pr(NO_3)_3$, with different Pr/Ti molar ratio (**TPr**)
- Ag-doped TiO_2 from $AgNO_3$, with different Ag/Ti molar ratio (**TAg**)
- N,Ag-codoped TiO_2 from urea and $AgNO_3$ (**TNAg**)

The following table (Table 2.5) summarizes all the classes of synthesized samples (except for home-made TiO_2 films used for solar cells), with their main synthetic features.

Sample	Synthesis	Dopant	Surfactant
T / T_x / T_xN (x = calcination temperature)	sol-gel	-	-
TN_TEA / TN_urea / TN_NH_3 / TN_x (x = N/Ti nominal molar ratio)	sol-gel	N *(TEA / urea / NH_3)*	-
TPr_x (x = Pr/Ti % molar ratio)	sol-gel	Pr *($PrNO_3$)*	-
TAg_x (x = Ag/Ti molar ratio)	sol-gel	Ag *($AgNO_3$)*	-
TNAg_ x (x = Ag/Ti molar ratio)	sol-gel	N *(urea)* Ag *($AgNO_3$)*	-
no abbreviations	template	-	DSC / GS3
see Table 2.4	microemulsion	-	LUTENSOL TO389 and/or TWEEN 80 / TRITON X-100

Table 2.5. Summary of all home-made sample categories.

As the Table 2.5 shows, the set of home-made powders included very different samples. Several synthetic features were systematically varied:

- the synthetic route (sol-gel, template or microemulsion-mediate route);
- the type of introduced dopant (N, Pr, Ag);
- in the case of N-doped TiO_2, the source of dopant: inorganic (NH_3) or organic (triethylamine, tea).

2.5. References

1. S. Sakthivel, M. Janczarek, H. Kisch *J. Phys. Chem. B* 108 (**2004**) 19384.
2. S. Sato, R. Nakamura, S. Abe Appl. Catal. B: Environ. 284 (**2005**) 131.
3. Y. Nosaka, M. Matsushita, J. Nasino, A. Y. Nosaka *Sci. Technol. Adv. Mat*. 6 (**2005**) 143.
4. T. Morikawa, R. Asahi, T. Ohwaki, K. Aoki, Y. Taga *Jpn. J. Appl. Phys*. 40 (**2001**) L561.
5. M. Andersson, L. Osterlund, S. Ljungstrom, A. Palmqvist J. Phys. Chem. B 106 (**2002**) 10674.
6. M. S. Lee, S. S. Park, G. D. Lee, C. S. Ju, S. S. Hong *Catal. Today* 101 (**2005**) 283.
7. A. Ghicov, J. M. Macak, H. Tsuchiya, J. Kunze, V. Haeublein, L. Frey, P. Schmuki *Nano Lett*. 6 (**2006**) 1080.
8. S. Han, S. H. Choi, S. S. Kim, M. Cho, B. Jang, D. Y. Kim, J. Yoon, T. Hyeon *Small* 1 (**2005**) 812.
9. M. Yan, F. Chen, J. Zhang, M. Anpo *J. Phys. Chem. B* 109 (**2005**) 8673.
10. A. Kiselev, M. Andersson, A. Mattson, A. Shchukarev, S. Sjöberg, A. Palmqvist, L. Osterlund *Surf. Sci.* 584 (**2005**) 98.
11. Y. Mori, Y. Okastu, Y. Tsujimoto *J. Nanopart. Res*. 3 (**2001**) 219.
12. M. S. Lee, S. S. Park, G. D. Lee, C. S. Ju, S. S. Hong *Catal. Today* 101 (**2005**) 283.
13. A. Hernandez, L. M. Torres-Martinez, T. L. *Mater. Lett.* 54 (**2002**) 62.
14. C.L. Bianchi, S. Ardizzone, G. Cappelletti. Nanocrystalline Oxides: Surfactants-Assisted Growth. Dekker Encyclopedia of Nanoscience and Nanotechnology. Page: 1-10. **2006**.
15. F. Spadavecchia, G. Cappelletti, S. Ardizzone, C. L. Bianchi, S. Cappelli, C. Oliva, P. Scardi, M. Leoni, P. Fermo *Appl. Catal. B: Environ.* 96 (**2010**) 314.
16. C. T. Kresge, W. J. Leonowicz Roth, J. C. Vartuli, J. S. Beck Nature 359 (**1992**) 710.
17. K. Nakajima, I. Tomita, M. Hara, S. Hayashi, K. Domen, J. N. Kondo *Adv. Mater.* 17 (**2005**) 1839.
18. A. Bhaumik, M. P. Kapoor, S. Inagaki *Chem. Commun*. (**2003**) 470.
19. D. A. Barros Filho *J. Appl*. Phys. 101 (**2007**) 34309.
20. J. W. Long, M. S. Logan, C. P. Rhodes, E. E. Carpenter, R. M. Stroud, D. R. Rolison *J. Am. Chem. Soc*. 126 (**2004**) 16879.
21. A. B. Dros, D. Grosso, C. Boissiere, G. J. D. A. A. Soler-Lia, P.-A. Albouy, H. Amenitsch, C. Sanchez *Micropor. Mesopor*. *Mater*. 94 (**2006**) 208.
22. S. Fujihara, T. Maeda, H. Ohgi, E. Hosono, H. Imai, S.-H. Kim *Langmuir*

20 (**2004**) 6476.
23. M. Grätzel *Nature* 414 (**2001**) 338
24. B. Zhang, S. A. Davis, S. Mann *Chem. Mater.* 14 (**2002)** 1369.
25. A. Mitra, A. Bhaumik, B. K. Paul *Microp. Mesop. Mater*. 109 (**2008**) 66.
26. Z. Y. Yuan, B. L. Su *J. Mater. Chem*. 16 (**2006**) 663.
27. A. Collins, D. Carriazo, S. A. Davis, S. Mann *Chem. Mater*. 14 (**2002**) 1369.
28. J. G. Yu, J. F. Xiong, B. Cheng, S. W. Liu *Appl. Catal. B: Environ.* 60 (**2005**) 211.
29. J. G. Yu, Y. R. Su, B. Cheng *Adv. Funct. Mater*. 17 (**2007**) 1984.
30. J. Yu, W. Wang, B. Cheng, B. Huang, X. Zhang *Res. Chem. Intermed*. 35 (**2006**) 452.
31. S. Ardizzone, C . L. Bianchi, G. Cappelletti *Surf. Interface Anal*. 38 (**2006**) 452.
32. M. J. Rosen and D. J. Tracy *J. Surfactants Deterg*. 1 (**1998**) 547.
33. F. M. Menger and J. S. Keiper *Angew. Chem*. 39 (**2000**) 1906.
34. S. K. Hait and S. P. Moulik *Current Sci*. 82 (**2002**) 1101.
35. F. M. Menger and C. A. Littau *J. Am. Chem. Soc*. 113 (**1991**) 1451.
36. F. M. Menger, J. S. Keiper, B. N. A. Mbadugha, K. L: Caran, L. S. Romsted *Langmuir* 16 (**2000**) 9095.
37. M. J. Rosen and D. J. Tracey *Chem. Tech*. 23 (**1993**) 30.
38. M. Macian, J. Seguer, M. R. Infante, C. Selve, M. P. Vinardell *Toxicology* 106 (**1996**) 1.
39. L. Perez, J. L. Torres, A. Manresa, C. Solans, M. R. Infante *Langmuir* 12 (**1996**) 5296.
40. G. Bai, J. Wang, H. Yan, Z. Li, K. Thomas *J. Phys. Chem. B* 105 (**2001**) 3105.
41. M. L. Corrin, H. B. Klevens, W. D. Harkins *J. Chem. Phys*. 14 (**1946**) 480.
42. L. K. Koopal, E. M. Lee, M. R. Böhmer *J. Colloid Interface Sci.* 170 (**1995**) 85.
43. P. Quagliotto, G. Viscardi, C. Barolo, E. Barni, S. Bellinvia, E. Fisicaro, C. Compari *J. Org. Chem.* 68 (**2003**) 7651.
44. M. A. Bhat, A. A. Dar, A. Amin, P. I. Rashid, G. M. Rather *J. Chem. Thermodynamics* 39 (**2007**) 1500.
45. J. J. Galan, A. González-Pérez, J. L. Del Castillo, J. R. Rodríguez *J. Thermal Anal. Calorim.* 70 (**2002**) 229.
46. K. Fujo and S. Ikeda *Bull. Chem. Soc. Jpn.* 65 (**1992**) 1406.
47. E. Alami, G. Beinert, P. Marie, R. Zana, *Langmuir* 9 (**1993**) 1465.
48. R. Zana, M. Benrraou, R. Rueff, *Langmuir* 7 (**1991**) 1072.
49. R. Zana *Langmuir* 12 (**1996**) 1208.
50. S. Manne, T. E. Schäffer, Q. Huo, P. K. Hansma, D. E. Morse, G. D.

Stucky, I. A. Aksay, *Langmuir* 13 (**1997**) 6382.
51. M. Cao, X. Song, J. Wang, Y. Wang *J. Colloid Interface Sci.* 300 (**2006**) 519.
52. A. N. Frumkin *Z. Phys. Chem.* (Leipzig) 166 (**1925**) 466.
53. R. H. Fowler, E. A. Guggenheim, Statistical Thermodynamics. Cambridge University Press, London, **1965**, p. 558.
54. A. de Keizer and L. G. J. Fokkink, *Colloids Surfaces* 51 (**1990**) 323.
55. S. Ardizzone, C. L. Bianchi, P. Quagliotto, G. Viscardi *Surf. Interface Anal.* 34 (**2002**) 652.
56. T. Mehrian, A. de Keizer, A. J. Kortweg, J. Lyklema *Colloids Surfaces* 73 (**1993**) 133.
57. R. H. Ottewill, M. G. Rasogi *Trans. Faraday Soc.* 56 (**1960**) 880.
58. P. Somasundaran and D. W. Fuerstenau *J. Phys. Chem*. 70 (**1966**) 90.
59. A. Fan, P. Somasundaran, N. J. Turro *Langmuir* 13 (**1997**) 506.
60. D. W. Fuerstenau and H. M. Yang *Langmuir* 7 (**1991**) 3138.
61. P. Kumar, K. L. Mittal, Handbook of Microemulsion Science and Technology. Mercel Dekker, New York, **1999**.
62. V. Degiorgio, M. Corti, in: V. Degiorgio, M. Corti (Eds.), Physics of Amphiphiles: Micelles, Vesicles and Microemulsions. North Holland, Amsterdam, **1985**.
63. H. Herrig and R. Hempelmann *Mater. Lett*. 27 (**1996**) 287.
64. M. P. Pileni *Langmuir* 13 (**1997**) 3266.
65. D. H. Chen, J. J. Yeh, T. C. Huang *J. Colloid Interface Sci*. 215 (**1999**) 159.
66. J. Qi, J. Ma, J. Shen *J. Colloid Interface Sci*. 186 (**1997**) 498.
67. M. L. Curri *J. Phys. Chem. B* 104 (**2000**) 8391.
68. A. Agostiano, M. Catalano, M. L. Curri, M. Della Monica, L. Manna, L. Vasanelli *Micron* 31 (**2000**) 253.
69. M. Wu, J. Long, A. Huang, Y. Luo *Langmuir* 15 (**1999**) 8822.
70. Y. Cong, J. Zhang, F. Chen, M. Anpo *J. Phys. Chem. C* 111 (**2007**) 6976.
71. F.A . Deorsola and D. Vallauri *Powder Technology* 190 (**2009**) 304.
72. S. Lopez-Cuenca, L. A. Perez Carrillo, M. Rabelero Velasco, R. Diaz de Leon, H. Saade, R. G. Lopez, E. Mendizabal, J. E . Puig *J. Nanomater*. 2011 (**2011**) 431382.

3.
Basic Characterizations

This chapter is comprised of results deriving from different techniques used to characterize nanosized titanium dioxide obtained in powdery form. While some methods are commonly adopted, other types of measurements are definitely less routinely applied to TiO_2 or less used in general. A separate chapter (chapter 4) is dedicated to a particular class of characterization techniques, namely electrochemical ones, for their relevant, quite unusual and extensive use in this thesis.

Depending on the nature of the samples and according to specific purposes, not all the techniques presented have been applied to all classes of home-made TiO_2 materials. As for instance, the synthesized series of Pr-doped titania with different Pr amounts has been widely characterized with the final aim of assessing the location of the dopant species into the TiO_2 lattice, which is one of the debated aspect concerning the doping of TiO_2.

For such a reason, this chapter, rather than tracing a structural classification of all the employed methods, is more focused on the different types of TiO_2 samples, giving for each of them a detailed description of peculiar aspects. Starting from titania materials obtained *via* template and microemulsion routes (paragraphs 2.2 and 2.3, respectively), doped samples are explored, with a more thorough study performed on N-TiO_2 nanoparticles.

First of all, the main structural and morphological features of the two commercial samples used in the present thesis for comparison with selected home-made samples are summarized in Table 3.1 and compared with a home-made undoped sample (labeled as “T”, see paragraph 2.1.1 for the synthetic procedure). Hombikat UV100 (Sachtleben) is a high purity anatase powder, characterized by the highest surface area among all the samples presented in this thesis. The commercial P25 (Evonik), very often used in the TiO_2 literature as a benchmark, is a mixed anatase-rutile TiO_2 powder with a surface area much lower than the home-made samples, the largest crystallite size and highly dispersibility in both aqueous and polar organic solvents.

Sample	% A	% B	% R	$<D_{anat}>$ (nm)	S_{BET} (m^2g^{-1})	V_{pore} (mL g^{-1})
P25	75	-	25	30.0 ± 0.3	50	0.26
Hombikat UV100	100	-	-	10.0 ± 0.3	354	0.35
T	66	37	-	4.8 ± 0.1	150	0.44

Table 3.1. Phase composition (A=anatase, B=brookite, R=rutile), average diameter of the anatase crystallites (XRPD), specific surface areas and pore volumes (BET-BJH analysis) for two commercial samples and a home-made one obtained by sol-gel synthesis (see paragraph 2.1.1.).

3.1. Density functional theory

In this thesis, density functional theory (DFT) calculations have been performed by a theoretical chemistry group (Dr. M. Ceotto, Università degli Studi di Milano) with different purposes, namely to reproduce EXAFS results for pristine TiO_2 and N-doped TiO_2 over the whole N/Ti molar range of the experimental samples (chapter 3), to quantify the primitive cell distortion under Pr doping – see comparison with XRPD outcomes – (chapter 3) and finally to study the Density of States (DOS) and evaluate the Fermi and quasi-Fermi level of undoped, N-doped, and Pr-doped titania (chapter 4).
Solid-state calculations DFT based on the atom-centered linear combination of Gaussian-type functions (LCGTF) have been performed by Dr. L. Lo Presti (Università degli Studi di Milano) to optimize the geometrical crystal structure of both pure and defective TiO_2 anatase (chapter 3, EXAFS analysis).

DFT is a quantum mechanical modeling method used in physics and chemistry to investigate the electronic structure of many-body systems, in particular atoms, molecules, and the condensed phases. With this theory, the properties of a many-electron system can be determined by using functionals, namely functions of the electron density.
Although DFT has its conceptual roots in the Thomas–Fermi model, DFT was put on a firm theoretical footing by Hohenberg and Kohn[1] and further developed by Khon and Sham.[2] The many electron Schrödinger equation can be very much simplified if electrons are divided in two groups: valence electrons and inner core electrons. The electrons in the inner shells are strongly bound and do not play a significant role in the chemical binding

of atoms, thus forming an almost inert core with the nucleus. Binding properties are almost completely due to the valence electrons, especially in metals and semiconductors. This separation suggests that inner electrons can be ignored in a large number of cases, thereby reducing the atom to an ionic core that interacts with the valence electrons. The use of an effective interaction, a pseudopotential, that approximates the potential felt by the valence electrons, was first proposed by Fermi in 1934 and Hellmann in 1935. In spite of the simplification pseudopotentials introduce in calculations, they remained forgotten until the late 50's.

During recent years, the development in electronic structure theory has lead to dramatically improved possibilities for calculations even on large molecular systems. However, despite recent improvements, there are still difficulties in using density functional theory to properly describe intermolecular interactions, especially van der Waals forces (dispersion), charge transfer excitations, transition states, bandgap in semiconductors, global potential energy surfaces and some other strongly correlated systems. Its incomplete treatment of dispersion can adversely affect the accuracy of DFT (at least when used alone and uncorrected) in the treatment of systems which are dominated by dispersion or where dispersion competes significantly with other effects. The development of new DFT methods designed to overcome this problem, by alterations to the functional[3] or by the inclusion of additive terms[4] is a current research topic.

In the literature, there are several theoretical papers devoted to the study of the electronic structure and some physico-chemical properties of the doped oxide by using different computational methods, such as the full-potential linearized augmented plane wave (FP-LAPW) method,[5] and the pseudopotential plane wave (PPW) method,[6,7] and the B3LYP hybrid Hartree–Fock (HF) density functional theory method.[8]

These calculations have given the possibility to obtain new information on the nature and processes of defect formation and the structural transformations occurring in the doped material. However, most of the calculations carried out in the near-Fermi region of the electronic spectrum of doped TiO_2 are in poor agreement with the experimental results, especially if dealing with bandgap arguments.

In the present context, since the excess charge localization and the strongly correlated nature of the occupied Ti 3d states seriously challenges DFT

calculations, the electronic structure calculations were conducted using both the GGA (Generalized Gradient Approximation) and the GGA + U method (GGA associated with the use of the Hubbard empirical U parameter, see the following),[9] which can lead to a good description for the reduced TiO_2, as shown in previous works.[10-12] The DFT + U approach introduces an on-site correction in order to describe systems with localized d and f electrons, which can produce better bandgap and midgap states energetics in comparison with experimental results. As already mentioned, the main disadvantage of the methods used in calculations of titanium dioxide is an inaccurate estimate of the bandgap. The use of the methods based on the electron density functional theory (such as the linear combination of atomic orbitals (LCAO), localized spherical wave (LSW), and pseudopotential methods) leads to an underestimation of the band gap, whereas the calculation performed within the Hartree–Fock approximation results in a substantially overestimated band gap as compared to the experimental value. In order to more accurately describe the electronic spectrum and optical properties, it is necessary to take into account the exchange–correlation interactions. In the present work, effective on-site Coulombic interactions U (U = U' - J) for Ti 3d were used. U' and J represent the energy cost of adding an extra electron at a particular site and the screened exchange energy, respectively.

3.2. Template titania: structure and morphology

Besides the possible promotion of a controlled pore network, the presence of an amphiphilic molecule can intervene in different ways by tuning the sample final morphology. Very interesting is, for instance, the recent work by Chen *et al*.,[13] where three-dimensionally ordered arrays of mesoporous titania spheres have successfully been synthesized through opal (ordered closed-packed face-centered cubic lattice of silica or latex spheres) template and triblock copolymer (Pluronic P123) as a mesopore-directing agent. The mean diameter of the titania spheres has been observed to be *ca.* 165 nm with a narrow distribution of the mesopore size in the range 2-6 nm.

Fig. 3.1 reports the relative phase enrichment (histograms) at different surfactant concentrations of samples submitted to a hydrothermal growth step in the presence of the DPC and GS3, subsequently calcined at 600 °C. The

polymorph composition appears to be directly dependent to the concentration of the surfactant in the solution adopted for the ageing. When such concentration corresponds to the existence of non-aggregated surfactant units (1, 10 mM for DPC and 1, 2.5 mM for GS3), the anatase polymorph is prevalent; the crystallite sizes (Table 3.2) appear to be smaller than those in the absence of surfactant.

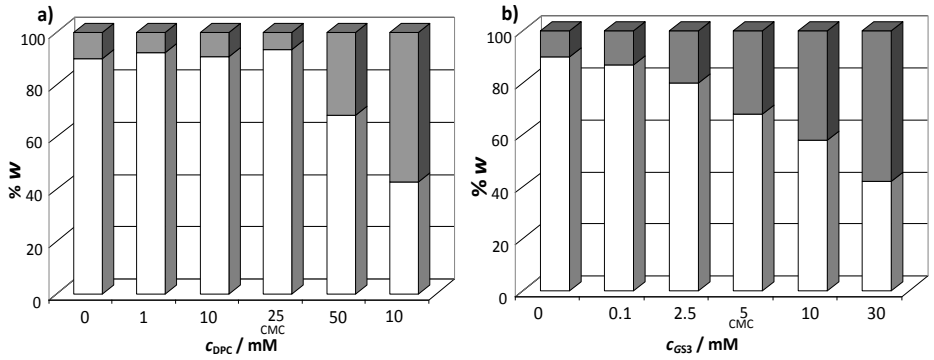

Figure 3.1. Relative phase enrichment in anatase (white part of histograms) and rutile (black part of histograms) TiO_2 polymorphs of samples grown in surfactant solutions (DPC, **a**, GS3, **b**) and subsequently calcined at 600°C.

The specific surface areas of the calcined oxide remain approximately the same (Table 3.2, last column).

By increasing the surfactant concentration at values larger than the CMC (>25 mM for DPC and >5 mM for GS3), the amount of anatase decreases and the anatase and rutile structures are almost equally promoted. The formation of rutile comes along with larger crystallite sizes and lower surface areas (Table 3.2).

Moreover the presence of GS3 at higher concentrations seems to preserve the surface area (11-14 m^2g^{-1}) and to limit the increase in rutile crystallite sizes (~75 nm) with respect to the DPC surfactant (5-8 m^2g^{-1} and >85 nm, respectively).

Sample		$<D_A>$ (nm)	$<D_R>$ (nm)	S_{BET} (m^2g^{-1})
no SURF		28	-	18
DPC	1 mM	20	-	19
	10 mM	22	-	19
	25 mM (~CMC)	24	-	16
	50 mM	32	86	8
	100 mM	41	>100	5
GS3	0.1 mM	23	—	20
	2.5 mM	30	54	16
	5 mM (~CMC)	37	63	13
	10 mM	44	73	14
	30 mM	43	76	11

Table 3.2. Anatase (A), rutile (R) domain sizes and BET surface area for all titania samples obtained by surfactant template route.

These results are considered to be significant since after a calcination at 600 °C both the surface area and the total pore volume are still appreciable at variance with samples prepared by template-free procedures.[14-16]
The trend in Fig. 3.1 is in agreement with the generally reported lower surface energy of anatase with respect to rutile[17,18] and with the consistent finding that the phase transformation to rutile occurs after the anatase grains have grown to a certain threshold size, of about 30-40 nm.[19] Actually, during the hydrothermal step particle growth through Ostwald ripening can be expected to occur.[20] When the growth occurs in the presence of a non-aggregated surfactant, the surface of the precursor particles is shielded from the

deposition of soluble Ti species by the presence of the surfactant film. The growth is slightly depressed, the particles remain smaller and stable supporting the formation of anatase. At higher concentrations, the micelles may act as carriers for the soluble Ti containing species promoting the growth. Further, the micelles may be, also, adsorbed at the surface of different particles and may therefore promote bridging phenomena leading to larger particles.

These considerations are closely mirrored by the particle morphology shown in SEM micrographs (Fig. 3.2). In the case of the sample prepared in the absence of the surfactant (Fig. 3.2a) small spheroidal particles with an average size of about 30 nm grouped in raspberry-like aggregates can be appreciated. Instead, in the case of the sample grown at high DPC concentration (Fig. 3.2b) the particles are much larger, with sizes ranging from about 100 nm (single crystals) and to about 200-300 nm as the result of sintering between crystallites. The large particles in Fig. 3.2b reveal a particularly smooth surface. This effect is presumably the result of a surface annealing provoked by the heat released during the surfactant combustion. In the case of titania particles grown at high GS3 concentration, the shape of the aggregates remains spheroidal, characterized by a diameter of ~ 60-70 nm.

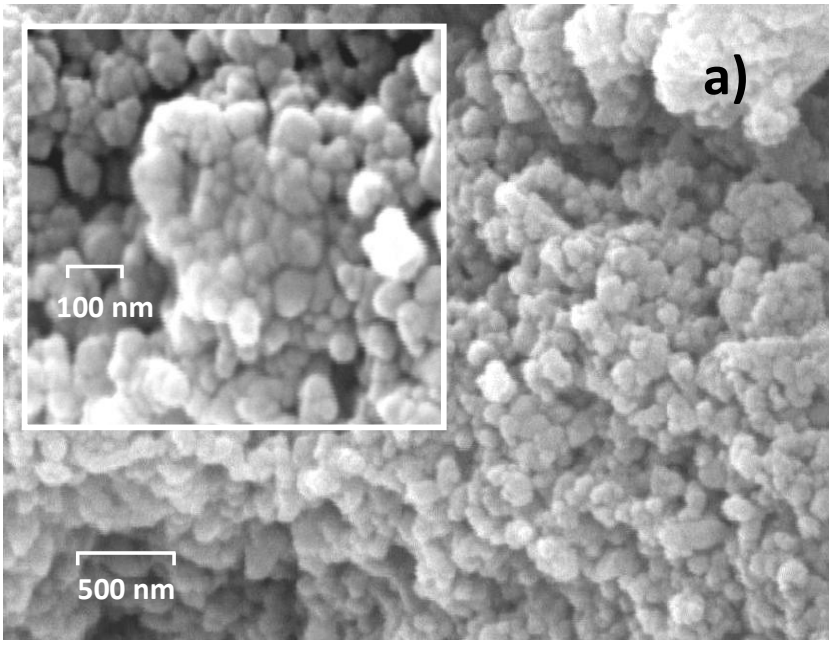

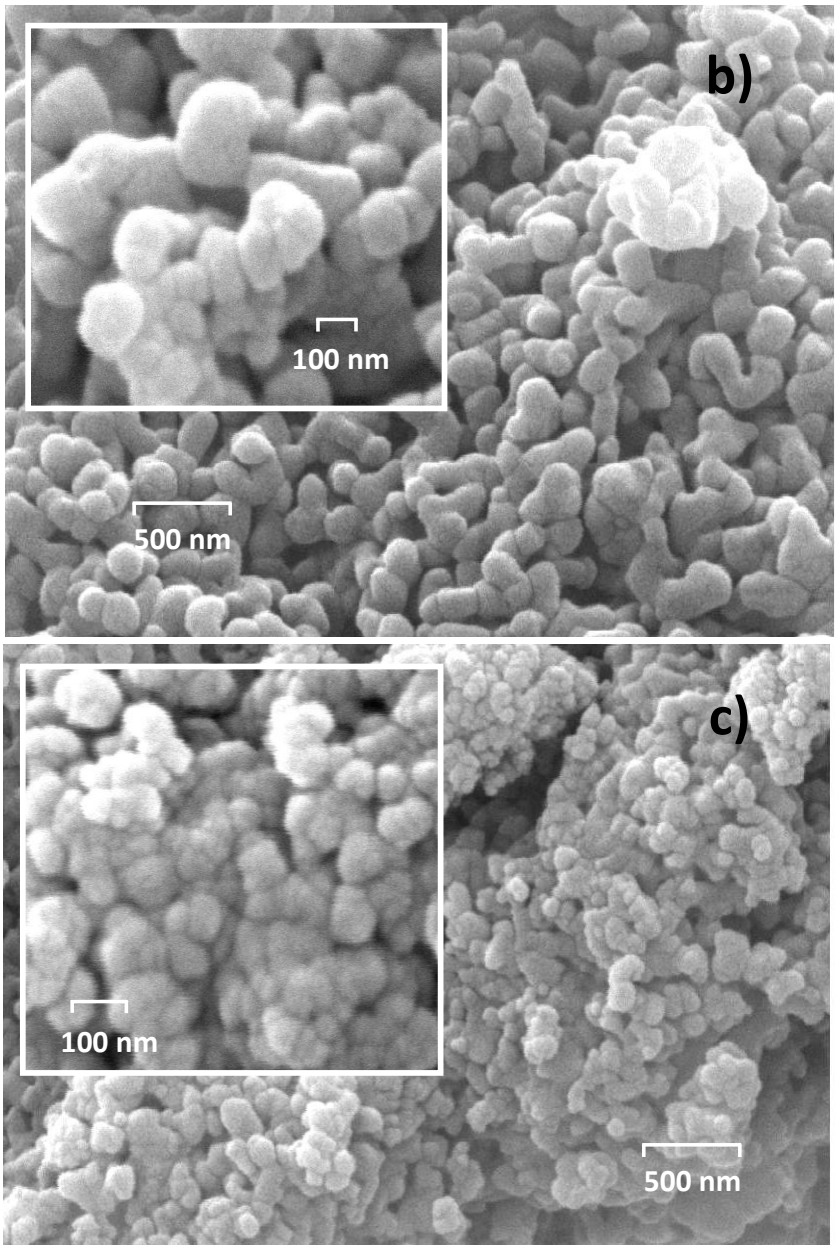

Figure 3.2. SEM micrographs of titania particles hydrothermally grown in absence of surfactant (**a**) and in presence of high concentration of (**b**) DPC (100 mM) and (**c**) GS3 (30 mM), subsequently calcined at 600°C.

Mesoporosity

The mesoporosity induced by micelles and further three-dimensional organization of both surfactants can be appreciated by the hysteresis loop of the nitrogen adsorption–desorption isotherm (Fig. 3.3), with respect to the reference material prepared without surfactant. The hydrothermal treatment in the presence of DPC micelles (c_{DPC} = 25 mM, Fig. 3.3a) leads to titania particles with bottle-neck shaped pores mainly in the range of 6< d <10 nm (Fig. 3.4a), comparable with the average diameter of the globular DPC micelles (~ 4 nm).[21]

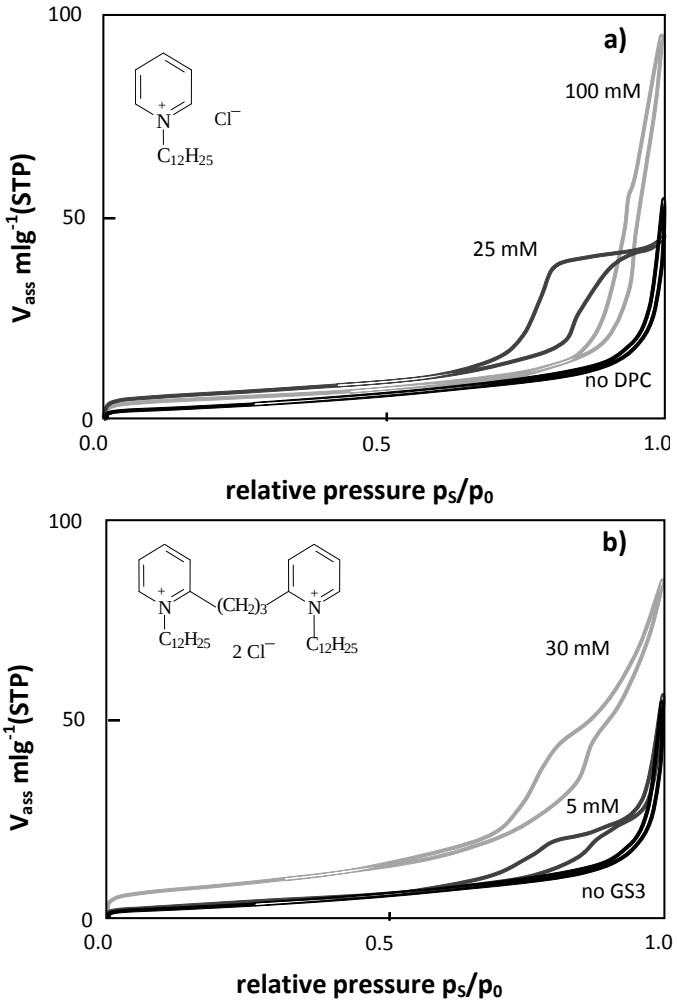

Figure 3.3. N_2 adsorption–desorption isotherms of TiO_2 samples aged in different surfactant solutions and calcined at 600°C. **a**) DPC, **b**) GS3

When the particles are grown at surfactant concentrations higher than CMC, in the case of DPC the shape of hysteresis loops is similar to the reference sample, the total pore volume increases, but the fraction of desired mesopores is not significantly large. On the other hand, the presence of GS3 cylindrical micelles and three-dimensional hexagonal arrangements (sketches in Fig. 3.4b) produces an increase of total pore volume at increasing surfactant concentration (Fig. 3.4b), especially the fraction of mesopores with diameters in the range 6< d <20 nm. The shape of the hysteresis loop is typical of open-ended slit-shaped pores (Fig. 3.3a).

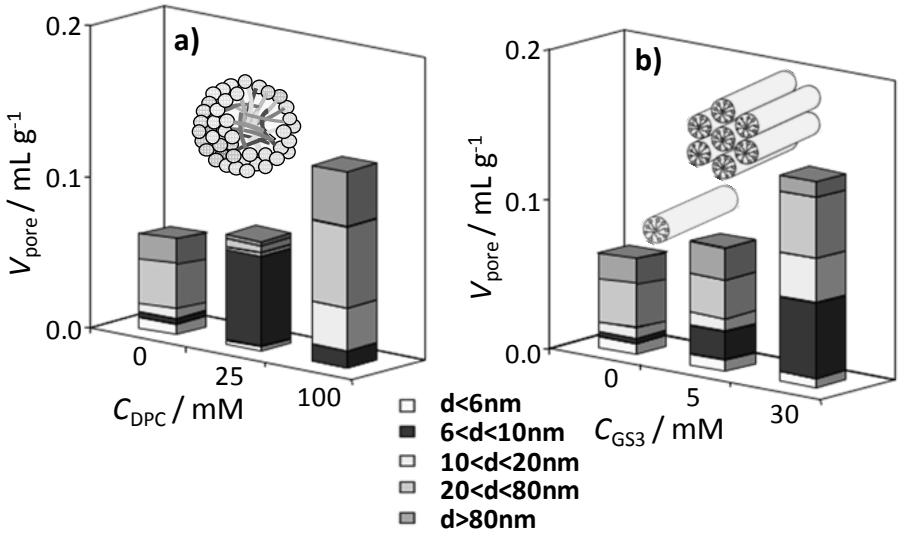

Figure 3.4. Pore volume distribution of TiO_2 samples after **a**) DPC and **b**) GS3 ageing as a function of surfactant concentration and calcined at 600°C. Insets: possible surfactant three-dimensional aggregations.

A typical pore size distribution curve for the hydrothermally treated TiO_2 in the presence of three-dimensional GS3 hexagonal arrangements is shown in Figure 3.5a. A fairly narrow size distribution, 6-20 nm, is achieved for the present sample at variance with the untreated one (calcined at 600 °C), which shows almost no porosity. This result indicates that the hydrothermal template treatment of the TiO_2 particles leads to their aggregation with evolution of a mesoporosity probably arising from the template structure, which is successively thermally decomposed.

Part of the mesoporous structure can be appreciated in the HRTEM image of Figure 3.5b.

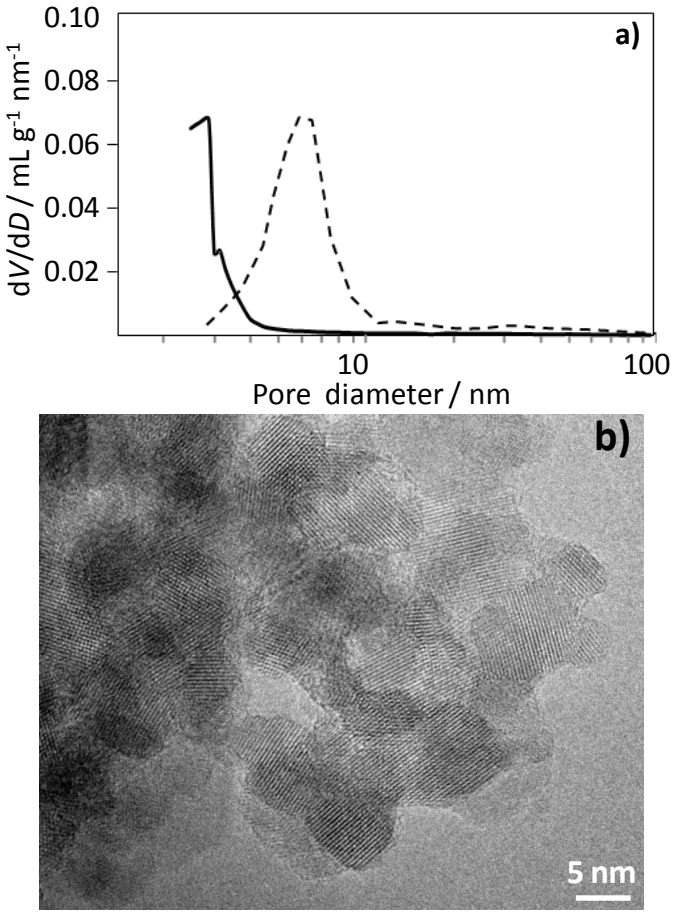

Figure 3.5. Pore size distribution curve of (a) TiO_2 bare particles and (b) after GS3 ageing (30 mM) calcined at 600 °C (**a**). HRTEM image of GS3 hydrothermally treated and calcined sample (**b**).

These results, together with the surface and morphological aspects, could be explained by invoking the different local heat of combustion (during the calcination step) for DPC and GS3, especially for high surfactant concentrations. Indeed, for growths performed at concentrations larger than the CMC, very numerous small (or having a random size distribution) DPC micelles are randomly embedded into the oxide, giving rise, during the

ensuing calcinations step to large heats of combustion, particle sintering and an almost un-controlled mesoporosity. In the case of gemini, instead, the relevant surfactant/oxide interactions allow the templating function of the surfactant to significantly occur. Possible ordered hexagonal GS3 arrangements may lead to lower surfactant/oxide ratio in the template growth, inherent in the rods *vs* globule structure, even if the GS3 surfactant is formed by double aromatic ring. This leads to a lower heat of combustion and to controlled particle shape, size and mesoporosity.

3.3. Microemulsion-mediate titania: structure and morphology

As expected, the crystallite size is slightly increased at increasing the calcination temperature (from *ca*. 8 nm to *ca*. 16 nm raising the temperature from 400 °C to 500 °C). All values are reported in Table 3.3, 2nd column. The qualitative phase identification shows the presence of anatase (mainly) and brookite in all specimens, with a low amount of rutile for some samples due to the calcination temperature higher than 400 °C. All diffraction lines(not shown) do not differ from those of sol-gel undoped sample (in the cases where a low amount of rutile is present, it is not detectable from the diffraction profile).

Fig. 3.6a shows the comparison among three selected hysteresis loops relative to a sample obtained with LUTENSOL TO389 (T_L0.9), one obtained with TWEEN 80 (T_TW0.6L) and another one obtain by using TRITON X-100 (T_TX1.2). The three isotherms are surely affected by the type of nitrogen source, though are all ascribable to type IV and the hysteresis loops seem to be H4 type (predominant slit-shaped pores), as in the case of undoped sol-gel sample named T and urea-doped samples (see paragraph 3.3.3).

Because of sintering phenomena related to the calcination temperature (500 °C) specific surface areas and pore volumes are lower than those obtained for samples calcined at 400 °C (see T_400N, T_TX1.2 and compare to samples presented in other sections): the only value well above 100 $m^2 g^{-1}$ refers to the sample obtained with TRITON X-100 which was calcined at 400 °C owing to the complete decomposition of the surfactant at that temperature. An easy comparison is that between samples T_400N and T_500N, which simply differ for the annealing temperature: the specific surface area drops from 136 down

to 68 m^2g^{-1} when reaching 500 °C during calcination. Out of this trend is sample T_L0.3, which is indeed hardly comparable with the others owing to the high pore volume and significant presence of macropores (Fig. 3.7b). As for the pore size distribution, it is possible to observe from Fig. 3.7b that micropores are only present in samples calcined at 400 °C, while they almost disappear when the calcination temperature is 500 °C. Also the type of surfactant deeply affects the pore size distribution: apparently, TRITON X-100 leads to oxides with very few macropores (>20 nm), which, in turn, are present in a large fraction in the samples obtained with either LUTENSOL TO389 or TWEEN 80. This result indicates that such microemulsion route leads to particle aggregation with evolution of a mesoporosity probably arising from the interparticle space.

Sample	S_{BET} ($m^2 g^{-1}$)	Pore vol. (mL g^{-1})	d^A_{101} (nm)	% A	% B	% R
T_400N	136	0.301	8	66	34	-
T_500N	68	0.208	16	77	23	0
T_L0.3	89	0.468	12	94	4	2
T_L0.6	68	0.205	14	88	10	2
T_L0.9	71	0.179	12	97	0	3
T_TW0.9	48	0.129	13	87	9	4
T_TW0.6L	75	0.279	12	72	23	5
T_TW0.8L	45	0.118	14	94	6	0
T_TW0.09L	79	0.237	13	87	13	0
T_TX1.2	125	0.218	8	77	23	0

Table 3.3. Specific surface areas and total pore volumes (BET-BJH analysis), anatase crystallite size and phase composition (XRPD measurements - A=anatase, B=brookite, R=rutile) of titania samples obtained *via* reverse microemulsion route.

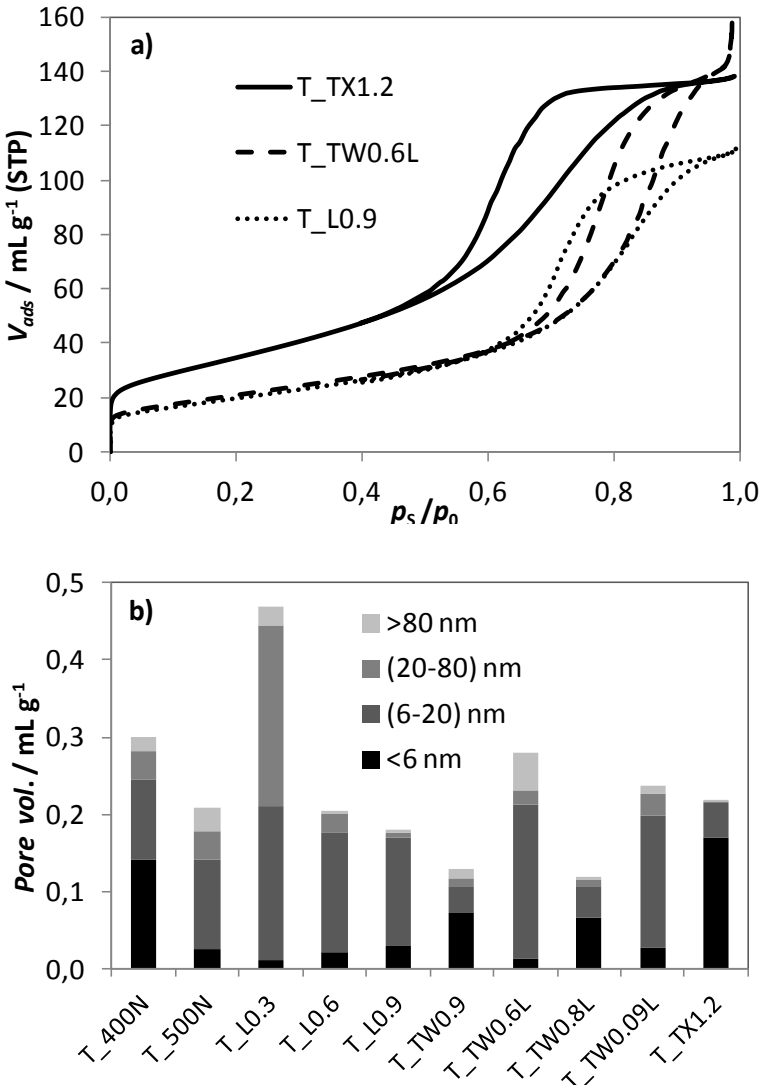

Figure 3.7. N_2 adsorption-desorption isotherms for selected samples (a) and pore size distribution of all titania samples (b) obtained via reverse microemulsion route.

TEM images of TiO_2 obtained by microemulsions are reported in Fig. 3.8 for selected samples (T_TX1.2 and T_TW0.6L). It can be observed that particles are fairly spherical, with a narrow size distribution that well agrees with the above mentioned results.

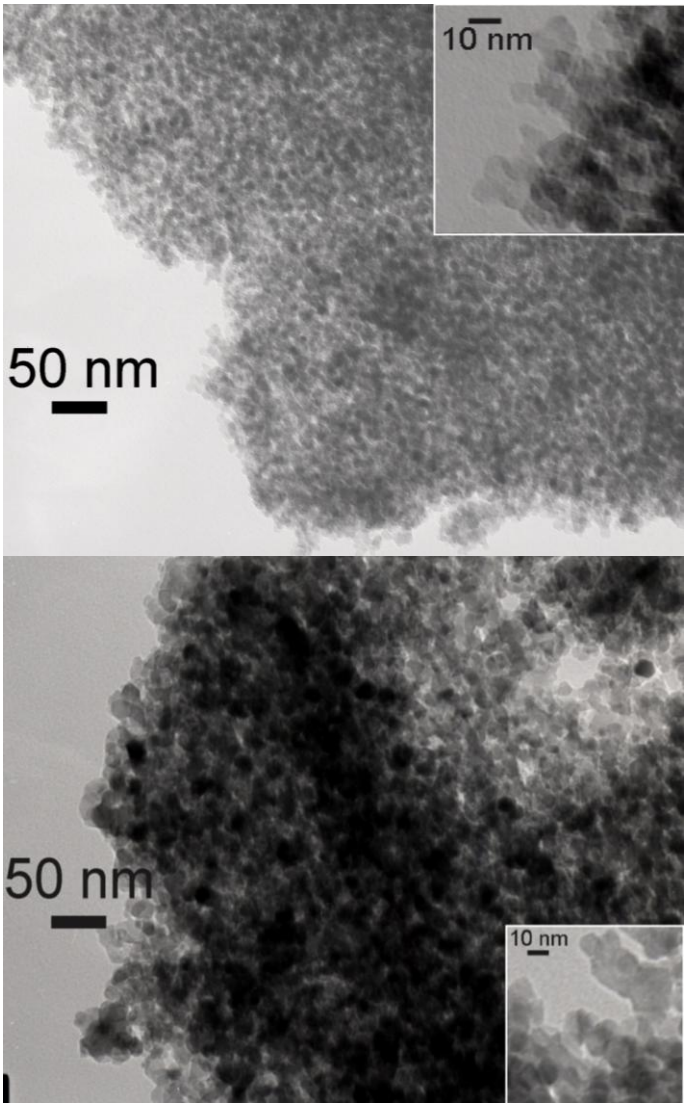

Figure 3.8. TEM images of samples T_TX1.2 and T_TW0.6L, obtained by a microemulsion route using a respectively a single surfactant, TRITON X-100, and two surfactants, namely TWEEN 80 and LUTENSOL TO389.

3.4. N-doped TiO_2

Nowadays, nitrogen incorporation can be achieved by both physical and wet-chemical synthetic methods (such as sol-gel synthesis, chemical treatments of the bare oxide, titanium nitride oxidation, sputtering with Ar-N_2 gas, N ion bombardments at high energies, molecular beam epitaxial growth, chemical

vapor deposition, post-treatment by NH_3 gas at elevated temperatures, spray pyrolysis and other super-critical methods).[22-24] Given such a jungle of synthetic routes, materials with largely different properties are produced. Therefore, direct comparison and unifying photocatalytic conclusions are difficult to draw.

In the following, XRPD and EXAFS detailed analyses will be presented for N-TiO_2 doped with triethylamine as N source, whereas, further on, a comparison among three different N sources (triethylamine, ammonia and urea) will be made focusing on the role of effect of the aging time (from the freshly synthesized powders to aged ones – up to two months) on the prepared titania doped materials.
The actual N contents in all N-doped samples presented hereafter were determined to be in the range 0.06–0.09 wt.% (corresponding to 0.003-0.005 molar ratio), based on the CHN analysis; such values are comparable to those reported by Silija *et al*.[25] It should be noted that the N/Ti atomic ratios determined by XPS analysis elsewhere[26] range around 0.015–0.022. These values are much lower (one order of magnitude) than the starting molar ratios adopted in the different synthetic routes and a little higher than those obtained by CHN analysis, thus indicating that most of the nitrogen is lost during the sample preparation. Triethylamine as a tertiary amine theoretically provides less nitrogen atoms to titania than the other adopted sources. As affirmed by Ananpattarachai *et al.*, this information would suggest that the chemical composition (N content) of N-doped TiO_2 largely depends on the molecular structure of the nitrogen dopant and the accessibility of nitrogen atoms to react with the titania precursor.[27] However, more or less the same amount of N was found in all N-doped samples, lying in the range mentioned above.

3.4.1. Structural features

XRPD is widely applied for the characterization of materials' structure and microstructure. The Rietveld method[28,29] and the WPPM (Whole Powder Pattern Modelling)[30] are the state of the art tools for quantitative phase analysis and for microstructure studies. In close analogy to the structural refinement provided by the Rietveld analysis, WPPM is a general technique for microstructure refinement which consists in a simultaneous modeling of all

peak profiles of the diffractogram from single or multi-phase polycrystalline materials, without using arbitrary profile functions.

A direct link between the chemical nature of the bulk nitrogen and the characteristics of the XRPD patterns has never been reported in the literature, probably because of the inherent difficulty in extracting reliable cell parameters for a mixture of nanopowders. To overcome this limitation, high-resolution synchrotron radiation XRPD will be employed here, as they combine a high signal/noise ratio with a negligible instrumental contribution to the diffraction profiles. The analyzed samples are those doped with triethylamine with different initial N/Ti molar ratios (0.01-0.05-0.1-0.2-0.4-0.5).

Ti K-edge XAS data will also be employed in the following to get an independent experimental evidence about the environment of Ti in the lattice.

Synchrotron Radiation XRPD data allowed a large portion of the reciprocal space to be accessed. This is of paramount importance for the analysis of nanocrystalline TiO_2. Anatase and brookite were the only identified phases: the latter gradually reduces from 25% in the undoped sample to 10 % in the TN_0.50 one (Table 3.4). In Table 3.4 also morphological features (specific surface area and pore volume) taken from a previous work are listed.

Sample	% A	% B	S_{BET} ($m^2 g^{-1}$)	Pore vol. (mL g^{-1})
T	75	25	171	0.44
TN_0.01	77	23	163	0.28
TN_0.05	77	23	130	0.48
TN_0.10	77	23	120	0.10
TN_0.20	83	17	98	0.02
TN_0.40	84	16	90	0.01
TN_0.50	90	10	87	0.04

Table 3.4. Phase composition (XRPD measurements - A=anatase, B=brookite), specific surface areas and pore volumes (BET-BJH analysis) for the series of titania samples doped with triethylamine.

An example of X-ray powder diffraction pattern (sample TN_0.10) is shown in Fig. 3.9, with raw data and result of the WPPM.

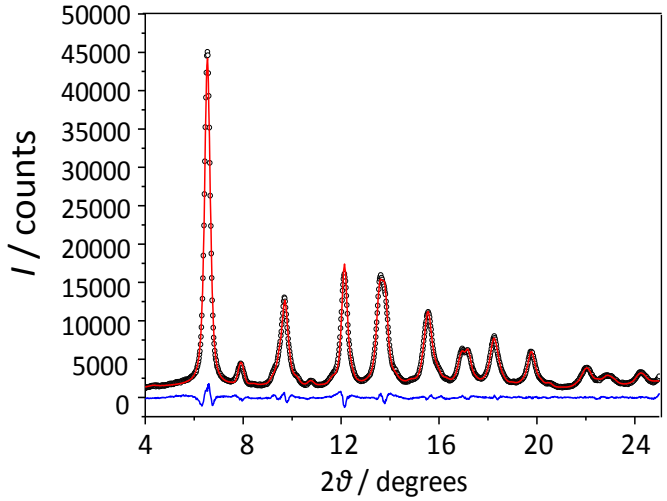

Figure 3.9. Powder X-ray diffractogram of sample TN_0.10: experimental points in black, the corresponding WPPM fitting curve in red and the point-by-point difference between "observed" and calculated intensities in blue.

Microstructure (WPPM) model parameters were refined directly on the XRPD pattern assuming the domains being spherical and lognormally distributed. Dislocations were also considered to account for the observed anisotropy in the line profile broadening. Even if the fitting quality (see Fig. 3.10) is not extreme, residuals are well-centered around the peaks and they average to zero, *i.e.*, cell parameter and intensity are fully matched, whereas the size/shape distribution is not perfect. The results suggest that the anatase domains increase with the N/Ti molar ratio and the brookite ones decrease, after reaching a maximum at nominal N/Ti=0.10 (Fig. 3.10). The domain size of anatase gradually increase from 4.8 nm for the undoped material to 5.8 nm for the TN 0.50 sample, while it seems that brookite reaches very small values ffor nominal N/Ti ≥ 0.2.

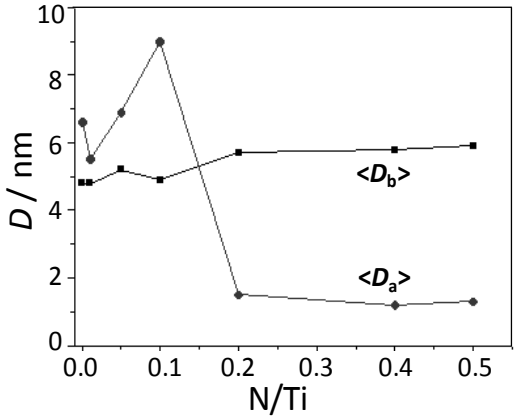

Figure 3.10. Average domain size for anatase <D_a> and brookite <D_b> as a function of the N/Ti initial molar ratio.

High-resolution transmission electron microscopy (HR-TEM) pictures reported in a previous paper[26] confirms the XRD conclusions in terms of average size and size uniformity. The tendency toward agglomeration increases by increasing the nitrogen content, showing a high particle superposition. Domains are well crystallized, even if the effects of the deformation field caused by the presence of dislocations can be observed. Quantities of dislocations in the powders are displayed in Fig. 3.11. The maximum is reached at nominal N/Ti = 0.1. This finding can be considered a possible explanation of the higher photocatalytic activity of sample TN_0.10, as found in a previous work.[26]

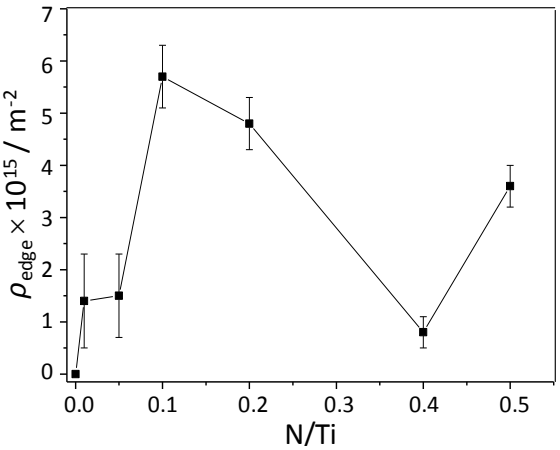

Figure 3.11. Amount of edge dislocations found in N-doped powders by WPPM analysis of XRPD measurements as a function of the initial N/Ti molar ratio.

Cell parameters were also extracted from the WPPM analyses and are reported in Table 3.5. Some correlation seems to exist between cell parameters and refined eccentricity of the capillary. However, forcing the eccentricity to be the same, reduces the number of parameters (thus the correlations). The overall trend of the data is qualitatively similar: the largest variations occur for the *c* axis that initially shrinks and then elongates reaching a quasi-plateau for a nominal doping N/Ti greater than 0.2.

Sample	a_{anat}	c_{anat}	a_{brook}	b_{brook}	c_{brook}
T	378.98(2)	944.7(2)	915.9(3)	545.8(2)	517.7(1)
TN_0.01	379.06(2)	944.6(2)	915.7(2)	544.8(1)	517.80(9)
TN_0.05	379.01(1)	945.7(1)	915.0(2)	545.2(2)	517.9(1)
TN_0.1	378.88(1)	947.50(6)	916.0(2)	545.7(1)	517.77(9)
TN_0.2	379.06(1)	948.51(6)	913.3(5)	543.6(4)	521.3(3)
TN_0.4	379.05(1)	948.55(4)	920.1(1)	531.1(5)	526.8(6)
TN_0.5	379.02(1)	949.08(4)	914.0(7)	543.3(5)	522.5(4)

Table 3.5. Cell parameters of N-doped powders obtained by WPPM analysis of XRPD measurements: a_{anat} and c_{anat} refer to anatase, while a_{brook}, b_{brook}, and c_{brook} refer to brookite.

Trend of the cell volume *vs* content of nitrogen is plotted in Fig. 3.12a,b for anatase and brookite, respectively.

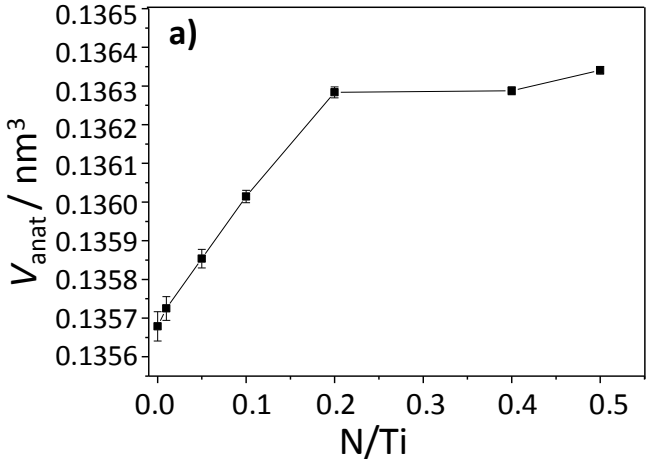

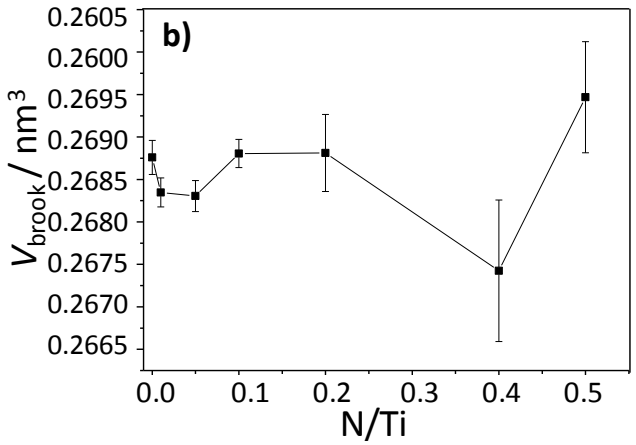

Figure 3.12. Anatase (a) and brookite (b) cell volume as a function of the N/Ti initial molar ratio.

The initial shortening of the *c* axis of the cell may be therefore attributed to a substitutional N-doping. Adding more nitrogen, promotes the transition to an interstitial position, expanding the cell along *c*. Saturation is eventually reached and a plateau is shown for the experimental data.
In order to assess these conclusions on a secure footing, Ti K-edge XAS was successfully employed (see the following), though abundant line defects might have been problematic for the analysis of the EXAFS signal.

3.4.2. N location in N-doped TiO_2

A challenging open question recurring in literature[31] concerns the location of nitrogen in the lattice of N-TiO_2. It is in fact still under debate whether the N anion in titania, generically labelled as N_b ("b" standing for bulk[32]), is interstitial (N_{int}) or substitutional, *i.e.*, it replaces an oxygen vacancy (N@O). While experimental characterization techniques failed in determining the exact location of N,[31] DFT calculations,[33] based on thermodynamic considerations under oxygen-rich conditions, have suggested N atoms to be preferably interstitially located in the lattice. However, these calculations have never been backed by experimental results. Also, it is still under debate whether other chemical species like NO_x or NH_x are present in bulk and why, in some cases, the photocatalytic performances become poorer by increasing N content, even if visible light absorption increases. Overall, the experimental

solid state picture of the N-doped titania remains scanty because detailed information about the crystal structure and the nature of the photoactive centers are still missing.

A clear understanding of these issues is necessary to build up focused syntheses and to get future improvements of N doped titania photocatalytic performances. It is essential to know whether N_b is primarily interstitial or substitutional because the very different behavior of N in these sites will accordingly affect the material photocatalytic properties. Fig. 3.13, based on DFT calculations, helps in understanding this concept. It schematically represents the electronic structure of substitutional (left side) and interstitial (right side) N-doped titania.[32] In the first case, after suitable irradiation, both A and B compounds are oxidized, whereas in the second case, only A is oxidized. Electron-hole recombination is more likely to occur in the interstitial case, because of the apparent band-gap narrowing induced by the N states, and any beneficial effect may vanish in this way. For these reasons, a rational comprehension of the synthetic route with the target of improved photocatalytic properties may be devised only if one is able to determine exactly the nature of the synthesis products, *i.e.*, the location of the N atom within the lattice.

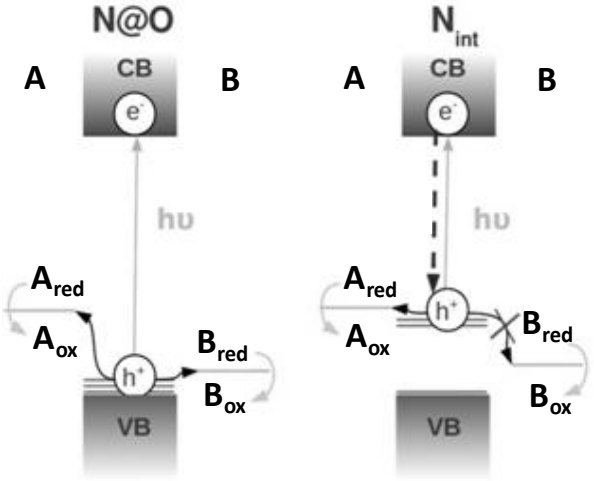

Figure 3.13. Schematic photocatalytic oxidations with substitutional (left) and interstitial (right) N-doped titania. “A” and “B” are molecules with different electronic energy levels. The subscript “Ox” stands for “Oxidized” form and “Red” for “Reduced” one. The dashed arrow indicates electron-hole recombination.

Several experimental techniques have been employed to understand where nitrogen is located in titania, reaching only partial conclusions. For example, X-ray photoelectron spectroscopy of the N 1s electron is quite noisy due to the low dopant concentration and presents questionable attribution of poorly resolved peaks, which are the convolution of more than one signal component. Then, this technique is representative of the outer part (surface and subsurface electronic states) of the material, rather than the actual bulk one. On the other side, electron paramagnetic resonance, which can detect very low paramagnetic species concentrations, is not able to discriminate between interstitial and substitutional doping. The spin density on N indicates that both doping models may account for the observed species.[33] X-ray Absorption Spectroscopy (and in particular EXAFS) is a promising alternative for the localisation of N, as it provides information on the local site symmetry and bond lengths. However, its potential in the field of doped titania has not been fully exploited yet.

An introduction to EXAFS technique

The dominant process in the X-ray absorption - at photon energies below 100 keV - is the photoeffect, whereby the absorbed photon transfers its energy to the ejected photoelectron. The X-ray absorption coefficient for the photoeffect decreases smoothly with increasing photon energy. However, when the photon energy reaches one of the deep inner-shell ionization energies of the atom, a sharp jump (absorption edge) appears and marks the opening of an additional photoabsorption channel. Immediately above the absorption edge, in a range up to 1000 eV, a precise measurement of absorption shows rich fine structure superimposed onto the smooth energy dependence. This is the so called Extended X-ray Absorption Fine Structure (EXAFS), and the information is stored in the resulting oscillations, which derive from constructive and destructive interference seen as local maxima and minima.

EXAFS spectrum measured above the absorption edge of a selected type of atoms contains scalar information on their local structure.[34] This is due to the fact that at high energy in the continuum of electrons participating in EXAFS, the effect of neighboring atoms becomes small and electron states approximate to spherical waves that are simply scattered by such atoms.

In particular, EXAFS provides information about distances between "central" and neighboring atoms, local atomic coordination, the nature of neighboring atoms (chemical/oxidation state), as well as changes in central-atom coordination with changes in experimental conditions. Besides the advantage that it applies to any element, it works at low concentrations, thus a minimal amount of sample is required.

By Fourier transformation (FT) of the measured EXAFS structure, the contributions of individual shells of atoms are separated visually. The peaks in FT magnitude spectra appear at the corresponding position of the *i* atom, r_i. To obtain quantitative information on the local environment, *i.e.*, number and species of neighboring atoms in a given shell, their distance from the absorbing atom and their thermal or structural disorder, the peak of interest is analyzed.

Contrary to XRD, which provides long-range geometric information, EXAFS is a local probe. That is why it is often so useful to compare XRD and EXAFS results. However, this comparison should not be misleading: first of all, XRD measures interplanar spacing, while EXAFS - interatomic distances, and they are absolutely not the same if disorder is present.

Absorption spectroscopy has seldom been used for the analysis of doped titania.[35,36] For this oxide, literature works usually identify the presence of 5-fold-coordinated species in the nanostructured anatase and rutile surfaces, with a shortening of the Ti-O first shell bond distance,[37,38] which in some cases is identified as a result of the presence of Ti hydroxyl groups at the surface.[37]

Pioneering tests on mesoporous N-TiO_2 have shown that accurate average distances can be obtained between Ti and the octahedrally coordinated neighbors:[35] a significant variation in bond distances was not found, even if the Ti coordination number effectively increased.[35]

It has to be said that EXAFS analyses are not routine ones, mostly because of the complexity of the elaboration of raw data and to the source they require (usually synchrotron light). Especially for systems like nanocrystalline semiconductor oxides (*i.e.*, TiO_2, ZnO, *etc.*), they are definitely not among the most commonly used types of characterizations.

Moreover, it should be stressed that the EXAFS amplitudes depend on several factors, other than the relative phase concentrations, such as the average coordination number (that may be different with respect to the crystallographic bulk structures), the amplitude reduction factor, and the

relative thermal motion of the neighboring atoms with respect to the probe element. As each of these parameters can assume different values for different phases, great care should be paid in providing quantitative estimates for the relative abundances of each phase from the EXAFS fitting results alone.

In this thesis, the chemical environment surrounding the (heavy) Ti atoms is studied for a series of N-doped samples by combining Ti K-edge EXAFS with DFT calculations. Indeed, the N-doping effects to the bulk geometry have been computationally explored at different levels of theory.
This can represent a general method for bulk characterization based on DFT and EXAFS joint approach, which can be extended to several systems. The main finding, as will be elucidated in the following, is that nitrogen substitutes oxygen at low levels of doping, whereas interstitial sites are preferred at higher concentrations. The possibility of achieving these results, together with results themselves, may pave the way to reinterpret photocatalytic data and properties in view of tailored syntheses with different N content and N lattice sites.
Home-made titania nanoparticles synthesized via wet chemistry with nominal N/Ti molar ratio ranging from 0 to 0.5 have proved to posses photocatalytic activity that changes dramatically according to the initial N content. Such a wide concentration range is necessary for catching how gradually doping sets in.

DFT

In order to have a fair comparison between EXAFS results and DFT calculations, first principles periodic boundary supercell calculations were performed by Dr. M. Ceotto (Università degli Studi di Milano) and arranged in such a way to reproduce the whole N/Ti molar range of the experimental samples. A realistic supercell arrangements for DFT calculations ranged from 48 up to 162 atoms. For the $Ti_{54}O_{108}$ supercell, reciprocal space sampling was restricted to the Γ-point, which is justified due to the rather large size of the used simulation supercells. For the $Ti_{16}O_{32}$ one, instead, a 5×5×5 Monkhorst-Pack[39] k-point mesh was adopted. In a symbiotic EXAFS and DFT approach, it was advisable to switch from the usual point of view based on a primitive or crystallographic cell to a less common one, where the fundamental unit is represented by Ti (the scatterer) and its nearest neighbors (oxygen and

nitrogen). In anatase, these atoms make up a Ti-centered octahedron. In order to put theory on a solid footing, DFT calculations were performed with PAW as well as LCGTF bases.

Atom centerd Gaussian DFT (all-electron and pseudopotential)

Solid-state calculations based on the atom-centered linear combination of Gaussian-type functions (LCGTF) were performed by Dr. L. Lo Presti (Università degli Studi di Milano) to optimize both pure and defective TiO_2 anatase. CRYSTAL06 code was adopted with triple-zeta basis sets previously optimized for calculations of inorganic solids[40,41] and both spin-polarized B3-LYP[42-44] and PBE0[45,46] hamiltonians. To speed up convergence, the frozen-core Stuttgart-Dresden ECP10MDF pseudopotential[47] was applied to Ti atoms in all the N_{int} interstitial solid state optimizations. Eventually, the starting electron populations on Ti, O and N were always chosen so that the crystal cell was always electrically neutral. The crystal structure (atom coordinates and lattice parameters) was iteratively refined until a minimum was found on the potential energy surface, *i.e.*, until the root-mean-square (RMS) of gradients and estimated atomic displacements, as well as their absolute values, fall below a given threshold. An 8x8x8 Monkhorst-Pack k-mesh was adopted for undoped TiO_2, whereas a broader net of 4x4x4 points was employed for defective structures.

For all the N_{int_p} interstitial calculations, the frozen-core Stuttgart-Dresden ECP10MDF pseudopotential[47] was applied for Ti atoms, while the all-electron basis sets reported above were always applied to lighter non-metal N and O atoms. Other program specifications remained the same as for the all-electron calculations, with the only exception of the tolerances on the maximum atomic displacement and the corresponding root mean square parameter. It should be noted that such a choice significantly (~ 50 %) reduces the computational time required for crystal structure optimizations, providing on the other hand structural results of comparable quality with respect to the all-electron ones. In other words, adopting a Stuttgart-Dresden pseudopotential for Ti in TiO_2 can be a reasonable strategy to significantly reduce the computational cost without losing accuracy. The results discussed in the main text are relative to the all-electron outcomes, with the only exception of B3LYP and PBE0 optimizations of the interstitial N-doped structure in *P*m

symmetry, where the pseudopotential approximation was chosen to speed up the convergence up to an affordable time.
More details on this part of the computational setup can be found in the related published paper.[48]

XANES *vs* XPS analyses

Pre-edge X-ray absorption near-edge structure (XANES) features are known to be sensible to the local environment of the absorbing species. The pre-edge part of the XAS spectra and the X-ray Photoelectron Spectroscopy (XPS) techniques can be both employed to gain insight into the different oxidation states of the metal present in the examined specimens.

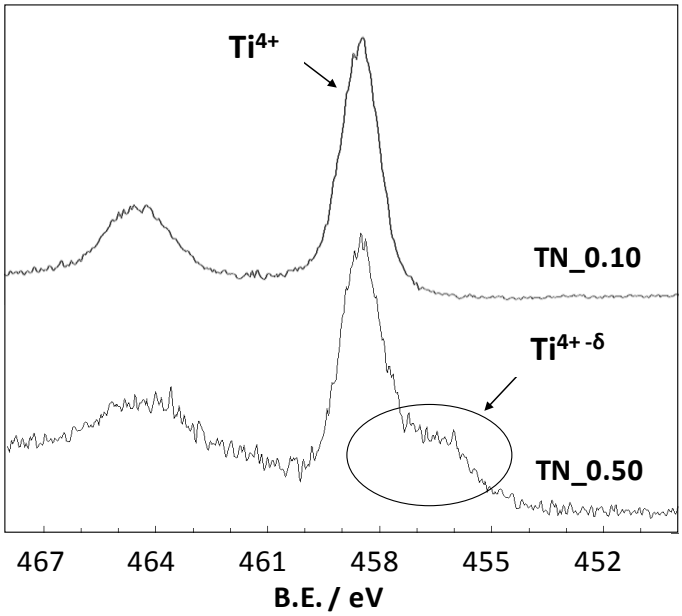

Figure 3.14. Ti 2p XPS region for TN_0.10 and TN_0.50 samples.

The combined inspection of the XPS and the pre-edge part of the XAS spectra enables to conclude as follows: (i) the so-called A2 features, *i.e.*, shoulders among peaks A1 and A3 just below the Ti K-edge, are clearly visible in all our samples. In the Literature, they are usually related to the presence of surface 5-coordinated Ti;[49,50] (ii) this evidence is consistent also with the picture provided by XPS spectra, where a broad shoulder in the 455-458 eV range is detected for the TN_0.50 sample, indicating the occurrence of defective Ti(IV-

δ) species - interestingly, the TN_0.10 spectrum does not show any feature attributable to Ti^{3+} species (Figure 3.14); (iii) due to the occurrence of significant lattice distortions, in turn ascribable to various reasons, a trend is not clearly recognizable in the intensity of the XANES signals, *i.e.*, no obvious relationships there exist that allow to correlate the intensity of the pre-edge peaks with the amount of nitrogen content (Figure 3.15). In any case, as the A2 feature is clearly already present in the undoped specimen, it is likely not directly related with bulk nitrogen dopant. On the other hand, post-edge EXAFS fitting, together with PAW and LCGTF periodic simulations, provided satisfying and more detailed information on the nature of bulk nitrogen in anatase.

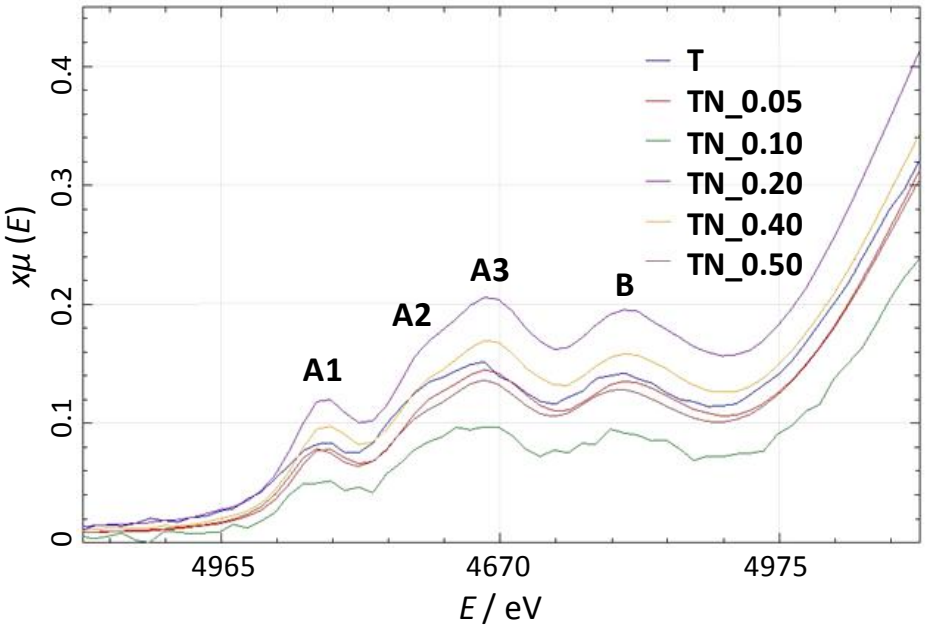

Figure 3.15. Normalized Ti K-edge absorption curves in the pre-edge (XANES) region of the spectra for six TiO_2 samples with various N/Ti nominal molar ratios. Specific absorption features are labeled according with the literature[49].

EXAFS analysis

Figure 3.16 summarizes, both in the real and *k* spaces, the overall matching among data and least-square model functions.

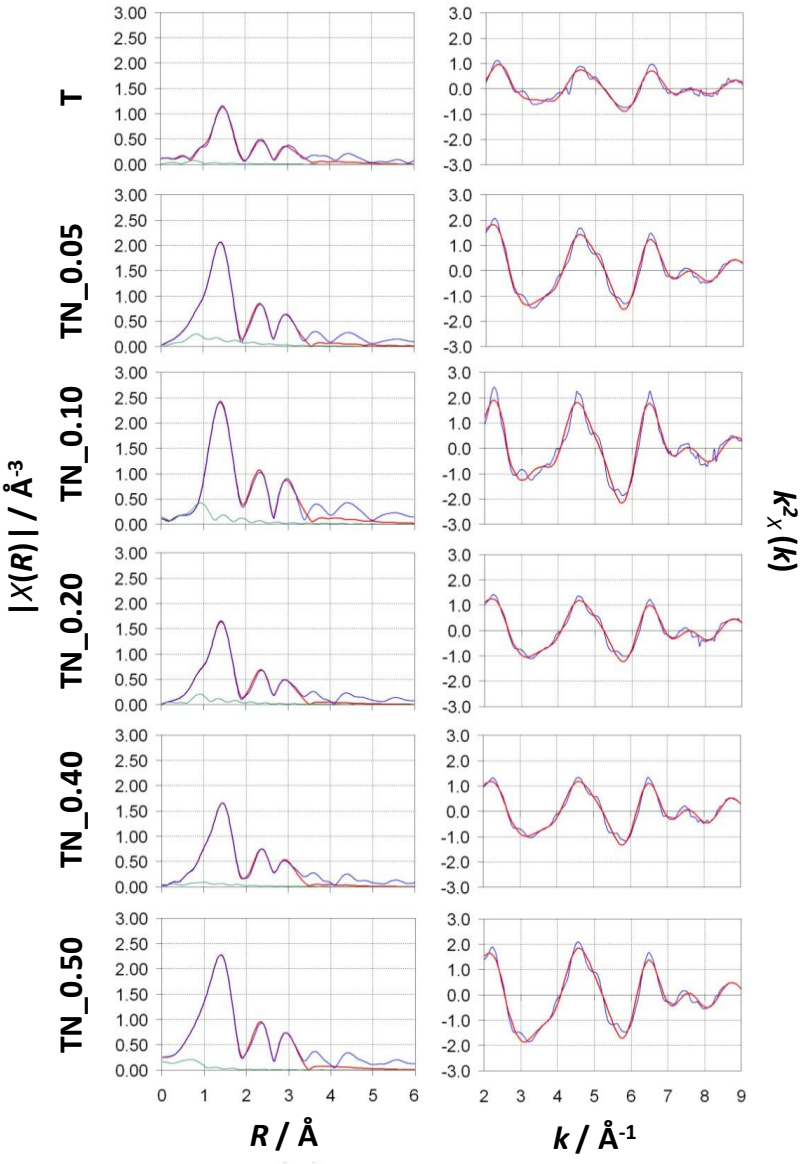

Figure 3.16. Fitted magnitude of the forward EXAFS Fourier transform (left) and corresponding fitted k^2-weighted Ti K-edge EXAFS spectra (right) of six TiO_2 samples with various initial N/Ti molar ratios. Blue curves: experimental data; red curves: least-squares fitting; green curves: least-square estimate of the background.

Fig. 3.17 shows the normalized background-corrected Ti K-edge absorption curves for the whole set of specimens. The pre-edge peaks are the same in all cases and are compatible with the presence of anatase.

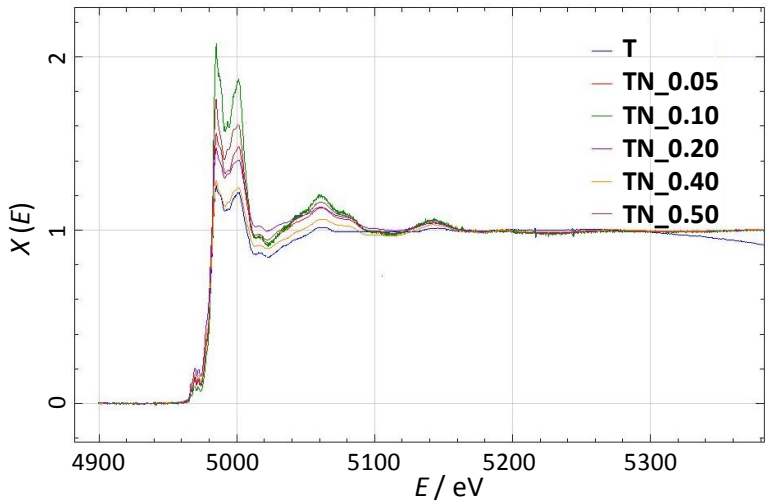

Figure 3.17. Background-corrected and normalized Ti K-edge absorption curves for undoped and several N/Ti molar ratio.

To obtain accurate information on the nearest neighbors of Ti (oxygens), the EXAFS data were modeled both considering just the first scattering paths (O and Ti nearest neighbors) and extending the analysis by including 22 scattering paths. An average anatase cell geometry was employed because of the similar electronic structure of oxygen and nitrogen. Analogous results were obtained in both cases for the first-neighbor distance, the errors being lower with the larger set of paths.

Figure 3.18a shows the final estimates for the average axial and equatorial first shell Ti-O distances in the anatase structure (scheme in Fig. 3.18b – oxygen atoms are numbered as in the following figures, namely Fig. 3.19 and Fig. 3.20). The numerical entries corresponding with data reported in Figure 3.18a can be found in Table 3.6, whereas the complete list of the fit results, together with final statistical agreement factors, can be found in the Supplementary Materials of ref [48]. Even if the estimated standard deviations are quite high with respect to the observed range of variation, especially for $\langle Ti\text{-}O \rangle_{axial}$ distances, a clear trend appears. In particular, $\langle Ti\text{-}O \rangle_{equatorial}$ remains basically constant throughout the overall doping range, whereas $\langle Ti\text{-}O \rangle_{axial}$ undergoes a ca. 0.1 Å reduction when the doping nitrogen exceeds the nominal 0.1 N/Ti molar ratio. Then, it remains constant up to the maximum dopant concentration.

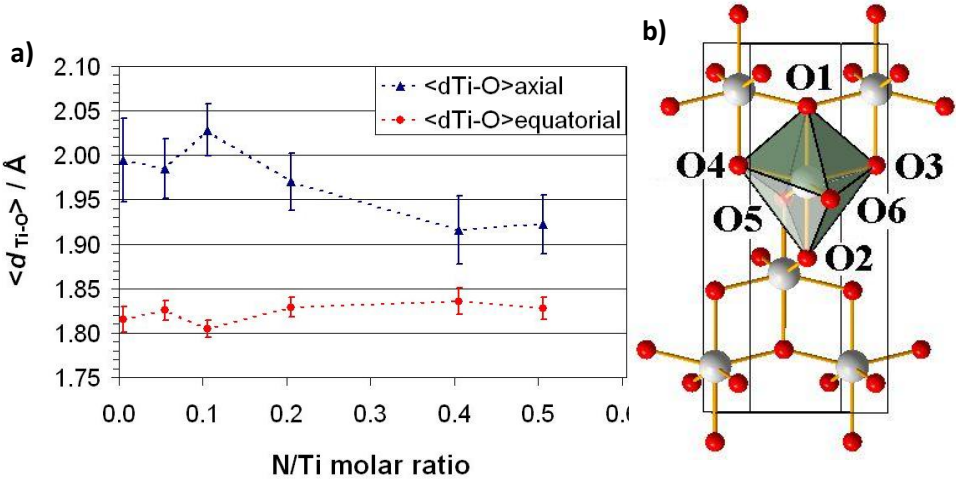

Figure 3.18. a) Average axial (blue triangles) and equatorial (red circles) Ti-O distances within the first coordination shell of titanium as a function of the N-doping extent. The error bars correspond to 1 estimated standard deviation; **b)** Crystallographic tetragonal unit cell of the TiO_2 anatase structure, with the distorted octahedral coordination of oxygen atoms (red spheres) around the Ti ions (grey spheres) highlighted.

N/ Ti molar ratio	0.00	0.05	0.10	0.20	0.40	0.50
$<d_{Ti-O}>_{axial}$	1.99(5)	1.99(3)	2.03(3)	1.97(3)	1.92(3)	1.92(3)
$<d_{Ti-O}>_{equatorial}$	1.82(1)	1.83(1)	1.80(1)	1.83(1)	1.84(1)	1.83(1)

Table 3.6. Ti-K edge EXAFS estimates of the average Ti-O distances (in Å) within the first coordination shell in pristine and N-doped nanostructured crystalline TiO_2 samples (anatase phase). Estimated standard deviations are reported in parentheses.

In other words, it is possible to distinguish between a low N/Ti doping regime from a high one, by inspecting the average distances of the Ti first coordination shell. The first doping region goes from pure TiO_2 to 0.10 N/Ti molar ratio: here, the ligand geometry around Ti is invariant with respect to the pure sample. The other relevant region appears when $0.4 \leq$ N/Ti nominal ≤ 0.5, and it is characterized by a significant reduction of the average Ti-O axial distances with respect to the low doping regime. In details, the average value

of the Ti-O distance ($<d_{Ti-O}>_{axial}$) among 0 and 0.1 N/Ti nominal molar ratio (first three columns of Table 3.6) is as large as 2.03(3) Å, to be compared with the axial distance evaluated by averaging the entries among 0.4 and 0.5 N/Ti doping concentrations (last two columns in Table 3.6), 1.92(3) Å. The entry in Table 3.6 corresponding to the 0.2 N/Ti ratio appears to be somewhat intermediate between these two limit situations, with $<d_{Ti-O}>_{axial}$ = 1.97(3) Å.
It should be stressed that the values reported in Figure 3.18a and Table 3.6 are not directly comparable with crystallographic results, since EXAFS, as said before, is sensible to the local environment around titanium and it is not able to provide information on the long-range structure. In this context, we use this technique to estimate the *relative*, *average* degree of distortion with respect to the undoped nanostructured material. As the presence of brookite is taken into account in the fitting procedure of the experimental signals, such local distortions of the anatase structure should be indirectly related to the amount of lattice nitrogen, and most importantly, to the preferential doping type (substitutional or interstitial) of N atoms for each specific doping concentration.

Titania DFT modeling

Possible substitutional and interstitial N-doping of the octahedron are represented in Fig. 3.19. The calculated distances between Ti and neighbors in stoichiometric anatase are reported in the second column of Table 3.7. The axial oxygen atoms are at 2.00 Å distance, while all the equatorial ones are at 1.94 Å. Then, it was possible to simulate how the shape of the octahedron changes under both substitutional and interstitial doping.

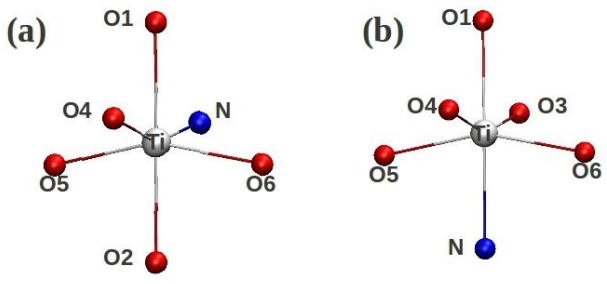

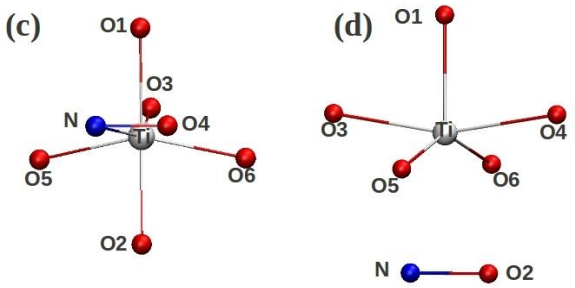

Figure 3.19. Nearest titanium neighbors: (a) and (b) for substitutional N doping, (c) and (d) for interstitial ones.

Even if (a) and (b), as well as (c) and (d), geometries look different for a single octahedron, they are potentially the same in a supercell periodic framework. Actually, the (a) substitution is equivalent to (b) (and (c) to (d)) when the neighboring Ti atom is taken as the octahedron center. Substitutional doping preserves the octahedral symmetry and the bond distances of the original anatase phase, as shown in Fig. 3.19.

Distances are reported in Table 3.7 (3rd column) for the equatorial oxygen atom substitution and (4th column) for the axial one, at three different levels of DFT calculations. In all cases the Ti neighbor-atom distances are almost unchanged: equatorial ones are on average equal to 1.94 Å and the axial ones are on average equal to 2.03 Å.

Despite the well-known differences among the LCGTF and PAW approaches, it is important to note that the LCGTF perfectly reproduces the PAW DFT and the experimental findings on the coordination geometry around Ti.

The picture changes dramatically in the case of interstitial doping. On panel (c) of Fig. 3.19, the interstitial doping occurs at the equatorial region. The octahedral symmetry is broken and the distances, except one, are increased, with an average value around 2.00 Å. The exception is due to the O3 atom, which is *trans*-equatorial with respect to O4 and quite distant from the interstitial nitrogen. Therefore, it is less affected by changes of the bonding network around titanium.

As reported in Fig. 3.19d, axial distances are very much elongated, whereas equatorial ones are left almost unchanged. This geometry could resemble the undoped one. However, it should be noted that geometry reported in panel (d) of Fig. 3.19 is the same as (c), if taken from another point of view. In other

words, both geometries are present in the case of interstitial N-doping. Thus, the octahedral is broken for the geometry in panel (d) of Fig. 3.19 as well.

Bond	Undoped	N @ O eq.	N @ O ax.	N_{int} eq.	N_{int} ax.
Ti-O1	2.00/2.00 /1.98[1]	2.01/2.04/ 2.02	2.03/2.03/ 2.00	2.00/2.04/ 2.02	1.89/1.85/ 1.85
Ti-O2	2.00/2.00 /1.98	2.01/2.01/ 1.99	-	1.97/1.96/ 1.94	2.37/2.38/ 2.35
Ti-O3	1.94/1.95 /1.94	-	1.93/1.94/ 1.93	1.90/1.91/ 1.90	1.94/1.96/ 1.95
Ti-O4	1.94/1.95 /1.94	1.94/1.94/ 1.92	1.93/1.94/ 1.93	2.12/2.13/ 2.11	1.94/1.96/ 1.94
Ti-O5	1.94/1.95 /1.94	1.93/1.94/ 1.93	1.94/1.95/ 1.94	1.98/2.04/ 2.02	1.94/1.95/ 1.94
Ti-O6	1.94/1.95 /1.94	1.93/1.94/ 1.93	1.95/1.95/ 1.94	1.99/1.99/ 1.98	1.94/1.95/ 1.94
Ti-N	-	1.96/1.98/ 1.96	2.08/2.10/ 2.09	2.08/2.06/ 2.04	2.33/2.48/ 2.42
N-O	-	-	-	1.34/1.37/ 1.36	1.34/1.37/ 1.36

Table 3.7. Ti nearest neighbors DFT distances. [1]First PAW calculations with PBE, second and third for LCGTF with B3-LYP and PBE0 Hamiltonians, respectively. “eq.” and “ax.” stand for “equatorial” and “axial”, respectively. The last four columns refer to cases a,b,c,d of Fig. 3.19.

For a more realistic modeling, one needs to consider the effect of the presence of vacancies in the local geometrical arrangement. Then, the purpose is to see how the original octahedral geometry changes by placing a vacancy at one of the oxygen atoms both with and without the presence of N-dopant. The arrangement where both O-vacancy and dopant are located in the same octahedron is quite rare, because the actual dopant bulk concentration has been estimated to be very small. Nevertheless, such an eventuality cannot be excluded, as in nanostructured materials the surface-to-bulk atom ratio is significantly higher with respect to conventional bulk

compounds. Moreover, the eventuality that some kind of defect clustering[51] could take place within the lattice cannot be *a priori* neglected.

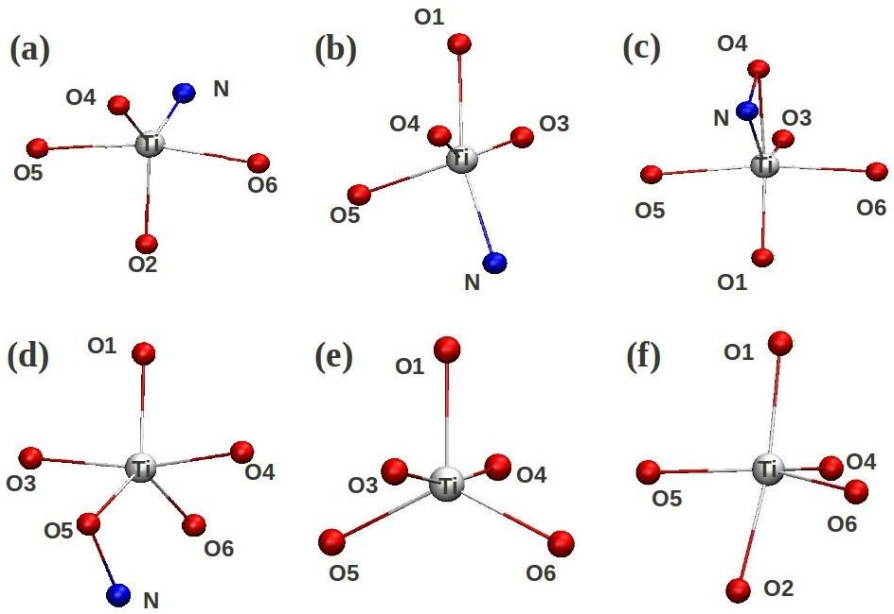

Figure 3.20. Nearest Ti neighbors in the presence of an oxygen vacancy: (a) and (b) for axial and equatorial substitutional N doping, respectively; (c) and (d) for the equatorial and axial interstitial N doping, respectively. Geometries (e) and (f) for undoped axial and equatorial vacancy, respectively.

Figure 3.20 reports the PAW-DFT equilibrium geometries for the concomitant occurrence of N-doping and O-vacancy around the same Ti ion, as well as for only O-vacancy. In geometries (a) and (b), the N-dopant atom is located respectively at equatorial and axial substitutional location, while the oxygen vacancy is respectively axial and equatorial. In geometry (a) the original octahedral shape is preserved, whereas in (b) the Ti-N axis is tilted with respect to the original octahedral axis in such a way to compensate for the equatorial oxygen vacancy. Geometries (c) and (d) represent the interstitial type of doping: in (c) the dopant is originally located at the equator and the vacancy at the axes, in (d) *viceversa*. From Fig. 3.20c, one can see how, during the DFT optimization procedure, the NO moiety (see Fig. 3.19c) migrates to compensate the O-vacancy by placing the oxygen next to the axial vacancy. Similarly, in Fig. 3.20d, the original axial NO moiety (see Fig. 3.19d) has arranged in a way to place the oxygen next to the equatorial vacancy. In

geometries (e) and (f) no dopant is present and the vacancy is located in axial and equatorial location, respectively.

For a better comparison, the distances between the central Ti atoms and the nearest neighbor-atoms are reported for the undoped (Fig. 3.20e-f) and doped (Fig. 3.20a-d) cases in Table 3.8. For the undoped defected octahedron (Fig. 3.20e-f and 2nd, 3rd columns of Table 3.8), the axial distances are reduced and are quite similar to the equatorial ones, which are left unchanged. In these cases one would observe a single set of distances, located at the equatorial anatase value. On the 4th column, the distances of the geometry in Fig. 4.20a for a substitutional doping at equator are reported: the equatorial distances are left unchanged, while the axial one is greatly reduced. As reported on the 5th column of Table 3.8, the axial distance is left invariant and the average equatorial one is slightly shorter, because the dopant is substitutionally located at the equator and an O-vacancy at the axis. Thus, in the case shown in Fig. 3.20b, the two sets of distances of the original anatase are almost unchanged. When the interstitial doping occurs, one can observe shorter equatorial and unchanged axial distances when the vacancy is placed on the axes, as reported in the 6th column of Table 3.8. Finally, in the last column the distances of Fig. 3.20d are almost identical with the ones of the last column in Table 3.7: the equatorial distances are unchanged, while the axial one are elongated in the case of Ti-N distance and shortened for Ti-O.

Bond	**Undoped ax. vac.**	**Undoped eq. vac.**	**N@O eq.**	**N@O ax.**	**N_{int} eq.**	**N_{int} ax.**
Ti-O1	X[1]	1.92	X	2.03	2.03	1.88
Ti-O2	1.86	1.96	1.88	-	X	X
Ti-O3	1.93	X	-	1.93	1.93	1.93
Ti-O4	1.92	1.81	1.90	1.93	1.93	1.93
Ti-O5	1.90	1.92	1.94	1.81	1.81	1.94
Ti-O6	1.90	1.91	1.94	X	1.81	1.94
Ti-N	-	-	1.90	1.90	1.90	2.24
NO	-	-	-	-	1.46	1.46

Table 3.8. Ti nearest neighbors PAW-DFT distances for oxygen defected octahedron. [1]X indicates the presence of oxygen vacancy. “eq.”, “ax.”, and “vac.” stand for equatorial”, “axial”, and “vacancy”, respectively. The last four columns refer to cases a,b,c,d of Fig. 3.20.

A rare configuration is achieved by placing both N doping and oxygen vacancy at equators. Would the picture have changed? Specifically, if both the N substitutional doping and oxygen vacancy had been equatorial, this would correspond to originally have two nearest neighbor vacancies. Instead, if the interstitial doping and oxygen vacancy had been equatorial, then the nitrogen would migrate into the vacancy (as can be seen from DFT calculations) and the arrangement would be equivalent to a substitutional equatorial doping.

EXAFS and DFT comparison / joint discussion

When trying to compare the EXAFS results with the DFT calculations, it should be remembered that EXAFS signals contain an average picture of the specimen, accounting for both doped and undoped regions. Thus, for a more realistic modeling, Table 3.9 reports the *average* equatorial versus axial distances values calculated from the PAW-PBE results in Table 3.7 and 3.8, since EXAFS results clearly allow us to make the equatorial-axial distinction. As for instance, under the column labeled "N@O" the average of all PBE equatorial Ti-nearest neighbor atoms taken from the 3rd and 4th columns of Table 3.7 is reported. This would be the EXAFS result if all Ti centers experienced a nearest-neighbor substitutional doping. Surely this is never the case and the EXAFS signal would presumably be an average (with different weights) among all possible scenarios reported in Table 3.9. The point is to see how the weight of each scenario changes with N content.

Distances (Å)	**Undoped**	**N@O**	**N_{int}**	**Undoped and O-vac.**	**N@O and O-vac.**	**N_{int} and O-vac.**
$<Ti\text{-}O(N)>_{equatorial}$	1.94	1.94	1.98	1.90	1.91	1.90
$<Ti\text{-}O(N)>_{axial}$	2.00	2.03	2.11	1.91	1.94	2.05

Table 3.9. Averaged Ti nearest neighbors (including N) from PAW-DFT distances in Tab. 3.7 and 3.8. "vac." stands for "vacancy"

Table 3.9, 3rd column, reinstates that the original octahedral distances are invariant when substitutional doping is predominant. Instead, if the interstitial doping prevailed, one should observe elongated axial distances (see 4th column). The creation of O-vacancies strongly affects the original octahedral

geometry, since distances become almost degenerate, as reported in the 5th column. Then, taking into consideration that doping happens to be within the same octahedron where an O-vacancy has been created, then the equatorial and axial distances are about the same when the doping is substitutional (6th column). Instead, last column, axial distances are elongated and equatorial ones shortened when it is the interstitial to share the same Ti center as the O-vacancy. As said above, a realistic picture includes all the different kind of Ti centers presented in Table 3.9. However, column 6th and 7th are clearly less frequent because they refer to a doping scenario where the dopant N atom and the O vacancy are both located near the same Ti atom. Although such a situation cannot be excluded *a priori* even if the O vacancies are few and randomly distributed, it is clear that it should become really significant only when the concentration of vacancies is very high. Therefore, columns 6th and 7th of Table 3.9 should be considered as limiting scenarios, corresponding respectively to (i) predominant substitutional N and (ii) predominant interstitial N together with the presence, in both cases, of high vacancy concentration.

The averaging over all possible scenarios confirms that the original anatase octahedral distances are unchanged only when substitutional doping prevails. Instead, the starting geometry would not be preserved if interstitial doping became dominant or O-vacancies concentration is significantly increased with respect to the original undoped sample. EXAFS averaged distance results show that there are much less Ti centers that experience a nearest-neighbor O-vacancy than a stoichiometric arrangement in the undoped sample, as reasonable. The original anatase octahedral geometry is preserved for doping below or equal to *ca*. 0.1 N/Ti initial molar ratio. By comparing the EXAFS results with all possible DFT scenarios in Table 3.9, one can safely deduce that N-doping is either superficial or bulk substitutional up to *ca*. 0.1 N/Ti initial molar ratio.

Instead, the scenario at higher dopant concentration is more complex. By increasing the dopant content, this geometry is significantly changed because some distances are elongated. Thus, with the help of theoretical calculations, it can be concluded that the doping is mainly substitutional at low concentration and then gradually interstitial sites are filled. This is in agreement with the conclusions reached using XRD data and related DFT considerations.

The decrement of axial distance observed by EXAFS can be explained by DFT calculations by assuming an indirect N-doping effect which increases the number of O-vacancies. According to DFT calculations, only the generation of O-vacancies can induce such an average axial distance shrinking (see the 'Undoped and O vacancy' column of Table 3.9). The same calculations allow for a concomitant N-doping increase: this can be either substitutional or interstitial, since both the N@O and N_{int} scenarios (see the 3rd and 4th columns of Table 3.9) are possible when O-vacancies predominate. At this level it is not possible to distinguish if the N-content is either substitutional or interstitial. The contemporary occurrence of a nitrogen atom and an oxygen vacancy near the same metal center (last two columns of Table 3.9) are considered quite remote possibilities.
In the light of theoretical simulations, EXAFS results point towards a picture where N-dopant atoms are present together with higher concentration of oxygen vacancies as doping increases. This finding is in line with results obtained by an independent set of experiments about electronic features of titania:[52] as it will be exposed in the following chapter, quasi-Fermi levels are almost invariant under N-doping and the amount of N-dopant, that acts as an electron acceptor, is always less than the O-vacancy concentration. The confirmation of the presence of O-vacancies can be supported also by XPS analyses in the Ti 2p region, with the presence of Ti^{3+} as a shoulder of the Ti^{4+} main component for the case of TN_0.50 (Fig. 3.14).

As far as photocatalysis is concerned, EXAFS data allowed us to have a direct interpretation of previous mineralization results of methylene blue.[26] In this case, the 0.05 N/Ti sample generated a 33 % improvements and the 0.1 a 133 % one, given the same surface area. Therefore, it can be safely asserted that only moderate interstitial N doping can considerably improve photocatalysis of methylene blue under solar irradiation.

Influence of the polymorphs

One may wonder if this distance change detected by the EXAFS experiments can be induced by a change of composition ratio between anatase and brookite that N doping generates.
Actually, brookite geometry is such that the Ti-O distances of the octahedron can be divided into three groups. Two distances are around 1.86 Å, other two

around 1.95 Å and the last two around 2.03 Å. We exclude that the brookite component is inducing the reported distances change because its component gradually decrease from 23 % in the undoped samples to a 10 % in the 0.5 N/Ti sample. If the brookite component was highly influencing the EXAFS analysis, clear axial and equatorial distances for the undoped sample should have been found. It is possible that part of the brookite signal was taken as part of the background signal included in the modeling for the undoped samples and this limited any spurious effect. This change could not justify the observed drastic change in the EXAFS signal, not only because it is of the order of the reported error bar, but also owing to the fact that the EXAFS signal changes abruptly at nominal 0.1 N/Ti, while the change in brookite content is modest and gradual.

Rutile polymorph content is excluded based on the relative low calcination temperatures.

Thermodynamics considerations

Can thermodynamics predict the sequence where first substitutional doping is followed by the interstitial one?

Some authors claim that there are "some evidences for a preference for interstitial sites"[33] and that interstitial doping may occur first, based on theoretical thermodynamics considerations.[22,32,33] However, these calculations take the crystal titania as the thermodynamic reference, while this is not the case in the majority of the syntheses. Actually, inclusion of nitrogen is concomitant with TiO_2 synthesis, which already starts during the gel formation at room temperature. Subsequent calcination at T = 400 °C is not able to reinstate a full thermodynamic equilibrium to a perfect crystal and to validate the above energetic considerations.

By DFT calculation it was possible to determine the N-doped titania formation energy starting from stoichiometric titania.

In the case of a perfect crystal semiconductor, energy differences and the molecular oxygen and nitrogen chemical potentials involved by theoretical DFT calculations using both a 2x2x2 and a 3x3x3 supercell were evaluated. Since nanoparticles were calcined under $O_{2(g)}$ stream, oxygen rich conditions have been taken for evaluating the oxygen chemical potential. Considering that doping is thermodynamically inefficient, the interstitial doping resulted to be the more probable one by 0.42 eV for a 2x2x2 set-up and 0.84 eV for a

3x3x3 primitive supercell. Remarkably, the Stuttgard-Dresden pseudopotential LCTGF calculations on a 2x2x2 primitive supercell also find the interstitial doping scenario to be the most favorable one by 1.96 eV (2x2x2 primitive supercell, PBE0 hamiltonian).

The same conclusions do not necessarily apply to the more realistic defected crystal as starting point. In this case, however, the interstitial doping is still found to be more probable by both plane wave (0.41 eV for a 2x2x2 set-up and 0.84 for a 3x3x3 one) and LCTGF (1.96 eV) methods. Still, referring to a sol-gel synthesis to which is added the N source, it is not correct to consider the reactant as perfect or partially defected crystals. Indeed, inclusion of nitrogen is concomitant with TiO_2 formation, when it is under a gel phase. Subsequent 400 °C calcination may not be able to reinstate a full thermodynamic equilibrium and validate the above energetics considerations. The reasons why the substitutional doping should be favored, even under oxygen rich conditions,[22,32] may lay on the kinetic barrier involved in breaking the octahedral shape. In other words, interstitial doping pays a higher kinetic price than substitutional one, as contemplated by the EXAFS data up to *ca* 0.1 N/Ti nominal molar ratio. A set of DFT calculations on vacancies, interstitial and substitutional nitrogen migration has shown that kinetic barriers change drastically depending on the bulk set-up.[53] As far as the oxygen vacancies creation is concerned, these are favoured under N doping likely because of the electron transfer from an F center (or Ti^{3+} state) to a midgap N electronic state.[52,54-56]

3.4.3. Morphology and structure of N-TiO_2 from different N sources

X-ray diffraction data show the presence of anatase and brookite polymorphs for all samples, with the former as the predominant one (Table 3.10, 2nd and 3rd columns). From the most intense reflection (101) of the TiO_2 anatase phase, the average diameter of the crystallites, d^A_{101}, (Table 3.10, 4th column) was estimated to be about 7-8 nm, thus not differing significantly for undoped and doped samples.[26]

Sample	% A	% B	d^{A}_{101} (nm)	S_{BET} ($m^2 g^{-1}$)	Pore vol. (mL g^{-1})
T	70	30	7	165	0.34
TN_TEA	78	22	8	114	0.04
TN_urea	74	26	7	162	0.30
TN_NH_3	77	23	8	149	0.20

Table 3.10. Specific surface areas and pore volumes (BET-BJH analyses), average diameter of the anatase crystallites and phase composition (XRPD - A=anatase, B=brookite) for N-TiO_2 from three different N sources (triethylamine, ammonia and urea, nominal N/Ti molar ratio = 0.1).

Fig. 3.21a and 3.21b shows the HR-TEM images of undoped and TEA-doped TiO_2, respectively. The latter has been selected as representative for all N-TiO_2 samples since no significant differences could be detected among the doped oxides. The micrographs show only a few isolated particles in the powders, which indeed show some degree of aggregation. As reported in a previous work,[26] the tendency to superposition is noticeable. All domains are well crystallized, though the presence of defects (dislocations mainly) and the related deformation field effects are not entirely negligible. Fig. 3.21b exhibits that N–TiO_2 particles are approximately in the range of 5-8 nm, similar to the N–TiO_2 made by sol–gel method by other authors.[57] Caratto *et al*.[58] found the shape of ammonia-doped TiO_2 to be more angular and a little more elongated respect to the undoped, without evidence that the increase of the NH_3 concentration modifies the crystallization process, the shape and dimensions of nanoparticles.

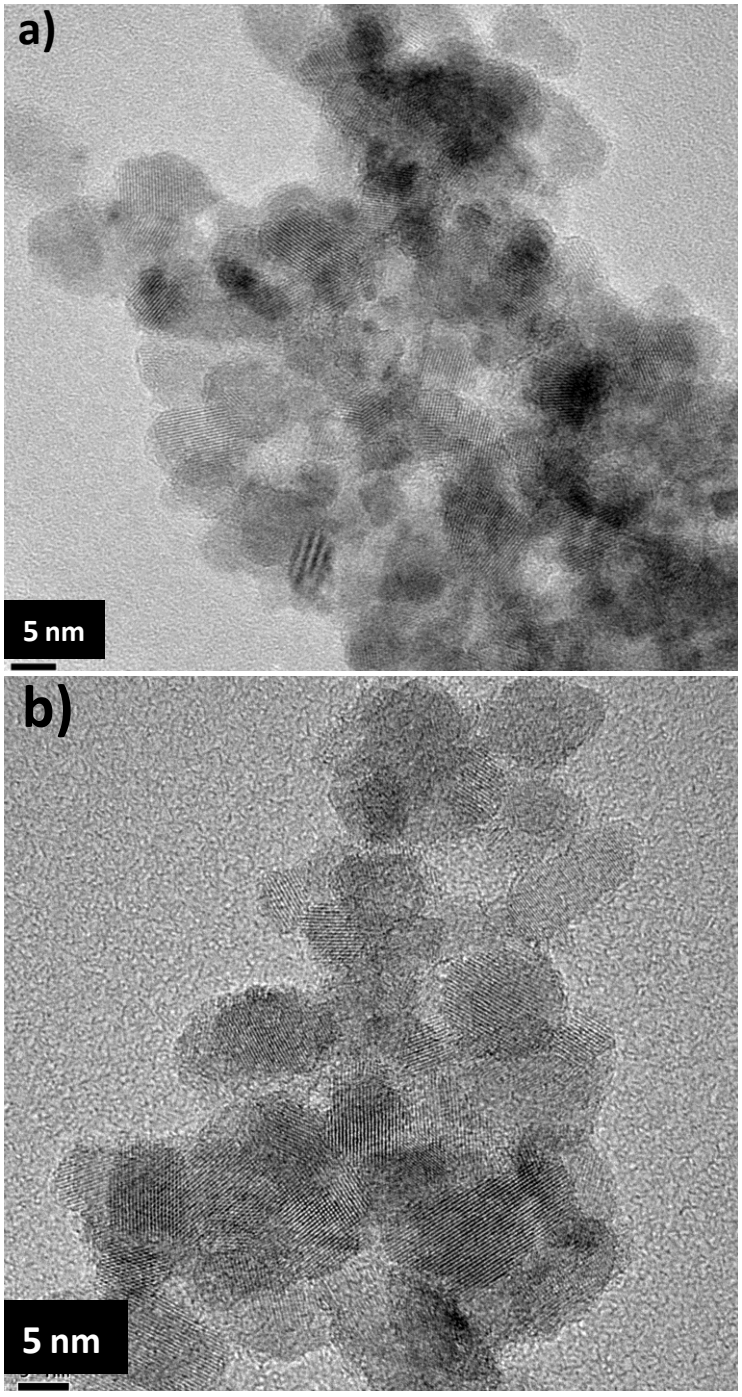

Figure 3.21. HR-TEM images of bare TiO_2 (**a**) and TN_TEA (**b**) as representative sample for nitrogen doping.

BET-BJH analysis

Unlike the above mentioned features of our doped powders, the shape of the N_2 adsorption-desorption hysteresis loops is deeply affected by the type of nitrogen source (Fig. 3.22a): they change from H4 type (predominant slit-shaped pores) in the case of the undoped and urea-doped samples, as also found by other authors,[25,59] to a prevailing ''bottleneck'' shape (H2) for both the TEA and NH_3 derived samples. However, the isotherms obtained for all samples are ascribable to type IV.

Interestingly, the isotherms of the undoped and urea-doped titania show similarities as for both the shape and the total amount of pores. When TEA and ammonia are used, the hysteresis loop becomes narrower implying a lower degree of porosity. At the same time, for such dopants, the maximum adsorbed volumes drop by about 50 % indicating a decreased surface area, as can be noticed by the values reported in Table 3.10, 5th column. The results of the BJH pore size statistics, *i.e.*, the pore size distribution curves, are shown in Fig. 3.22b, which was derived from the desorption branches of the isotherms, and the total pore volumes are summarized for each sample in Table 3.10, 6th column. Also these data partly support such differences among the three N-doped samples. The oxide showing the largest pore volume is the one derived from urea (TN_urea), the increase concerning the smallest pore sizes (<6 nm), while the sample obtained from triethylamine (TN_TEA) shows a significant collapse of the total pore volume.

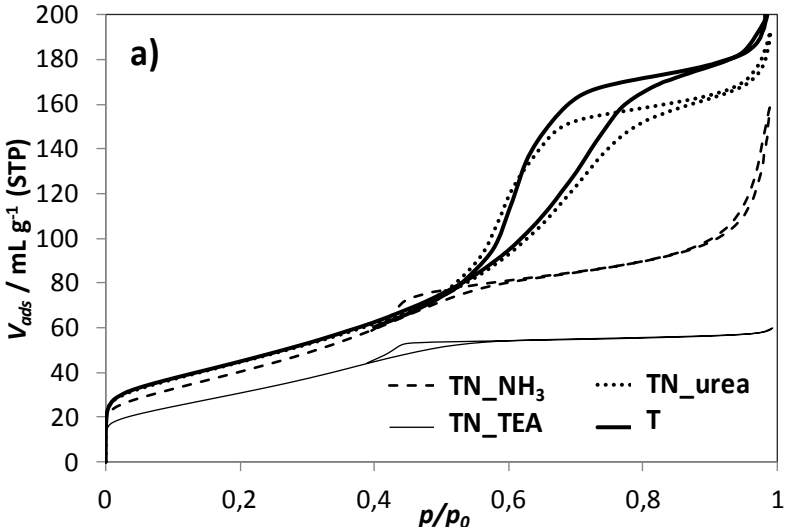

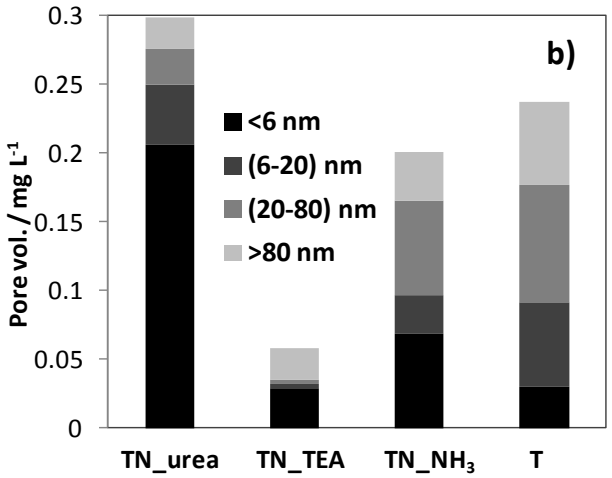

Figure 3.22. N_2 adsorption-desorption isotherms with relative hysteresis loops (**a**) and pore size distribution (**b**) of the N-doped samples.

3.4.4. "Aging" effects on the dry powders

Structural, morphological - and optical, as demonstrated hereafter - characterizations have pointed out that the fresh N-doped samples not only differ from undoped TiO_2, thus attesting that the promotion by the non-metal element has occurred, but also show different features depending on the nitrogen source adopted in the synthesis.

In the following it will be shown that significant differences exist not only among the adopted N-doped powders, but also between "fresh" and "old" ones (samples are named "old" if they are simply stored in closed flasks for months in the dark and under ambient atmosphere). This is valid not only in term of physico-chemical properties but also for the final photocatalytic performances, as it will be shown in chapter 5. Hereafter, samples have been studied also after several days from preparation mainly by means of EPR and DRS to explore the "time effect" on the concentration of paramagnetic species and on the optical features, respectively. To the author's best knowledge no studies are present in the open literature on the topic of the stability of defects induced by the addition of nitrogen doping.

DRS analysis

To gain information on the light absorption features of the various samples, experimental data of diffuse reflectance were collected (Fig. 3.23a) and presented in derivative form (Fig. 3.23b) to better highlight the differences among the samples. The former figure permits a comparison of the shape of the diffuse reflectance spectra (DRS) according to the different N dopants. The undoped T sample presents the traditional sigmoidal form of the pure oxide, while in the visible region (λ >400 nm, hν <3.1 eV) all doped samples show a marked absorption which differs depending on the N source. Indeed, the spectra of TN_urea and TN_NH_3 almost overlap, whereas the TN_TEA sample sharply differs from the others because it does not show two inflection points but a broad absorption in the visible region.

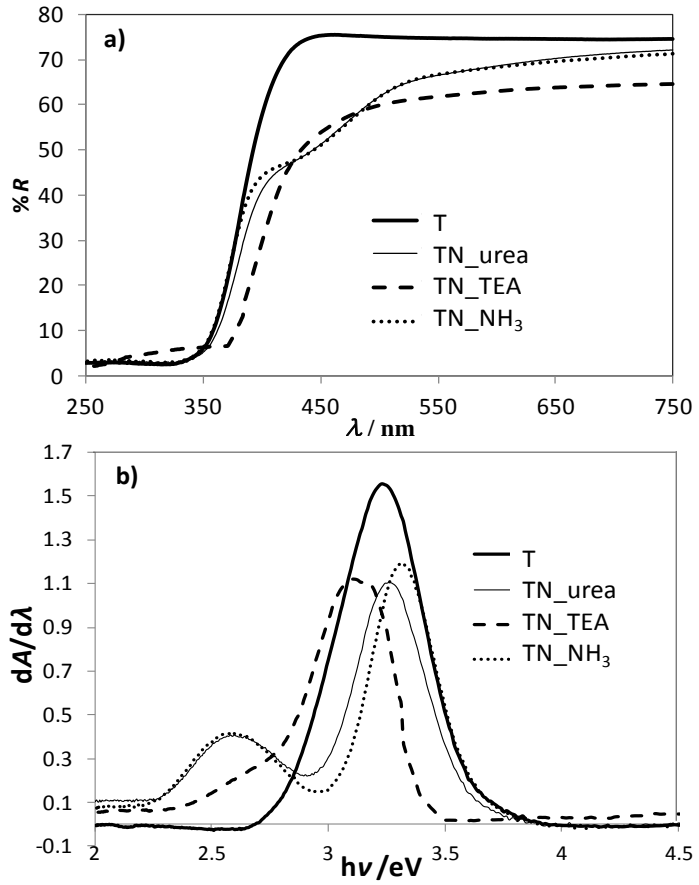

Figure 3.23. Diffuse reflectance spectra (a) and the respective derivative plots (b) for all samples.

The derivative plots of the absorption spectra show that the absorption maximum lies at 3.2-3.3 eV for T, shifting to lower energy (~3.0 eV) for TN_TEA. At lower energies (2.5-2.6 eV), contrary to the very weak absorption of the TN_TEA sample, the urea- and ammonia-doped samples present a well-defined secondary maximum, which denotes a noticeable absorption into that specific visible range, this being in agreement with the $h\nu_{max}$ numerical values reported by Kuznetsov and Serpone.[55] They distinguished a few regions of single dominating absorption bands where values of $h\nu_{max}$ differ slightly. Then, they supported the evidence that only the intrinsic defects in TiO_2 are responsible for these bands, which they affirmed to be independent of the nature of the anion or cation dopant, although the relative intensities of the bands depend on the contribution of the reductive and oxidative treatments performed on the oxide.

The effects of time after synthesis and calcinations on the N-doped samples is clearly shown in Fig. 3.24. Indeed, after keeping the doped powders in dark and in closed vessels for a certain period, they show a clear, even though slight, tendency to modify their light absorption features: the diffuse reflectance spectrum of the "2-month old" TN_NH3 sample lies higher than the "fresh" one, as occurs in the case of TN_TEA. On the contrary, the TN_urea displays striking dissimilarities with respect to the other doped ones: even after 5 months of ageing (in Fig. 3.24 it is reported the 2-month-old for the sake of comparison), its spectrum perfectly overlaps with the one of the relative fresh sample.

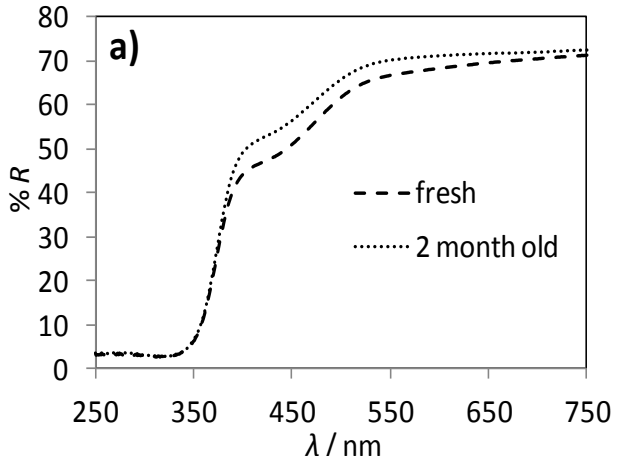

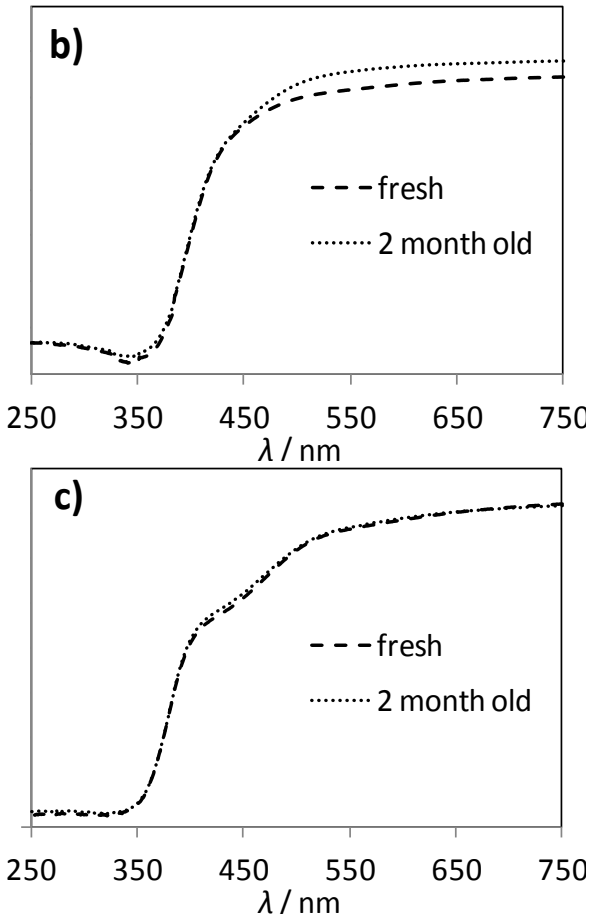

Figure 3.24. DRS of the "fresh" and of the "2-month old" powder for TiO_2 doped with ammonia (a), triethylamine (b) and urea (c).

EPR investigation

Employing electron paramagnetic resonance, Livraghi *et al*. detected paramagnetic bulk species of N ($N_b^{\bullet}$) at a g-value of 2.005, which formed localized states within the band gap of their N-doped TiO_2.[60] The authors proposed a reversible electron transfer between the $N_b^{\bullet}$ and Ti^{3+} centers forming the diamagnectic bulk species of N (N_b^{-}) and Ti^{4+}. A similar phenomenon was also observed by Napoli *et al.* when they exposed a prereduced TiO^2 to a N plasma.[61] The N-induced states of N_b^{-} species are higher in energy than that of corresponding $N_b^{\bullet}$ species due to greater

Coulombic repulsion, thus enabling excitation with photons of longer wavelengths.[62]

In the present study, to better enlighten the effects of time on the stability of the paramagnetic defects induced by the presence of the N dopants, their concentration has been monitored by EPR spectroscopy 24 h after the calcination (first dot in the plot, Fig. 3.25) and then periodically every 5-10 days.

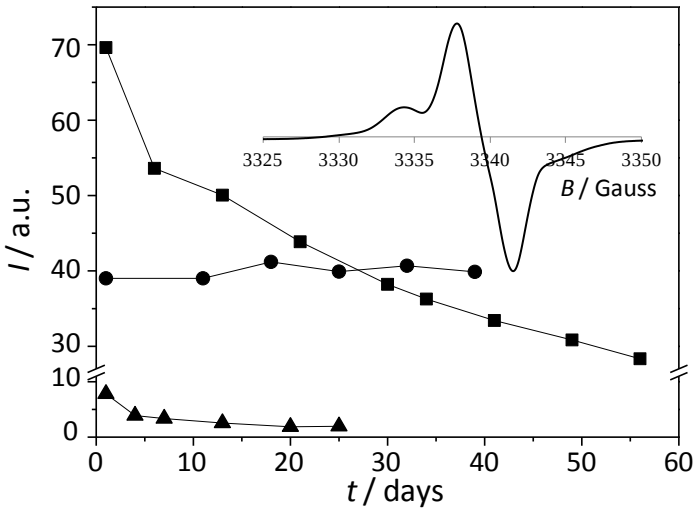

Figure 3.25. EPR signal decay normalized by weight for all the N-doped samples. Inset: EPR signal obtained at room temperature and assigned to the paramagnetic species $N_b^{\bullet}$, as representative for all N-doped titania.

All reported intensities have been normalized by the weight of the powders in the capillary tube. The spectral profile is simulated by hypothesizing an unpaired electron with Zeeman energy parameters g_x = 2.0066; g_y = 2.0054; g_z = 2.0040 and interacting with a nuclear magnetic moment I = 1 through the hyperfine coupling parameters $A_x \approx A_y \approx 3$ G and $A_z \approx 32.2$ G.[26] As a general consideration, this EPR signal associated to $N_b^{\bullet}$ decreases with time. The TN_urea sample behaves quite uniquely: the amount of paramagnetic species is nearly constant. The TN_TEA sample shows a very low signal compared to the other ones (Fig. 3.25). For this reason its weak decay can be considered as a nearly time-independent behavior. Table 3.25 reports elaboration of selected EPR data shown in Figure 3.25: to make a tighter comparison, EPR signal intensities corresponding to one day and to thirty days after calcination

have been normalized to the sample with the highest intensity (TN_NH_3). Thus, it is immediately clear what stated above: constant values of EPR intensity for TN_urea, and low signals – however decreasing, as for TN_NH_3 – for TN_TEA.

Sample	Relative EPR signal intensity	
	1 day after annealing	30 days after annealing
TN_NH_3	1	0.55
TN_urea	0.56	0.58
TN_TEA	0.11	0.03

Table 3.11. EPR signal intensities, as reported in Figure 3.25, have been normalized to the sample with the highest intensity (TN_NH_3). Values refer to the EPR signals recorded one day or thirty days after annealing (calcination treatment) to compare the decay of paramagnetic species ($N_b^{\bullet}$) for all the N-doped samples.

An analogous, even though less pronounced, behavior of these doped powders with time has been also shown in Fig. 3.24.
Apparently the life-time of the induced defects (Ti^{3+} and/or oxygen vacancies) at room temperature and ambient pressure depends on the specific structure and chemical environment of the defect itself. The “fast” ageing features shown by TN_NH_3 might suggest a prevailing surface localization of the defects and their consequent lower stability upon the contact with O_2/humidity. The situation might be opposite in the case of urea which is by far less volatile than NH_3 and might therefore give rise to more “permanent” defective sites during the synthetic steps.

3.5. Pr-doped TiO_2

Pr-doped titania explored in this study consists in a series of samples with different Pr/Ti molar ratio (0.2-0.3-0.5-0.7 %). They have been characterized not only by the morphological, structural and optical point of view: also electrochemical tools have been used to evaluate specific features of such samples. However, since two separate chapters have been overall dedicated to characterizations of all the titania materials presented in this thesis (except

for TiO_2 employed in solar cell devices), results related to electrochemical techniques, *i.e.*, electronic aspects, will be discussed in chapter 4. For Pr-TiO_2 samples this sharp separation could sound unfavorable for a logical discussion, but the whole "story" on Pr-doped titania to determine the Pr location in the lattice will be however exposed and conclusions will be drawn in the following chapter.

The praseodymium dopant at different molar ratio was introduced into the titania precursor by a synthesis that is typically a bulk procedure. The whole range of Pr nominal amount is comparable with concentrations employed in the literature. EDX analyses confirmed the presence of the Pr species and the relative concentration in the titania powders (0.18 to 0.62 % Pr/Ti atomic ratio). Moreover, Pr could be considered to be randomly present in both anatase and brookite TiO_2 polymorphs, and its manifest effect also lies in a progressive increase in the average lattice distortion (see infra).

Computational setup

The following computational details are valid for both geometric and electronic (see paragraph 4.2) calculations on undoped and Pr-doped titania.

Spin-polarized calculations were performed within the Generalized Gradient Approximation (GGA)[63] to Density Functional Theory (DFT)[1,2] with the Perdew–Burke–Ernzerhof (PBE) exchange correlation functional.[45,64] The Kohn-Sham scheme was solved using the plane wave basis with projected augmented wave method (PAW)[65,66] implemented in the Vienna Ab-initio Simulation Package code (VASP),[67,68] with an energy cutoff of 400 eV. The ground state optimizations were obtained by minimizing the partial derivatives of free energy with respect to the atomic position, including the Harris-Foulkes correction to forces,[69,70] using the conjugate-gradient scheme.[71,72] Iterative relaxation of atomic positions was stopped when the change in total energy between successive steps was less than 0.001 eV. Electronic property calculations were carried out using the block Davidson scheme.[73] The supercell and atomic relaxations were carried out until the residual forces were below 0.01 eV $Å^{-1}$. The bulk doped systems were constructed from the relaxed 3x3x3 162-atom anatase TiO_2 supercell. Reciprocal space sampling was restricted to the Γ-point, which is justified due to the rather large size of the used simulation supercells. Given the nature of the atoms considered and

to properly describe the reduced Ti ions, we have applied the GGA+U method, formulated by Dudarev *et al.*,[9] to account for the strong on-site Coulomb repulsion amid the localized Ti 3d and Pr 4f electrons. Comparison with UPS (ultraviolet photoelectron **s**pectroscopy) data suggested a value of U = 3 eV.[74] However, there is no agreement on a precise value of U for all oxidation states of Ti, and the values of U span a range from 2 to 8 eV, as a result of the U dependence on the oxide, the Ti oxidation states, and the underlying exchange-correlation functional.[12,75-78] Theoretical calculations for catalysis showed that U values can also be derived from the oxidation of Ti_2O_3 to TiO_2 reaction energy and one should prefer using either PBE+U or PW91+U, with U =2-3 eV.[79] Finally, it is possible to adopt a self-consistent linear response approach for the determination of the Hubbard U correction term.[80,81] Mattioli *et al*.[82] found a value of 3.23 eV for the anatase Ti 3d electrons using this approach. In conclusions, these and other studies[12,74,83] provided evidence of the unsuitability of exchange-correlation functionals for describing the reduced Ti ions. Consequently we chose to perform our calculations with the U = 3 eV, 3.3 eV, 4 eV and 5 eV. As far as the U value for the 4f Pr orbitals, there have been several theoretical works to study the effects of lanthanide doping into titanium dioxide by first- principles calculations.[84,85] According to experiments,[86,87] Pr_2O_3 is a dielectric material with band gap energy equal to 3.9 eV. The Pr_2O_3 electronic structure was simulated with U = 0-1-2-3-4 eV and found the band gap to be, respectively, 3.81-3.85-3.94-4.03-4.12 eV. The 4f Pr electrons U value was then fixed to 2 eV.

The optimized undoped stoichiometric supercell lattice parameters were found, by theoretical calculations, to be a=11.547 Å and c=16.472 Å (a=3.849 Å and c=9.535 Å for a primitive cell), in good agreement with experimental results.[88]

3.5.1. Morphological and structural characterizations

HR-TEM

To shed some light on the external habit of the various TiO_2-based materials under study, both conventional transmission electron microscopy (C-TEM) and high-resolution transmission microscopy (HR-TEM) have been performed. The main features exhibited by the materials are summarized in Fig. 3.26: it can be observed that, despite the presence/absence of Pr, all samples show rather

small particles, with average crystallites sizes in the 7-10 nm range, highly packed but also highly individual (see the three left-hand images, referring to a low magnification investigation). If we inspect in more detail the ultimate morphology exhibited by the crystallites, we can evidence that, in the absence of Pr species, the plain TiO_2 particles (Fig. 3.26a) possess roundish but highly defective edges and high crystallinity, as witnessed by the presence of both fringe and thickness (Moirè's) patterns:[89] the crystal planes which generate this feature are in the majority of the cases due the (101) crystal planes of the TiO_2 anatase polymorph. When Pr species are present (Fig. 3.26b,c), the overall features above described remain almost unchanged, in particular for what concerns both phase and family of planes most exposed, but for the edges: for both Pr-doped materials it can be evidenced a more regular shape of the crystallites, with slightly less defectivity. In no cases either the presence of segregated Pr-rich phases or the formation of rutile-rich phases has ever been observed.

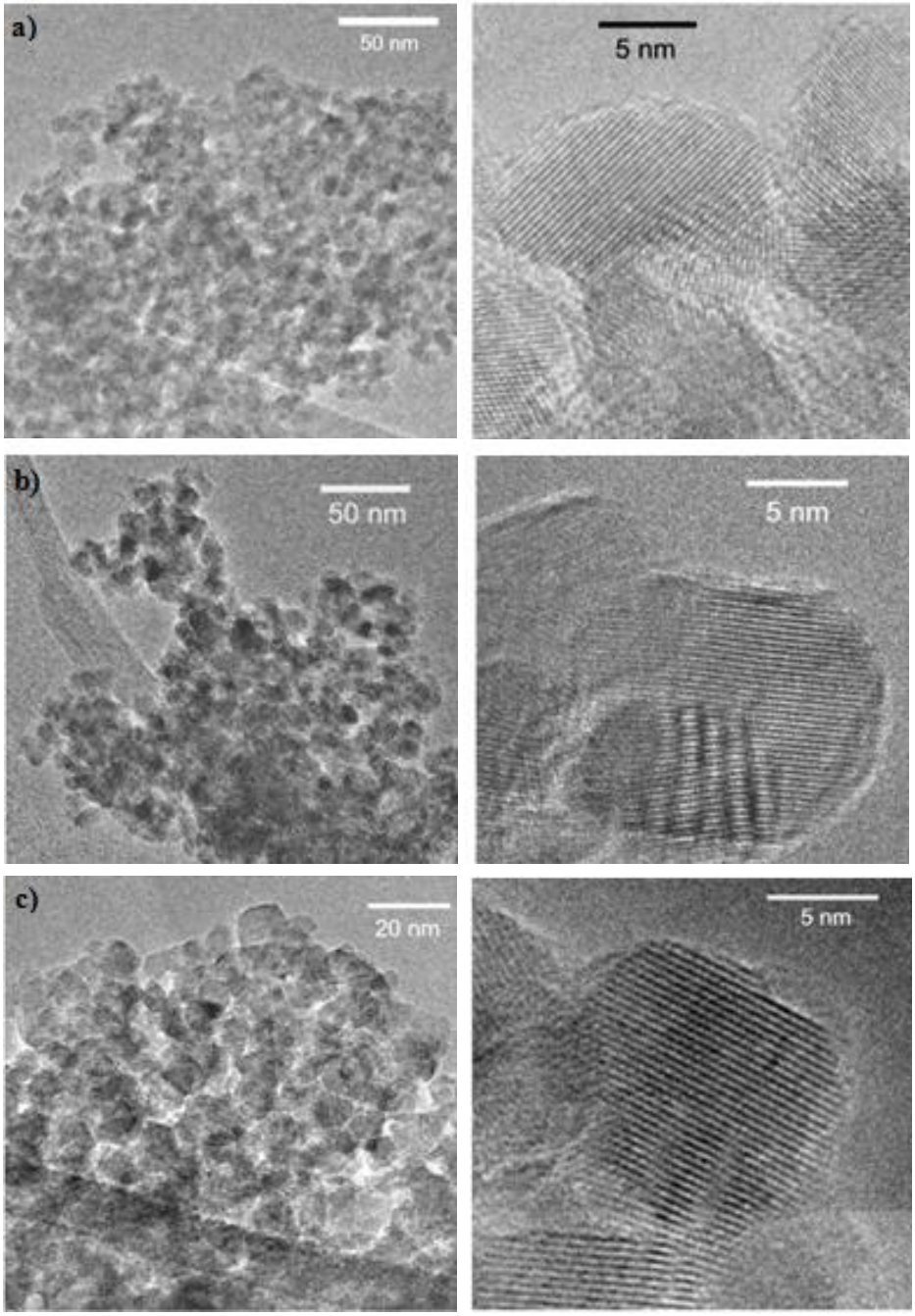

Figure 3.26. HRTEM images of undoped (a), 0.2% (b) and 0.5% (c) Pr-doped TiO_2 particles.

BET-BJH analysis

As concerns the specific surface areas, those of Pr-doped samples are lower than that of the undoped oxide, being reduced by even one third for the sample with the highest Pr content (see Table 3.12, 2nd column). Moreover, no specific linear trend occurs at increasing the Pr content. Accordingly, a substantial loss of the total pore volume is found with respect to the undoped TiO_2. Then, most of the survived pores are micropores (with the diameter lower than 6 nm), as reported in Table 3.12. This is in absolute accordance with Yana *et al.*, who affirmed that all doped samples show a conspicuous percentage of micropores, with a quite sharp and narrow distribution.[90]

Sample	S_{BET} ($m^2 g^{-1}$)	Pore vol. (mL g^{-1})	<6 nm pores (%)	6-80 nm pores (%)	>80 nm pores (%)
T	160	0.34	64	27	9
TPr_0.2	108	0.17	86	12	2
TPr_0.3	102	0.15	90	8	2
TPr_0.5	111	0.15	91	7	2
TPr_0.7	118	0.16	91	7	2

Table 3.12. Specific surface areas and pore volumes (BET-BJH analysis). Specifically, both the total pore volume and the percentages of three different pore sizes are reported.

The lowering of the specific surface areas could be in accordance with a less prominent presence of defects, thus leading to less favorable charge recombination events, which resemble the chronoamperometric results (see paragraph 4.2).

XRPD

X-ray powder diffraction experiments were performed on the freshly prepared nanostructured TiO_2 samples to evaluate the amount of their brookite content and possible changes in the lattice parameters, crystallite size and lattice strain as a function of the doping extent.

Figure 3.27 shows the diffraction patterns collected on the nanostructured TiO_2 powders at various doping extent, together with the corresponding least-squares fitting results. The significant intensity changes among different XRPD

patterns (see, for example, the peak at ~ 25.5° in each diffractogram of Figure 3.27) were attributed to the effect of the preferred orientations of crystallites.

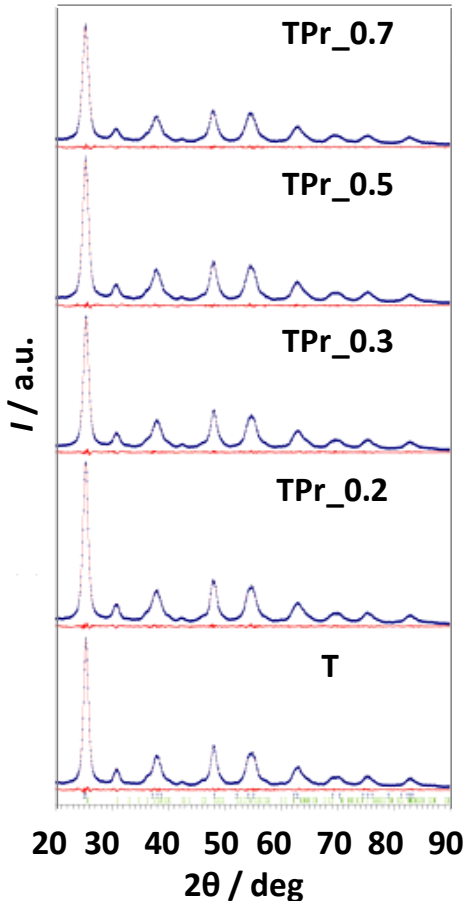

Figure 3.27. Collected powder patterns (blue crosses), with the corresponding least-square fitting curve and the point-by-point difference between "observed" and calculated intensities (red lines). The computed angular positions of both anatase and brookite reflections in pristine TiO_2 (T) are marked at the bottom of the plot.

All the specimens are clearly biphasic, as the large peak at 2θ ~ 30.8° is entirely due to the (211) reflection of brookite. However, the anatase structure appears to be the predominant one in all the diffractograms. No other phases were detected: attempt to add the rutile[91] or the Pr_2O_3 structures[92,93] to the model invariably led to the worsening of the least-square fit. As a matter of fact, most papers report the anatase phase as the only one

found in rare-earth-doped TiO_2,[94-97] therefore corroborating the lacking of any detectable segregated Pr-based phase in the present samples. The sole exception is represented by Amlouk *et al*. who synthesized transparent xerogel monoliths and detected traces of the $Pr_4(Ti_9O_{24})$ phase.[98] However, Amlouk *et al*.[98] employed a very different procedure (the monoliths grew in 90 days and underwent a very high calcination temperature, 1200 °C) compared to the classical sol-gel route we followed, which was also used by the authors of the other cited papers.

As a function of the Pr doping, no clear trends are detectable in the cell parameters of both the anatase and brookite phases (see Table 3.13), as their changes are non-monotonic and barely significant in terms of the corresponding estimated standard deviations.

Sample	Anatase			Brookite			
	a (Å)	c (Å)	V (Å^3)	a (Å)	b (Å)	c (Å)	V (Å^3)
T	3.7850(2)	9.473(1)	135.72(2)	9.151(3)	5.439(2)	5.161(2)	256.84(14)
TPr_0.2	3.7847(2)	9.475(1)	135.73(2)	9.156(3)	5.439(2)	5.166(2)	257.26(14)
TPr_0.3	3.7849(2)	9.471(1)	135.68(2)	9.145(3)	5.439(2)	5.173(2)	257.31(14)
TPr_0.5	3.7844(2)	9.472(1)	135.65(3)	9.166(4)	5.437(2)	5.166(2)	257.46(16)
TPr_0.7	3.7848(2)	9.471(1)	135.67(3)	9.154(4)	5.436(2)	5.173(2)	257.42(17)

Table 3.13. XRPD anatase ($I4_1/amd$) and brookite (Pbca) symmetry-independent lattice parameters and unit cell volumes for all Pr-TiO_2 samples. Estimated standard deviations (esd's) from the Rietveld fitting are given in parentheses.

Moreover, the brookite content was found to be invariant throughout the whole sample series (see Table 3.14). More in details, the weight fractions of anatase and brookite were estimated from the refined phase fraction coefficients to be, on average, as large as 0.612(1) and 0.388(1), respectively.

Sample	Anatase	Brookite
T	0.614(1)	0.386(2)
TPr_0.2	0.612(1)	0.388(2)
TPr_0.3	0.613(1)	0.387(2)
TPr_0.5	0.611(1)	0.389(2)
TPr_0.7	0.610(1)	0.380(2)

Table 3.14. Weight fractions of anatase and brookite phases for all Pr-TiO_2 samples, as retrieved from the Rietveld refinement on the XRPD data. Estimated standard deviations (esd's) are given in parentheses.

The full width at half maximum (FWHM) values, corrected for the instrumental line broadening, of some representative reflections belonging to the anatase structure are shown in Figure 3.28. Brookite reflections exhibit an analogue behavior.

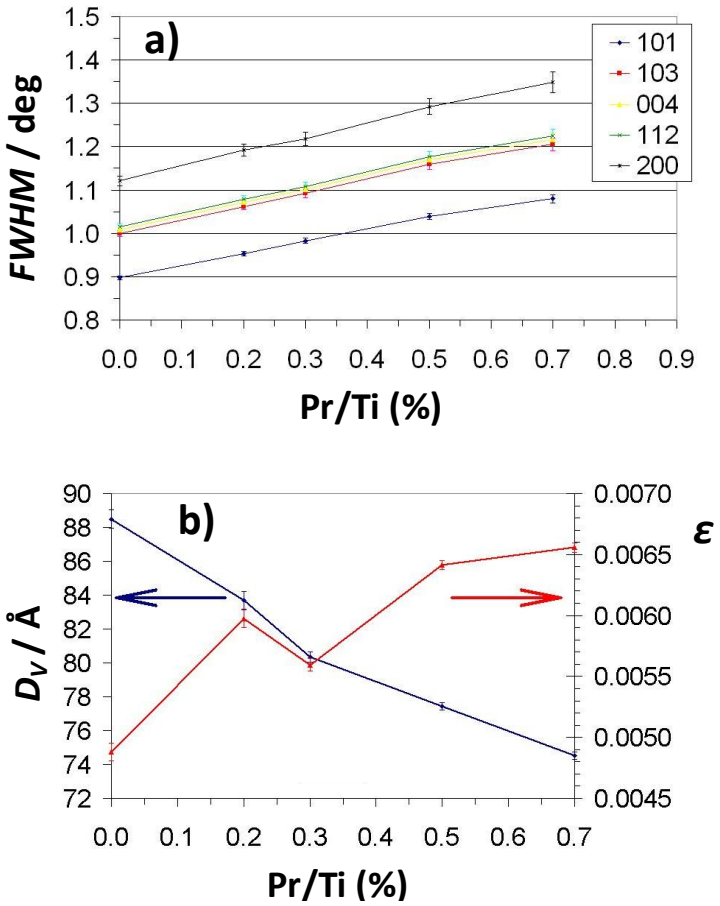

Figure 3.28. Behavior of some reflection-broadening parameters as a function of the Pr doping extent. (a) Full-width at half maximum (FWHM) of some low-angle reflections belonging to the anatase structure, as computed from the least-squares optimized profile coefficients in GSAS. The plotted curves serve as eye guidelines. (b) Volume-weighted average crystallite dimensions, D_V (blue squares, left axis) and average lattice strain, ε (red triangles, right axis), as computed from the Williamson-Hall method for the anatase reflections below $2\theta = 60°$. The plotted curves serve as eye guidelines. The error bars correspond to ±1 estimated standard deviations (esd's).

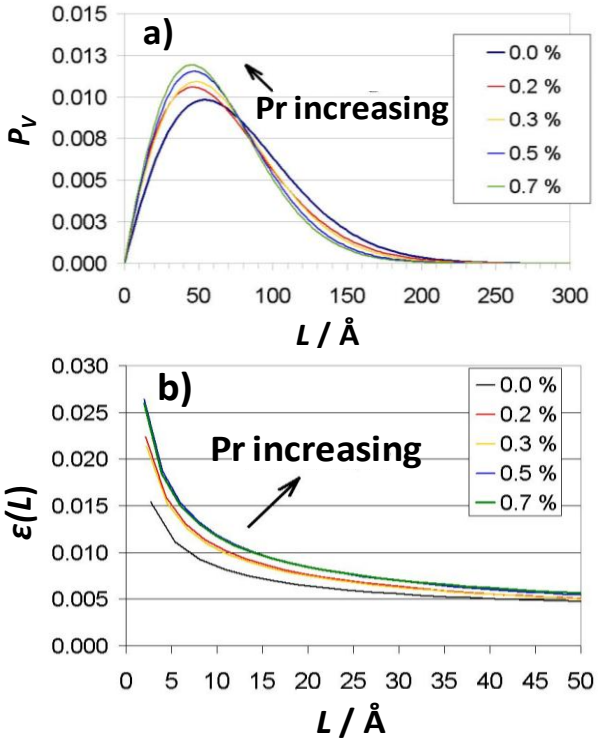

Figure 3.29. Volume-weighted column-length distribution, normalized on unit volume, of the anatase crystallites along the real vector modulus (L) orthogonal to the anatase (101) plane family, as computed from the double-Voigt method assuming a lognormal distribution of the crystallites (a). The same is depicted in panel (**b**) for the lattice strain distribution estimated from the double-Voigt method.

Interestingly, at increasing the nominal Pr/Ti molar ratio, the diffraction profiles systematically broaden. Such an effect may provide information on the behavior of the lattice strain and the average crystallite sizes as a function of the doping extent. It should be noted, however, that these quantities are quite difficult to be computed when, as in the present case, the diffraction patterns suffer of significant peak superposition.[99] Therefore, it has been chosen to provide a couple of size-strain estimates from two well-routed methods that face the problem from different perspectives. First of all, the Williamson-Hall recipe[100] was applied to the reflections belonging to the anatase structure up to 2θ = 60°. From Figure 3.28b it can be seen that the average volume-weighted domain size, $\langle D_V \rangle$, undergoes a ~ 16 % roughly linear reduction on going from the undoped sample (Pr/Ti = 0.0 %) to the most

doped one (Pr/Ti = 0.7 %). In general, it should be noted that the XRPD estimates for the crystallite dimensions agree quantitatively with the HRTEM outcomes commented above, providing a further evidence of the very high crystalline nature of such nanostructured compounds. On the other hand, the average lattice strain parameter, ε, undergoes a significant increase on going from the pure nanostructured TiO_2 to the doped specimens (Figure 3.28b)). It should be noted that ε(TPr_0.2) ≈ ε(TPr_0.3) within 3 estimated standard deviations, *i.e.*, the apparent decrease in ε upon going from the Pr/Ti = 0.2 % sample to the 0.3 % one is poorly significant from a statistical viewpoint.

Secondly, the double-Voigt method[101] implemented in the program BREADTH[102] was employed. Within this approach, the Lorentzian and Gaussian size and strain contributions to the physical profile broadening are singled out, provided that at least two reflections belonging to the same crystallographic family are analytically modelled with known suitable functions. In the present case, three reflections of anatase were used, namely the (101), (202) and (303) ones, approximating their experimental line profile with pseudo-Voigt functions, whose FWHM (amplitude) and η (mixing) parameters were retrieved from the optimized GSAS profile coefficients.[103] In this way, we were able to estimate the corresponding volume-weighted column length and strain distributions as a function of the real-space distance along the scattering vector, upon the assumption that the crystallite size distribution is lognormal (see Figure 3.29a,b). Some estimates for $\langle D_V \rangle$ and $\langle \varepsilon^2 \rangle^{1/2}$, based on such distributions, can be found in Figure 3.30.

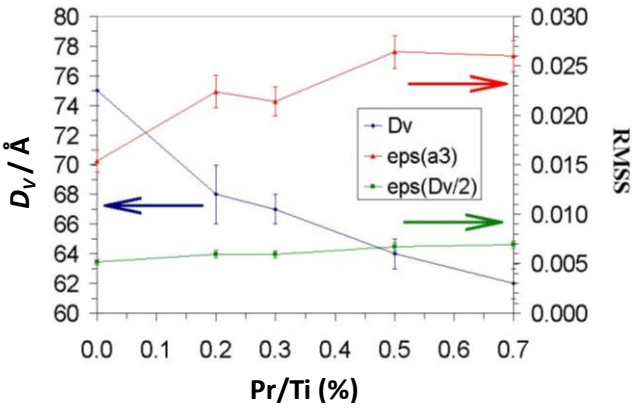

Figure 3.30. Outcomes of the double-Voigt method for size-strain estimates, referred to the anatase lattice, as a function of the Pr doping extent. The dark blue points (left axis) refer to the average volume-weighted crystallite domain size, D_V. The red triangles and the green squares (right axis) show the behavior of two different root mean square strain estimates, RMSS ($\langle \varepsilon^2 \rangle^{1/2}$), averaged over the a_3 (the edge of the orthorhombic cell, orthogonal to the diffracting planes) or the $D_V/2$ real distances.

It should be stressed that the integral breadth-based methods, including the Williamson-Hall approach, only give the volume-weighted domain size and the upper limit of the microstrain.[104] On the contrary, the knowledge of the crystallite distribution, although being based on some (reasonable) *a priori* assumptions, is required to fully characterize the sample microstructure.[105] As concerns the present case, the results provided by the double-Voigt approach agree well with the conclusions above sketched on the basis of the Williamson-Hall method. More in detail, it can be seen that an increment of the dopant concentration implies the shift of the most probable value of the size distribution (the mode) towards lower values, *i.e.*, it implies the corresponding reduction of the average crystallite size. At the same time, a progressive increment of the lattice strain can be also detected, with ε(TPr_0.7) ≈ ε(TPr_0.5) > ε(TPr_0.3) ≈ ε(TPr_0.2) > ε(T) at equal L.

In conclusion, it can be stated that the increment of the lattice strain observed by both the methods correlates with the increasing amount of Pr, as the brookite content remains the same throughout the sample series here considered. Together with the lacking of segregated Pr-based phases in our compounds, this evidence implies that the RE ions are likely disorderly dispersed in the bulk matrix, being either in the octahedral interstitial sites or the substitutional positions of anatase TiO_2. At the same time, the average crystallite size tends to become a little smaller as the Pr concentration is increased, in agreement also with previously reported literature results on nanostructured Pr-TiO_2 systems.[106] In any case, both the Williamson-Hall and the double-Voigt methods provide an estimate for this quantity in good agreement with the HRTEM outcomes.

DFT geometric calculations

As the diffraction experiments are not conclusive from the perspective of locating the Pr site within the TiO_2 lattice, a plane-wave DFT geometric optimization of a bulk Pr-doped 3x3x3 supercell was performed to understand if the XRPD outcomes are compatible either with substitutional or interstitial doping.

A supercell composed of 27 primitive cells was chosen to reproduce the averaged cell distortions that can be observed by XRPD analysis. In other words, the attention was drawn to the distortion effects on the averaged cell

parameters. The values of the cell anatase parameters after distortion, *i.e,. a*, *b*, *c*, and of the averaged primitive cell volume (*V*), are reported in Fig. 3.31.

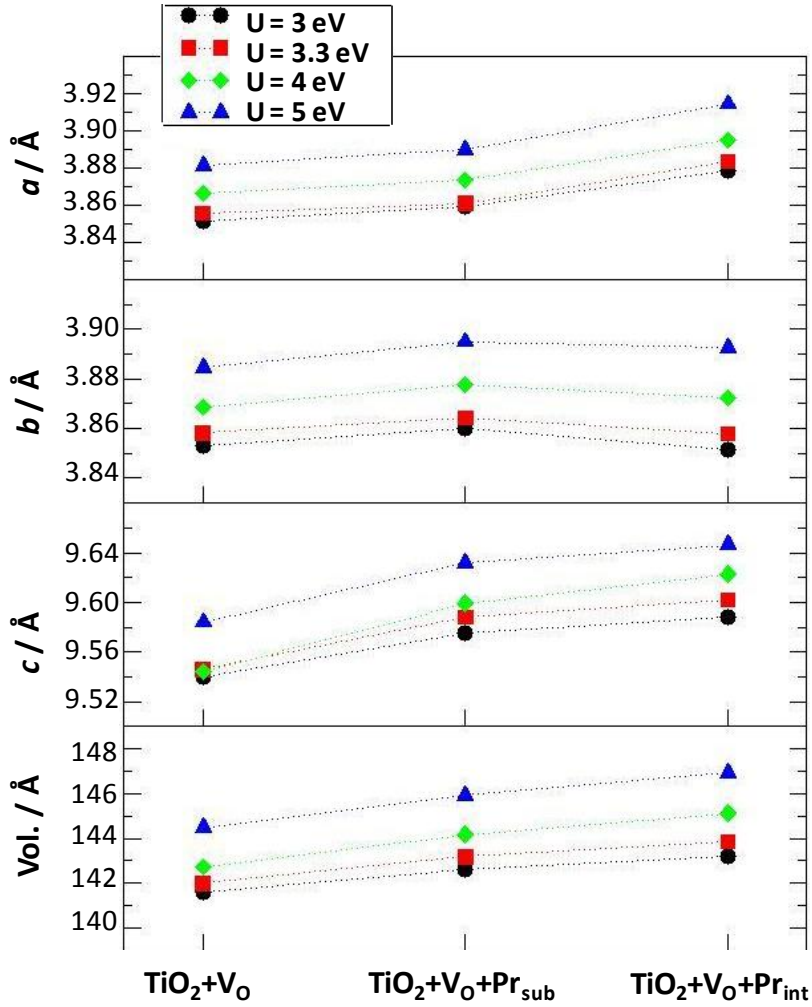

Figure 3.31. Primitive cell parameters (*a*,*b*,*c*) and cell volume (*V*) variation under Pr doping and for different values of U.

All the parameters increase under substitutional doping given the bigger effective ionic radius of Pr^{3+} (0.99 Å) with respect to Ti^{4+} (0.61 Å).[107] Nevertheless, these changes are more evident in the case of interstitial doping. To quantify the primitive cell distortion under doping, the distortion parameter $d = 2(a-b)/(a+b)$ was introduced, where *a* and *b* are the primitive cell parameters obtained as an average over all the primitive cells considered

in the simulation. If the primitive cell angles had been unchanged under doping, this parameter would have been the orthorombic cell distortion parameter. In this case, the angle changes are contained within 0.1°, and *d* is very similar to the orthorombic one. In Fig. 3.32 the values of *d* are reported for the undoped supercell in the presence of an oxygen vacancy (TiO_2+V_O), for the Pr substitutional doped supercell (TiO_2+V_O+Pr_{sub}) and for the interstitial Pr doped supercell (TiO_2+V_O+Pr_{int}). While substitutional doping leaves the *d* parameter unchanged, this is no longer true when the interstitial doping is considered. Thus, it would have not been possible to fit accurately interstitial Pr doping XRPD data with the anatase crystallographic model. Instead, as described above, XRPD data fit with good statistical accuracy into the anatase model. Moreover, theoretical results do not depend significantly on the U value and the same conclusions can be reached for any U.

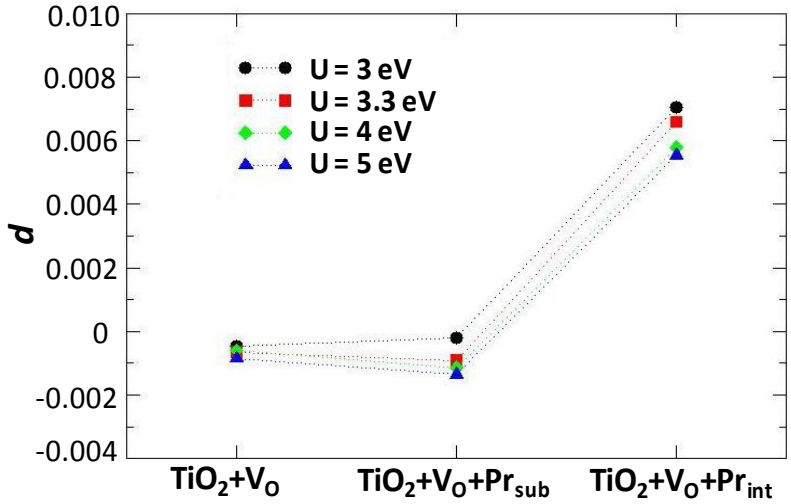

Figure 3.32. Averaged distortion *d* parameter of the primitive cell. Different colors and symbols for difference U (Pr) values.

All these geometric considerations have been done on the averaged cell. In order to have a local insight, Table 3.15 reports the distances between the Ti or Pr atom and the O atoms placed at the octahedron vertexes. These distances do not change for different U values in the case of the Ti central atom. Instead, minor differences can be seen in the case of Pr. Specifically, for each U value, the Pr centered octahedron presents slightly elongated

distances by still keeping the octahedral shape. This view of the substitutional doping is compatible with the XRPD patterns previously discussed.

U values	System	$d_{(X-1)}$	$d_{(X-2)}$	$d_{(X-3)}$	$d_{(X-4)}$	$d_{(X-5)}$	$d_{(X-6)}$
3-3.3-4-5	X = Ti	1.97	1.97	2.00	2.00	1.97	1.97
3	X = Pr	2.15	2.15	2.29	2.27	2.15	2.14
3.3	X = Pr	2.13	2.13	2.22	2.23	2.12	2.12
4	X = Pr	2.13	2.13	2.22	2.22	2.13	2.13
5	X = Pr	2.13	2.13	2.22	2.22	2.13	2.13

Table 3.15. Nearest oxygen atoms from substitutional center (in Å).

As a general remark, it should be stressed that, when DFT+U methods are employed to study the positions of dopant-induced defect states in a metal oxide, extreme care must be taken when making even qualitative conclusions without reference to more accurate approaches or experiments.

3.5.2. Optical characterizations

As already noticed by Xu *et al.*, the presence of RE^{3+} ions in the TiO_2 matrix may lead in general to a red-shift of the O 2p to Ti 3d charge transfer band.[96] Indeed, when the dopant content is increased, a slightly more pronounced absorption in the visible region is obtained for all our doped samples (Fig. 3.33), with the presence of some peculiar absorption features. In the literature, Li *et al.*[95] reported that neodymium dopant did not significantly shift the main absorption band edge, but brought some new absorption peaks attributable to 4f internal electron transitions in the visible region. It was further confirmed that significant photoluminescence emission occurred in the visible range of 350-700 nm; this is likely due to the electron transfer between Nd^{3+} and TiO_2 owing to introduction of a Nd 4f level.[108] Compared to the undoped sample having a bandgap of 3.2 eV, all the doped ones have an apparent bandgap of about 3.0 eV, according to the Kubelka–Munk equation.[26]

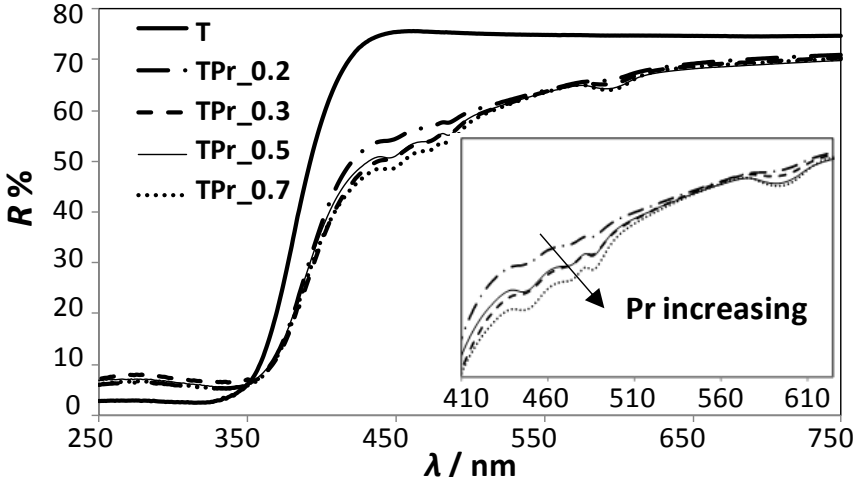

Figure 3.33. Diffuse reflectance spectra of the undoped (T) and all Pr-doped samples.

It should be noted that the photoexcited states of lanthanide ions attributed to 4f-5d or f-f transitions could transfer their excess energy to other molecules adsorbed to the semiconductor surface. These "host/guest" energy and electron transfer processes, on the other hand, should be a vital route in suppressing the recombination of charge carriers, thus playing a beneficial role in photocatalytic reactions.

3.6. Ag- and N,Ag-doped TiO_2

As far as metal-doped titania is concerned, no doubt that the study Ag-doped TiO_2 or Ag/TiO_2 composites, which are both known to exhibit photocromism,[109] falls within a quite controversial and complex scenario since, as for instance, the determination of the oxidation state is not a straightforward issue. Indeed, the reversible change of color of $Ag\text{-}TiO_2$ under illumination relies on the modification of the nanoparticle size distribution through photoactivated redox reactions occurring specifically with the titania matrix. However, few information is available about the dependence of composition and properties of such nanocomposites on external stimulations and on the change of the silver oxidation state.[110] Photooxidation of Ag to Ag^+ and photoreduction of Ag^+ to Ag are discussed in the literature concomitantly with photochromism.[111]

The present (N,)Ag-doped yellowish powders turned grey when exposed to ambient or UV light. A potentiometric titration has been used to determine the amount of Ag^+ species in the Ag-TiO_2 samples.
In order to verify the role played by Ag species in the recombination of the semiconductor charge carriers, the chemical reduction of selected samples (TAg0.01, TAg0.05, TNAg0.01, TNAg0.05) was performed by a treatment with $NaBH_4$ (see paragraph 2.1.1).

3.6.1. Morphological and structural characterizations

XRPD spectra show that doped samples are anatase-brookite composites, with crystallite size not differing significantly with respect to the undoped sample (in the range of 6-8 nm). None of the spectra shows the presence of silver oxide segregated phases.

The addition of silver ions lead to higher surface areas and pore volumes, as determined by BET analysis, with respect to the undoped TiO_2. Figure 3.34a shows a typical adsorption-desorption isotherm plot for the nitrogen sorption (77 K) of the samples. All plots correspond to the “type IV” isotherm in the Brunauer classification. At increasing the amount of silver dopant in the samples, surface areas decrease. The hysteresis loop observed in the plot is associated with the filling and emptying of mesopores by capillary condensation. Pore size distributions were then determined by the BJH method applied to the adsorption branch in the plot. While TN (the sample doped with urea only) exhibits bottle-neck pores, the other doped samples show the presence of open-ended cylindrical ones.
Porous oxide materials often contain micropores (<2 nm), which can also contribute to the nitrogen adsorption, influencing the type of the isotherm. In the present case, all samples show a marked presence of micropores, as can be deducted from the sharp decline in the low relative pressure region of the isotherms (Fig. 3.34a) and can be argued from the black part of the histograms in Fig. 3.34b.

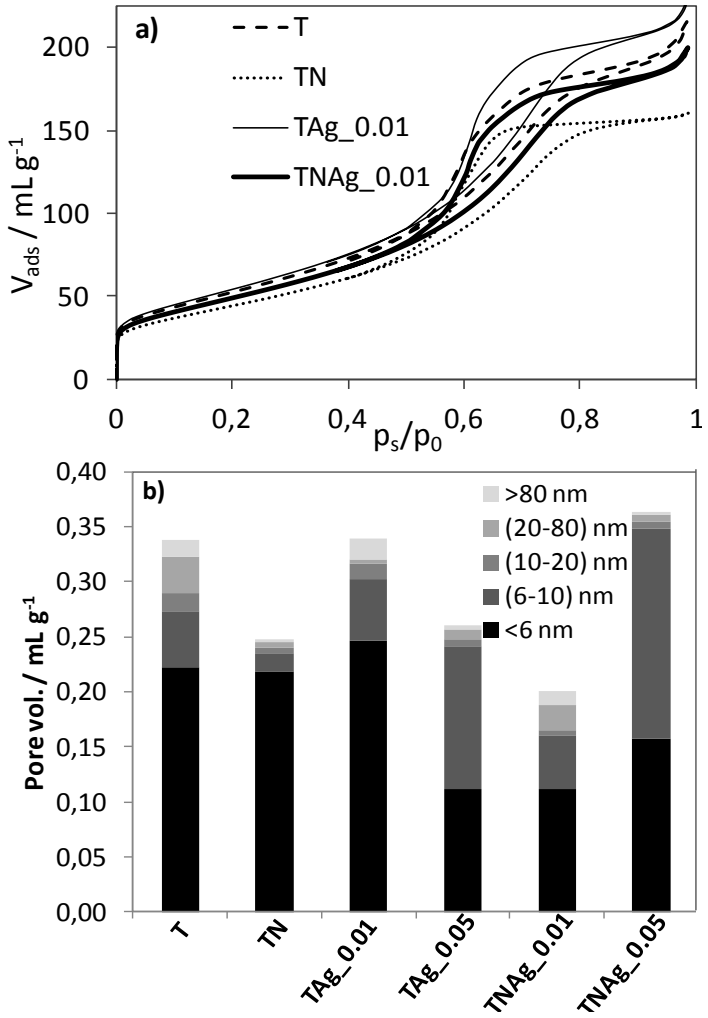

Figure 3.34. N_2 adsorption-desorption isotherms for selected samples (a) and pore size distribution (b) of the Ag-doped and Ag,N-codoped titania samples.

3.6.2. Optical characterizations

Diffuse reflectance spectra of all samples are displayed in Fig. 3.35. The present codoped samples show a broad absorption in the visible region. This is only partly due to the contribution of the N dopant: with increasing the starting Ag amount in the samples a more pronounced absorption covering the whole visible region is registered.

Ag-doped and N,Ag-codoped titania simply differ for the shape of the spectra (see the two inflection points for the N-doped oxides). Instead, the increase of the silver amount from 1 % to 5 % gives rise to much lower apparent band gap values (Table 3.16). Indeed, there is a difference in the onset of absorption for samples TAg_0.05 and TNAg_0.05 with respect to TAg_0.01 and TNAg_0.01.

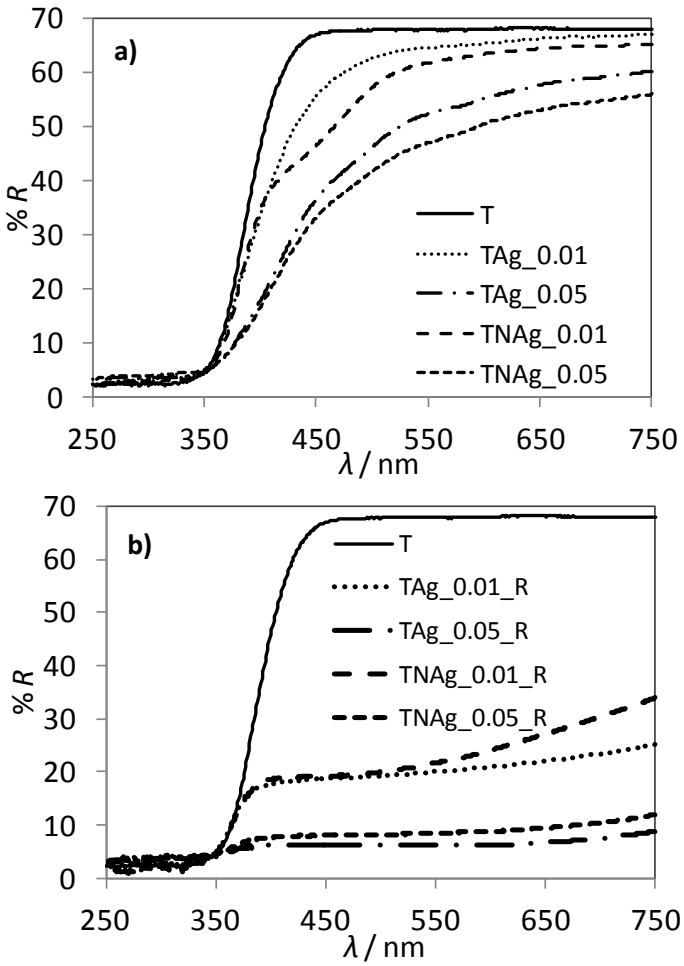

Figure 3.35. Diffuse reflectance spectra of undoped, single-doped and codoped samples (**a**) and of their respective reduced form (**b**).

Nevertheless, Ag content higher than 5% could be detrimental: a 10 % led to a non-homogeneous sample with a decreased surface area and segregated metal species. Moreover, as in other cases, superfluous dopants could have a

negative effect since they could act as recombination centers of photogenerated e^-–h^+ pairs.[112] Indeed, the photocatalytic activity towards photodegradation of ethanol (pollutant disappearance and mineralization followed by gas-chromatography) was the highest for titania with 1 % Ag/Ti molar ratio, and even higher for the same material when codoped with N.

Sample	S_{BET} ($m^2 g^{-1}$)	Pore vol. (mL g^{-1})	d< 10 nm pores (%)	d^{A}_{101} (nm)	% A	% B	b.g. (eV)
T	189	0.34	81	7	59	43	3.2
TN	159	0.25	89	7	74	26	3.1
TAg_0.01	196	0.34	96	7	57	43	3.2
TAg_0.05	157	0.31	95	8	48	52	2.7
TNAg_0.01	178	0.31	85	7	57	43	2.9
TNAg_0.05	142	0.32	94	8	69	31	2.7

Table 3.16. Specific surface areas, total pore volumes and percentage of pores with diameter smaller than 10 nm (BET-BJH analysis); anatase crystallite size, anatase and brookite percentage (XRPD analysis - A=anatase, B=brookite) and apparent band gap values (DRS) of Ag-doped and Ag,N-codoped samples.

3.7. References

1. P. Honenberg and W. Khon *Phys. Rev*. 136 (**1964**) B864.
2. W. Khon and L.J. Sham *Phys. Rev*. 140 (**1965**) A1133.
3. S. Grimme *J. Chem. Phys.* 124 (**2006**) 034108.
4. S. Grimme *J. Comp. Chem.* 25 (**2004**) 1463.
5. R. Miloua, Z. Kebbab, N. Benramdane, M. Khadraoui, F. Chiker *Comput. Mater. Sci.* 50 (**2011**) 2142.
6. C. Di Valentin, G. Pacchioni, A. Selloni *Chem. Mater*. 17 (**2005**) 6656.
7. J. G. Tao, L. X. Guan, J. S. Pan, C. H. A. Huan, L. Wang, J. L. Kuo, Z. Zhang, J. W. Chai, S. J. Wang *Appl. Phys. Lett*. 95 (**2009**) 062505.
8. E. Finazzi, C. Di Valentin, G. Pacchioni *J. Phys. Chem*. C 113 (**2009**) 220.
9. S. L. Dudarev, C. A. Botton, S. Y. Savarsov, C. J. Hunphreys, A. P. Sutton *Phys. Rev. B* 57 (**1998**) 1505.
10. E. Finazzi, C. Di Valentin, G. Pacchioni, A. Selloni *J. Chem. Phys.* 129 (**2008**) 154113.
11. G. Mattioli, F. Filippone, P. Alippi, A. Amore Bonapasta *Phys. Rev. B* 78 (**2008**) 241201.
12. B. J. Morgan and G. W. Watson *Surf. Sci.* 601 (**2007**) 5034.
13. J. Chen, Z. Hua, Y. Yan, A. A. Zakhidov, R. H. Baughmand, L. Xu *Chemm. Commun*. 46 (**2010**) 1872.
14. J. Yu, Y. Su, B. Cheng *Adv. Funct. Mater.* 17 (**2007**) 1984.
15. J. Yu, L. Zhang, B. Cheng, Y. Su *J. Phys. Chem. C* 111 (**2007**) 10582.
16. J. Yu, W. Wang, B. Cheng, B. Huang, X. Zhang *Res. Chem. Intermed.* 35 (**2009**) 653.
17. P. M. Oliver, G. W. Watson, E. T. Kelsey, S. C. Parker *J. Mater. Chem.* 8 (**1998**) 2073.
18. M. Lazzeri, A. Vittadini, A. Selloni, *Phys. Rev. B* 63 (**2001**) 155409.
19. C. C. Wang and J. Y. Ying *Chem. Mater*. 11 (**1999**) 3113.
20. G. Cappelletti, C. Ricci, S. Ardizzone, C. Parola, A. Anedda *J. Phys. Chem. B.* 109 (**2005**) 4448.
21. S. Manne, T. E. Schäffer, Q. Huo, P. K. Hansma, D. E. Morse, G. D. Stucky, I. A. Aksay *Langmuir* 13 (**1997**) 6382.
22. A. V. Emeline, V. N. Kuznetsov, V. K. Rybchuk, N. Serpone *Int. J. Photoenergy* 2008 (**2008**) 258394.
23. P. Roy, S. Berger, P. Schmuki *Angew. Chem., Int. Ed.* 50 (**2011**) 2904.
24. S. Ardizzone, G. Cappelletti, D. Meroni, F. Spadavecchia *Chem. Commun.* 47 (**2011**) 640.
25. P. Silija, Z. Yaakob, M. A. Yarmo, S. Sugunan, N. N. Binitha *J. Sol-Gel Sci. Technol*. 59 (**2011**) 252.

26. F. Spadavecchia, G. Cappelletti, S. Ardizzone, C. L. Bianchi, S. Cappelli, C. Oliva, P. Scardi, M. Leoni, P. Fermo *Appl. Catal. B: Environ*. 96 (**2010**) 314.
27. J. Ananpattarachai, P. Kajitvichyanukul, S. Seraphin *J. Hazardous Mat*. 168 (**2009**) 253.
28. H. M. Rietveld *J. Appl. Crystallogr.* 2 (**1969**) 65.
29. R. A. Young The Rietveld Method. Oxford University Press, Oxford, UK, **1993**.
30. P. Scardi and M. Leoni *Acta Crystall. A* 58 (**2002**) 190.
31. B. Othani *J. Photochem. Photobiol., C* 11 (**2010**) 157.
32. C. Di Valentin, E. Finazzi, G. Pacchioni, A. Selloni, S. Livraghi, M. C. Paganini, E. Giamello *Chem. Phys.* 339 (**2007**) 44.
33. C. Di Valentin, G. Pacchioni, A. Selloni, S. Livraghi, E. Giamello *J. Phys. Chem. B* 109 (**2005**) 11414.
34. G. Bunker, Introduction to XAFS. A practical guide to X-ray absorption fine structure spectroscopy. Cambridge University Press, Cambridge, UK, **2010**.
35. Y. Izumi, T. Itoi, S. Peng, K. Oka, Y. Shibata *J. Phys. Chem. C* 113 (**2009**) 6706.
36. P. C. Angelome, L. Andrini, M. E. Calvo, F. G. Requejo, S. A. Bilmes, G. J. Soler-Illia *J. Phys. Chem. C* 111 (**2007**) 10886.
37. L. X. Chen, T. Rajh, Z. Wang, M. C. Thurnauer *J. Phys. Chem. B* 101 (**1997**) 10688.
38. K. L. Yeung, A. J. Maira, J. Stolz, E. Hung, N. K.-C. Hu, A. C. Wei, J. Soria, K.-J. Chao *J. Phys. Chem. B* 106 (**2002**) 4608.
39. H. J. Monkhorst and J. D. Pack *Phys. Rev. B* 13 (**1976**) 5188.
40. F. Corà *Mol. Phys.* 103 (**2005**) 2483.
41. R. Pandey, J. E. Jaffe, N. M. Harrison *J. Phys. Chem. Solids* 55 (**1994**) 1357.
42. R. Dovesi, V. R. Saunders, C. Roetti, R. Orlando, C. M. Zicovich-Wilson, F. Pascale, B. Civalleri, K. Doll, N. M. Harrison, I. J. Bush, P. D'Arco, M. Llunell *CRYSTAL06 User's Manual*, University of Torino, Torino, Italy, **2006**.
43. A. D. Becke *J. Chem. Phys*. 98 (**1993**) 5648
44. S. H. Volsko, L. Wilk, M. Nusair *Can. J. Phys.* 58 (**1980**) 1200.
45. J. P. Perdew, K. Burk, M. Ernzerhof *Phys. Rev. Lett.* 77 (**1996**) 3865.
46. C. Adamo, V. Barone *J. Chem. Phys.* 110 (**1999**) 6158.
47. M. Dolg, U. Wedig, H. Stoll, H. Preuss *J. Chem. Phys*. 86 (**1987**) 866.
48. M. Ceotto, L. Lo Presti, G. Cappelletti, D. Meroni, F. Spadavecchia, R. Zecca, M. Leoni, P. Scardi, C. L. Bianchi, S. Ardizzone *J. Phys. Chem. C* 116 (**2012**) 1764.

49. V. Luca, S. Djajanti, R. F. Howe J. *Phys. Chem. B* 102 (**1998**) 10650.
50. Q.-L. Zhang, L.-C. Du, Y.-X. Weng, L. Wang, H.-Y. Chen, J.-Q. Li *J. Phys. Chem. B* 108 (**2004**) 15077.
51. C. Belver, R. Bellod, S. J. Stewart, F. G. Requejo, M. Fernández-García *Appl. Catal. B: Environ.* 65 (**2006**) 309.
52. F. Spadavecchia, G. Cappelletti, S. Ardizzone, M. Ceotto, L. Falciola *J. Phys. Chem. C* 115 (**2011**) 6381.
53. L. Tsetseris *Phys. Rev. B* 81 (**2010**) 165205.
54. K. Yang, Y. Dai, B. Huang, Y. P. Feng *Phys. Rev. B* 81 (**2010**) 033202.
55. V. N. Kuznetsov, N. Serpone *J. Phys. Chem. C* 113 (**2009**) 15110.
56. N. Serpone *J. Phys. Chem. B* 110 (**2006**) 24287.
57. D. Huang, Y. Miyamoto, J. Ding, J. Gu, S. Zhu, Q. Liu, T. Fan, Q. Guo, D. Zhang *Mater. Lett*. 65 (**2011**) 326.
58. V. Caratto, L. Setti, S. Campodonico, M. M. Carnasciali, R. Botter, M. Ferretti *J. Sol-Gel Sci. Technol*. 63 (**2012**) 16.
59. R. Kun, S. Tarjan, A. Oszko, T. Seemann, V. Zöllmer, M. Busse, I. Dekany *J. Solid State Chem*. 182 (**2009**) 3076.
60. S. Livraghi, M. C. Paganini, E. Giamello, A. Selloni, C. Di Valentin, G. Pacchioni *J. Am. Chem. Soc*. 128 (**2006**) 15666.
61. F. Napoli, M. Chiesa, S. Livraghi, E. Giamello, S. Agnoli, G. Granozzi, G. Pacchioni, C. Di Valentin *Chem. Phys. Lett.* 477 (**2009**) 135.
62. S. Hoang, S. P. Berglund, N. T. Hahn, A. J. Bard, C. B. Mullins *J. Am. Chem. Soc*. 134 (**2012**) 3659.
63. J. P. Perdew, K. Burke, M. Ernzerhof *Phys. Rev. B* 54 (**1996**) 16533.
64. J. P. Perdew, Y. Wang *Phys. Rev. B* 45 (**1992**) 13244.
65. P. E. Bhöchl *Phys. Rev. B* 50 (**1994**) 17953.
66. G. Kresse and D. Joubert *Phys. Rev. B* 59 (**1999**) 1758.
67. G. Kresse and J. J. Hafner *Phys. Rev. B* 47 (**1993**) 558.
68. G. Kresse and J. Furthmüller *Phys. Rev. B* 54 (**1996**) 11169.
69. J. Harris *Phys. Rev. B* 31 (**1985**) 1770.
70. W. C. M. Foulkes and T. Haydock *Phys. Rev. B* 39 (**1989**) 12520.
71. M. P. Teter, M. C. Payne, D. C. Allan *Phys. Rev. B* 40 (**1989**) 12255.
72. D. M. Bylander and L. Kleinman, S. Lee *Phys Rev. B* 42 (**990**) 1394.
73. Davidson, E. R. in *Methods in Computational Molecular Physics;* Dierksen, G. H. F., Ed.; NATO Advanced Study Institute, Series C; Plenum, New York, NY, **1983**; Vol. 113, p. 95.
74. M. Nolan, S. D. Elliott, J. S. Mulley, R. A. Bennett, M. Basham, P. Mulheran *Phys. Rev. B* 77 (**2008**) 14.
75. A. I. Poteryaev, A. I. Lichtenstein, G. Kotliar *Phys. Rev. Lett.* 93 (**2004**) 086401.
76. R. Pentcheva and W. E. Pickett *Phys. Rev. B* 74 (**2006**) 035112.

77. D. D. Cuong, B. Lee, K. M. Choi, H. S. Ahn, S. Han, J. Lee *Phys. Rev. Lett.* 98 (**2007**) 115503.
78. C. J. Calzado, N. C. Hernández, J. F. Sanz *Phys. Rev. B* 77 (**2008**) 045118.
79. Z. Hu and H. Metiu *J. Phys. Chem. C* 115 (**2011**) 5841.
80. M. Cococcioni and S. De Gironcoli *Phys. Rev. B* 71 (**2005**) 035105.
81. H. J. Kulik, M. Cococcioni, D. A. Scherlis, N. Marzari *Phys. Rev. Lett.* 97 (**2006**) 103001.
82. G. Mattioli, P. Alippi, F. Filippone, R. Caminiti, R. Amore Bonapasta *J. Phys. Chem. C* 114 (**2010**) 21694.
83. P. M. Kowalski, M. F. Camellone, N. N. Nair, B. Meyer, D. Marx *Phys. Rev. Lett.* 105 (**2010**) 146405.
84. A. Rubio-Ponce, A. Conde-Gallardo, D. Olguin *Phys. Rev. B* 78 (**2008**) 035107.
85. Z. Y. Zhao and Q. J. Liu *J. Phys. D: Appl. Phys* 41 (**2008**) 085417.
86. G. Adachi and N. Imanaka *Chem. Rev.* 98 (**1998**) 1479.
87. H. J. Osten, E. Bugiel, J. Dabrowski, A. Fissel, T. Guminskaya, J. P. Liu, H. J. Mussig, P. Zaumseil Gate Insulator, IWGI, Tokyo, **2001**, p. 100.
88. J. K. Burdett, T. Hughbandks, G. J. Miller, J. W. Richardson, J. V. Smith *J. Am. Chem. Soc*. 10 (**1987**) 3639.
89. R. I. Bickley, T. Gonzales-Carreno, J. S. Lees, L. Palmisano, R. J. D. Tilley *J. Solid State Chem.* 92 (**1991)** 178.
90. X. Yana, J. Hea, D. G. Evans, X. Duana, Y. Zhub *Appl. Cat. B: Environ.* 55 (**2005**) 243.
91. W. Z. Gonschorek *Kristallogr.* 160 (**1982**) 187.
92. O. Greis, R. Ziel, B. Breidenstein, A. Haase, T. Petzel *J. Alloys Comp.* 216 (**1994**) 255.
93. U. Kolitsch, H. J. Seifert, F. Aldinger *J. Solid State Chem.* 120 (**1995**) 38.
94. J. Yang, J. Dai, J. Li *Appl. Surf. Sci.* 257 (**2011**) 8965.
95. J. H. Li, X. Yang, X. D. Yu, L. L. Xu, W. L. Kang, W. H. Yan, H. F. Gao, Z. H. Liu, Y. H. Guo *Appl. Surf. Sci.* 255 (**2009**) 3731.
96. A.-W. Xu, Y. Gao, H.-Q. Liu *J. Catal.* 207 (**2002**) 151.
97. K. T. Ranjit, I. Willner, S. H. Bossmann, A. M. Braun *Environ. Sci. Technol.* 35 (**2001**) 1544.
98. A. Amlouk, L. El Mir, S. Kraiem, M. Saadoun, S. Alaya, A. C. Pierre *Mat. Sci. Eng B* 146 (**2008**) 74.
99. C. Meneghini, M. C. Dalconi, S. Nuzzo, S. Mobilio, R. H. Wenk *Biophys. J.* 84 (**2003**) 2021.
100. G. K. Williamson, W. H. Hall *Acta Metall*. 1 (**1951**) 22.
101. D. Balzar *Voigt-function model in diffraction line-broadening analysis*, in *Microstructure Analysis by Diffraction*, R. L. Snyder, J. Fiala, H. J. Bunge, IUCr series, Oxford University Press, **2000**.

102. D. Balzar *J. Appl. Cryst.* 28 (**1995**) 244.
103. A. C. Larson, R. B. Von Dreele *General Structural Analysis System (GSAS)*; Los Alamos National Laboratory Report, LAUR 86, 2004.
104. D. Balzar *J. Appl. Cryst*. 25 (**1992**) 559.
105. J. Langford I. *Crystallite Size from Diffraction Data*; in Newsletter No. 24, Commission of Powder Diffraction, IUCr, 2000.
106. C. Liang, C. Liu, F. Li, F. Wu *Chem. Eng. J.* 147 (**2009**) 219.
107. R. D. Shannon *Acta Cryst*. A32 (**1976**) 751,
108. F. B. Li, X. Z. Li, K. W. Cheah *Environ. Chem.* 2 (**2005**) 130.
109. Y. Ohko, T. Tatsuma, T. Fujii, K. Naoi, C. Niwa, Y. Kubotas, A. Fujishima *Nat. Mater*. 2 (**2003**) 29.
110. N. Crespo-Monteiro, N. Destouches, L. Nadar, S. Reynaud, F. Vocanson, J. Y. Michalon *Appl. Phys. Lett*. 99 (**2011**) 173106.
111. K. Naoi, Y. Ohko and T. Tatsuma *J. Am. Chem. Soc*. 126 (**2004**) 3664.
112. R. Dholam, N. Patel, A. Santini, A. Miotello *Int. J. Hydr. Energy* 35 (**2010**) 9581.

4.
Electrochemical Characterizations

In this chapter three main types of electrochemical measurements employed to characterize the home-made TiO_2 nanopowders will be discussed.
Capacitance analyses based on electrochemical impedance spectroscopy (EIS) and formulated in the Mott-Schottky plot shed light on band bending occurring in titanium dioxide when in contact with an electrolyte. They have been used mainly to evaluate the flatband potential of the semiconductor. On the other hand, photovoltage measurements as a function of the pH of the TiO_2 suspension give access to the quasi-Fermi level of electrons. In this way, two viable routes have been explored to gain access to the electronic structure of titania, capturing a picture of semiconductor energetic both in the dark and under illumination. Then, chronoamperometry under chopped illumination will be presented in terms of photocurrent transients which can give a reliable insight into TiO_2 charge carrier recombination rate.

To understand reactions occurring at the electrode surface, the electrochemical approach is a useful method, since it allows the relationship between the potential, current and charge to be measured.

4.1. Dark behavior

Undoped semiconductors are referred to as intrinsic semiconductors. Doped semiconductors in which the dominant (or majority) charge carriers are electrons are referred to as *n-type* semiconductors, whereas those in which holes are the majority charge carriers are referred to as *p-type* semiconductors. It has to be noted that pristine titanium dioxide, both commercial and home-made synthesized, can be considered an n-type semiconductor because defects such as oxygen vacancies act as electron donors. In the following, indeed, the term “pure” will never be used, whereas “pristine” or “bare” TiO_2 will be adopted to indicate undoped materials, as opposite to doped ones.

For an intrinsic semiconductor the Fermi level (E_F) lies at the mid-point of the bandgap. This statement derives from the definition of the Fermi function f(E): according to thermal equilibrium the probability of finding an occupied energy level at a specific value *E* is given by:

$$f(E) = \frac{1}{1+e^{\frac{(E-E_F)}{k_B T}}} \quad \text{(eq. 4.1)}$$

Pristine TiO_2 can be considered as an n-type semiconductor, with its Fermi level located quite close to the conduction band (E_{CB}). Doping changes the distribution of electrons within the solid, and hence changes the Fermi level. For a n-type semiconductor, the Fermi level lies just below the conduction band, whereas for a p-type semiconductor it lies just above the valence band.

Simple promotion of electrons from the valence band to the conduction band is not sufficient to generate a net current flux, since non-radiative relaxation of excited electrons to the ground state is quite facile in solid state. This deactivation pathway can be overcome by placing the semiconductor in contact with a second phase prior to photoexcitation to generate a charge separating electric field at the semiconductor surface. This interfacial electric field can be used to spatially separate photoinduced electron-hole pairs, thereby preventing their non-radiative recombination. The second phase placed in contact with the semiconductor must have a free energy different from that of the semiconductor: the best given example is an electrolyte, which is the most interesting contact phase from an electrochemical point of view.

Through the formation of a three–dimensional and interconnected TiO_2 network using the sol–gel process as well as the microemulsion route and template procedure, the voids between the semiconductor nanoparticles are connected and filled with an electrolyte.

As a rule of thumb, contact between a semiconductor and another phase (*i.e.*, gas, liquid, or solid) involves a redistribution of electric charges in the form charge carriers transfer in order to reach the kinetic and thermodynamic equilibrium at the interface. The direction of electron flow during this process will depend on the relative values of the Fermi level and the redox potential. In theory, both the free energy of the semiconductor and the free energy of the electrolyte should change in order to establish the equilibrium conditions. However, since there exists a significant excess of charge carriers in the electrolyte (*i.e.*, the number of electroactive molecules) compared to the number of charge carriers in the semiconductors, the redox potential of the electrolyte is virtually unaffected by this process. Rather, the semiconductor Fermi level shifts to the electrolyte redox potential.

The transfer of electric charge produces a region on each side of the junction where the charge distribution differs from the bulk material, and this is known as the space–charge layer. On the electrolyte side, this corresponds to the

well-known electrolytic double layer, that is, the compact (Helmholtz) layer followed by the diffuse (Gouy–Chapman) layer. Unlike a metal, where excess charge resides at the surface, charge in a semiconductor is not free to move about and forms a "space charge layer" which extends into the bulk for a significant distance (100-10,000 Å).[1] This region has an associated electrical field. Hence, there are two double layers to consider: the interfacial (electrode/electrolyte) double layer, and the space charge double layer.

As for metallic electrodes, changes in the potential applied to the electrode shift the Fermi level. The band edges in the interior of the semiconductor (*i.e.*, away from the depletion region) also vary with the applied potential in the same way as the Fermi level. However, the energies of the band edges at the interface are not affected by changes in the applied potential. Therefore, the change in the energies of the band edges on going from the interior of the semiconductor to the interface, and hence the magnitude and direction of band bending, varies with the applied potential. Different situations have to be considered.

At a certain potential, the Fermi energy lies at the same energy as the solution redox potential. There is no net transfer of charge, and hence there is no band bending. This potential is therefore referred to as the *flatband potential*, V_{fb} (Fig. 4.1a), which plays the same role as the potential of zero charge for metals. Since for an *n*-type semiconductor electrode at open circuit the Fermi level is typically higher than the redox potential of the electrolyte, electrons will be transferred from the electrode into the solution. Therefore, there is a positive charge associated with the space charge region, and this is reflected in an upward bending of the band edges. Since the majority charge carrier of the semiconductor has been removed, this region is also referred to as a depletion layer (Fig. 4.1b). Hence, a positive excess charge formed by immobile ionized donor states is left behind. If electrons accumulate at the semiconductor side one obtains an accumulation layer (Fig. 4.1c). Finally, electron depletion can go so far that their concentration at the interface falls below the intrinsic level. As a consequence, the semiconductor is p-type at the surface and n-type in the bulk, corresponding to an inversion layer (Fig. 4.1d). The illustration in the figure refers to n-type materials where electrons are the mobile charge carriers. Analogous considerations apply for p-type semiconductors, in which positive holes are the mobile charge carriers and the

immobile negatively charged states of the acceptor dopant form the excess space charge within the depletion layer.

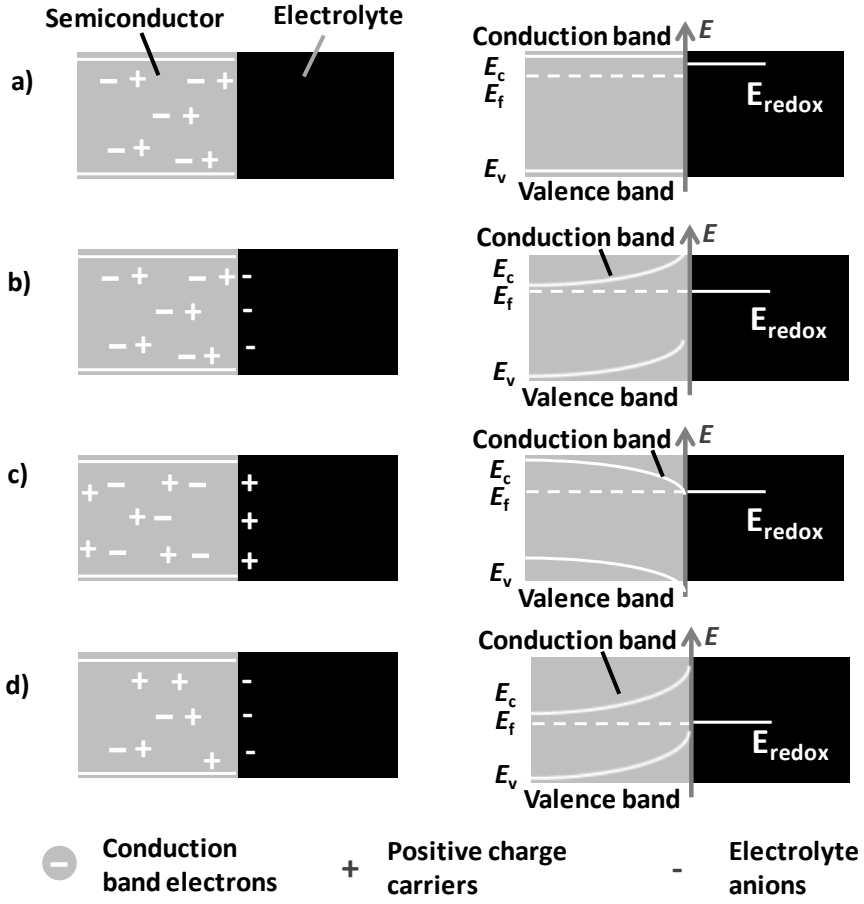

Figure 4.1. Sketch of the electronic energy levels at the interface between an n-type semiconductor and an electrolyte containing a redox couple in four different situations: **a)** flat band potential, where no space-charge layer exists in the semiconductor; **b)** depletion layer, where electrons have moved from the semiconductor to the electrolyte, producing an upward bending of the bands; **c)** accumulation layer, where excess electrons have been injected into the solid producing a downward bending of the conduction and valence band towards the interface; **d)** inversion layer, where the electrons have been depleted below their intrinsic level, enhancing the upward band bending and rendering the semiconductor *p*-type at the surface. Re-drawn from ref [2].

At first glance, band bending appears to suggest that the energetic of the semiconductor surface are fixed while the bulk energetic are changing; the opposite is true.

If a semiconductor responds in an ideal way, the potential applied to the back side of the electrode will be dropped across the internal electrode-electrolyte interface, contrary to what happens for a metal-electrolyte interface. This has two implications: the potential applied to a semiconducting electrode does not control the electrochemistry, and in most cases there exists a "built-in" barrier to charge transfer at the semiconductor-electrolyte interface, so that electrochemical reversible behavior never exists.

According to Grätzel,[2] the nanostructuring of the semiconductor introduces profound changes in its photoelectrochemical properties. Of great importance is the fact that a real depletion layer (see Fig. 4.1) cannot be formed in the solid: the particles are simply too small. The voltage drop within the nanocrystals remains small under reverse bias, typically a few millivolts. As a consequence there is no significant local electric field present to assist in the separation of photogenerated electron–hole pairs.[3] Thus, the photoresponse of the electrode is determined by the rate of reaction of the positive and negative charge carriers with the redox couple present in the electrolyte. This came as a great surprise already in 2001 to a field where the traditional thinking was to link the photoresponse to formation of a charge-depletion layer at the semiconductor–electrolyte interface. Along with the absence of a proper electric field in mesoporous semiconductor electrodes, no band bending occurs in nanocrystals and whole film (since the maximum band bending in a spherical semiconductor particle is negligible at room temperature. Electrons are charge-compensated by ions in the electrolyte and transported by diffusion, as supported by Sodergren *et al.* who proposed a diffusion model for electron transport in these porous films.[4]

Band positions and energy levels

The determination of the flat band potential facilitates the location of the energetic position of the valence and conduction band edge of a given semiconductor material. Electron transfer from the semiconductor to adsorbed species is ruled by the band energy position of the semiconductor compared to the redox potential of the adsorbate. In order to have electron donation from the conduction band to an acceptor, energetic level of the last

must be below (on a potential scale more positive than) the conduction band potential of semiconductor. The potential level of the donor, instead, needs to be above (more negative than) the valence band position of the semiconductor in order to donate an electron to the vacant hole.[5]
Similarly, electron transfer from the semiconductor to a molecule (*e.g.*, a dye) adsorbed on the semiconductor to the semiconductor itself is determined by the reciprocal position of the energetic levels. Band positions of several semiconductors compared to the standard potentials of two fundamental redox couples (H_2/H_2O, H_2O/O_2) are presented in Fig. 4.2.

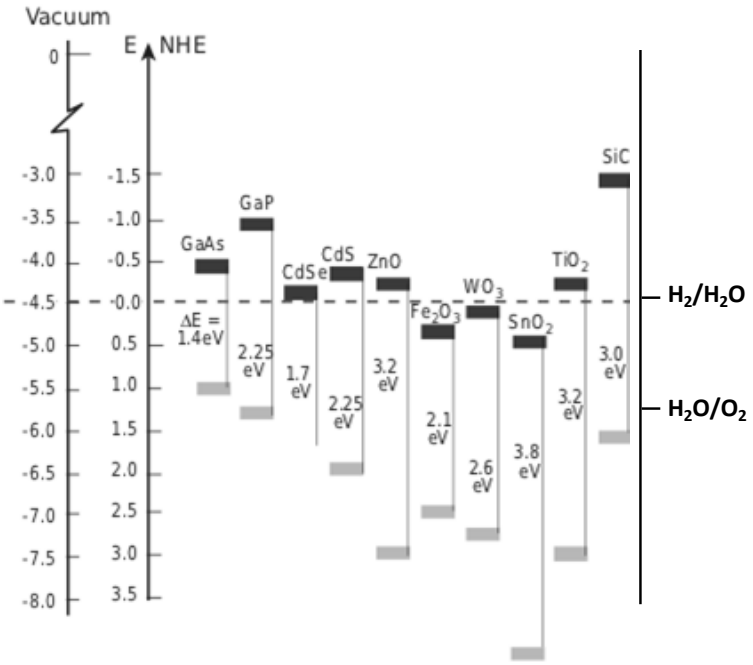

Figure 4.2. Band positions of several semiconductors in contact with an aqueous electrolyte at pH = 1. The lower edge of the conduction band and upper edge of the valence band are presented along with the bandgap. The energy scale is indicated in eV using either the normal hydrogen electro4de (NHE) or the vacuum level as a reference. On the right side, the standard potentials of two main redox couples are presented against the normal hydrogen electrode potential.[2]

4.2. Behavior under illumination

When TiO_2 particles are irradiated with UV-visible light, a non-equilibrium population of electrons and holes is generated, thereby splitting the Fermi level into two quasi-Fermi levels, one for the holes and the other for the electrons. That is to say, the population of electrons, $p(e^-)$ is distributed in the conduction band states with the Boltzman factor:[6]

$$p(e^-) = e^{-\frac{E - {}^{n}E_f^*}{k_B T}} \quad \text{(eq. 4.2)}$$

where ${}^{n}E^{*}_{F}$ is the quasi-Fermi level for electrons. Similarly, there is a quasi-Fermi level for holes ${}^{p}E_f$*, and the holes are distributed in the valence band states as:

$$p(h^+) = e^{-\frac{E - {}^{p}E_f^*}{k_B T}} \quad \text{(eq. 4.3)}$$

The quasi-Fermi level for electrons, which practically merges with the TiO_2 conduction band, is to be considered since the electrons are the majority charge carriers in such a material. In the presence of an electrolyte – a condition that holds for all the present studies – ${}^{n}E_f$* will equilibrate with the potential of the redox couple in solution.

The Fermi level (E_f) of the semiconductor is directly related to the number of accumulated electrons as illustrated in the expression:

$$E_F = E_{CB} + kTln\frac{n_c}{N_c} \quad \text{(eq. 4.4)}$$

where n_c is the density of accumulated electrons, and N_c is the charge carrier density of the semiconductor.

If more electrons are accumulated in TiO_2 or in a doped/composite system, a negative shift in the Fermi level of the TiO_2 would be expected. By shifting the Fermi level closer to the conduction band, it would therefore be possible to improve the energetics of the semiconductor system. This holds in the case of a species to be reduced in solution, as the gap between the two potentials involved would be larger.

Kongkanand and Kamat[7] determined the concentration of electrons accumulated in the TiO_2 particle using thionine dye as an acceptor. By determining the number of reduced dye molecules, they estimated an

accumulation of about 300 electrons per 15-nm TiO_2 particle during extended UV irradiation.

4.3. Flat-band potential / quasi-Fermi level determination techniques

There are plenty of experiments used to measure the flatband potential of a semiconductor and the various parameters related to its electronic features. For semiconductor powder suspensions, as most commonly employed in semiconductor photocatalysis, photocurrent[8,9] or photovoltage measurements are the methods of choice, besides the less used flash photolysis.[11] They resemble the experimental conditions applied in photocatalysis much better since no electrochemical potential has to be applied to the semiconductor. However, the same intrinsic features studied for suspension particulate can be exploited when the system is slightly different, namely when nanoparticles are deposited on conducting substrates and used as photoanode in a photoelectrochemical cell. For semiconductor electrodes capacitance measurements,[12-15] modulation spectroscopy,[16,17] and spectro-electrochemistry[18,19] were applied.

The most used methods to determine the flatband potential consist in measuring the photopotential as a function of radiation intensity, or the onset of the photocurrent, or, alternatively, the capacitance of the space charge region. Among these techniques, the simplest one is to measure the open-circuit potential (photopotential) of the electrochemical cell under radiation of varying intensity. For a system under equilibrium, the photopotential is the change in the Fermi level due to the promotion of electrons to the conduction band, and it reaches a maximum at the flatband potential. Therefore, a plot of photopotential versus light intensity will attain a limiting plateau at the flatband potential.

For the second method, although the onset of the photocurrent might be simplistically considered to be the flatband potential, it is actually the potential at which the dark current and photocurrents are equal. Therefore, such measurements should be used with caution.

The third method will be explained more in details in the following paragraph (3.1).

Furthermore, under open circuit conditions the electrons accumulate and equilibrate with the redox couple in the electrolyte. The measured open circuit voltage in a photoelectrochemical cell is the difference between the apparent Fermi level of the semiconductor film and the reduction potential of the redox couple employed. Thus, the open circuit voltage is a direct measure of the apparent Fermi level of the semiconductor film if one equilibrates using the same redox couple centers.[7] Indeed, Beranek and Kisch[20] determined E_{FB} from the dependence of the electrode open-circuit voltage (V_{OC}) on the illumination intensity, since at sufficiently high intensity V_{OC} becomes constant, representing V_{fb}.[21]

In a more extended manner, when recordering photocurrents at different applied potentials under UV illumination, the zero-current potential correspond to apparent flatband potential of the nanostructured semiconductor film. At this applied potential, all the photo-generated electrons and holes recombine without producing any net current flow. Any built-in driving force within the film for driving electrons to the collecting surface of the optically transparent electrode is neutralized by the applied negative bias.

Among the variety of techniques for the electrochemical semiconductor features determination, two intentionally different kinds of measurements have been employed in the present study and applied to selected samples: impedance spectroscopy in the form of Mott-Schottky plot and photovoltage method, leading to the evaluation of the flatband potential and quasi-Fermi level, respectively.

4.3.1. Mott-Schottky plot

One of the traditional methods to evaluate the flatband potential of a semiconductor, as mentioned above, involves measuring the apparent capacitance of the semiconductor–electrolyte junction as a function of applied potential to increase the potential step across the junction. It is based on the Mott-Schottky (MS) relationship:

$$\frac{1}{C^2} = \frac{2}{N_D A^2 R^2 \varepsilon_0 \varepsilon_r e}\left(V_a - V_{fb} - \frac{k_B T}{e}\right) \quad \text{(eq. 4.5)}$$

where *C* is the space charge capacitance, *V* the externally applied potential, V_{fb} the flatband potential at semiconductor/electrolyte junction, N_D the donor density, ε_0 the permittivity of the free space, ε_{TiO2} the permittivity of the semiconductor electrode (considered equal to 30,[22] e_0 the elementary charge, k_B the Boltzmann's constant, and *T* the operation temperature. *A* and *R* the geometric area and the roughness of the substrate, respectively.

As most of impedance measurements, also these are conducted in a range of frequencies, usually centred at 1 kHz or starting from 1 kHz and increasing the frequency of one or two orders of magnitude.

Plotting (C^{-2}) *vs V* should thus yield a straight line, intersecting the potential axis at V_{fb}, as depicted in Fig. 4.3. The respective donor density ND can be calculated from the slope of this line.

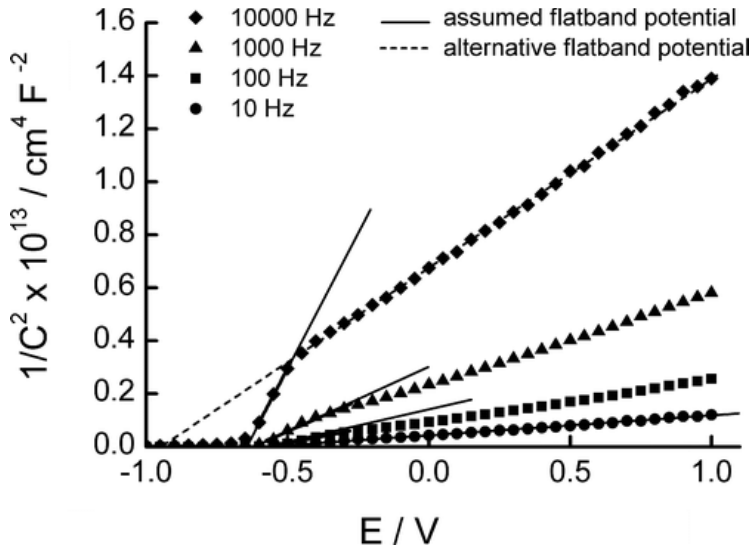

Figure 4.3. Mott-Schottky plot obtained at different frequencies for the TiO_2 thin film electrode prepared with 125 mmol $TiOSO_4$, 37.4 mmol Silres MP42E, 28 mmol NH_3, and 0.5 mmol Pluronic F-127. Ag/AgCl and Pt were used as reference and counter electrodes, respectively, in 0.1 M KCl, pH = 7.0. Taken from ref [15].

When a Mott-Schottky measurement is performed, the semiconductor is in contact with a solution where a redox couple is present. Then, an exchange of electrons can occur in order to match the two Fermi energies (Ef and Eredox) as depicted in Fig. 4.4.

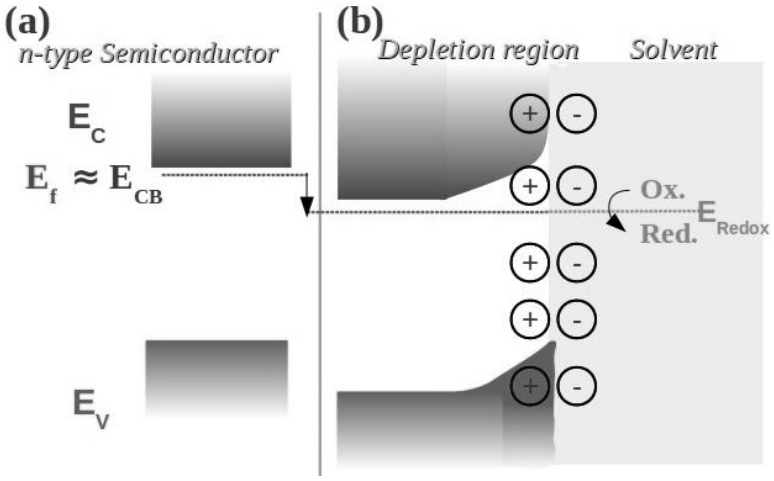

Figure 4.4. Pictorial representation of the electronic energy levels for titania in two different situations: (a) for the gas phase titania where CB is the conduction band energy, VB the valence band energy, E_f the Fermi energy and E_{CB} the conduction band edge; (b) for titania in contact with a solution where a redox couple is dissolved. "Ox" stands for oxidated form, "Red" for reduced form and "E_{redox}" is the redox potential. The depletion region is the one where the band is bent.

The variation of capacitance can be measured using a frequency response analysis (impedance method).

As already mentioned, the flatband potential that can be measured by an MS plot is defined as the counter-potential that flats the potential back again by compensating the migrated charges capacitance effect. When analyzing data, there are two capacitances to be considered, the space-charge capacitance and the capacitance of the Helmholtz layer (C_H) present at the electrolyte side of the interface. Since these capacitances are in series, the total capacitance is the sum of their reciprocals. In the depletion regime the space charge capacitance is much smaller than Helmholtz capacitance. Therefore, the capacitance value calculated from this model is assumed to be the value of the space charge capacitance.[7] As underlined by Zhang *et al.*,[23] especially in the case of contact between the substrate and the electrolyte permeating through the voids of the analyzed material, the capacitance relationship should be described taking the Helmholtz capacitance into account.

The equivalent circuit used in this model to represent the metal oxide/electrolyte system is a series combination of a resistor and a capacitance (the space charge capacitance). The capacitance is calculated from the imaginary component of the impedance (Z") using the relationship $Z'' = 1/2\pi fC$. The model is adequate provided the frequency is high enough (on the order of kHz).

Experimental setup

The flat-band potentials of the both pristine and doped titanium dioxide were measured by impedance spectroscopy using the Mott-Schottky plots.[10,24] The measurements were performed in a conventional thermostatted (25 °C) three-electrode cell, with a 2 cm^2 platinum flag as counter electrode and a saturated calomel electrode as reference.

The working electrode was a TiO_2 thin film prepared as follows: the TiO_2 powder was well dispersed with 2-propanol and the suspension was applied on an indium-doped tin oxide conducting glass (ITO), 2×1 cm^2, by drop casting. After being dried, the film was finally annealed at 400°C for 1 h. The experiment was performed in aqueous 0.5 M Na_2SO_4 solution at pH~6. The potential was systematically varied between +1.7 and -1.3 V (*vs* NHE) with the frequency range being modulated between 500 to 2000 Hz by an ECO-CHEMIE Autolab PGStat 30-Potentiostat Galvanostat equipped with Frequency Response Analyzer (FRA).

Deviations from ideal behavior

In the derivation of equation 4.5 several assumptions are made which can be summarized as follows. Both the electrolyte and the bulk semiconductor have zero resistance; the interface is perfectly planar, two-dimensionally infinite and possesses perfectly blocking properties. Neither surface states nor interfacial layers, such as the Helmholtz layer, are present. The dielectric constant ε is frequency-independent. Only one type of localized electronic defect is present, being a completely ionised donor (or acceptor, for p-type semiconductors); the spatial distribution of such defects is homogeneous. In real cases, several of these conditions will not be sufficiently met, as exposed in a paper by Cardon and Gomes.[25] This is the complex reason why, contrary to an easily obtainable estimation of the bandgap from diffuse reflectance measurements, the flatband potential and quasi-Fermi level

evaluation generally requires more efforts: not only the techniques themselves are more delicate, but also real semiconductors necessarily differ from the ideal counterpart.

When surface states are present, phenomena like e^-/h^+ trapping and recombination are to be rediscussed. Surface states can be considered as intermediate for charge transfer reactions and charge trapping can occur, thus leading to unpinning of band edges. This happens because surface states can act as channels for electron transfer, if they lie at the appropriate energy. Techniques such as EIS, photocurrent transients, and photoluminescence are indeed the most used for studying to what extent surface states affect charge transport and recombination.

Then, another main cause of non-ideal behavior is photodecomposition of the electrode; that is, oxidation of the electrode itself by holes in the depletion region. This can be avoided by the addition of an appropriate electroactive species to the solution that competes with the auto-oxidation, or by the stabilization of the electrode surface by chemical modification.

Last but not least, differences in the substrate roughness could account for different slopes found for the Mott-Schottky plot response, thus affecting the donor density.

4.3.2. Photovoltage technique

This method to determine the quasi-Fermi level of titanium dioxide consists in the measurement of the photovoltage developed on irradiating the TiO_2 suspension in the presence of an electron acceptor, methylviologen (MV^{2+}/MV^+) in the present case.

Since the redox potential of the MV^{2+}/MV^+ couple is pH independent, the observation of a pH effect on the measured photovoltage must be related to changes within or on the surface of the TiO_2. The most likely source of this effect is shifting of the Fermi level energy with pH.[8]

As already mentioned, after light irradiation inducing the separation of electron-hole pairs, the associated energy states are named quasi-Fermi energy levels and are located just below the conduction band for the electrons and just above the valence band for the holes. Because of the protolitic equilibrium between the semiconductor and the aqueous solution taking place at the titanium oxide interface, the electronic levels of the

semiconductor can be rigidly shifted by varying the pH of the solution. Once the pH is high enough to guarantee that the electron quasi-Fermi energy level is more negative (on the electrochemical scale) than the one of the pH-independent redox couple in solution, the electrons will flow from the semiconductor to the solution (see Fig. 4.5). Thus, a sudden voltage change versus the pH will be observed in a titration curve fashion. Indeed, the photovoltage method is based on the pH-dependence of the quasi-Fermi level of TiO_2 according to eq. 4.6:

$$^{n}E_f^*(pH) = V_{fb}(pH = 0) - k\,pH \quad \text{(eq. 4.6)}$$

wherein the factor k is usually equal to 59 mV.[13] From the pH value at the inflection point (pH0) - at which the quasi-Fermi level and the potential of the redox couple are equal - one can calculate the quasi-Fermi electron energy levels at any pH as reported in eq. 4.7:

$$^{n}E_f^*(pH) = E_{red}(MV^{2+}/MV^{+}) - k\,(pH - pH_0) \quad \text{(eq. 4.7)}$$

Thus, $^{n}E_f$* is shifted towards more negative values upon increasing the pH value. In the presence of a pH-independent redox system like methylviologen (MV^{2+}) the interfacial electron transfer from the photogenerated reactive electron to MV^{2+} can be therefore controlled by changing the suspension pH value. Reduction to the blue radical cation occurs only if the quasi-Fermi potential of electrons matches the methylviologen reduction potential, that is for pH > pH0. The photogenerated hole oxidizes water or an added electron donor (hole acceptor).

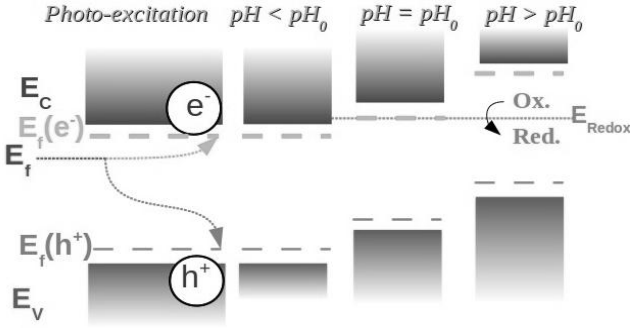

Figure 4.5. Sketch of the photoexcitation process and the electron-hole pair energy levels in titanium dioxide. "$E_f(e^-)$" indicates the electron quasi-Fermi energy levels, while "$E_f(h^+)$" the hole one.

Experimental setup

The quasi-Fermi level of electrons was measured using methylviologen dichloride ((MV)Cl2, $E_{red}(MV^{2+}/MV^{+})$ = -0.4421 V *vs* NHE) as a pH-independent redox system, according to the literature.[10] A two-electrode cell using a 2 cm^2 platinum flag and a saturated calomel electrode (SCE) as working and reference electrodes, respectively, was adopted. A combined glass electrode was also employed for pH measurements. 30 mg of semiconductor powder were suspended and sonicated in 50 mL of 0.l M KNO_3, and then placed in a thermostatted (25°C) cell. After being degassed with N_2 for 0.5 h, 6 mg of methylviologen dichloride was added to the suspension, and again degassed for about 15 min. The pH of the suspension was adjusted to pH 1 using 1 M HNO_3 and then it was raised by adding NaOH solutions. Stable photovoltages were recorded about 30 min after changing the pH value by irradiation of a UV lamp (see the Appendix for details). Magnetic stirring and nitrogen flow were kept constant during the measurement. The cell potential differences between the working electrode and the reference SCE were recorded with a KEITHLEY 619 differential Electrometer/Multimeter, with an input impedance greater than 10^{14} Ω. The precision of potential difference measurements was 0.01 mV. For pH measurements, an AMEL 338 pH-meter was used, after appropriate calibration.

Both the plotted potential data and quasi-Fermi level values are given relative to the normal hydrogen electrode (NHE).

In the following, both the “quasi-Fermi level” and “flatband potential” terms will be used according to the techniques adopted, though the former would be more accurate to describe both determinations for small crystal size (about 5 nm, in the case of our home-made titania, both pure and N-doped) which presumably does not produce a relevant band-bending. However, the main difference lies in the following: MS plot gives information about the electronic structure of the metal oxide in the dark, whereas the photovoltage technique gives access to the quasi-Fermi level, that is to say a picture of the semiconductor under illumination.

Factors affecting the flatband potential / quasi-Fermi level

Besides attesting that an accurate assessment of the flatband potential/quasi-Fermi level for poly-crystalline semiconductor particles is still problematic and

not straightforward, recent works are not abundant on this topic. In this context, the focus is addressed to undoped and N-doped TiO_2, since nitrogen is the most studied of all dopants from the electronic point of view. However, literature data concerning the evaluation of these electronic properties for doped TiO_2 nanoparticles are very scarce. Actually, as shown in Table 4.1, there is also a significant variation in the literature values concerning undoped TiO_2 powders. Comments on the comparability of the data reported in Table 4.1 are not possible, since the available metrology protocol details are sometimes poor and quite often the uncertainty of the measure is not given. Moreover, one should consider that different synthetic and doping procedures may lead to materials with largely different properties. Since not only the metrology methods but also the types of electrode deposition vary considerably among the reported values, it is definitely difficult to ascribe the wide range of results to precise factors and to compare them unambiguously. For instance, Bolts *et al.*[8] found by MS measurements that Efb values differ by up to -0.3 V for the various determinations. Instead, Beranek and co-workers[20] affirmed that they determined ${}^{n}E_f$* from the dependence of the electrode open-circuit potential on the illumination intensity, since capacitance measurements did not give reliable data due to a high frequency dispersion of the resulting Mott-Schottky plots. Still, Hirai *et al.*[26] declared that their experimental results do not show an ideal MS-behavior, so the flatband potential could not be determined by the impedance method, though a value is reported. Then, in Table 4.1 only the values of flatband potential/quasi-Fermi level related to powders are considered, thus excluding single crystals, nanotubes, array electrodes, and so on. Indeed, the crystallinity degree of the oxide, related to its specific surface area, should be taken into account: the defective nature of nanoparticles can introduce large differences from one sample to another. For this reason, in the present work, both home-made and commercial samples with very dissimilar specific surface areas and average crystallite diameters have been purposely chosen.

	Mott-Shottky plot		Photovoltage / photocurrent method / spectroelectrochemistry	
	V_{fb} (V *vs* NHE)	**pH**	**$^{n}E_f$* (V *vs* NHE)**	**pH**
Undoped TiO_2	-0.01 V	5	-0.08	0
	-0.41 V	7	-0.71 V	7
	-0.9 V	10	-0.52 V	7
	-0.9 V	13	-0.68 V	7
	-0.2 V	0	-0.55 V	7
	-0.40V	7.5	-0.56 V	7
	-0.40 V	6.5	-0.82 V	11
	-0.42 V	8	-0.05	0
	-0.16 V	0	-0.14 V	0
	-0.10 V	7	-0.28 V	6.6
			-0.53 V -0.52 V	6
			-2.00 V	n.r.[a]
			-1.2 V	n.r.
			-0.50 V	n.r.
N-doped TiO_2	-0.52 V	7	-0.20 V, -0.22 V	7
			-0.47 V -0.48 V -0.49 V	7
			-0.59 V, -0.64 V	7
			-0.35 V	7
			-0.16 V[b]	7
			-2.04 V, -2.10 V	n.r.
			-0.42 V, -0.48 V[c]	7
			-0.35 V	n.r.

Table 4.1. Literature values of flatband potential (V_{fb}) and quasi-Fermi level ($^{n}E_F$*) obtained by different metrology methods for undoped and N-doped TiO_2 powders. [a] n.r. = Value not reported in the reference. [b] Value derived from the dependence of the electrode open-circuit potential on the illumination intensity. [c] N,C-codoped TiO_2 sample. References to the papers from which numerical values have been taken can be found in a previous work.[27]

Apart from the intrinsic features of the semiconductor, the flatband potential/quasi-Fermi level depends on the nature and composition of the electrolyte. In aqueous solution and for most oxide semiconductors, it shifts by 0.059 V when the pH is changed by one unit, as exposed in eq. 4.6. This is a consequence of the fact that protons are potential-determining ions for these solids. Previous studies have even shown that changes in local pH occurring during the photo-oxidation process when TiO_2 in aqueous media is exposed to UV irradiation lead to variations in band bending and changes in the flat-band potential.[28] As a negative mark, it has to be stressed that there a few literature works do not even report the pH at which the flatband potentials/quasi-Fermi levels are determined, thus providing an incomplete information. According to Nelson and coworkers,[29] the measurement of the flat-band potential of porous semiconductor electrodes can be used to aid in understanding surface potential, especially when compared to electrophoretic mobility measurements of colloidal suspensions of the same oxide. Nelson *et al.*[29] demonstrated how changes in adsorbed species on the surface such as hydronium and hydroxide ions, as well as protolyzable anions (phosphate and arsenate, in their case) affect the space charge layer and even surface conductivity and can be used to control the adsorption of charged molecules.

4.4. Home-made undoped and doped-TiO_2

4.4.1. N doping

Mott-Schottky measurements

Flatband potential values from impedance experiments were obtained, according to the literature,[13] from the extrapolation of Mott-Schottky plots (C^{-2} *vs* V, electrode potential), as mentioned above. As a rule of thumb, a judicious selection of electrodes (surface/interface) preparation methods is necessary, in order to optimize titania as working electrode and to assure that the electrochemical parameter is not influenced by spurious contributions.

Examples of the Mott-Schottky plots obtained for bare TiO_2 layers on indium-doped tin oxide (ITO) glass substrates for different frequencies are shown in Fig. 4.6a. The experimental points were fitted by linear extrapolation in the range (0.2-1.2 V *vs* NHE) and the final value of V_{fb} was obtained by the intersection with the potential axis (V_{fb} = −0.5 V *vs* NHE). While in the case of

this sample and of undoped commercial ones, the reproducibility was pretty good, that of N-doped samples - triethylamine as N source and different nominal N/Ti molar ratios - is less satisfactory (Fig. 4.6b, TN_0.10 as representative for N-doped TiO_2). This is more probably due to the formation of heterogeneous films ensuing the increasing polydispersity of the doped powders. In particular, the frequency dispersion behavior is usually explained by a non-uniform distribution of donors, dielectric relaxation phenomena associated with irregularities in the surface structure of the electrodes, and a possible amorphous nature of the films, as stated in the literature.[30,31]

To ensure a straightforward comparison of the results for the TiO_2 thin film electrodes prepared here, flatband potential values were calculated from the capacity measurements performed at 1000 Hz. Moreover, the same range (0.2-1.2 V *vs* NHE) was adopted for the extrapolation for all samples. This can be a debated aspect, since the assumed flatband potential value could be different if alternative linear parts of the data set would be considered. As for instance, here the substrate response to the measurement is not taken into account. This is fairly questionable due to the nature of the titania films: as they are nanoporous, it cannot be excluded that the electrolyte came in contact with the underlying ITO. However, a steeper slope would be expected for ITO than for TiO_2 since the donor density should be higher in the former (highly-doped material).

As average datum deriving from all impedance measurements, a flatband potential of (-0.6 ± 0.2) V *vs* NHE can be provided for both undoped and N-doped titania. Thus, no significant effects are introduced by doping with nitrogen.

Further discussion can be found on Mott-Schottky plots of titanium dioxide in chapter 6 (paragraph 6.3.1), as two different types of TiO_2 films for hybrid solar cells are characterized and compared to be used as “blocking layers” toward charge recombination.

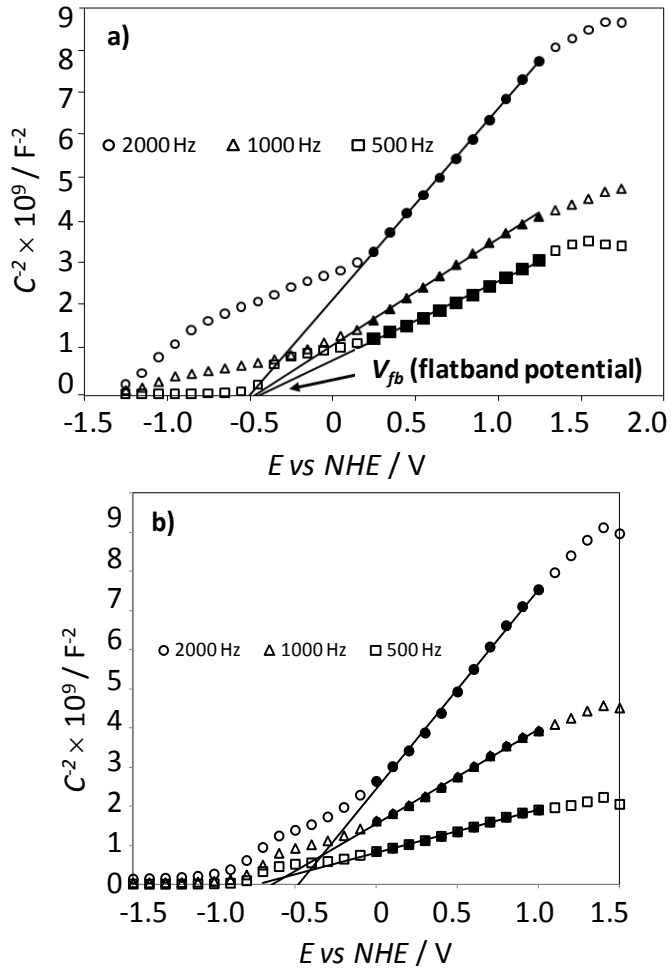

Figure 4.6. Mott-Schottky plot obtained at different frequencies for undoped TiO_2 (sample T, **a**) and N-doped TiO_2 (sample TN_0.10, **b**).

Photovoltage measurements

The photovoltage method has the important advantage of directly employing TiO_2 as a powder in suspension, thus overcoming the possible problems connected with the deposition of the powder onto the solid support. This is a crucial issue, especially when heterogeneous and polydisperse samples are concerned. For such a reason and for the inherently connected problem arisen with the Mott-Schottky plot on nanoporous systems, the evaluation of the Fermi/quasi-Fermi level for other types of doped-TiO_2 has been done by photovoltage analysis.

As already mentioned, this technique is based on the linear pH-dependence of the TiO_2 quasi-Fermi level, according to a Nernstian behavior of the semiconductor. This behavior can be associated with the protonation/deprotonation equilibrium of the oxide surface. Thus, upon recording the photovoltage as a function of pH, a curve with a shape similar to a titration curve is obtained, as shown in Figure 4.7 for selected samples. Usually, an inertia is noticeable in reaching a more or less constant value of the measured potential. Constant photovoltage values can be obtained after shorter time at pH values quite far away from the pH of the inflection point, especially at high pH.

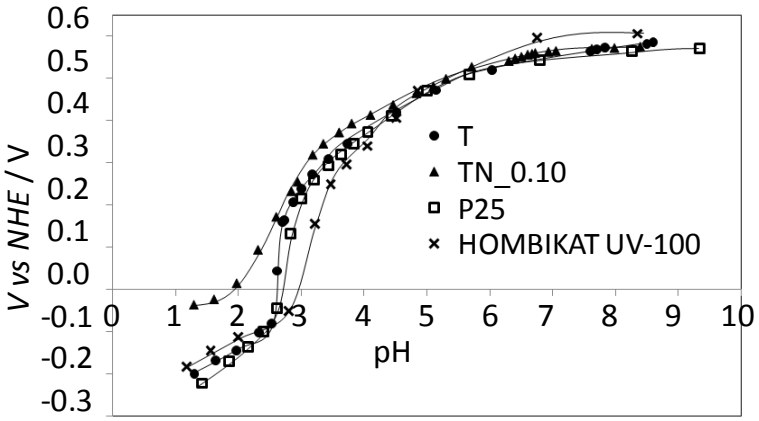

Figura 4.7. Photovoltage *vs* pH for selected TiO_2 suspensions in the presence of $(MV)Cl_2$.

Table 4.2 reports the obtained values of the quasi-Fermi level at pH 6, referred to the NHE scale. There is no significant variation among all the N-doped samples - triethylamine as N source - which range around -0.7 V, nor between doped and undoped ones.

Overall, we found the measurement of the photovoltage to be quite simple and reliable (notwithstanding a considerable work devoted optimization of the method), even more accurate and reproducible with respect to many other techniques, such as Mott-Schottky analysis by impedance spectroscopy, though the latter is absolutely well-known in the field of semiconductors and validated when applied to single crystals. Thus, photovoltage measurements

can be probably considered the most suitable technique for the quasi-Fermi level experimental evaluation in nanosized semiconductor powders.

Sample	${}^{n}E_F$* (V *vs* NHE)
T	-0.67 ± 0.07
TN_0.10	-0.67 ± 0.07
TN_0.20	-0.71 ± 0.06
TN_0.40	-0.67 ± 0.06
TN_0.50	-0.66 ± 0.01
P25	-0.64 ± 0.04
HOMBIKAT UV100	-0.62 ± 0.04

Table 4.2. Quasi-Fermi levels evaluated at pH 6 by photovoltage method for home-made and commercial samples.

DFT calculations

Results deriving from theoretical calculations are partially integrated in this thesis because of their highly interconnected nature with the experiments herein reported. They have been conducted by the theoretical chemistry group held by Dr. M. Ceotto of the Università degli Studi di Milano. The aim was that of more systematically and fully explore some aspects of pristine and doped TiO_2 by placing theory and experiment side by side. More specifically, calculations were included to gain novel insights with respect to the current literature into the interplay among structural and electronic degrees of freedom that underlie the observed photochemical properties of TiO_2. Indeed, theoretical DFT calculations in conjunction with both photovoltage and impedance experiments allowed to outline a comprehensive picture of the electronic structure of titania nanoparticles, especially N-doped ones.

Computational setup

All spin-polarized calculations were performed using the VASP code.[32,33] The projector augmented wave (PAW) pseudopotentials was employed to treat the valence-core interactions and the Perdew-Burke-Ernzerhof (PBE) parametrization[34] of the generalized gradient approximation[35] was adopted for the exchange-correlation potential. Forces on the ions were calculated through the Hellmann-Feyman theorem as the partial derivatives of free energy with respect to the atomic position, including the Harris-Foulkes correction to forces.[36,37] More details can be found in a reference paper.[27]

In a DFT + U study, a value of U = 5 eV was used, which has previously been shown to properly account for the electronic structure of the Ti 3d states.[38-41] The bulk doped systems were constructed from the relaxed 3×3×3 162-atom anatase TiO_2 supercell. The optimized supercell lattice parameters were a = 11.392 Å and c = 28.606 Å (a = 3.797 Å and c = 9.535 Å for a primitive cell), in good agreement with experimental results.[42] Both of these results indicate that our computational approach is reasonable. A variety of positions of N atoms in the TiO_2 lattice were considered, such as substitutional N (N@O) and several interstitial N (N_{int}) geometries. Reciprocal space sampling was restricted to the Γ-point, which is justified due to the rather large size of the used simulation supercells.

Electronic scenario from DFT calculations

To study Density of States of N-doped titania in the presence of oxygen vacancies, DFT calculations have been performed on a bulk anatase supercell containing either substitutional or interstitial nitrogen doping, plus one or two oxygen vacancies located as far as possible from the N-centers, so as to avoid any direct defect-impurity interaction.

In the presence of N impurities, oxygen vacancies excess electrons are transferred from the higher energy Ti^{3+} states to the empty N mid-gap states. Even if this internal charge transfer occurs independently of the exchange-correlation functional used, depending on the stoichiometric ratio between vacancies and impurities, this transfer can involve only some of the Ti^{3+} 3d electrons, leaving others on the Ti ions sites. Due to such a strongly correlated nature of the d-electrons in titania,[43] plain DFT could not be a proper choice for calculations. Thus, the so-called DFT + U[44] has been used, as mentioned in the "Computational Setup" section. It implies the addition of a Hubbard-U term in the functional representing an on-site Coulomb repulsion among selected orbitals associated with the given atomic sites in order to better describe the electron correlation effects. Different U parameters have been tested to correct the self-interaction error and the resulting bias toward non-integer orbital occupations in DFT.[45] Thus, the results can depend on the value of the interaction parameter U in the DFT + U scheme. As for hybrid functional,[46] both these methods suffer from dependence on a tunable parameter. Although schemes for calculating the U parameter have been derived from DFT, the resulting U can be quite different, dependent on the

scheme used.[47] The extent to which the excess electrons was found to spread over the system differed considerably.[48-50]

The results of DFT calculations for Density of States are reported in Figures 4.8 and 4.9. As usual for periodic PBE calculations, the bandgap is underestimated around 2.2 eV instead of 3.2 eV,[51] as shown on panel (a) of Fig. 4.8. To the author's knowledge, among DFT based approaches only hybrid functional gives a better agreement to the band-gap energy.[43] Once a oxygen vacancy is generated, examination of DOS in Fig. 4.8b reveals that for U = 0 the Ti 3d-like state lays just below the conduction band, as previously reported.[52,53] At the PBE level, the two extra electrons are fully delocalized on all of the Ti ions in the supercell, and consequently, the singlet and triplet spin solutions are degenerate. The structural deformation of the lattice is very small and symmetric, with the three undercoordinated Ti ions around the vacancy showing a slight outward relaxation with respect to their equilibrium position.

Instead, two distinct peaks in the density of states can be observed in Fig. 4.9b where DOS were calculated for U = 5 eV. Since the TiO_2 is more of a charge-transfer type semiconductor than a Mott-Hubbard insulator, one should not expect to be able to open up the bandgap to its experimental values using a physically reasonable value of U.[54]

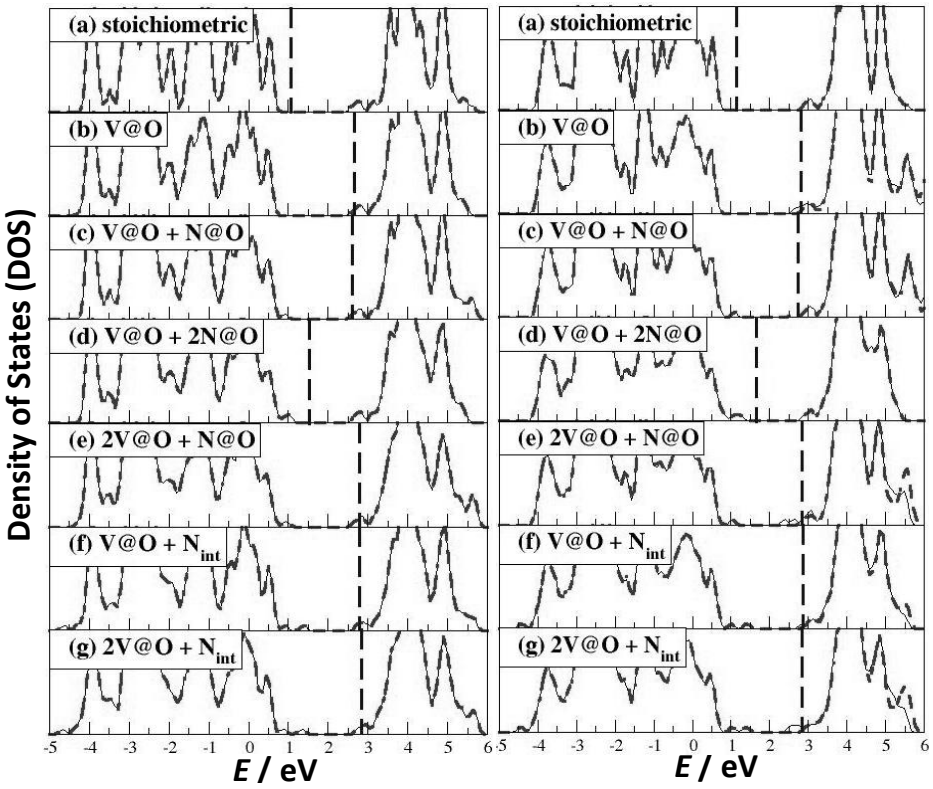

Figures 4.8 (left) – 4.9 (right). Density of electronic States (DOS) at the level of GGA for different combinations of oxygen vacancies (V@O) and N doping locations (N@O for substitutional and N_{int} for interstitial) and their stoichiometric ratio (left panel). DOS obtained from calculations at the level of GGA + U (U = 5 eV) is represented in the right panel. Spin polarized states are in continuous black and dashed red lines; Fermi energy levels are indicated by the vertical dashed lines.

Once the substitutional nitrogen is introduced concomitant with an oxygen vacancy, the localized N states just above the valence band behave as excellent electron traps. These shallow gap states just above the valence band - reported on panels (c), (d) and (e) of Fig.s 4.8 and 4.9 - are originated from the combination of the substitutional N 2p orbitals with the oxygen ones and they were detected by the optical measurements described above. If interstitial N doping is considered, the N orbitals are deeper into the bandgap as shown on panels (f) and (g) of Fig.s 4.8 and 4.9. It has been suggested that these states may act as recombination ones, annihilating the electron-hole

photogenerated pair. However, from an optical point of view, also these states explain the apparent bandgap narrowing observed in the DR measurements. Either N-substitutional shallow or N-interstitial deeper electronic states play a crucial role as acceptors promoting the conversion of the Ti^{3+} species into the Ti^{4+} ones.[55,56] However, the three N p states originally host five electrons and can accept only one more. For this reason when an equal number either of substitutional or interstitial N doping is present, as in the cases reported in panel (c) and (f) of Fig.s 4.8 and 4.9, one Ti^{3+} electron is still present out of the two originally created by a single oxygen vacancy, and the Fermi energy is still pinned at the bottom of the conduction band. This is pictorially represented on panel (a) of Fig. 4.10.

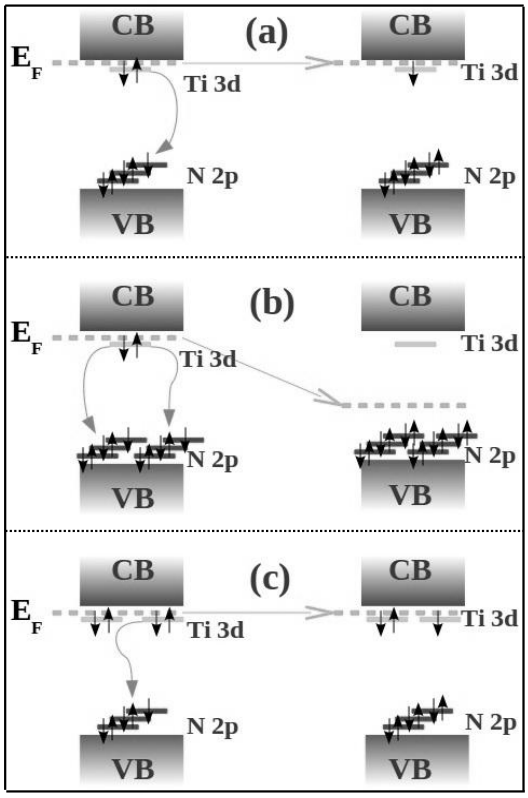

Figure 4.10. Pictorial representation of the electron transfer process during nitrogen substitutional doping: (a) an oxygen vacancy and a substitutional N is present and the Fermi energy is invariant; (b) an oxygen vacancy and two substitutional N are present and the Fermi energy level is shifted at the top of the valence band; (c) two oxygen vacancies and a single substitutional N are present and the Fermi energy is invariant. The same reasoning can be applied to interstitial doping energy levels.

Similar conclusions have been reached by Graciani *et al.*,[57,58] but in the case of the rutile surface and subsurface oxygen vacancies in the presence of nitrogen doping. Only when enough N states are introduced, as shown on panel (d) of Fig.s 4.8 and 4.9, the charge transfer from the Ti^{3+} states is complete and the Fermi energy is lowered to just above the valence band. Each nitrogen impurity traps one Ti 3d electron as shown on panel (b) of Fig. 4.10. Another possible set-up is the one reported on panel (e) and (g) of Fig. 4.8 and 4.9, where vacancies stoichiometric coefficient is double respect to the N doping one. In these cases, the Fermi energy is even more pinned at the bottom of the conduction band, since an extra number of Ti^{3+} states are present. The orbitals representation of this electronic arrangements is the one on panel (c) of Fig. 4.10. Finally, by comparing panels (b), (e) and (g) of Fig. 4.8 versus the ones of Fig. 4.9, one can appreciate how DFT + U was necessary to describe the Ti^{3+} states. Localized states arise on panels (b) of Fig. 4.9 and clearly increment their populations when the number of vacancies is doubled, as it is evident from the DOS of panels (e) and (g) of Fig. 4.9. However, the same conclusions can be reached in terms of Fermi energy location, indicated by vertical lines in Fig.s 4.8 and 4.9, using both DFT or DFT + U approach.

The experimental-theoretical joint picture

The present DFT calculations, in agreement with literature previous results, clearly indicate that the apparent bandgap narrowing observed in the DR measurements is due to the presence of intra-gap states induced by the N p orbitals mixing with the oxygen ones.[55] However, from this partial point of view, the photogenerated electrons fate is still unclear and opened to the possibility of complete or partial transfer into the empty N orbitals generated by doping. Thus, only partial conclusions can be drawn by comparison between optical experiments and DFT calculations.

Then, considering that the visible light response could be induced not directly by the doping, but by oxygen vacancies, stabilized by the presence of nitrogen as a result of charge compensation, and acting as color centers,[59,60] the motivation for other electronic experiments in conjunction with DFT calculations is clear and the theoretical findings allow one to have a comprehensive interpretation of the impedance and photovoltage experimental results.

On one hand, by inspection of the Ti^{3+} 3d states pictorially reported on Fig. 4.10 just below the conduction band, we can safely conclude that these states are originated by the oxygen vacancies and are invariant under N doping. On the other hand, the quasi-Fermi energy levels determined by photovoltage experiments are the electronic orbitals populated under light irradiation and they should be distinguished from the Fermi energy level which, instead, indicates the half population energy. Thus, a direct comparison between the quasi-Fermi energy levels and the Ti^{3+} 3d states can be made, showing the agreement with the photovoltage results.

Instead, the Mott-Schottky plots, which are obtained under dark conditions, allow one to measure E_{fb}. This value indicate the average occupation number, *i.e.*, the Fermi level. For an n-type semiconductor, it represents also the conduction band edge. A comparison between the Mott-Schottky and the theoretical results can be done by looking at the vertical dashed lines (Fermi energy) in Fig.s 4.8 and 4.9. This excludes panels (d) of both Fig. 4.8 and 4.9 to be a realistic doping set up.

Besides, the Mott-Schottky flatband and the photovoltage quasi Fermi energy values show that these are located at the same levels on an electrochemical scale. Taking into consideration that the Mott-Schottky measurements are under dark and the photovoltage ones under light irradiation, one can univocally identify the location of the conduction band and conclude that this is invariant under N-doping for all our samples.

At the light of these considerations and by comparison with the several different N-doping and O vacancies ratio scenarios simulated at the level of DFT + U calculations (Figures 4.8 and 4.9), one can safely conclude that in the case of the present samples, oxygen vacancies are more numerous than N doping centers, since doping is not changing significantly the Fermi energy location. Thus, on one side, partial accommodation of oxygen vacancies electrons into N 2p states occurs and leads to the formation of charged diamagnetic N impurities and re-oxidized Ti ions. On the other side, this electron transfer process induces the formation of extra oxygen vacancies, that has been proved to be favored in the presence of N-doping.[61] Eventually, re-oxidation of Ti ions is somewhat compensated by the formation of Ti 3d states and the Fermi energy is left invariant, *i.e.*, pinned at the bottom of the conduction band. Thus, a likely comprehensive picture is that one represented by panel (c) of Figure 4.10.

In conclusion, the effects of N doping sites may be multiple, since they not only act as electron scavengers, but also stabilize the color centers.[62]
All these findings derived from joint experimental and theoretical investigations are rationalized by assuming that the position of the conduction band is not affected by the doping. These considerations can be extended to the Fermi energy level. Then, only with the help of theoretical calculations it is possible to assert that oxygen vacancies are more numerous than N doping centers in our samples and that the electron transfer from Ti^{3+} 3d orbitals occurs only in part, keeping the Fermi Energy pinned at the bottom of the conduction band.

4.4.2. Pr doping

Photovoltage measurements and DFT electronic calculations
Also for Pr-doped titania samples the position of the quasi-Fermi level ($^{n}E_f$*) was determined by measuring the photovoltage as a function of the suspension pH. The obtained values are reported in Table 4.3, 2nd column. It can be noticed that the quasi-Fermi levels are only slightly shifted away from the conduction band of the oxide.

Sample	$^{n}E_f$* (V *vs* NHE)
T	-0.67
TPr_0.2	-0.65
TPr_0.3	-0.64
TPr_0.5	-0.59
TPr_0.7	-0.62

Table 4.3. Quasi-Fermi levels evaluated at pH 6 (photovoltage method). The standard deviation is 0.2 V for all samples.

These data were compared with electronic DFT computations (see section 3.4 for computational details): the Fermi and quasi-Fermi (the first excited Kohn-Sham orbital) energy levels variation under Pr doping were calculated. From Fig. 4.11, it can be observed that there is not a unique answer for Fermi energy shift under substitutional Pr doping, but it depends on values of U for Pr. Instead, the interstitial Pr doping shifts the Fermi energy level toward the conduction band edge for any U value.

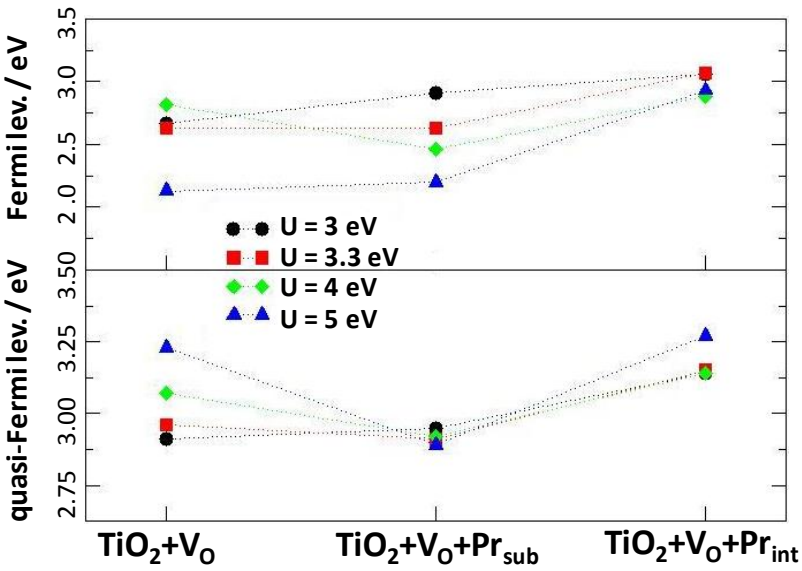

Figure 4.11. Fermi (upper panel) and quasi-Fermi (lower panel) energy levels for different Pr doping and for different values of U for Pr.

However, during a photovoltage experiment, it is the quasi-Fermi energy level to be populated under irradiation and to be measured. Only as an approximation, the Fermi is assumed at the same level as the quasi-Fermi one, given that TiO_2 is a n-type semiconductor. For this reason, the quasi-Fermi energy variation under doping is plotted on the lower panel of Fig. 4.11, highlighting a common trend for any U value for both doping sites: when a substitutional Pr doping is performed, the quasi-Fermi levels are lowered with respect to the conduction band, whereas when an interstitial doping occurs, the quasi-Fermi levels are raised toward the conduction band.

Given the experimental photovoltage observations, the presence of substitutional Pr doping in the present samples can be asserted once more. The quasi-Fermi energy levels shift originated by substitutional Pr doping also confirms the apparent bandgap narrowing observed by the Kubelka-Munk transformed DRS data.

To perform a closer comparison between experimental data and theoretical calculations, the density of electronic states (DOS) of the doped supercell arrangements is plotted in Fig. 4.12. In all panels the total spin polarized DOS of the Pr doped oxygen defected TiO_2 are reported in continuous black and

dashed red curves. The Fermi energy is indicated by the vertical dashed line. As far as the Pr electrons are concerned, the d and f DOS have been magnified 10 times and put into evidence because these are located in the proximity of the valence and conduction bands. More specifically, in the case of substitutional doping (left panel of Fig. 4.12) and for U >3 eV, the d states (blue curves) are located just above the valence band and they are filled, while the f orbitals (green curves) are just below the conduction band and they are empty. Small deviations are seen by varying the U value between 3.3 eV and 5 eV, while for U = 3 eV the Pr d orbitals place as mid-gap states. Instead, for Pr interstitial doping (right-handed panel of Fig. 4.12), the d and f orbitals generate a set of mid-gap states, whose location vary with the value of U. Interestingly, these mid-gap f orbitals are filled, since Pr is not employed in any bond.

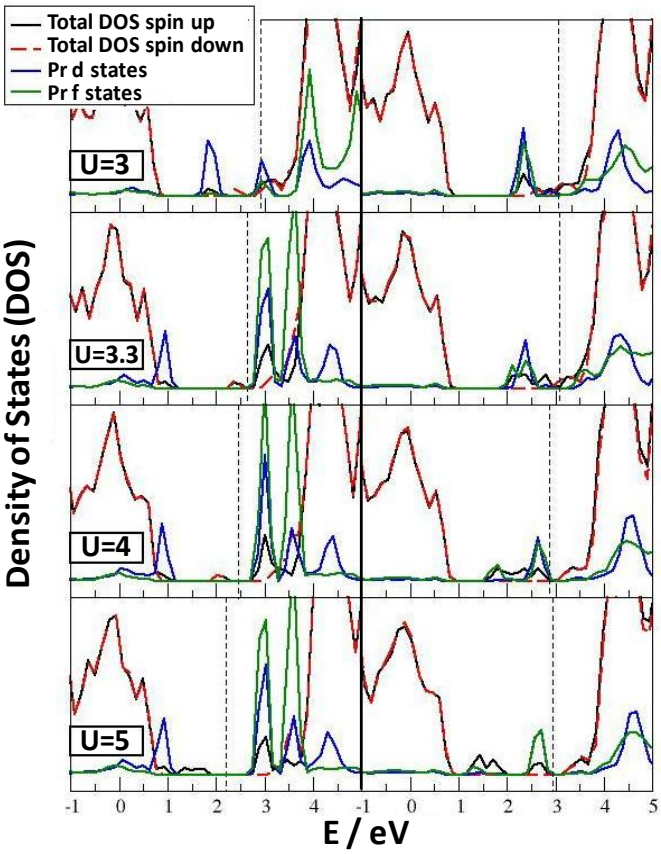

Figure 4.12. Electronic density of states (DOS) for substitutional (left column) and interstitial (right column) Pr doping of anatase TiO_2. Comparison among different U

values for Pr on each panel. Continuous black and dashed red lines for the oxygen defected Pr doped TiO_2 spin-polarized calculation, continuous green line for Pr 4d orbitals and continous blue line for Pr 4f orbitals. The Pr 4d and 4f DOS has been magnified 10 times for convenience. The Fermi energy is indicated by the vertical dashed lines.

From this electronic description, it can be inferred that electronic transitions can occur from either filled d Pr orbitals or valence band states to empty f orbitals just below the conduction band in the case of substitutional Pr doping. Instead, with the interstitial Pr doping set-up, the possible electronic transitions are from either d or f filled Pr orbitals to Ti 3d ones, which delimit the bottom of the conduction band. On the basis of the DRS results, which put into evidence the f orbitals contribution to the absorption, it can be safely concluded that substitutional Pr doping should be preferred.

4.4.3. Ag doping

Photovoltage analyses on (N,)Ag-doped titania samples were performed on both “chemically reduced” and “not chemically reduced” materials. However, results on the samples not chemically reduced were not straightforward. As a consequence, only “reduced” samples are discussed hereafter.
Surprisingly, all photovoltage curves did not show a single definite inflection point, in the cases of both single doping and codoping. For this reason, In Table 4.4 two tentatively pH_0 values and are reported. It can be noticed that the first inflection point is shifted towards very low pH values (negative ${}^{n}E_f$*) for TNAg0.05_R, whereas the second one coincides with the main pH_0 point of TAg0.01_R. Note that for this latter sample pH_0 (2) is reported in brackets as it was definitely less marked as the other ones. The coincidence of two pH_0 values for the two samples together with the presence of an additional inflection point for the codoped samples could suggest an influence of the non-metal dopant on such electronic feature of the system. This finding is, however, not supported by any literature evidence. By comparing the numerical results with the undoped sample, having a quasi-Fermi level of -0.67 V (NHE), it can be noticed either a shift towards more negative values, if considering the first inflection point for TNAg0.05_R, or a substantial invariance of the quasi-Fermi level, considering a standard deviation of about 0.05 V.

Sample	pH_0 (1)	pH_0 (2)	${}^{n}E_f$* (1)	${}^{n}E_f$* (2)
TAg0.01_R	4.5	(6.8)	-0.60	(-0.36)
TNAg0.05_R	1.8	4.5	-0.76	-0.60

Table 4.4. pH_0 values (pH values corresponding to the inflection point of the photovoltage curve) and quasi-Fermi levels (V *vs* NHE) for two (N,)Ag-doped titania samples chemically reduced in the synthetic step. The standard deviation is 0.05 V for both samples.

Then, the presence of the metal element in the oxide can be extensively discussed, even though no certainties exist on the actual oxidation state of silver in these samples nor on the definite nature of the semiconductor-metal system, which is not exactly defined as a composite. TEM and possibly EXAFS analyses are planned for future investigations on this topic.

No doubt that electron transfer between photoexcited semiconductor and metal is an important phenomenon in photocatalysis. Indeed, TiO_2 nanoparticles modified with precious metals have been extensively employed in photocatalytic water-splitting reactions.[63,64] Recent studies have shown that metal or metal ion doped semiconductor composites exhibit shift in the Fermi level to more negative potentials.[65-68] Such a shift in the Fermi level improves the energetics of the composite system and enhances the efficiency of interfacial charge-transfer process. The unusual property of gold nanoparticles to undergo quantized charging makes them a unique candidate to achieve Fermi-level equilibration.[69] Platinum metal, on the other hand, introduces ohmic contact facilitating a quick transfer of electrons to the electrolyte.[65] If such metal particles come in contact with a charged semiconductor nanostructure or nanoparticle, the Fermi levels of the two systems equilibrate, as in the case of the semiconductor-electrolyte interface. One factor that can potentially influence the electronic properties of the nanocomposite is the size of the metal particle. A greater shift in the energy level for each accumulated electron, along with a higher catalytic activity, is expected in smaller size metal nanoparticles than in larger ones.[7]

Subramanian *et al.* probed the effect of particle size of gold nanoparticles on the charge distribution and Fermi level equilibration of the composite system.[70] Besides, Kongkanand and Kamat stated that the shift of the Fermi

level of the composite TiO_2/Au system to more negative potential is the result of a higher degree of electron accumulation causing the composite system to be more reductive than the pristine TiO_2 system.[7] The double-layer charging around the metal nanoparticle facilitates storage of the electrons within the gold nanoparticle. When the semiconductor and metal nanoparticles are in contact, the photogenerated electrons are distributed between TiO_2 and Au nanoparticles. The transfer of electrons from the excited TiO_2 into Au continues until the two systems attain equilibration (Fig. 4.13). Since the electron accumulation increases the Fermi level of Au to more negative potentials, the resultant Fermi level of the composite shifts closer to the conduction band of the semiconductor.

According to such an explanation, a negative shift of ${}^{n}E_f{}^{*}$ would be expected for the reported samples. This occurred for the first inflection point of the codoped oxide, whereas the substantial invariance of the quasi-Fermi level as a result of the above mentioned experiment on Ag-doped titania sounds slightly conflicting. As already stated, further work will be devoted to a deeper study of the complex Ag-TiO2 system obtained by our synthetic procedure.

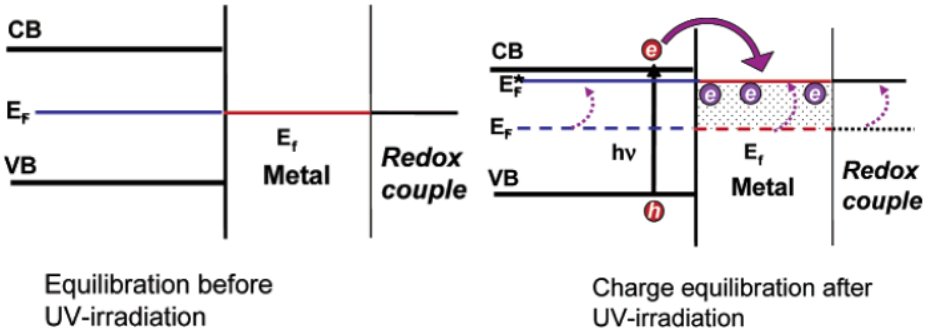

Figure 4.13. Equilibration of semiconductor-metal nanocomposites with the redox couple before and after UV Irradiation.[7]

The following second part of this chapter is devoted to another electrochemical method (photocurrent transient measurements) used to evaluate charge carrier recombination in titanium dioxide.

4.5. Charge carriers' behavior

For an n-type semiconductor like defective nano-TiO_2, illumination with above-bandgap light promotes and accumulates electrons in the conduction band of the nanostructured film, as a result of the separation of electron and hole charge carriers. As an intrinsic feature and as a quite relevant drawback, TiO_2 also exhibits recombination of excited electrons and holes at a rate that is often detrimental to its photocatalytic activity. The recombination rate of charge carriers is connected to photocatalytic activity by an unambiguous relationship. Indeed, photogenerated holes can be trapped either deeply or shallowly and, in the former case, charge carriers do not contribute to the photocatalytic activity.[71] To facilitate its direct applications, it is challenging to succeed in extending the photoactive response of TiO_2 to visible light and concurrently inhibiting the electron-hole recombination.

Although the hole dynamics in the photoexcited TiO_2 film is relatively simple (quick trapping within a few hundred fs and long lifetime), the electron dynamics is more complicated. Surface-trapped electrons and energetically dispersed bulk trapped electrons must both be considered. In Fig. 4.14 Tamaki *et al*. depicted the energy levels for the surface-trapped electrons and bulk electrons suggested from the observed relaxation dynamics.[72] Immediately after photoexcitation, some of the free electrons are trapped at surface sites, whereas the rest of the free electrons are trapped in the bulk. Since these two species are energetically equivalent and probably very close to the conduction band edge, electrons can migrate between surface trap sites and shallow bulk trap sites that are in equilibrium. All the possible trapping sites represented in Fig. 4.14 by the energetically distributed levels enable shallow trapped electrons to relax into deeper sites with a through a hopping process involving trapping sites (time constant in the order of ps). It is underlined that when electrons relax into deep sites, they become less mobile, making it difficult for them to recombine with surface-trapped holes.

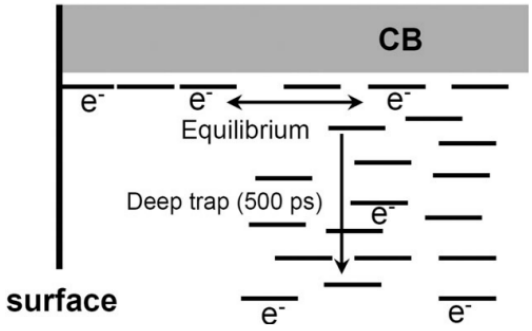

Figure 4.14. Schematic illustration of spatial and energetic distribution of electron traps in a TiO_2 film (taken from ref [73]).

As a matter of fact, nanometer-sized particles are generally too small to sustain significant electric fields so that transport of electrons (majority carriers) in the network of particles is expected to be dominated by a gradient in the chemical potential of the electrons (diffusion) rather than by an electrical potential gradient (drift).[4] The driving force of the diffusion process is the concentration gradient of the charge carriers. To create an electron concentration gradient in the nanostructured semiconductor film, it is important to quickly remove one type of photogenerated charge carriers (in our case the holes). Accordingly, fast hole kinetics at the semiconductor/electrolyte interface is of paramount importance to prevent recombination of the photogenerated charges. This is something which should be pursued in case the desired process is, as for instance, an efficient water splitting in a photoelectrochemical cell after bandgap excitation or whatever photocatalytic process of either reduction or oxidation. In this context, the application of a potential bias can be thought as a possible way to increase the electron-hole separation and consequently to enhance quantum yield.[74]

When dealing with a semiconductor in contact with an electrolyte, the depletion layer in the semiconductor nanoparticles is practically absent due to their small size, so that an applied potential, as the one present in photocurrent measurements, exerts a significant weaker action on the efficiency of electron-hole separation, compared to compact electrodes.[75] As a consequence, electron transport may be considered as a random motion between equivalent sites, while hole diffusion is not important as the particles are very small and totally surrounded by the electrolyte.[76]

This statement can be supported by the analysis of linear sweep voltammetries (see below): for nanostructured electrodes the photocurrent is almost indipendent of potential (*V*) in a rather wide range of *V*. However, the nature of electron migration in these electrodes is not straightforward and several mechanisms for electron transport have been suggested. In particular, the exact role of electron trapping remains unclear: some authors reported that soon after electrons are injected into the conduction band of titania a large fraction of them is trapped in surface states (from which they need to proceed with a hopping mechanism,[77,78] while some others reported the possibility of tunneling through a potential barrier between the particles.[79] No doubt, however, that in nanoparticulate TiO_2 systems electron transport a is strongly affected by trapping and detrapping events,[80] with the transit time of trapping about three orders of magnitude faster than that of detrapping, indicating that most of the photoinjected electrons are localized in the trap states.[81]

Concepts like *electron transport time* and *electron lifetime* will be encountered hereafter. The former can be defined as the average time required to the electrons to reach the conductive glass substrate from the location where they are photogenerated (*i.e.*, the time constant under short circuit conditions in intensity-modulated photocurrent spectroscopy (IMPS),[82] whereas the latter is the average time for recombination of an electron in the semiconductor with species in the electrolyte or adsorbed onto the semiconductor (*i.e.*, the time constant under open circuit conditions in intensity-modulated photocurrent spectroscopy (IMPS). When electrons have to cross more grain boundaries (many cases of defective titanium dioxide, in particular at decreasing the particle size), a slower electron transport can occur. This means that a smaller particle size can lead to inefficient electron diffusion. On the other hand, the electron lifetime usually increases as the particle size decreases.[83] For a solar cell to be efficient, the electron transport time must be significantly shorter than the electron lifetime.

Fig. 4.15 shows a schematic representation of the different reaction pathways for the photogenerated electron–hole pair for an n-type semiconductor. It is generally accepted that three major processes limit the photoelectrochemical current in semiconductors: (a) bulk recombination via bandgap states, or (b) directly electron loss to holes in the valence band (eventually followed by emission of light) ,and (c) surface recombination.[84] These three limiting factors

are general. If a proper electron scavenger is present (in Fig. 4.15 represented by O_2), electrons can also be lost from the conduction band (process (d)). Similarly, holes can be scavenged by a hole acceptor, but this implies the presence of an additional species into the system. When considering a photoelectrochemical cell, any acceptor in the electrolyte collecting electrons will decrease the efficiency of the working cell. This should be true regardless of the way the charge carriers are created.

The kinetics of the charge transfer at the semiconductor-electrolyte interface (SEI) of the particles constituting the film essentially determine the direction and magnitude of the photocurrent. If the semiconductor is porous, the electrolyte penetrates the depth of the colloidal film up to the surface of the back contact.

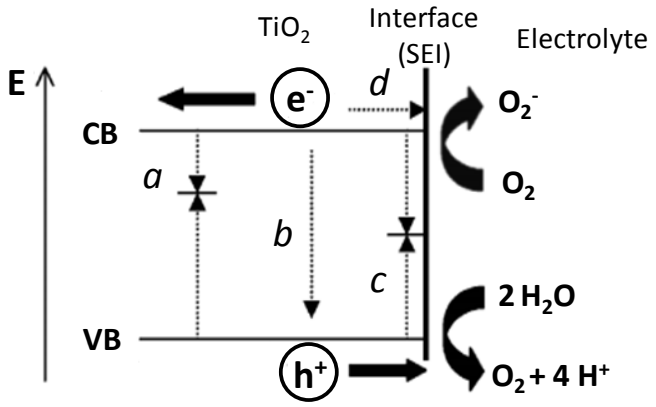

Figure 4.15. Sketch of the reaction pathways for a photogenerated electron–hole pair in semiconductor in contact with an aqueous electrolyte.

Electron diffusion processes

Experimental measurements as well as computer simulations have been carried out extensively to study the electron diffusion coefficient, which is affected by the following parameters: the structure of the mesoporous film,[85] the necking of neighbouring nanoparticles,[86,87] the composition of the electrolyte via an ambipolar diffusion mechanism,[88] and the incident light intensity.[3]

A great variety of experimental methods have been used to study the electron transport processes in mesoporous TiO_2 films, ranging from small-amplitude modulation methods such as intensity-modulated photocurrent

spectroscopy[89-91] and transient photocurrent measurements[88,92] to electrical impedance spectroscopy applied to both mesoporous TiO_2 electrodes[93] as well as to complete dye-sensitized solar cells (DSCs).[94] Charge transport measurements have been also conducted in open-circuit conditions by a transient voltage rise method.[95] DC conductivity measurements of mesoporous TiO_2 electrodes have been performed in redox inactive electrolytes,[96] while conductivity measurements by microwave absorption[97] and terahertz spectroscopy[98] have been performed in the absence of electrolyte. Experimental results have demonstrated that the measured (effective) diffusion coefficient is closely related to the quasi-Fermi level in the mesoporous TiO_2.[93,94]

4.6. Probing electron-hole recombination: the choice of photocurrent measurements

Photogenerated electrons and holes in TiO_2 can recombine or react with molecules at the surface; therefore, generation and relaxation processes of electrons and holes are crucial in determining the efficiency of a photocatalytic reaction. Minority carriers are not primarily responsible for current transport so that electrons may be collected with high efficiency as long as recombination in the form of electron transfer to an electron acceptor in the solution (or to the oxidized form of the dye in a dye-sensitized solar cell) can be minimized.

To understand these primary processes, many kinds of experimental methods have been utilized. Among them, transient absorption spectroscopy is one of the most powerful methods because it provides very high temporal resolutions (about 100 fs) and allows identification of transient chemical species. It has been used extensively to study the trapping dynamics of electrons and holes.[99,100] Thanks to the different absorption wavelengths, it is also possible to state the type of charge carrier excited by light.[101] Absorption spectra of electrons and holes in TiO_2 are very broad, extending from the UV to the IR region and overlapping in the visible wavelength range.[102-104] Although the spectroscopic features of electrons and holes in TiO_2 are said to be well understood,[73] this is, however, not straightforward. Notwithstanding such a slight uncertainty, using spectroscopic investigations on colloidal titania suspension upon illumination and in the absence of any hole scavenger, it has

been found that, while photogenerated electrons are trapped instantaneously (ns time scale, see Fig. 4.16), holes can be trapped in electronically shallow or deep states. Holes in deep traps are rather long lived and inactive, while shallowly trapped holes are in thermal equilibrium with free holes and exhibit a very high oxidation potential.[71]

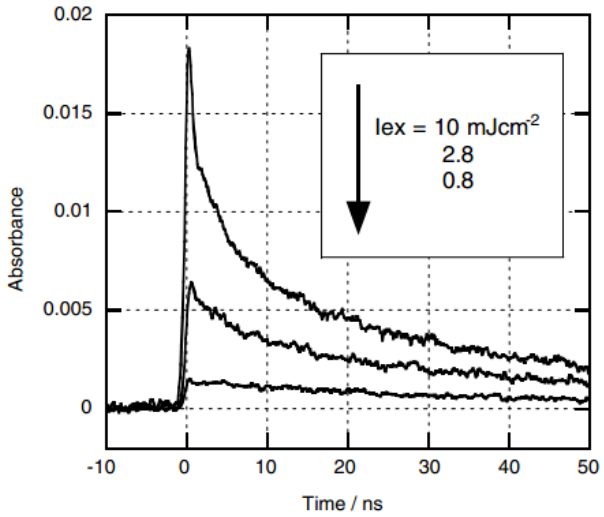

Figure 4.16. Decay profiles of transient absorption in a rutile TiO_2 single crystal under various excitation intensities, as reported in inset (taken from ref [105]).

However, photocurrent transient measurements on a longer time scale (seconds) as those presented in the present research can give a picture of the average scenario of excitation-relaxation phenomena involving electrons in TiO_2.

Going through literature about titanium dioxide, especially doped, and other semiconductors, it is well established that photoluminescence (PL) - namely, the spontaneous emission of light from a material under optical excitation - is a useful tool to explore electron-hole recombination (Fig. 4.17). In general, the quenching of photoluminescence implies an enhanced photocatalytic activity because PL emission is the result of the combination of excited electrons and holes[106,107] Features of the emission spectrum can be used to identify surface, interface, and impurity levels and to gauge disorder and interface roughness, with the intensity of the PL signal providing information on the quality of surfaces and interfaces. Under pulsed excitation, the transient PL intensity yields the lifetime of non-equilibrium interface and bulk states. Variation of

the PL intensity under an applied bias can be used to map the electric field at the surface of a sample. The fundamental limitation of PL analysis is its reliance on radiative events. Thus, materials with poor radiative efficiency, such as some indirect bandgap semiconductors, are difficult to study via ordinary PL. Similarly, identification of impurity and defect states depends on their optical activity. Although PL is a very sensitive probe of radiative levels, one must rely on secondary evidence to study states that couple weakly with light.

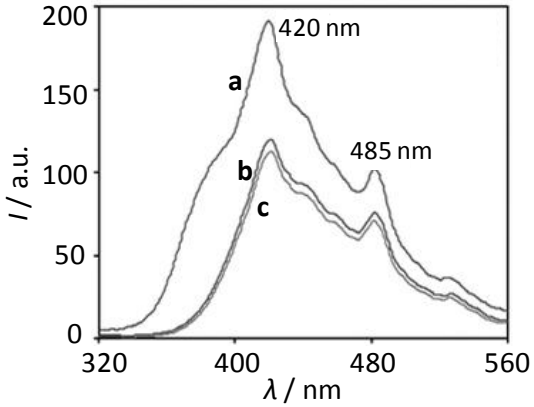

Figure 4.17. Photoluminescence (PL) spectra of (**a**) bare TiO_2, (**b**) TiO_2-P25 and (**c**) N-TiO_2 (from a hydrazine hydrate nitrogen precursor, wet synthetic method). TiO_2 exhibited two photoluminescence emission peaks at 420 and 485 nm. Since PL emission is the result of the recombination of excited electrons and holes, the lower PL intensity of N-TiO_2 indicates a lower recombination rate of excited electrons and holes (taken from ref [108]).

Photocurrent transient measurements

Alternatively, chronoamperometry with chopped light can be applied to TiO_2 nanopowders to gain information on the charge recombination processes which take place in the oxide and affect its photocatalytic performance. The photocurrent is generated by the separation and transfer of photo-generated electron-hole pairs on the surface of TiO_2 particles, and then subsequent diffusion of electrons among the connected nanoparticles to the back collector in the photoelectrodes. Overall, the photocurrent transients can be attributed to photoinduced electron–hole separation, trapping, recombination, and scavenging. During the hops of electrons from one

nanoparticle to another until hitting the back collector, they can be trapped in surface states from each TiO_2 particle making up the photoelectrode.

Because of their successful use in combined studies on dye-sensitized solar cells, photocurrent transients following the injection of electrons from the excited state of the dye into the conduction band of the semiconductor have been quite widely investigated in literature,[109,110] as a means to probe the working electrode and to understand the factors which determine the final operative short circuit current of the cell. In these cases and when the photocurrent is recorded as a function of the applied potential, the system under study is composed not by the bare TiO_2 electrode alone: this latter is either sensitized by the dye or measurements are directly performed on the assembled solar cell.[111,112]

Cao *et al.*[3] deeply studied the electron transport in porous nanocrystalline TiO_2 photoelectrochemical cells, namely dye-sensitized solar cells, by photocurrent transient measurements and intensity-modulated photocurrent spectroscopy. They stated that the photocurrent transients are characterized by a fast and a slow component (see Fig. 4.18), with a rise time of the transients in the range of milliseconds to seconds. Overall, the transient response of these cells is dominated by electron transport in the TiO_2 film through diffusion (with a diffusion coefficient for electrons in the particle network being a function of the light intensity).

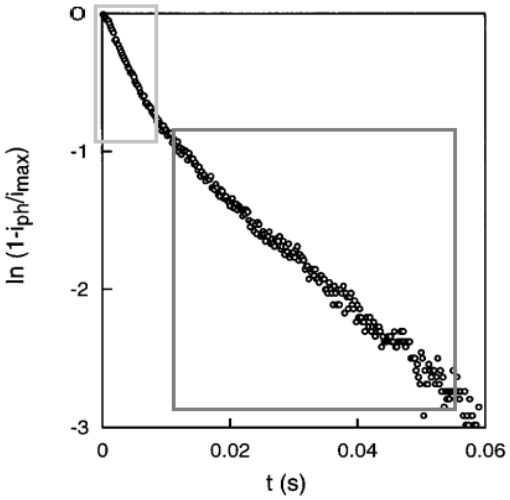

Figure 4.19. Semilogarithmic plot of a photocurrent transient under monochromatic (514 nm) illumination at 4 mW cm^{-2} for a porous nanocrystalline TiO_2 photoelectrochemical cell (taken from ref [3]).

Indeed, recombination is primarily an interfacial process in DSCs, in contrast to the bulk process that occurs in conventional p-n junction solar cells.[113]

The aim of this part of the work was to test the bare (doped-)TiO_2 electrode, without dye, keeping the system as simple as possible in order to characterize the charge recombination behavior of home-made samples by a useful traditional photoelectrochemical technique which is very rarely used for this specific purpose.

Nevertheless, other literature works present chopped light amperometric measurements on nano-TiO_2 electrodes[76,114] or other inorganic semiconductor devices[23] under potentiostatic conditions in aqueous electrolytes. Such experimental data allow to qualitatively judge the photocurrent and eventually compare it with the dark current. Alternatively, polarization curves on irradiated TiO_2 layers were measured by Waldner *et al.* in various electrolytes, namely sodium hydroxide, sulfuric acid, oxalic acid, and potassium oxalate.[74,115] The shape of such curves was interpreted in terms of response time to irradiation and photocurrent depletion. Besides, the photocurrent developed following a nanosecond laser pulse (bandgap excitation) has been monitored under steady-state conditions in a certain number of literature studies,[3,112] in some cases to give a merely qualitative description of charge carrier separation and charge transport in nanocrystalline porous TiO_2 electrodes. Then, electron migration in nanostructured anatase TiO_2 films by intensity-modulated photocurrent spectroscopy was investigated by Goossens *et al.*,[116] who described the transport of electrons by a macroscopic diffusion model.

However, very few papers deal with chronoamperometric measurements and the consequent evaluation of the transient time constant (τ) making use of this characterization mainly to investigate the electronic properties of the tested samples and also to judge their photoactivity.

Indeed, the use of such a tool as a helpful prescreen of semiconductor oxides synthesized in powdery form is herein proposed. No literature examples exist with this specific aim. In particular, a method which turns out to be useful for any type of nano-TiO_2, starting from both powders and films, will be proposed. As most of metal or non-metal doped titania samples are obtained by wet methods, like the sol-gel route, they are usually produced and used in

photocatalytic applications as powders. Then, their deposition as suitable electrodes for chronoamperometric tests is not trivial at all.

The lack of widely accepted experimental procedures in this field led to focus mainly on the optimization of the analysis procedures, testing and reviewing most of the possibilities proposed in literature. Thus, hereafter is a comprehensive evaluation of the optimal conditions that allow reproducible quantitative photocurrent measurements on thin TiO_2 films by varying different experimental parameters such as the type of electrolyte, the illumination source, and the presence of a hole acceptor.

Since the efficient utilization of the solar spectrum is one of the important subjects for improving the future generation of TiO_2-based photocatalysts, also metal and non-metal doped titania have been analyzed by chopped light chronoamperometry.

Doping TiO_2 with metal or non-metal ions also affects the lifetime of photoinduced charge carriers in doped TiO_2, as appears from the different τ values reported by Dholam *et al*. (see Fig. 4.20).[117]

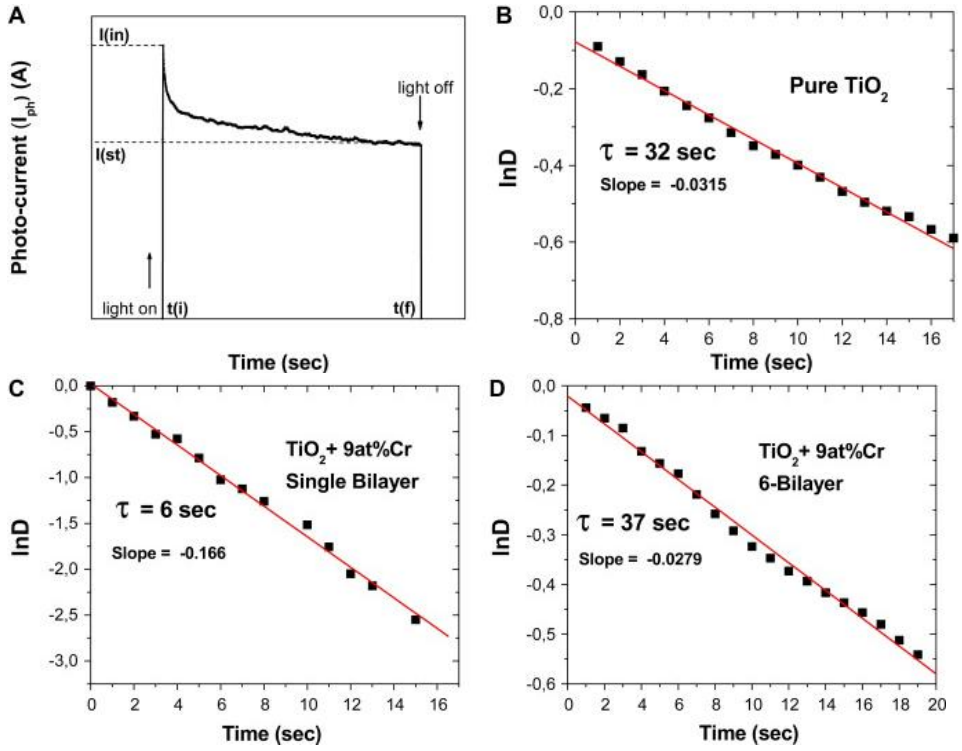

Figure 4.20. (A) Schematic representation of the photocurrent transient curve. Normalized plot of current-time dependence for: (B) pure TiO_2, (C) single bilayer, and (D) 6-bilayers of "ITO/Cr9-doped TiO_2" multilayer film (taken from ref [117]).

Regarding transition metal ions Choi *et al.*[118] proved that both type and concentration of the dopant are important factors in determining recombination processes.

In particular, there might be an optimal dopant ion concentration.[119] Below this concentration recombination processes may be reduced thanks to the introduction of electrons and/or holes traps,[120] but also benefits deriving from the dopant itself may not be signicant. At appropriate concentrations, instead, the dopants can selectively trap one type of charge carrier, *i.e.*, allowing the other one to reach the particle surface, being able to take part in the desired redox reaction.[71]

A kinetic information

The photocurrent transient can be defined by the following kinetic equation:[121]

$$D = e^{-\frac{t}{\tau}} \quad \text{(eq. 4.8)}$$

where D is defined as

$$D = \frac{I_t - I_{st}}{I_{in} - I_{st}} \quad \text{(eq. 4.9)}$$

Here τ is the transient time constant, I_t is the current at time t, I_{in} is the current at t = 0, and I_{st} the stationary current. The slope of the plot ln*D vs* time provides the transient time constant τ, which is related to the time for charge recombination processes in the films. The higher the transient time constant, the more inhibited the recombination processes are.

Thus, I_{in} denotes the initial anodic photocurrent spike. This current signal is mainly determined by the separation of photo-generated electron-hole pairs within the photoelectrode: holes transfer at the photocatalyst/electrolyte interface, while the electrons are transported to the back contact.[122,123] After I_{in} has been attained, then a continuous decrease of the photocurrent with time is observed until a steady-state photocurrent, I_{st}, is reached. The photocurrent decay indicates that charge recombination processes are occurring: the holes accumulated at the TiO_2 surface competitively recombine with electrons from the TiO_2 conduction band, instead of being trapped or captured by reduced species in the electrolyte (to oxidize water and form OH radicals or peroxo complexes, in the absence of any sacrificial reagent); that is, the decay is largely determined by the efficiency of the transfer of conduction

band electrons towards back contact and, at the same time, by the rate at which minority carriers trapped at surface states capture majority carriers.[122] Charge carriers that are generated deep within the film take a longer time to reach the surface than those generated close to the surface, and so are more likely to be lost to recombination before they can be collected. The photocurrent becomes constant after the equilibration of competitive separation and recombination of electron-hole pairs.

Two concepts are mainly enclosed in a photocurrent transient: the separation of photo-generated electron-hole pairs, related to the intensity of the photocurrent signal, and the recombination of charge carriers, which appears in the evolution of the anodic photocurrent spike. Both types of phenomena, however, are not the only causes of the final profile of the curve: in the case of the former issue, the photocurrent intensity also depends on intrinsic parameters of the film, *e.g.*, the film thickness, whereas the photocurrent decay, can be influenced, in turn, by other factors, *e.g.*, the presence of electron/hole acceptors in the electrolyte.

Indeed, when dealing with real systems, different photocurrent profiles can be obtained. As reported in the pioneering paper by Peter about dynamic aspects of semiconductor photoelectrochemistry,[124] three main classes of decay can be sketch out (Fig. 4.21): no recombination (a), almost complete recombination (b), partial recombination (c).

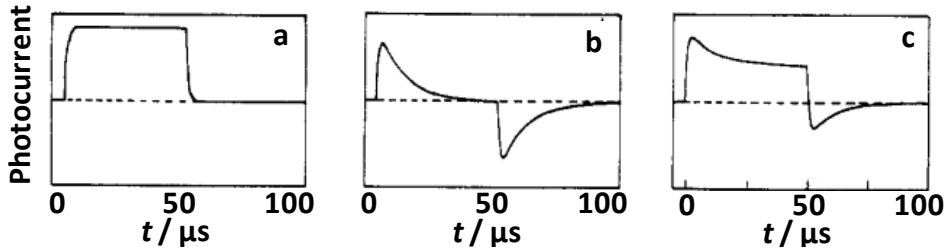

Figure 4.21. Transient photocurrent response to chopped illumination calculated for a GaP semiconductor electrode with surface states: (a) no recombination; (b) almost complete recombination; (c) partial recombination (taken from ref [124]).

Besides this quite hasty simplification, another round up of photocurrent profiles can be given according to the disparate literature. Fig. 4.22 shows three different shapes of decays, the first one definitely being the most common for semiconductors, such as titania, exhibiting recombination until

generation of a steady-state current. Cases b) and c) in Fig. 4.22 have been displayed by Liu *et al.* and refer to undoped and nitrogen doped TiO_2 thin films, respectively under UV–Vis irradiation (0.1 M Na2SO4 electrolyte at 0.3 V *vs* SCE and illumination intensity of around 100 mW cm^{-2}).[125] Jin and coworkers also reported similar shapes of the photocurrent transient for their "2D-ordered dome films" of nano-titania, both undoped and doped with Ag^{2+} (2D-Ag- TiO_2), prepared by RF magnetron sputtering.[126]

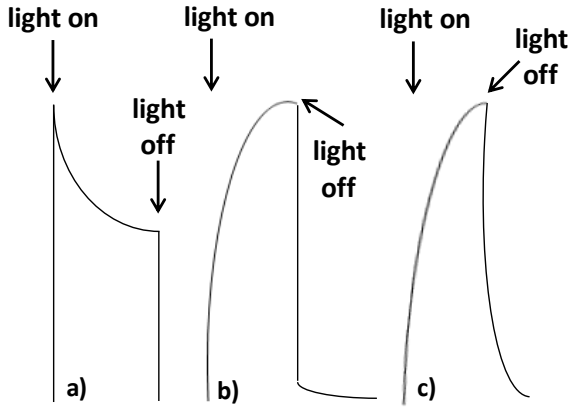

Figure 4.22. Possible shapes of photocurrent *versus* time profiles of titanium dioxide synthesized under different conditions or analyzed with different experimental set-up. A typical response of (undoped) TiO_2 under UV or visible irradiation in inert electrolyte (a); undoped (b) and nitrogen doped (c) TiO_2 thin films under UV–Vis irradiation (0.1 M Na2SO4 electrolyte at 0.3 V *vs* SCE and illumination intensity of around 100 mW cm^{-2}) as reported by Liu *et al.*[125]

Such a jungle of experiments points out that the use of photocurrent measurements for the characterization of semiconductor thin film electrodes could be not straightforward, due to the lack of a widely accepted experimental procedure and the several parameters involved in this type of analysis (layer reproducibility, choice of extrapolation time range, photoanode modification during analysis, *etc.*).

In the context of the present thesis, an optimization of experimental parameters, in order to achieve a reliable insight into the relation between the type/concentration of a dopant and charge carriers recombination rate, has been performed.

Experimental setup

Working electrode preparation

TiO_2 thin films were prepared by spin-casting a 2-propanol suspension of the oxide powder (100 mg of semiconductor in 1 mL of 2-propanol, 15 min in an ultrasonic bath) with a Spin150 spin-coater (SPS, ATP GmbH) onto fluorine-doped tin oxide (FTO) conducting glass (Aldrich, 2.3 mm thick, ca. 7 Ω/sq surface resistivity) after 10 min of rest to favour large particles sedimentation. The suspension was drop cast on the substrate and spun at 2000 rpm for 20 s using a scotch tape as a frame in order to have an active area of 3 cm^2; the deposition was repeated for eight layers. The as-prepared films were finally annealed at 400 °C in stationary air for 1 h to improve adhesion and homogeneity of the films. TiO_2 photoanodes were thus ready to be used as working electrodes (WE) in the photoelectrochemical cell.

Electrochemical setup

The photocurrent developed by irradiating the photoanode (TiO_2) with either UV or visible light was recorded by a microIII Autolab potentiostat/galvanostat (EcoChemie, The Netherlands) using an unconventional three-compartment cell (see sketch in Fig. 4.23). It was equipped with two counter electrodes (CE), both consisting in a Pt wire parallel to the working electrode, a saturated calomel electrode as reference (RE), a Luggin capillary in order to minimize the ohmic drop, and a TiO_2 film located in the middle of the cell as working electrode.

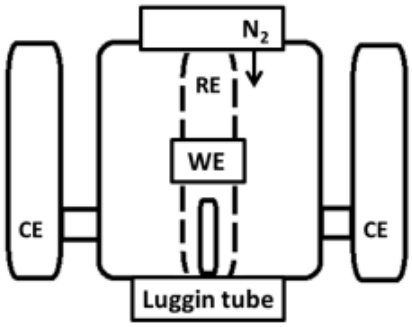

Figure 4.23. Sketch of the electrochemical cell used to record photocurrent transients (chronoamperometric analysis following linear sweep voltammetries as pre-screen).

Different aqueous electrolytes were used with spontaneous pH: NaCl, NaOH and $NaClO_4$ at the concentration of 0.1 M (selected as the best one). Besides

these, the influence of a hole acceptor (10^{-3} M aq. oxalate) in the presence of the best selected inert electrolyte ($NaClO_4$) was studied.
The photoanode was alternatively exposed to dark and light, from the electrode-electrolyte side, using either UV or visible lamp. All the measurements have been carried out in N_2 atmosphere, after degassing the cell with nitrogen flow for at least 10 minutes. Stirring and N_2 bubbling are avoided during the tests in order to eliminate any noise in the signal.
Preliminary linear sweep voltammetries (LSV) have been recorded in the same experimental conditions at a scan rate of 50 mV s^{-1} in order to evaluate the potential at which the photocurrent is constant to be chosen as working potential for the chronoamperometric tests. The photocurrent-time behavior under constant electrode polarization was then obtained with hand-chopped light. Before recording the transient, the applied potential was kept constant in the dark for 600 s in order to establish dark current equilibrium[122] and nitrogen was flown into the cell. Afterwards, N_2 bubbling was stopped and the electrodes were exposed to light for 200 s. During this time, the current transient was recorded. A 100 s dark exposition followed after a new exposure to light. The dark/light alternation was repeated for at least 6 times, in order to obtain reproducible transient patterns.

These conditions were successfully applied for the characterization of selected doped samples and seem a viable and fast route to investigate the dynamics of charge carriers in a thin films, under either visible or UV illumination. An exception is represented by Ag doped titania samples, as explained in the following.
Overall, with this optimized method, suitable conditions to compare doped and undoped TiO_2 powders, deposited as films, which showed different morphological features (*i.e.*, specific surface areas and pore volumes in the range of 95-170 $m^2 g^{-1}$ and 0.10-0.31 mL g^{-1}, respectively, for N- and Pr- TiO_2 samples) were designed.

As a general rule, the photocurrent response of the titania electrodes was first studied by linear sweep voltammetry to examine charge-carrier characteristics at the semiconductor/electrolyte interface and to evaluate the optimized potential at which the photocurrent was the highest or remained constant. LSV in a dark room showed minute current in the 10^{-7}–10^{-6} A cm^{-2} range from

0 V up to approximately + 1.0 V (SCE). LSV performed by irradiating the system with UV or visible light, starting from negative potentials, presented a very similar shape to that obtained in the dark, just shifted to higher current in the positive potential range, in the presence of an inert electrolyte (0.1 M $NaClO_4$), as can be appreciated in Fig. 4.24a.

In the case of other electrolytes (NaCl, NaOH), the photocurrent increased incessantly moving to positive potentials, not saturating completely below 1.0 V: an optimized depletion layer was not fully formed. The increase of photocurrent enlightened the effective charge separation because the recombination of photoinduced electron–hole pairs was inhibited by the increase of positive potential. According to Poznyak *et al.*,[75] in the case of nanostructured electrodes, the photocurrent is almost independent of potential in a rather wide range of potential values and starts to change sharply just near the onset potential (*i.e.*, flat band potential/quasi-Fermi level under irradiation). Thus, chronoamperometry measurements were recorded at +1.0 V (SCE), except for the experiments conducted in aqueous NaOH; in such cases, the potential was set at +0.4 V (in basic media the flat band potential is shifted because of the Nernstian dependence with pH).

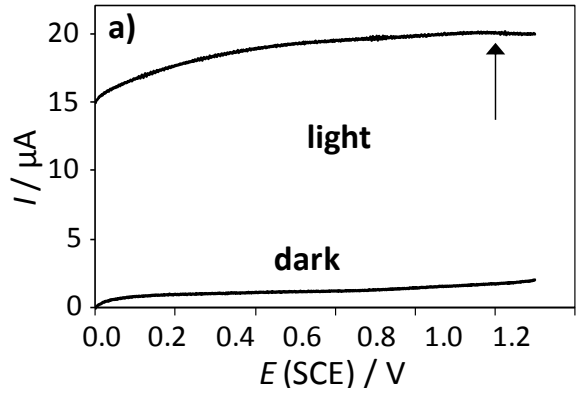

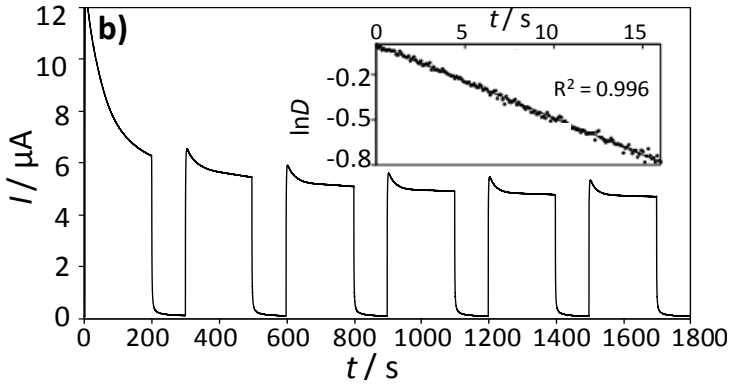

Figure 4.24. Linear sweep voltammetries (LSV) recorded for a selected sample (undoped TiO_2, T) under dark and illumination before performing the chronoamperometric test (**a**); the arrow indicates the potential chosen for the chronoamperometric measurements. Typical example of photocurrent transients (sample T) with the normalized plot of current-time dependence in inset (**b**).

Then, the photocurrent–time response of the semiconductor electrode was evaluated by chronoamperometry under a constant potential using hand chopped light. The typical output of the experiment, in the case of a proper inert electrolyte, is shown in Fig. 4.24b.

Notably, in all plots the photocurrent value rapidly decreases to zero as soon as the irradiation is switched off, but it does not always come back to a constant value when the light is switched on again, especially in the case of doped titania samples.

In this work, the numerical value of τ is extracted by at least three transient peaks (from 700 to 1550 s after switching the lamp on), and an average value is given for each sample. The choice of the same transients for quantitative elaborations allows to make a reasonable comparison among all samples. In the literature, no clear details on the data point used to extract the transient time constants are provided. Dholam *et al.*[117] adopted transient time constants from chronoamperometric measurements on the time scale of tens/hundred of seconds to exploit the recombination behavior of multilayer Cr-doped TiO_2.

However, in the normalized plot of current–time dependence, the choice of the time range for quantitative extrapolation is not straightforward and varied for different samples. Moreover, it has been found that some authors

compare the photocurrent absolute intensity of different systems without taking into account every intrinsic or experimental differences that lie in the home-made semiconductor electrodes: Zhang *et al.*[23] showed the photocurrent transient generated under chopped UV irradiation for ZnO nanowires, multiwalled carbon nanotubes (MWCNTs), and a composite system in which the nanowires were adhesively grown on the MWCNTs; they commented on the very weak photoresponse of the MWCNTs and made comparison on the numerical values obtained for each device though the thickness of each deposited system was not the same.

The linear behavior observed for all the tested materials indicates that the decay mechanism is only due to surface recombination leading to a first-order kinetics in electron surface concentration, as found by Dholam *et al.*[117] for Cr-TiO_2 and asserted by Tafalla and coauthors.[127]

All measurements have been carried out in nitrogen atmosphere allowing the achievement of more reproducible data. Thus, the cell was deareated avoiding the presence of oxygen which plays the role of electron acceptor. Byrne *et al.*[76] also reported that when oxygen is present in the anode compartment, the photocurrent response is smaller than when oxygen is absent from both compartments or present only in the cathodic one. Moreover, the quenching of anodic photocurrent, due to the presence of oxygen in the anode, is said to occur even at positive potentials up to 1.0 V, as previously observed also by Rensmo *et al.* and Hagfeldt *et al.*[122,128] They hypothesized that since the conduction band electrons at the surface of a relatively thick TiO_2 film have a finite distance to travel before reaching the substrate, adsorbed oxygen actively scavenges such electrons from the oxide surface preventing them from reaching the substrate and a reduction in the anodic current is observed. Since semiconductor particles in a nanostructured film are surrounded by electrolyte and photoelectrons may be trapped by an electron acceptor in the electrolyte during the time they need to reach the back contact, the probability of such process would grow as the distance from the substrate increases. Therefore, the thickness of the films has been kept nearly constant (about 1–2 μm, measured by DekTak 150 step-profilometer) by depositing the same amount of TiO_2 suspension (8 layers).

Film thickness is a tricky parameter to vary; this is the reason why, in this context, no dependence studies on the film thickness have been done, while a certain thickness has been kept constant for a proper comparison among

different samples. Below a certain thickness the photocurrent usually decreases drastically.[129] On the other hand, Dholam *et al.*[117] affirmed that the reduced thickness of their Cr-doped TiO_2 film, deposited on ITO, significantly contributed to reduce the charge recombination rates. This occurs because the generated photoelectrons, traveling into TiO_2 film of limited thickness, rapidly enter the space charge interface of the ITO- TiO_2 films from where they are instantaneously injected into the ITO layer and then removed towards the cathode of the photo-electrochemical cell. Then again, when their multilayer film was exposed to visible light, they observed an increase of the photocurrent as a function of the number of bilayers. The enhanced photocurrent was attributed to both higher absorption of visible light by Cr-doped- TiO_2 and to the number of space charge ITO/ TiO_2 interfaces in multilayer films.

Open circuit potential

The open circuit potential (OCP) is a mixed potential of all the redox potentials in the solution, at the surface and at the interface, and it is related to changes of the surface of the electrode. A drop down to much more negative values upon illumination found for most of the analyzed samples can be regarded as a result of the sudden generation of electron-hole pairs. After some seconds under irradiation, a steady state between generation and depletion of photogenerated charge carriers is reached. If a hole scavenger, such as chloride or oxalate ion, is present, OCP values recorded upon illumination shift to even lower values as the concentration of the hole scavenger increases, due to consumption of holes and the accumulation of negative charged electrons on the electrode.[74,130] This statement was confirmed comparing the result obtained when using an inert electrolyte containing a low concentration of oxalate, to that recorded with NaOH as the sole electrolyte. OPC, thererefore, can be regarded as an overall index of the electronic situation in the electrochemical cell. Beside a preliminary investigation of the different values obtained with different experimental parameters, the OCP was recorded before starting a new measurement to ensure the absence of any possible alteration of the cell atmosphere during the measurements, *e.g.*, the presence of oxygen.

The role of electrolyte type and concentration

Photogenerated electrons and holes are quickly trapped at surface states in nanocrystalline TiO_2 films;[75] in this way they can participate independently in surface reduction and oxidation processes, respectively, involving redox-active species in solution.

The response of the electrode in the presence of different electrolytes (see the above experimental section) has been deeply analyzed with the aim of comparing the most used systems in the literature.

Acidic conditions were avoided on the grounds of literature evidences.[131,132] Chuang *et al.* reported that even though a slightly higher photocurrent was observed in the acidic electrolyte (0.1 M HNO_3) due to the fact that the mobility of H^+ ions was much higher than that of OH^- ions, under irradiation of both UV and visible light in 0.1 M HNO_3, the utilization of doped TiO_2 nanoparticle thin films as a photoelectrodes became unsuitable.[131] Wang *et al*. in their study on a commercial titania sample found out that the charge decreases with the proton concentration in the solution.[132]

Chloride and idroxide anions

Chloride ion may be adsorbed on the positively charged photoanode, where it might be oxidized by the photogenerated holes.[130,133]

$$TiO_2–Cl_{ads} + Cl^- \rightarrow Cl_2 + TiO_2 + e^- \quad \text{(eq. 5.0)}$$

This process has been investigated for its great economical and technological interest: chlorine is widely used in many kinds of commercial applications, ranging from industry to the disinfection of drinking water, and Zanoni *et al.*[133] have proposed the use of titania electrodes biased at +1.0 V (SCE) - a voltage selected to increase electron-hole lifetime - and upon UV illumination to reduce costs of chlorine production and decrease undesired products generated from side reactions.

Charge carrier recombination can be strongly affected by the concentration of chloride ion: at concentration below 0.1 M.[130] chloride ions might reach the electrode surface controlled by mass transfer and electron-hole pairs might recombine preferentially, while at higher chloride concentration it is likely that adsorption effects predominate, avoiding recombination. In this situation, the photocurrent was probably limited by the electrode-solution interfacial

reaction and by the photogenerated hole capture process. In the same paper, the behaviour in $NaNO_3$ solution was also investigated (see the comparison in Fig. 4.25): nitrate might absorb the UV photons, which results in the decrease of light intensity on the electrode. Therefore, this setup was not considered in the present research.

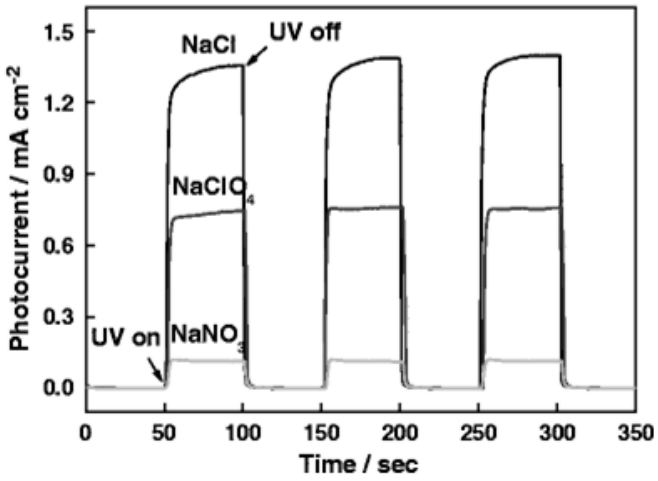

Figure 4.25. Photocurrent response upon UV irradiation in 0.25 M NaCl, $NaClO_4$ and $NaNO_3$ solutions at applied potential equal to 0.5 V (SCE); taken from ref [130].

One of the first attempts to increase the photocurrent intensity in this research was carried out by the means of an electrolyte containing chloride; however, it is possible to observe that no photocurrent decay is noticeable and a final rise without a satisfactory steady-state photocurrent appears in the transient obtained with NaCl (Fig. 4.25), as also reported by Xiao *et al.*[130] in the case of TiO_2/Ti nanotube electrodes, even if the type of lamp used was a different one. In other words, the anodic photocurrent spike is not sharp and almost equal to the stable photocurrent, and, at the same time, recombination is not responsible for this, since a steeper decay is obtained with the same sample but different electrolyte. The reason of this unsatisfactory behavior might be found in the strong interaction between the electrolyte and the semiconductor film, as outlined above. Such situation does not seem promising for the aim of exploring the nature of electron transport in semiconductor films.

It has to be noted that, in the literature case reported in Fig. 4.25, also photocurrent transients recorded in $NaClO_4$ do not show a significant decay but that could be due either to no substantial recombination of the analyzed system or to experimental conditions not properly suited to enhance the intrinsic recombination decay of the semiconductor oxide.
Fig. 4.26 displays the chronoamperometric tests registered when the home-made titania electrode is in contact with either NaCl or NaOH.

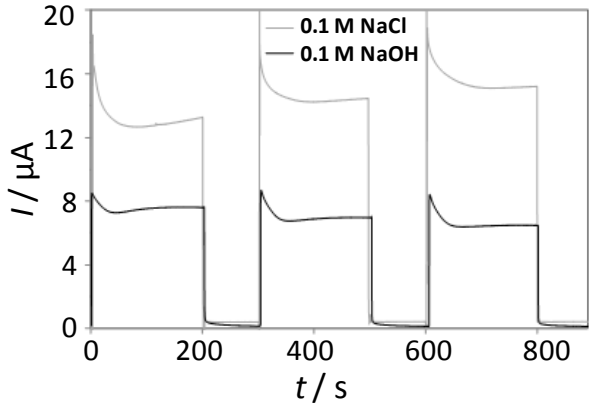

Figure 4.26. Selected examples of photocurrent responses obtained for undoped titania spin coated electrodes in 0.5 M NaCl, 1.0 V (SCE) (grey line) and 0.1 M NaOH, 0.4 V (SCE) (black line) recorded up on UV-visible illumination.

It is possible to observe that a minor photocurrent decay is noticeable in the latter case and a final rise without a satisfactory steady-state photocurrent appears in the transient obtained with NaCl, as also reported by Xiao *et al.* in the case of TiO_2/Ti nanotube electrodes.[130] As a hole acceptor, chloride ions can lead to deviations in transient shapes due to modification of the photoanode surface according to the following adsorption phenomena:[130]

$$TiO_2–h^+ + Cl^- \rightarrow TiO_2–Cl_{ads} \quad \text{(eq. 5.1)}$$

Moreover, because of this ability in scavenging holes, chloride ions may promote the separation of electron-hole pairs. Then, at chloride concentrations lower than 0.1 M, the electron/hole pairs generated at a steady-state rate can recombine preferentially since chloride ions are weakly adsorbed onto the semiconductor electrode. However, at higher concentrations of chloride, it is likely that the adsorption effect would

predominate, avoiding charge recombination, as Zanoni *et al.* suggested.[133] In our work, this fact results in transients with the same order of photocurrent values as those obtained with other electrolytes and a disadvantageous profile of the photocurrent decay.
Thus, on the basis of the present results, 0.1 M $NaClO_4$ is chosen as the best inert electrolyte.

Oxalate as hole acceptor
In the literature the experimental set-up is sometimes more complex than that presented in this work and it is quite common to use a hole acceptor other than the bare electrolyte.
Methanol, oxalate, chloride and iodide ions are probably the most used chemicals to enhance the photocurrent response. In the case of iodide, as for instance, Beranek and Kisch demonstrated that recombination can be suppressed: the reacting holes can escape recombination more easily since the oxidation of iodide (E_0 = 1.3 V) is thermodynamically more favorable than water oxidation (E_0 = 2.0 V). This suggests that, in absence of iodide, the photogenerated holes preferentially undergo fast relaxation to deep surface states and to a lesser extent oxidize water.[20]
Among all possible hole scavengers, oxalate can be considered a good candidate because its electrochemical oxidation occurs via an irreversible process involving two electrons, without the production of intermediate species and yielding carbon dioxide as the only product, as established on a pyrolitic graphite electrode.[76]
A great increase in the photocurrent intensity is expected, due to a phenomenon known as current doubling generated in presence of oxalate and other organic species.[76]

$$^{-}OOC–COO^{-} + h^{+} \rightarrow COO^{-} + CO_2 \rightarrow 2CO_2 + e^{-} \quad \text{(eq. 5.2)}$$

Such mechanism is said to further increase by the use of a porous electrode. This results in a high surface area available and enables a significant oxalate adsorption, that decreases recombination rates.[115]
In particular, prior to illumination, due to strong adsorption, oxalate ions penetrate the whole TiO_2 particulate layer. When irradiation starts, adsorbed oxalate ions are oxidized rapidly by holes at the porous TiO_2/solution interface

and photogenerated electrons diffuse through the layer to the contact, producing the high initial anodic spike. After that, the transient shape seems to depend on the concentration of oxalate:[115] at a concentration around 5×10^{-2} M, oxalate ions are quickly replaced by pore diffusion, and, consequently, the photocurrent does not decay. At lower bulk concentrations, instead, the oxalate concentration in the electrolyte within the film is depleted, leaving oxalate–depleted regions with a high concentration of surface trapped holes which can recombine with electrons hindering them to reach the contact, hence resulting in the photocurrent decay with time. Therefore, very different behaviors are expected at variance with the concentration of oxalate, as shown by both Byrne *et al.* and Krysa *et al.*[115,134] (Fig. 4.27). As a final result, the signal depends on a balance between adsorption assisted by the positive potential applied, and photocatalytic removal (thus depletion in the surroundings of titania nanoparticles) upon irradiation.

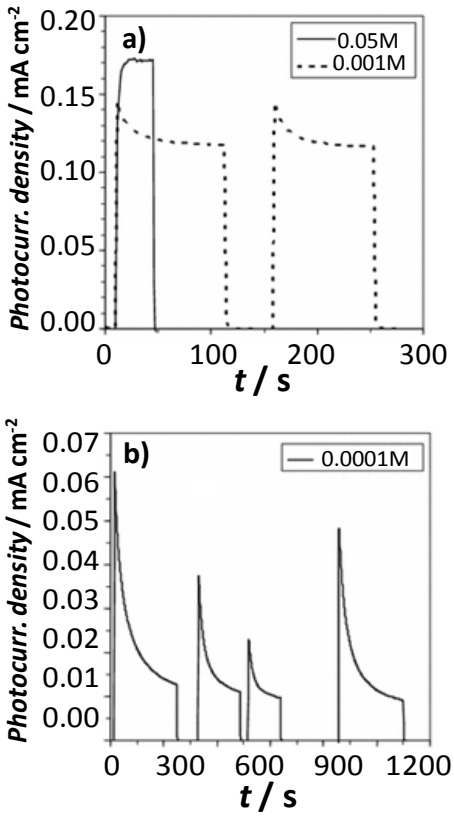

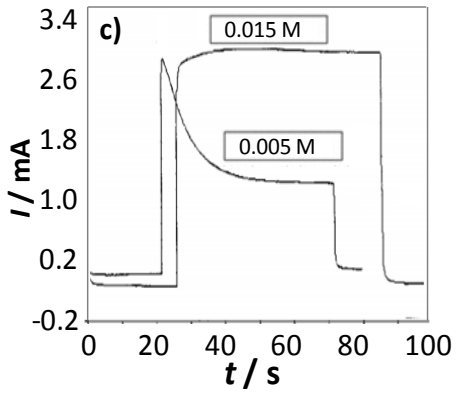

Figure 4.27. Photocurrent density *vs* time behaviour of Evonik P25 film at 0.8 V (SCE) for oxalic acid concentrations 5×10^{-2}, 10^{-3} M (a), and 10^{-4} M (b); adapted from ref [115]. *Idem* for panel (c), with two different concentrations of oxalate (5×10^{-3}, 5×10^{-3}) and TiO_2 anode biased at 800 mV; adapted from ref [134]).

Adding a low concentration of oxalate (10^{-3} M) to the inert electrolyte used in the present work ($NaClO_4$ 0.1 M) yielded, as expected, a larger photocurrent intensity as compared to the system with the inert electrolyte alone (see Fig. 4.28). When using this setup and tailored light-dark periods[115] necessary to maintain a steady concentration of oxalate in the surrounding of the electrode, a satisfactory transient behavior was found for the undoped sample. However, notwithstanding the enhanced photocurrent density, the adopted dark-light periods which differ from previous analyses in the presence of a different electrolyte composition might lead to deviations in transient shapes (as expected, considering how dark-light periods affect the local concentration of oxalate).

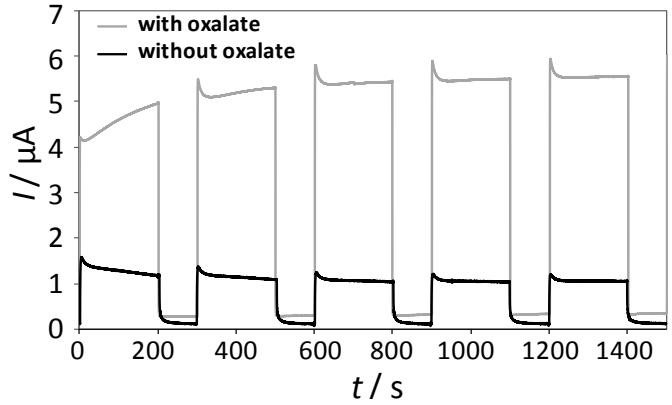

Figure 4.28. Photocurrent transients recorded for the undoped oxide (sample T) with or without a hole acceptor (oxalate) using aqueous 0.1 M $NaClO_4$ as electrolyte.

Overall, dark-light periods in presence of oxalate seem to affect the final response: the shape of the photocurrent decay does not present a constant behavior in all the transients used for the quantification of the time constant, thus not allowing a reliable elaboration of the data.

Compared with compact polycrystalline and single-crystal electrodes, porous nanocrystalline TiO_2 films considerably have a stronger dependence of their photoelectrochemical properties on the presence of electron and hole acceptors in solution.[75] Indeed, an efficient hole acceptor in the solution is able to minimize direct electron-hole recombination in the film,[3,135] thus altering the intrinsic behavior - tendency to recombination - of the analyzed semiconductor.

Poznyak *et al.*[75] also found some difficulties in explaining the influence of the hole acceptors taking into consideration only the increase in the efficiency of the removal of the photogenerated holes and stated that the dissolved substances hinder photoanodic oxygen formation on the electrode surface, thereby sharply reducing the effect of recombination via photoelectrochemical reaction products which is essentially characteristic of nanostructured electrodes.

The depletion of the photocurrent signal is inversely proportional to the concentration of oxidizable species, but for film thicknesses in the range of 1-2 μm or above, this effect is superimposed by the relatively slow response to irradiation.[74] This photocurrent depletion has been postulated[76] as being due to a depletion of the Helmholtz layer in oxalate after an initial current spike; therefore, the oxidation of water and the electron-hole recombination become more probable, thus decreasing the probability of electrons reaching the back contact.

Moreover, considering the different oxalate adsorption phenomena on the oxides samples depending on the specific surface areas (chapter 3), comparison among the samples has been performed in the absence of oxalate in solution, since those factors affect the evaluation of the intrinsic charge recombination properties of each sample.

Role of the illumination source

Fig. 4.29a compares the photocurrent recorded on T sample under UV or visible irradiation. The higher photocurrent obtained when using UV light could be attributed to extra photogenerated charge carriers at the

semiconductor/electrolyte interface, which would even result in the increase of the electric field produced in the depletion layer in case of bigger semiconductor particles. Moreover, in the case of UV irradiation the photocurrent decay is steeper, probably due to the fact that the electronic levels involved are different from those populated by visible light excitation. However, the trend of the transient time constants obtained for a set of samples is maintained when using the two types of irradiation sources. It has to be noted that the so called "visible light" is produced by a lamp presenting a spectrum that shows a residual emission in the UV-A region (see Fig. 4.29b) and extends until the IR region – however, this radiation emission is cut whenever working with a thermostatted reactor which is surrounded by circulating water.

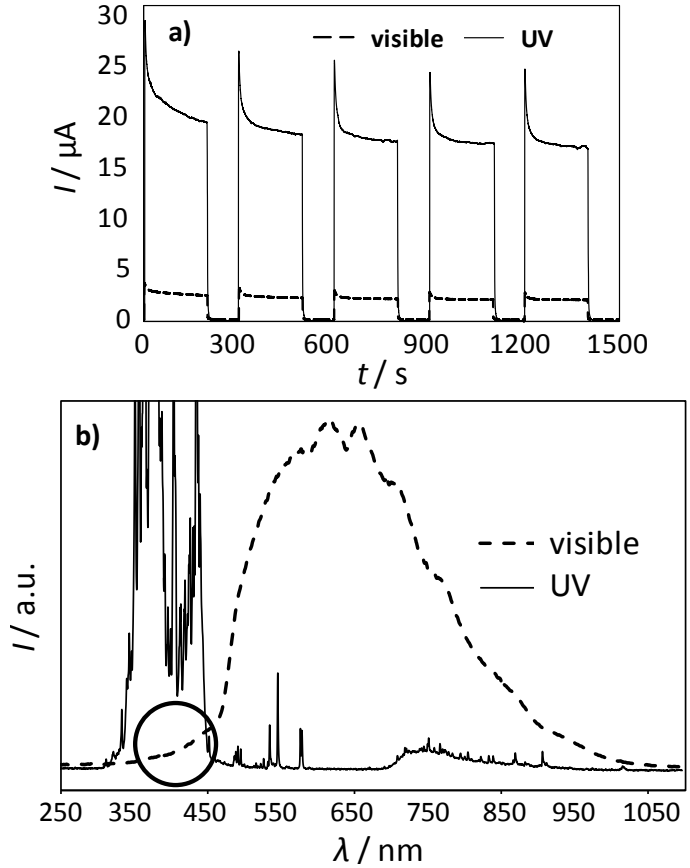

Figure 4.29. Example of photocurrent transients recorded under UV or visible light (a); emission spectra of the two lamps employed during electrochemical measurements (b).

4.7. Home-made undoped and doped-TiO_2

In order to properly characterize doped TiO_2 samples which exhibit a marked absorption in the visible region (as discussed in chapter 3), possibly due to intra-gap states leading to a shrinking of the apparent bandgap, visible light photocurrent measurements have been recorded. Recalling some distinctive features of doped titania samples already exposed in the previous chapter, while Pr-TiO_2 samples show lower surface areas and pore volumes than N-TiO_2 ones, both dopants lead to titania with similar phase composition (anatase as main poly-morph and brookite as the secondary one). The crystallite size is only slightly higher for T_Pr. Note that, in this context, N-doped and Pr-doped TiO_2 are labeled T_N and T_Pr, respectively. The effect of doping on charge carriers' recombination can be considered twofold: it is said to be detrimental due to the introduction of sites in the lattice — or electronic levels in the bandgap — that accelerate the rate of electron–hole recombination, or positive, owing to the creation of sites which can selectively trap charge carriers. As a final balance, it depends on the position of electronic levels introduced by doping in the bandgap, on the amount of doping, on the photocatalytic reaction, and on several other factors involved in it.[119,132]

Whenever keeping the same parameters used to elaborate data relative to the undoped sample also to analyze doped ones, some difficulties arose concerning unsatisfactory steady photocurrent and enhanced noise. This fact could be ascribed to the different specific surface areas of the photoanode (which affect the kinetics of oxalate oxidation on the electrode) or to the polydispersity and heterogeneity of the doped powder.

By analyzing each photocurrent transient (Fig. 4.30a), a less steep decay is obtained for our N-doped and Pr-doped samples. As derived by the normalized plot of current–time dependence (Fig. 4.30b), both doped oxides show a higher τ, thus a slower recombination rate, than the undoped one: values of (10.1 ± 0.2) s, (22.8 ± 0.1) s, and (22.0 ± 0.5) s are obtained for T, T_N, and T_Pr, respectively. It should be noted that the standard deviations reported here are lower than those presented in the following for the series of Pr-TiO_2 samples. Also the τ value of the undoped samples is slightly different in the two cases, even though the trends and the conclusions are unaltered.

These two observations are the consequence of a higher level of precision reached in the final measurements (data reported here above) after several experiments.

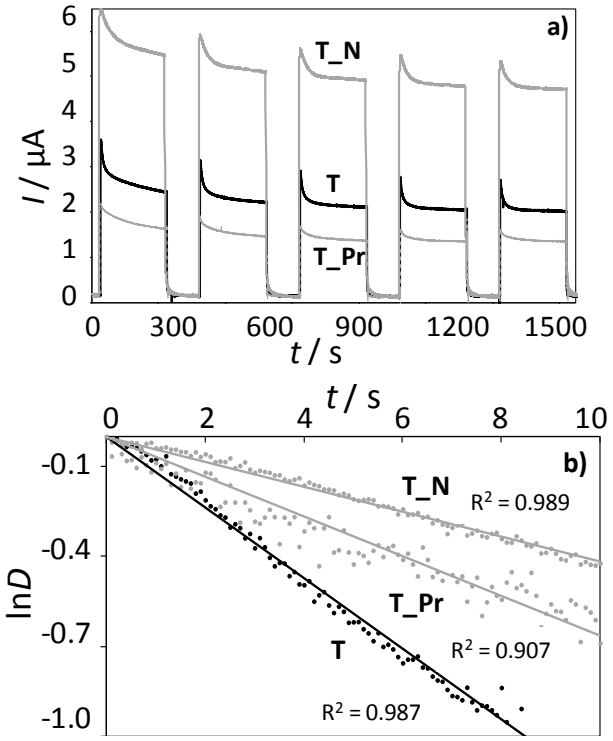

Figure 4.30. Comparison of photocurrent transients for doped and undoped titania samples (a); normalized plot of current-time dependence for the same samples (b).

By performing time–resolved laser flash photolysis on colloidal aqueous TiO_2 suspensions, Bahnemann *et al.*[103] showed that deeply trapped holes (*i.e.*, surface–bound hydroxyl radicals) are rather long-lived and unreactive, while shallowly trapped holes are in a thermally activated equilibrium with free holes and exhibit a very high oxidation potential. Further, according to Grabtchak *et al.*,[136] much of the information on the form of the density of states over an energy range of up to 0.5 eV depth is contained in the detailed form of the initial decay of the photocurrent on a timescale $<10^{-10}$ s in which only the shallowest traps are expected to have an effect. Our time scale is definitely larger so that all types of electrons/holes traps can be active.

Liu and coworkers noticed a distinctly different photocurrent response from undoped and nitrogen doped mesoporous TiO_2,[125] as reported in Fig. 4.31. The far slower photocurrent increase rate upon light irradiation and decay rate in dark of N-TiO_2 than those of undoped TiO_2, consistent with the more abundant surface states in the former, suggested that the abundant surface states play a vital role in trapping carriers and prolonging the lifetime of carriers. Due to the nature of localized surface states, the mobility of trapped carriers in the surface states can be greatly hindered.[137] Therefore, the transfer and diffusion of carriers and hence the photocurrent must be significantly retarded due to the trapping. This is because when carriers are trapped in the surface states, electrons and holes are localized so that the spatial overlap of the charge carriers is reduced to retard their recombination.[137]

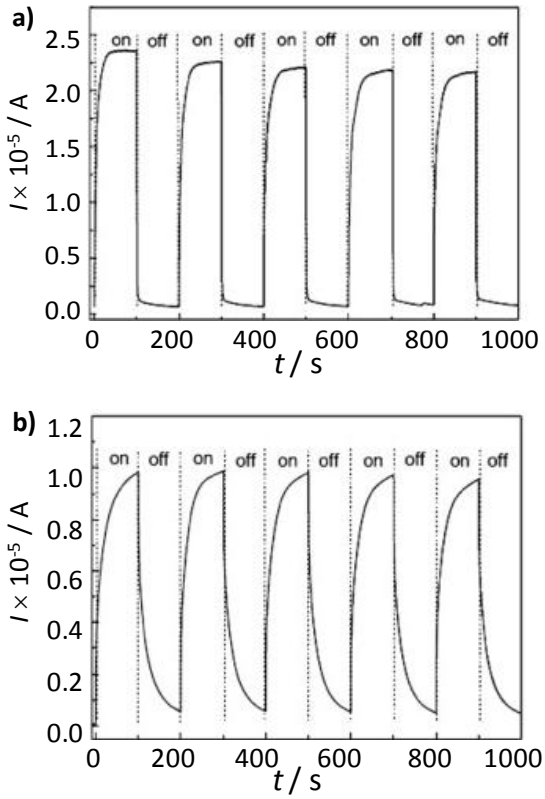

Figure 4.31. Photocurrent *vs* time profiles of undoped (**a**) and nitrogen doped (**b**) TiO_2 thin films under UV–Vis irradiation (0.1 M Na_2SO_4 electrolyte at 0.3 V *vs* SCE and illumination intensity of around 100 mW cm^{-2}).[125]

As evidenced by both PL spectra and photocurrent response, the prolonged lifetime of trapped carriers in abundant surface states could be as the main reason for an enhanced UV-vis photocatalytic activity of N- TiO_2.

An unusual study about multilayer films with different numbers of ITO/Cr-doped-TiO_2 layers to lower the charge recombination rate is presented by Dholam *et al.*[117] The ITO/TiO_2 stack film is able to partially limit the recombination of photo-generated electrons and holes because the conduction band edge of ITO (located at about - 4.5 eV) is at an energy value lower than that of TiO_2 (about - 4.0 eV) thus making favorable for the electrons injection from the later into the former. Thickness of doped-TiO_2 layer (125 nm) in each bilayer may be lower than the total thickness of the space charge layer of the pertinent interface. Thus photoelectrons generated are already in space charge region where the electric field provides them the driving force to instantaneously inject into the ITO layers. When semiconductors having different energy bands are brought in contact with each other, a band bending occurs near the interface to make Fermi level equal on both sides. This band bending generates an interface space charge layer, having thickness of several tens of nanometer, where a large electric field is developed. When photoelectrons are generated in this interface region (or very near) they are instantaneously pushed out to the adjacent semiconductor due to the driving force provided by the electric field and the electron-hole separation is definitely obtained, a process well known in pen semiconductor junctions. In the above mentioned ITO/TiO_2 system, the interface region presents electrical features that are similar to p-n junction thus providing an efficient route for the electron-hole separation. Hence by adopting a multilayer structure, Dholam and coworkers were able to produce many interfaces of ITO/TiO_2 which establish fast transport channels along with efficient electron-hole separation.

4.7.1. N doping

Preliminary conclusions on the effect of N doping on the recombination of photogenerated charge carriers has been already exposed in the previous paragraph. Hereafter, a trend of τ of all triethylamine doped samples at increasing the initial N amount is reported (Fig. 4.32). The reliability of the

computed transient time constants seems to be affected by the type of the nanopowder: even though the same experimental setup and sample pretreatment have been adopted for the series of N-doped titania, the standard deviations differ quite much (see Fig. 4.32). This is not surprising considering the fact that doping induces relevant modification in nanoparticle size and surface area (see characterizations' results reported in chapter 3). Trends observed in charge recombination rate, as directly connected with the electronic structure of the material, can give an insight into the nature and location of nitrogen dopant ions, also investigated by DFT calculations and structural investigations (XRP and EXAFS analyses). According to previous results (reported in chapter 3), the interstitial or substitutional location of the nitrogen introduces different electronic levels. However, in the former case, these intragap levels brought in by the dopant act as efficient recombination centers. As it was assessed that the nitrogen interstitial location is present over a certain initial N/Ti molar ratio, the experimentally found decrease of τ, thus a higher charge carriers' recombination rate, perfectly match with the first conclusions. Then, the presence of oxygen vacancies must be seriously taken into account. Indeed, comparisons with theoretical calculations allowed to assert that vacancies are more numerous than N doping centers in the present samples. In conclusion, the effects of N-doping sites may be manifold, as they act not only as electron scavengers, but also as stabilizers of the color centers.

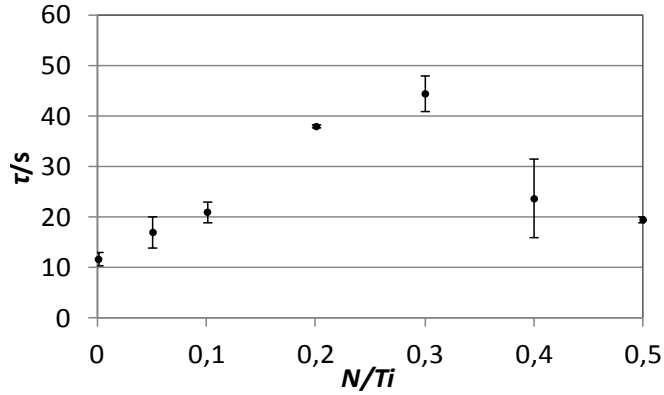

Figure 4.32. Dependence of the transient time constant (average on two or more samples for the same type of nanopowder) on the initial N/Ti molar ratio.

4.7.2. Pr doping

To the best of the author's knowledge, no photoelectrochemical properties of the Pr-doped materials are reported in literature, although they are of basic importance when studying photocatalysis. Thus, charge recombination was studied by photocurrent kinetics curves[117] also for the series of Pr-doped titania samples with different Pr amount.

The shape of the curves of the different samples is comparable except for the absolute values of the photocurrent maxima, as shown in Fig. 4.33 (sample TPr_0.3 as a representative one). Nevertheless, the decays of the photocurrent within a few seconds are steeper in the case of the undoped oxide, meaning that this sample is more affected by recombination of the photogenerated charges. Surprisingly, such an effect is just the result obtained when incorporating foreign ions into the TiO_2 lattice,[119] given the formation of defects sites. The presence of points defects (such as oxygen vacancies) and their predominance in a specific type of TiO_2 sample could not be *a priori* supported. Fig. 4.33b shows a comparison between sample T (undoped titania) and TPr_0.3 as for ln*D vs* time plot. The linear behavior[117,127] indicates that the decay mechanism should be only due to surface recombination, leading to a first-order kinetics in electrons surface concentration; the same functional behavior seems to occur for all the samples tested, though it is more evident in the case of the undoped one. The transient time constants reported in Table 4.5, for the Pr-doped samples are greater (18-25 s) than both that of the undoped sample (15 s) and most of those observed for compact single–crystal or polycrystalline titania electrodes in the literature.[117,138]

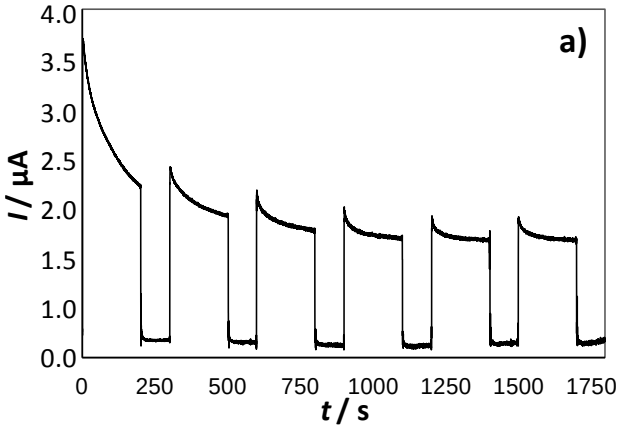

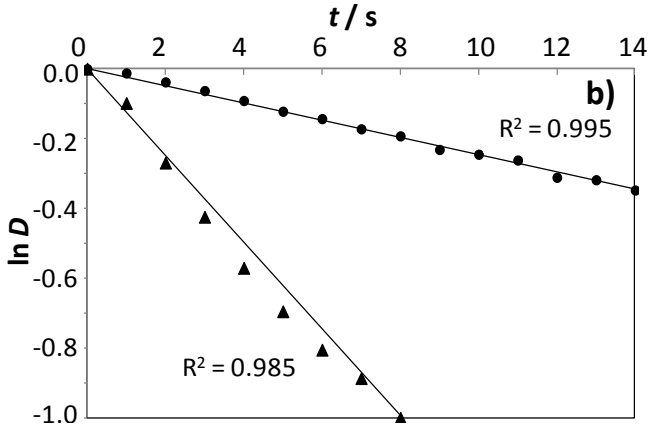

Figure 4.33. (a) Photocurrent transient curve for a selected sample (TPr_0.3). (b) Normalized plot of current-time dependence for the same doped sample (circles) compared to the undoped one (triangles).

Sample	τ / s
T	15
TPr_0.2	18
TPr_0.3	25
TPr_0.5	21
TPr_0.7	19

Table 4.5. Transient time constants (photocurrent measurements) for Pr-doped TiO_2. The standard deviation is 2 s for all samples.

About this issue, it must be said that the shape of the photocurrent transients and the time constants themselves could be strongly affected by several parameters such as the concentration of the electrolyte, the presence of a certain hole acceptor, the light-dark cycles duration, and so on[76,115] (see above). They all play an important role on the local concentration of electrons/holes acceptors. However, this dependence is not problematic since the main interest lies in the comparison among a series of samples, keeping constant all experimental parameters.

Eventually, the chronoamperometric measurements suggest that the Pr-doped titania can either favor charge separation or suppress recombination processes or give both such effects. In this respect, they could be considered promising materials for photocatalytic remediation.

Pr doping benefits and Pr location

From the optical experimental results it was found that Pr doping significantly modifies the DR spectra of the final material in the visible region (see Fig. 3.33) and improve electron-hole separation, increasing the estimated τ (see Tab. 4.5). These two experimental findings not only witness TiO_2 doping has occurred, but also prove that the final materials definitely got some benefit from the presence of praseodymium.

However, the reason of this enhancement was initially not clear and a debate could be opened on several factors, such as the chemical nature of the doping centers, their role on the band structure modifications of the solid and, consequently, the mechanism of photoactivation.

Only after the electrochemical and structural measurements performed in this work, complemented by periodic DFT calculations, it was possible to have a complete understanding of photoelectrochemical features and performances.

Specifically, by comparing DFT and DRS results, it can be asserted that Pr atoms are hosted in a Ti substitutional fashion within the present samples. In this case, the visible light absorption enhancement is due to electronic transitions from valence band states or shallow d Pr orbitals to the f Pr empty orbitals just below the conduction band (see Fig. 4.12, left-handed panel, U >3 eV).

From a purely structural perspective, also theoretical calculations suggest that the dopant ions introduced into the TiO_2 lattice could be mainly located as substitutional for titanium, since no major structural effects are obtained by substitutional doping versus the interstitial one, in agreement with the XRPD analysis. Moreover, Pr could be considered randomly present in both anatase and brookite TiO_2 polymorphs and its manifest effect also lies in a progressive increase of the average lattice distortion.

Since the generated mid-gap levels are finally 4f states, and their location is quite close to the conduction band, the above mentioned electron transitions could easily happen, causing the absorption peaks in the visible region detected by the optical measurements of diffuse reflectance.

On the contrary, it has been computationally found that the presence of localized mid-gap states is much more prominent in the Pr interstitial case. Such levels can promote the recombination processes of the photogenerated charge carriers; thus, the interstitial Pr arrangement is not consistent with the

estimated τ increase with respect to the dopant amount found by photocurrent measurements.
Since also in the case of substitutional Pr there are new electronic levels present in the bandgap, morphological aspects of the home-made samples have to be considered as well. Accordingly, at increasing the dopant amount, the specific surface areas of the powders gradually decreased. This means that less accessible surface and a smaller amount of morphological defects, acting as possible charge carrier traps, exist in the doped samples. Also the τ estimates are found to be higher, therefore suggesting a lower importance of the recombination processes.

4.7.3. Ag doping

When considering home-made Ag-doped titania, namely doped samples other than N- and Pr-TiO_2, the selected applied potential of +1.0 V *vs* SCE was not the proper condition to record the photocurrent without affecting the sample features. On this topic, Chuang and coworkers[131] stated that, to avoid the oxidation of Ag cores to Ag^+ ions when recording photocurrent measurements, the bias was applied mainly in the range of negative potential.

Here a negative potential was avoided not to reach the flatband potential, otherwise conditions would have been different. According to the Pourbaix diagram, known as a potential/pH diagram which maps out possible stable (equilibrium) phases of an aqueous electrochemical system, different potentials in the range 0.2-0.4 V (SCE) – besides +1.0 V, which is the potential chosen for all other reported samples – were tested to record photocurrent. However, it was not easy to find a proper compromise between a sufficiently high potential to obtain a decent signal (low noise) without reaching values forbidden by the Pourbaix diagram. Additionally, it was challenging to analyze Ag-doped samples because of the nominal/actual oxidation state of silver itself: chemically reduced samples should contain only Ag(0) species, while the samples which have not undergone the reductive step may present allegedly Ag^+ ions. This should allow photocurrent measurements to be recorded at higher potentials, back to values comparable to the one selected for all other tests (+1 V *vs* SCE). The Ag-doped sample with the lower Ag amount (Ag/Ti molar ratio = 1 %) shows a transient time constant of (18 ± 3) s, while for the corresponding reduced sample a value only slightly higher with a larger

standard deviation was obtained, namely (19 ± 9) s. This latter value definitely cannot be considered indicative of the sample recombination processes due to the very large standard deviation. In the case of TAg_0.05 (Ag/Ti molar ratio = 5 %), there is a larger gap between the reduced samples and the "not reduced" one: a τ of (11 ± 5) s was found for the former, whereas (44 ± 10) s was obtained for the latter. Again standard deviations are excessively large, but denote a different trend, that is a more marked divergence passing from the bare Ag-TiO_2 to the chemically reduced sample.

Examples of photocurrent measurements on titania samples containing Ag species are totally absent in the literature. The only case of a multi-exponential dynamic model employed to described the photocurrent decay is that of "2D-ordered dome films" of nano-titania, both undoped (2D-TiO_2) and doped with Ag^{2+} (2D-Ag-TiO_2), prepared by RF magnetron sputtering by Jin and coworkers.[126] It should be noted that the system is pretty different here: experiments are performed with titania films sensitized by a dye. Two components are identified for the 2D-TiO_2 film, involving recombination of electrons with the cationic dye radicals, from either TiO_2 conduction band or level associated with oxygen vacancies. When doping with silver ions, a new longest lifetime component appears, owing to electrons trapped by new bands composed of Ag 4d and Ti 3d orbitals in the bandgap.[139]

4.8. References

1. A. J. Bard, L. R. Faulkner, Electrochemical Methods. John Wiley & Sons, New York, **1980**.
2. M. Grätzel *Nature* 414 (**2001**) 338-344.
3. F. Cao, G. Oskam, P. C. Searson *J. Phys. Chem*. 100 (**1996**) 17021.
4. S. Sodergren, A. Hagfeldt, J. Olsson, S. E. Lindquist *J. Phys. Chem*. 98 (**1994**) 5552.
5. A. L. Linsebigler, G. Lu, J. T. Yates *Chem. Rev*. 95 (**1995**) 735.
6. F. Clifton, Lecture notes: Compound Semiconductor Devices. Massachusets Institute of Technology, **2003**.
7. A. Kongkanand and P. V. Kamat *ACS NANO* 1 (**2007**) 13.
8. M. D. Ward, J. R. White, A. J. Bard *J. Am. Chem. Soc*. 105 (**1983**) 27.
9. J. R. White, A. J. Bard *J. Phys. Chem.* 89 (**1985**) 1947.
10. A. M. Roy, G. C. De, N. Sasmal, S. S. Bhattacharyya *Int. J. Hydrogen Energy* 20 (**1995**) 627.
11. D. Duonghung, J. Ramsden, M. Grätzel *J. Am. Chem. Soc.* 104 (**1982**) 2977.
12. R. Memming *J. Electrochem. Soc*. 116 (**1969**) 785.
13. J. M. Bolts, M. S. Wrighton *J. Phys. Chem*. 80 (**1976**) 2641.
14. F. Fabregat-Santiago, G. Garcia-Belmonte, J. Bisquert, P. Bogdanoff, A. Zaban *J. Electrochem. Soc.* 150 (**2003**) E293.
15. C. Baumanis and D. W. Bahnemann *J. Phys. Chem. C* 112 (**2008**) 19097.
16. S. F. Pond *Surf. Sci.* 37 (**1973**) 596.
17. G. Boschloo, A. Goossens, J. Schoonman *J. Electrochem. Soc*. 144 (**1997**) 1311.
18. G. Boschloo and D. Fitzmaurice *J. Phys. Chem. B* 103 (**1999**) 2228.
19. G. Rothenberger, D. Fitzmaurice, M. Grätzel *J. Phys. Chem*. 96 (**1992**) 5983.
20. R. Beranek and H. Kisch *Electrochem. Commun*. 9 (**2007**) 761.
21. Y. V. Pleskov, V. M. Mazin, Y. E. Evstefeeva, V. P. Varnin, I. G. Teremetskaya, V. A. Laptev *Electrochem. Solid-State Lett*. 3 (**2000**) 141.
22. M. Dolata, P. Kedzierzawaski, J. Augustynski *Electrochim. Acta* 41 (**1996**) 1287.
23. W.-D. Zhang, L.-C. Jiang, J.-S. Ye *J. Phys. Chem. C* 113 (**2009**) 16247.
24. J. Bandara and U. W. Pradeep *Thin Solid Films* 517 (**2008**) 952.
25. F. Cardon and W.P. Gomes *J. Phys. D: Appl. Phys*. 11 (**1978**) L63.
26. T. Hirai, I. Tari, T. Ohzuku *Bull. Chem. Soc. Jpn*. 54 (**1981**) 509.

27. F. Spadavecchia, G. Cappelletti, S. Ardizzone, M. Ceotto, L. Falciola *J. Phys. Chem. C* 115 (**2011**) 6381.
28. D. Tafalla and P. Salvador *J. Electroanal. Chem. Interfacial Electrochem*. 270 (**1989**) 285.
29. B. P. Nelson, R. Candal, R. M. Corn, M. A. Anderson *Langmuir* 16 (**2000**) 6094.
30. E. C. Dutoit, R. L. Van Meirhaeghe, F. Cardon, W. P. Gomes, *Ber. Bunsenges. Phys. Chem*. 79 (**1975**) 1206.
31. A. Di Paola *Electrochim. Acta* 34 (**1989**) 203.
32. G. Kresse and J. Hafner *J. Phys. Rev. B* 47 (**1993**) 558.
33. G. Kresse and J. Furthmüller *Phys. Rev. B* 54 (**1996**) 11169.
34. J. P. Perdew, K. Burk, M. Ernzerhof *Phys. Rev. Lett.* 77 (**1996**) 3865.
35. J. P. Perdew and Y. Wang *Phys. Rev. B* 45 (**1992**) 13244.
36. J. Harris *Phys. Rev. B* 31 (**1985**) 1770.
37. W. M. C. Foulkes and T. Haydock *Phys. Rev. B* 39 (**1989**) 12520.
38. B. J. Morgan and G. W. Watson *Surf. Sci.* 601 (**2007**) 5034 .
39. E. Finazzi, C. Di Valentin, G. Pacchioni, A. Selloni *J. Chem. Phys.* 129 (**2008**) 154113.
40. G. Mattioli, F. Filippone, P. Alippi, A. Amore Bonapasta *Phys. Rev. B* 78 (**2008**) 241201.
41. H. Cheng and A. Selloni *J. Chem. Phys*. 131 (**2009**) 0547031.
42. J. K. Burdett, T. Hughbandks, G. J. Miller, J. W. Richardson, J. V. Smith *J. Am. Chem. Soc.* 10 (**1987**) 3639.
43. A. Janotti, J. B. Varley, P. Rinke, N. Umezawa, G. Kresse, C. G. Van de Walle *Phys. Rev. B* 81 (**2010**) 085212.
44. V. I. Anisimov, I. V. Solovyev, M. A. Korotin, M. T. Czyżyk, G. A. Sawatzky *Phys. Rev. B* 48 (**1993**) 16929.
45. S. Kümmel and L. Kronik *Rev. Mod. Phys.* 80 (**2008**) 3.
46. A. D. Becke *J. Chem. Phys.* 98 (**1993**) 1372.
47. M. Cococcioni and S. De Gironcoli *Phys. Rev. B* 71 (**2005**) 035105.
48. A. Vijay, G. Mills, H. Metiu *J. Chem. Phys.* 118 (**2003**) 6536.
49. X. Y. Wu, A. Selloni, S. K. Nayak *J. Chem. Phys*. 120 (**2004**) 4512.
50. M. D. Rasmussen, L. M. Molina, B. Hammer *J. Chem. Phys.* 120 (**2004**) 988.
51. R. Long and N. J. English *Appl. Phys. Lett.* 94 (**2009**) 132102.
52. M. Ramamoorthy, D. Vanderbilt, R. D. King-Smith *Phys. Rev. B* 49 (**1994**) 16721.
53. A. T. Paxton and L. Thiên-Nga *Phys. Rev. B* 57 (**1998**) 1579.
54. J. Stausholm-Moeller, H. H. Kristoffersen, B. Hinnemann, G. K. H. Madsen, B. Hammer *J. Chem. Phys.* 133 (**2010**) 144708/1.
55. M. Batzill, E. H. Morales, U. Diebold *Phys. Rev. Lett.* 96 (**2006**)

026103.
56. M. Batzill, E. H. Morales, U. Diebold *Chem. Phys.* 339 (**2007**) 36.
57. J. Graciani, L. J. Alvarez, J. A. Rodriguez, J. F. Sanz *J. Phys. Chem. C* 112 **2008**) 2624.
58. J. Graciani, A. Nambu, J. Evans, J. A. Rodriguez, J. F. Sanz *J. Am. Chem. Soc.* 130 (**2008**) 12056.
59. T. Ihara, M. Miyoshi, Y. Iriyama, O. Matsumoto, S. Sugihara *Appl. Catal., B* 42 (**2003**) 403.
60. A. V. Emeline, V. N. Kuznetsov, V. K. Rybchuk, N. Serpone *Int. J. Photoenergy* 2008 (**2008**) 1.
61. C. Di Valentin, G. Pacchioni, A. Selloni, S. Livraghi, E. Giamello *J. Phys. Chem. B* 109 (**2005**) 11414.
62. F. Spadavecchia, G. Cappelletti, S. Ardizzone, C. L. Bianchi, S. Cappelli, C. Oliva, P. Scardi, M. Leoni, P. Fermo *Appl. Catal. B: Environ.* 96 (**2010**) 314.
63. A. J. Bard and M. A. Fox *Acc. Chem. Res*. 28 (**1995**) 141.
64. V. N. Parmon *Adv. Hydrogen Energy (Hydrogen Energy Prog.)* 8 (**1990**) 801.
65. A. Wood, M. Giersig, P. Mulvaney *J. Phys. Chem. B* 105 (**2001**) 8810.
66. G. Burgeth and H. Kisch *Coord. Chem. Rev*. 230 (**2002**) 41.
67. M. Jakob, H. Levanon, P. V. Kamat *Nano Lett*. 3 (**2003**) 353.
68. V. Subramanian, E. E. Wolf, P. V. Kamat *J. Phys. Chem. B* 107 (**2003**) 7479.
69. S. Chen and R. Murray *J. Phys. Chem. B* 103 (**1999**) 9996.
70. V. Subramanian, E. E. Wolf, P. V. Kamat *J. Am. Chem. Soc*. 126 (**2004**) 4943.
71. H. Zhang, G. Chen, D. W. Bahnemann *J. Mater. Chem*. 19 (**2009**) 5089.
72. Y. Tamaki, A. Furube, M. Murai, K. Hara, R Katoh, M. Tachiya *Phys. Chem. Chem. Phys.* 9 (**2007**) 1453.
73. Y. Tamaki, A. Furube, M. Murai, K. Hara, R. Katoh, M. Tachiya *Phys. Chem. Chem. Phys.* 9 (**2007**) 1453.
74. G. Waldner, J. Krýsa, J. Jirkovský, G. Grabner *Int. J. Photoen*. 5 (**2003**) 115.
75. S. K. Poznyak, A. I. Kokorin, A. I. Kulak *J. Electroan. Chem*. 442 (**1998**) 99.
76. J. A. Byrne and B. R. Eggins *J. Electroan. Chem*. 457 (**1998**) 61.
77. R. Koenenkamp, R. Henniger, P. J. Hoyer *J. Phys. Chem*. 97 (**1993**) 7328.
78. R. Humphry-Baker and M. Grätzel *J. Phys. Chem*. 98 (**1994**) 952.
79. P. Hoyer and H. Weller *J. Phys. Chem*. 99 (**1995**) 14096.
80. I.A. Shkrob and M.C. Sauer *J. Phys. Chem. B* 108 (**2004**) 12497.

81. A.C. Fisher, L.M. Peter, K.G.U. Wijayantha *J. Phys. Chem. B* 104 (**2000**) 949.
82. W. Guo, L. Wu, Z. Chen, G. Boschloo, A, Hagfeldt, T. Ma *J. Photochem. Photobiol. A: Chem.* 219 (**2011**) 180.
83. S. Nakade, Y. Saito, W. Kubo, T. Kitamura, Y. Wada, S. Yanagida *J. Phys. Chem. B* 107 (**2003**) 8607.
84. S.U.M. Khan and J.O.M. Bockris *J. Phys. Chem*. 88 (**1984**) 2504.
85. K. D. Benkstein, N. Kopidakis, J. Van de Lagemaat, A. J. Frank *J. Phys. Chem. B* 107 (**2003**) 7759.
86. K. Fredin, S. Ruhle, C. Grasso, A. Hagfeldt *Sol. Energy Mater. Sol. Cells* 90 (**2006**) 1915.
87. M. J. Cass, A. B. Walder, D. Martinez, L. M. Peter *J. Phys. Chem. B* 109 (**2005**) 5100.
88. N. Kopidakis, E. A. Schiff, N. G. Park, J. Van de Lagemat, A. J. Frank *J. Phys. Chem*. 104 (**2000**) 3930.
89. L. Dloczik, O. Ileperuma, I. Lauermann, L. Peter, E. Ponomarev, G. Redmond, N. Shaw, I. Uhlendorf *J. Phys. Chem. B* 101 (**1997**) 10281.
90. P. E. De Jongh and D. Vanmaekelbergh *J. Phys. Chem. B* 101 (**1997**) 2716.
91. G. Schlichthörl, N. G. Park, A. J. Frank *J. Phys. Chem. B* 103 (**1999**) 782.
92. A. Solbrand, H. Lindström, H. Rensmo, A. Hagfeldt, S.-E. Lindquist, S. Södergren *J. Phys. Chem. B* 101 (**1997**) 2514.
93. F. Fabregat-Santiago, J. Bisquert, G. Garcia-Belmonte, G. Boschloo, A. Hagfeldt *Sol. Energy Mater. Sol. Cells* 87 (**2005**) 117.
94. Q. Wang, S. Ito, M. Grätzel, F. Fabregat-Santiago, I. Mora-Sero, J. Bisquert, T. Bessho, H. Imai *J. Phys. Chem. B* 110 (**2006**) 25210.
95. B. C. O'Regan, K. Bakker, J. Kroeze, H. Smit, P. Sommeling, J. R. Durrant *J. Phys. Chem. B* 110 (**2006**) 17155.
96. H. Greijer-Agrell, G. Boschloo, A. Hagfeldt *J. Phys. Chem. B* 108 (**2004**) 12388.
97. J. E. Kroeze, T. J. Savenije, J. M. Warman *J. Am. Chem. Soc*. 126 (**2004**) 7608.
98. E. Hendry, M. Koeberg, B. O'Regan, M. Bonn *Nano Lett*. 6 (**2006**) 755.
99. K. Iwata, T. Takaya, H. Hamaguchi, A. Yamakata, T. Ishibashi, H. Onishi, H. Kuroda *J. Phys. Chem. B* 108 (**2004**) 20233.
100. Y. Tamaki, A. Furube, R. Katoh, M. Murai, K. Hara, H. Arakawa, M. Tachiya *C. R. Chim*. 9 (**2006**) 268.
101. D. Bahnemann *Solar Energy* 77 (**2004**) 445.
102. G. Boschloo and D. Fitzmaurice *J. Phys. Chem. B* 103 (**1999**) 7860.
103. D. W. Bahnemann, M. Hilgendorff, R. Memming *J. Phys. Chem. B* 101 (**1997**) 4265.

104. G. Ramakrishna and H. N. Ghosh *Langmuir* 19 (**2003**) 505.
105. R. Katoh, M. Murai, A. Furube *Chem. Phys. Lett*. 461 (**2008**) 238.
106. T. C. Jagadale, S. P. Takale, R. S. Sonawane, H. M. Joshi, S. I. Patil, B. B. Kale, S. B. Ogale *J. Phys. Chem. C* 112 (**2008**) 14595.
107. B. S. Kwak, J. Chae, J. Kim, M. Kang *Bull. Korean Chem. Soc*. 30 (**2009**) 1047.
108. K. Selvam and M. Swaminathan *RSC Adv.* 2 (**2012**) 2848.
109. S. M. Feldt, G. Wang, G. Boschloo, A. Hagfeldt *J. Phys. Chem. C* 115 (**2011**) 21500.
110. T. W. Hamann *Dalton Trans*. 41 (**2012**) 3111.
111. G. K. Boschloo and A. Goossens *J. Phys. Chem.* 100 (**1996**) 19489.
112. G.-W. Lee, S.-Y. Bang, C. Lee, W.-M. Kim, D. Kim, K. Kim, N.-G. Park *Curr. Appl. Phys.* 9 (**2009**) 900.
113. B. A. Gregg, F. Pichot, S. Ferrere, C. L. Fields *J. Phys. Chem. B* 105 (**2001**) 1422.
114. J. Zheng, H. Yu, X. Li, S. Zhang *Appl. Surf. Sci.* 254 (**2008**)1630.
115. J. Krýsa, M. Zlamal, G. Waldner *J. Appl. Electrochem*. 37 (**2007**) 1313.
116. A. Goossens, B. Van der Zanden, J. Schoonman *J. Chem. Phys. Lett*. 331 (**2000**) 1.
117. R. Dholam, N. Patel, A. Santini, A. Miotello Int. *J . Hydrogen Energy* 35 (**2010**) 9581.
118. W. Y. Choi, A. Termin, M. R. Hoffmann *J. Phys. Chem*. 84 (**1994**) 13669.
119. M. Radecka, M. Rekas, A. Trenczek-Zajac, Z. Zakrzewska *J. Power Sources* 181 (**2008**) 46.
120. M. I. Litter and J. A. Navìo *J. Photochem. Photobiol. A: Chem*. 98 (**1996**) 171.
121. M. Redecka, M. Wierzbicka, S. Komornicki, M. Rekas *Physica* B 348 (**2004**) 160.
122. A. Hagfeldt, H. Lindstrom, S. Sodergren, S. Lindquist *J. Electroanal. Chem*. 381 (**1995**) 39.
123. H. Yu, X. Quan, S. Chen, H. Zhao *J. Phys. Chem. C* 111 (**2007**) 12987.
124. L. M. Peter Chem. Rev. 90 (**1990**) 753.
125. G. Liu, X. Wang, L. Wang, Z. Chen, F. Li, G. Q. Lu, H.-M. Cheng *J. Coll. Interf. Sci.* 334 (**2009**) 171.
126. S. Jin, Y. Li, H. Xie, X. Chen, T. Tian, X. Zhao *J. Mater. Chem*. 22 (**2012**) 1469.
127. D. Tafalla, P. Salvador, R. M. Benito *J. Electrochem. Soc*. 137 (**1990**) 1810.
128. H. Rensmo, H. Lindstrom, S. Sodergren, A. Willstedt, A. Solbrand, A. Hagfeldt, S.-E.Lindquist *J. Electrochem. Soc*. 143 (**1996**) 3173.
129. M. Takahashi, K. Tsukigi, T. Uchino, T. Yoko Thin Solid Films 388 (**2001**)

231.
130. S. Xiao, J. Qu, H. Liu, X. Zhao, S. Wan *J. Solid State Electrochem*. 13 (**2009**) 1959.
131. H.-Y. Chuang, D.-H. Chen Int. *J. Hydrogen Energy* 36 (**2011**) 9487. H.
132. Wang, J. He, G. Boschloo, H. Lindstrom, A. Hagfeldt, S.-E. Lindquist *J. Phys. Chem. B* 105 (**2011**) 2529.
133. M. V. B. Zanoni, J. J. Sene, H. Selcuk, M. A. Anderson *Environ. Sci. Technol*. 38 (**2004**) 3203.
134. J. A. Byrne, B. R. Eggins, S. Linquette-Mailleyb, P. S. M. Dunlop *Analyst* 123 (**1998**) 2007.
135. G. Hodes, I. D. J. Howell,L. M. Peter *J. Electrochem. Soc*. 139 (**1992**) 3136.
136. S. Grabtchak, C. Main, S. Reynolds *J. Non-Crys. Sol.* 266–269 (**2000**) 362.
137. N. Daude, C. Gout, C. Jouanin *Phys. Rev. B* 15 (**1977**) 3229.
138. B. O'Regan, J. Moser, M. Anderson, M. Grätzel *J. Phys. Chem.* 94 (**1990**) 8720.
139. X. G. Hou, A. D. Liu, M. D. Huang, B. Liao, X. L. Wu *Chin. Phys. Lett.* 26 (**2009**) 077106.

5.
Photocatalytic Tests

Development of materials for photo-oxidation and photocatalysis in general has followed an evolutionary pathway from conventional bulk metals and semiconductors to colloidal materials (in the size range of 10–1000 nm) and even to strictly nanosized materials or clusters (<10 nm). The differences among these classes of materials reflect themselves in how physical properties depend on surface area and its relation to electronic and photocatalytic behavior, as already exposed in paragraph 1.2. Indeed, the photocatalytic results are strongly material-dependent.
As with other treatment technologies not discussed in this contest, the design of a photocatalytic experiment is governed by several factors, which range from experimental tunable parameters to intrinsic issues of the pollutant(s) to be degraded, such as the influent/effluent contaminant concentration, background water quality parameters (*i.e.*, pH, alkalinity, bromide concentration, *etc*.) or type and concentration of gaseous pollutants, and so on. The main key design parameters for AOPs, as well as photocatalysis, include chemical dosages and ratios with other chemicals, reactor contact time, and reactor configuration. The optimum dosages, reagent ratios, and contact time are specific for each treatment scenario. Very often, for large scale applications, they are determined through pilot studies, using the water matrix of interest in the case of liquid pollutants. As can be expected, higher chemical dosages and contact times are typically expected to result in higher removal rates; however, increasing dosages results in higher costs and possible by-product formation. However, in some cases, the formation of by-products can be limited by higher chemical ratios.

In this study, photocatalytic tests were performed on both pristine TiO_2 and doped samples, with a main aim of focusing on the pollutants (scantily studied in the literature of photocatalysis) in the former case, whereas, in the latter, to evaluate the performance of the photocatalyst.
Hereafter, all photocatalytic experiments sorted by the different pollutants are described. First, a brief background of the pollutant is given; then, the photocatalysts employed are presented; finally, the experimental set-up and photocatalytic results are displayed.
A great part of the characterization results is devoted to N-doped TiO_2, whereas photocatalytic tests on such samples had been already performed and reported in a previous work[2] which almost covers my master thesis

activity.[1] Ethanol degradation experiments were performed to test only selected N-doped oxides also to evaluate the differences between “fresh” and “old” samples (see paragraph 5.3).
All reactants employed in this thesis were purchased by Sigma-Aldrich and used without any other purification treatment; doubly distilled water passed through a Milli-Q apparatus (Millipore Corporation) was used to prepare solutions and suspensions.

5.1. Methylene blue

The pollutant

Methylene blue (MB) is a heterocyclic aromatic chemical compound with the molecular formula $C_{16}H_{18}N_3SCl$. It has many uses in a range of different fields, mainly biology (as a fungicide) and chemistry (as a dye). It is a potent cationic dye with maximum absorption of light around 670 nm. The specifics of absorption depend on a number of factors, including protonation, adsorption to other materials, and metachromasy (the formation of dimers and higher-order aggregates depending on concentration and other interactions). Such an heterocyclic aromatic compound is deeply used as coloring paper agent, temporary hair colorant, dye for cottons and wools, coating for paper stock, *etc*.
Moreover, methylene blue is widely used as a redox indicator in analytical chemistry. Solutions of this substance are blue when in an oxidizing environment, but will turn colorless if exposed to a reducing agent. The reduced form of MB is called “leucomethylene blue” (LMB).
MB is also a photosensitizer used to create singlet oxygen when exposed to both oxygen and light: it is used in this regard to make organic peroxides by a Diels-Alder reaction which is spin forbidden with normal atmospheric triplet oxygen.
In biology methylene blue is used as a dye for a number of different staining procedures. As these are temporary staining techniques, MB can also be used to examine RNA or DNA under the microscope or in a gel. It can even be used as an indicator to determine if a cell such as yeast is alive or not. The blue indicator turns colorless indicating living cells - however, if it stays blue it doesn't necessarily mean that the cell is dead or there are no cells. Methylene

blue may be regarded as a model compound of flavin co-enzymes, and its reactions in solution are interesting from a biochemical viewpoint.[3]
At pharmacologic doses MB has reducing agent properties: it is owing to this reason that methylene blue is employed as a medication for the treatment. However, several texts indicate that, at (much) higher doses, it has oxidizing agent properties.
In the literature, the removal of methylene blue as a model compound for basic dyes is very often proposed.

The photocatalyst

Titanium dioxide samples prepared by microemulsion-mediate route (see paragraph 2.3) were employed in the photocatalytic degradation of MB on the "dry" TiO_2 film. This is an unusual way to evaluate MB degradation, as it is often performed in aqueous media.
TiO_2 films were prepared by drop casting on glass supports (100 cm^2) a fixed amount of the powder (40 mg) dispersed in 2-propanol (5 mL) and by successive evaporation of the solvent (40 °C). The powders were finely grinded before the deposition to improve the homogeneity of the final layers.

Phtotcatalytic set up

The TiO_2 film was impregnated by 500 µL of methylene blue (MB), giving a (60±5) cm^2 stain, in ethanol solution (0.02 M) and allowed to dry. The films were subsequently irradiated in air for 7 h at room temperature; the position of the lamp (35 cm from the TiO_2 stained film) was selected such as to produce an irradiated area matching the MB stain one. The MB mineralization was followed by COD (chemical oxygen demand) determinations after extraction of MB from the scratched powder with a fixed amount of HCl solution. COD analysis enables to assess the amount of oxygen required to oxidize the organic compound to carbon dioxide and water. COD values (reported as mineralization percentage) are normalized with respect to both the specific surface area of the oxide and the initial MB (non-irradiated) COD value, that is (730±10) mg L^{-1}.

Photocatalytic results

The molecule can be either transformed into LMB through reduction by electrons in the conduction band or oxidized, by interactions with the valence

band holes or native hydroxyl species, starting with a demethylation step to be finally mineralized. For long reaction times also LMB can be further degraded and mineralized. Spectrophotometric measurements can numerically assess the discoloration of the MB stain, but such measurements themselves cannot verify if discoloration is the result of LMB formation or of the actual molecule mineralization. Instead, this confirmation can be achieved by COD determinations at the end of the reaction. Table 5.1 reports, for each sample, the mineralization percentages, which were calculated using the following equation:

$$\%\ \text{mineralization} = \frac{\text{COD}_0 - \text{COD}_t}{\text{COD}_0} \times 100 \quad \text{(eq. 5.1)}$$

where COD_0 and COD_t represent the initial COD value and the COD at time "t", respectively.

All home-made samples are more active than commercial P25 (Evonik) but less than the other commercial TiO_2 used as reference, HOMBIKAT UV 100 (Sachtleben). It seems that samples obtained with the use of surfactant LUTENSOL TO389 could reach a slightly higher mineralization degree than those obtained by TWEEN 80. No literature data exist at all about the photocatalytic activity of titania samples obtained with the use of such surfactants. Then, T_TX1.2, obtained by TRITON X-100 definitely shows the highest mineralization among all home-made oxides, namely 80 %, which is very close to that achieved by commercial HOMBIKAT UV-100.

Overall, a high performance toward the degradation under UV irradiation of a complex molecule like methylene blue was achieved, since all sample overwhelm the P25 undisputed benchmark and reached over 50 % mineralization.

Further, it can be recalled that, as a result of a previous work,[2] sample TN_TEA_0.10 produced the best MB mineralization (above 90 %) among all triethylamine-doped titania samples using the same photocatalytic experiment. That sample, highly discussed throughout this thesis, also shows a complex XPS pattern[2] with also substitutional N sites and the largest content of edge dislocations.

Sample	Mineralization %
P25	33
HOMBIKAT UV-100	83
T_L0.3	53
T_L0.6	78
T_L0.9	63
T_TW0.9	45
T_TW0.6L	53
T_TW0.8L	58
T_TW0.09L	50
T_TX1.2	80

Table 5.1. Mineralization percentage by COD determinations for all titania samples obtained by microemulsion-mediate route.

5.2. Advanced oxidation processes

Oxidation reactions that produce radicals are usually followed by additional oxidation reactions between the radical oxidants and other reactants (both organic and inorganic) until thermodynamically stable oxidation products are formed. According to their ability to initiate chemical reactions in terms of oxidation potential, the most powerful oxidants are fluorine, hydroxyl radicals ($^{\bullet}OH$), ozone, and chlorine with oxidation potentials of 2.85, 2.70, 2.07 and 1.49 eV, respectively.[4]

Advanced oxidation processes (AOPs) combine ozone (O_3), ultraviolet (UV), hydrogen peroxide (H_2O_2) and/or catalyst to offer a powerful water treatment solution for the reduction (removal) of residual organic compounds as measured by COD (chemical oxygen demand), BOD (biochemical oxygen demand) or TOC (total organic carbon). All AOP are designed to produce *in situ* hydroxyl radicals,[5] which are the responsible species to effectively destroy organic compounds, even when highly recalcitrant ones are concerned.[6-8] Indeed, $^{\bullet}OH$ radicals are extraordinarily reactive species with the rate constants of reactions with the majority of organic molecules in the order of 10^6-10^9 M^{-1} s^{-1}.

Thus, AOPs are successfully used to decompose many hazardous chemical compounds to acceptable levels, without producing additional hazardous by-products or sludge which require further handling.

AOP can act on organic compounds in water in several ways. Primarily, they convert one compound into another (conversion), or, alternatively, conversion is reached along with a reduction in toxicity and mineralization (breaking the organic down to CO_2 and inorganic salts).

The versatility of AOPs reflects in different options for production of $^{\bullet}OH$ radicals, depending on the requirements of the specific treatment. The AOPs are characterized by a variety of radical reactions that involve combinations of chemical agents (*i.e.*, O_3, hydrogen peroxide H_2O_2, transition metals, and metal oxides) and auxiliary energy sources (*i.e.*, UV-VIS radiation, electronic current, γ-radiation and ultrasound). Other examples of AOP include H_2O_2/UV, Fenton (Fe^{2+}/H_2O_2), photo- and electro-Fenton, chelating agent assisted Fenton/photo-Fenton, heterogeneous photo-oxidation using titanium dioxide (TiO_2), γ-radiolysis, and sonolysis.[9]

The main advantages of AOPs consist in their rapid reaction rates, small foot print, and excellent potential to reduce toxicity and possibly complete mineralization of organics treated. Moreover, they generally do not produce wastes with high concentrations for further treatments and do not need dangerous additives: they cause remediation and disinfection in one treatment; eventually, most advanced oxidation processes are scalable from a few to many millions of liters per day. Also, their lack of selectivity is an advantage when dealing with highly contaminated waters.

As for photolytic oxidation based processes, it has to be underlined that they operate at room temperature and offer the possibility to effectively use sunlight or near UV for irradiation, which could result in considerable economic savings especially for large-scale operations.

However, the implementation of AOPs and the determination of their effectiveness are difficult for several reasons. As with all treatment technologies, the effectiveness of AOPs will be largely determined by the specific water quality matrix of the contaminated water. However, in the case of AOPs, the effects of background water quality on contaminant removal are much less well understood than for other technologies. In general, most of the technical difficulties associated with AOPs stem from the fact that oxidation processes are non-selective with the potential for significant interference. To

compensate for these limitations, more energy or higher chemical dosages may be required, potentially resulting in higher costs.
As a consequence, AOPs can be definitely considered capital intensive, besides their need of a complex chemistry to be tailored to specific applications. Due to the usage of expensive reactants such as H_2O_2 and O_3, AOPs should not, therefore, replace the more economic, biological treatment.[10]
Moreover, AOPs can be installed either as tertiary treatment after the biological (secondary) treatment of wastewater, or as pre-treatment stage in order to enhance the biodegradability of trace organic contaminants. In the latter case, the usage of AOPs for partial oxidation of trace organic contaminants might not be an appropriate approach in the cases where other organic matter is predominantly present, since the oxidant requirement can be exceedingly high in order to achieve effective degradation of trace organics.

In this thesis, single (ozonation, photolysis, photocatalysis) and combined (photocatalytic ozonation) AOPs have been employed to promote the mineralization of 4-cumylphenol (4-CP). A complete mineralization is a desired outcome since intermediate oxidation products of alkyl phenols may exert an endocrine activity even higher than that of the parent compound.[11]
The tested AOPs were chosen also on the grounds of their plant scale feasibility. Ozonation is commonly employed in commercial water treatment plants. On the other hand, there are currently no plant-scale applications of TiO_2 photocatalysis, although this technique has proven to degrade efficiently numerous recalcitrant organic pollutants. This is possibly due to the fact that a plant scale application of photocatalysis would require to solve the problems related to the use of TiO_2 powder suspensions.

5.2.1. 4-cumylphenol

The pollutant

Like bisphenol A, 4-cumylphenol is considered an endocrine-disrupting chemical (EDC), thus representing environmental hormones that can interfere with the function of the endocrine system. EDCs disturb the normal endocrine system, affecting the reproductive and hormonal control of development of animals.

Alkylphenols (APs), EDCs with estrogenic effects, are very common in aqueous environments, as already mentioned in the case of BPA. APs are generated mainly from the biodegradation of alkylphenol ethoxylates (APEOs), which are non-ionic surfactants widely used as emulsifiers in paints and pesticides as well as in industrial and household detergents.[12] They tend to bioaccumulate in lipids of living organisms.[13] APs have been linked to physiological and reproductive effects in fish and other wildlife.[14,15] and to effects on human fertility via the food chain (bioaccumulation).[16] These findings have raised public concern over the effects of EDPs on the environment in general and human health in particular.[17]

Among all APs, 4-cumylphenol has been recognized as one of the most important pollutants of the alkyl phenol family. It has a wide range of anthropogenic sources: it is commonly employed as an antioxidant and in the manufacture of plastics, surfactants and fungicides. Furthermore, it is a key by-product in the phenol production process and a non-ionic detergent metabolite. Such a widespread use, together with very low biodegradability[18] have led to an increasing environmental distribution of this pollutant. 4-CP has been identified as a component of atmospheric particulate matter[19] and as a contaminant in sea water[20] and drinking water wells.[21] Its adsorption on sediments is significant (log Kow = 3.8) and concentrations as high as 70 000 mg kg-1 of sediment has been reported.[22]

4-CP endocrine disruptor ability has been clearly proved.[23,24]

A recent study has also reported the pollutant capability of inducing multiple renal cysts in neonatal rats.[25]

Despite the wide environmental distribution and great health concerns related to its toxicity, 4-CP removal techniques are almost not investigated in the literature. The relatively high partition coefficients of alkylphenols lead to their significant adsorption onto sludges of biological wastewater treatment plants.[26] However, since 4-CP has a very low biodegradability, biological treatment does not lead to a degradation of the contaminant, which is merely adsorbed onto the biological sludge.[26,27] Therefore, 4-CP is simply transferred from one phase to the other and biological sludges need to be disposed of as hazardous waste. No other remediation procedure for 4-CP removal could be found in the literature.

The photocatalyst

The commercial sample P25 (Evonik) was employed as photocatalyst (see chapter 3 for details).

Also in this second type of photocatalytic test, TiO_2 was deposited on a support. However, in this case, the degradation reaction occurs in a liquid medium. Titania films were used instead of suspension in order to eliminate the main problems encountered with powdered slurries: 1) the need of expensive and time-consuming separation and filtration procedures at the end of the treatment to remove the catalyst, 2) the difficult use in continuous-flow systems, 3) the alteration of the powders' activity as a consequence of aggregation phenomena,[28-30] 4) the need of powerful sources to activate the photocatalytic process since the amount of adsorbed light is reduced by the cloudiness of the suspension.[31] Related to this latter issue, the use of TiO_2 immobilized as thin films is of paramount importance for the plant-scale applicability of the process, especially if a low intensity irradiation source, such as solar light, is to be exploited.

Thin TiO_2 films were deposited by a specific procedure in order to obtain photocatalytically active films with high surface area and good mechanical stability. An Al lamina was employed as a cheap and reusable support, with a native oxide (Al_2O_3) that improves the adhesion of the TiO_2 particles to the metallic support, which had been previously sand blasted and etched in oxalic acid 10% in order to increase the surface roughness. The aluminum lamina was washed and sonicated in water and 2-propanol for 1 hour in order to remove all the used powder before performing the final polishing treatment with oxalic acid. Such a prolonged sonication time was essential and gave evidence of the strong adhesion of the particles to the lamina. Thus, the as-deposited TiO_2 nanopowders would have a good physical stability if used in water treatment plants, since the rough investigation of their physical stability via sonication as a sort of disruption technique represented the worst case scenario. The good physical stability of the photocatalyst is crucial as it would ensure the synergistic effect of adsorption-solar photocatalysis processes.

Titania thin films were deposited by drop-casting a suspension of P25 (0.2 g) in 2-propanol, on both sides of the aluminum plate (total geometric area: 170 cm^2). The suspension stability was improved by adding sodium dodecyl sulfate (SDS). However, the surfactant was not used all the times the photocatalyst was immobilized on a support because of the problems related to its removal,

though a simple calcination at 400 °C under stationary air is sufficient to burn it completely. Finally the films were calcined in air at 300 °C for 2 h in order to both remove the surfactant and improve the adhesion between the TiO_2 particles and the metallic substrate.
As-deposited films showed optimal stability, also ascertained by no appreciable weight variation of the coated Al laminas after the degradation experiments.

The Al lamina and TiO_2 films were morphologically characterized by Scanning Electron Microscopy (SEM) equipped with energy-dispersive X-ray spectroscopy (EDX), and by Atomic Force Microscopy (AFM). SEM and AFM photographs were acquired by LEO 1430 and by NT-MDT Solver PRO-M, respectively.
As appears from both Fig. 5.1 and 5.2, the films exhibit high surface roughness. SEM image (Fig. 5.1a) of the bare Al foil after the surface treatments clearly shows high roughness on the micron scale. In the SEM image (Fig. 5.1b) of the coated layer, the individual nanometric particles can be appreciated; a homogeneous distribution of spherical aggregates without cracks and cleavages was achieved by drop-casting deposition of the above-mentioned suspension. AFM images (Fig. 5.2), especially in the 3D representation (Fig. 5.2b), give an estimation of the average roughness of the TiO_2 coating, occurring in the range 0–200 nm. A semi-quantitative elemental analysis of the TiO_2 film was obtained by EDX analyses, which revealed the presence of low percentages (around 1%) of Al in the TiO_2 film, possibly as result of thermal diffusion of Al ions from the native Al_2O_3 oxide into the titania film.

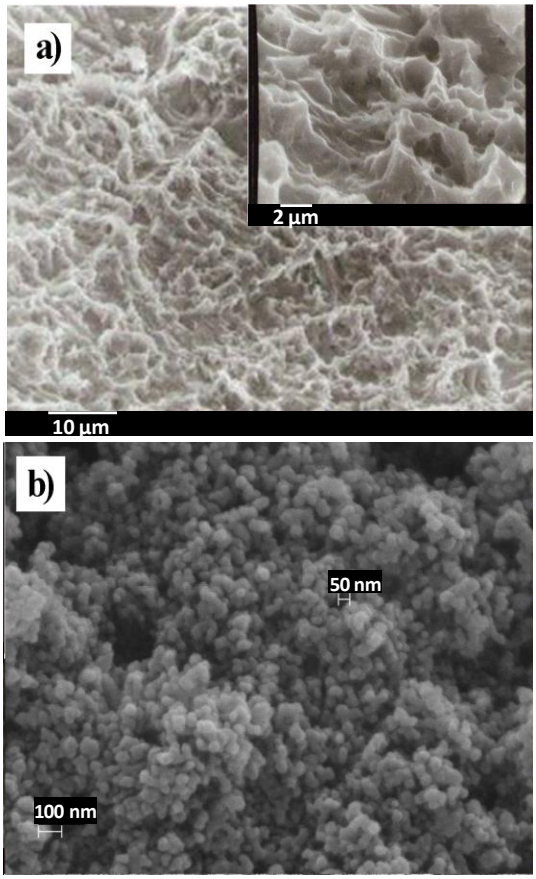

Figure 5.1. SEM images of (a) the bare aluminum lamina after the surface treatments and of (b) the final TiO_2 layer.

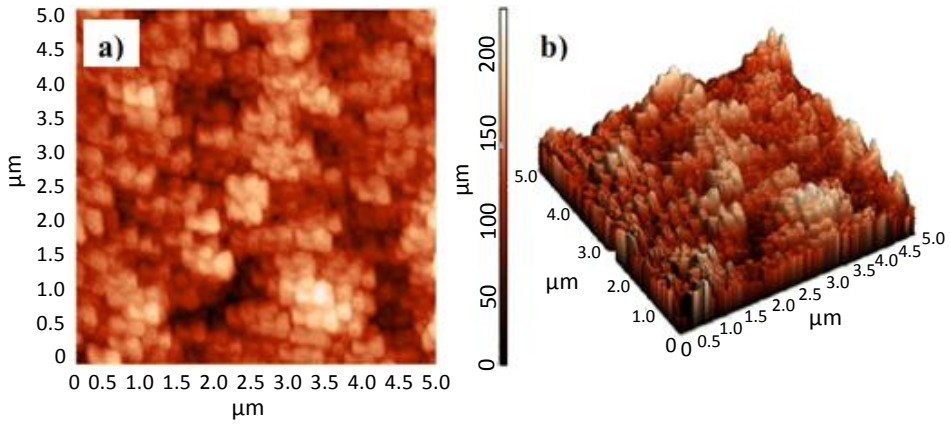

Figure 5.2. AFM 2D (ca) and 3D (b) images of the TiO_2 film.

Photocatalytic set up

All 4-CP degradation tests were carried out in batch at 25 °C and at spontaneous pH (the experimental set-up is presented in Fig. 5.3). A 600 mL cylindrical jacketed glass reactor was utilized.

Tests of photolysis, photocatalysis and photocatalytic ozonation were performed under UV-A irradiation. The photon sources were provided by two UV lamps (see the Appendix for details).

The initial concentration of the 4-CP solution was varied in the range 0.2-0.4 mM, while a constant O_3 concentration of 3 mg L^{-1} was employed.

During ozonation and photocatalytic ozonation tests, an ozone generator (Ozono Elettronica Internazionale S.r.l.) was employed to produce the ozone feed from pure oxygen. In photocatalytic ozonation, the ozone feed was started 90 min before switching on the lamp in order to allow a complete ozone solubilization. The ozone flow rate (30 L h^{-1}) was maintained through all the duration of the degradation test in order to keep a constant dissolved ozone concentration of 3 mg L^{-1} (determined by iodometric analyses).

The progressive disappearance of 4-CP was monitored by measuring the absorbance at 275 nm using a Beckman DU 640. The degree of mineralization was instead determined by means of chemical oxygen demand (COD) analysis kit (Spectroquant Merck).

Blank experiments performed with pure oxygen instead of O_3 showed no significant improvement with respect to plain photocatalysis. Also the effect of photolysis on mineralization was negligible.

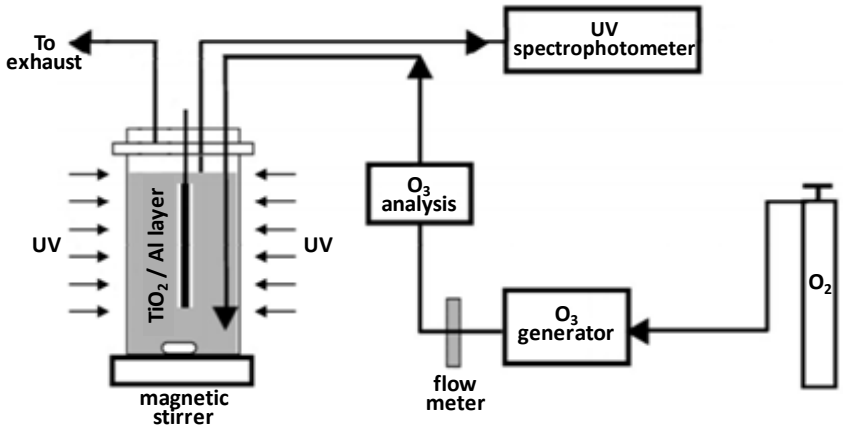

Figure 5.3. Experimental set up employed for 4-cumylphenol degradation tests.

Intermediate products of 4-CP oxidation during photocatalytic ozonation were identified by high performance liquid chromatography-mass spectrometry (HPLC/MS) determinations on solutions sampled at different reaction times and by Attenuated Total Reflectance Fourier Transform Infrared Spectroscopy (ATR-FTIR) analyses of the used catalyst at the end of the reaction. The HPLC/MS analyses were performed using an Agilent 1100 chromatographic system (quaternary pump, autosampler, thermostatted column holder) equipped with a diode array detector and a Bruker ion-trap Esquire 3000+. The column was a Supelco Ascentis-Express (50 x 4.6 mm, 2.7 µm). A two phase mixture was used as the mobile phase with a flow-rate of 1 mL min^{-1} in gradient mode. Phase A was Milli-Q water containing 0.05 % (v/v) TFA or 10 mM ammonium acetate in the case of ESI+ or ESI- respectively; phase B was Acetonitrile (LC-MS grade), containing 0.05 % TFA only in the case of ESI+. The adopted gradient was the following: from 5 % B to 95 % B in 6 min, washing at 100 % B for 1 min, equilibration at 5 % B in the next 3 min. Peak UV detection was carried out at 220 and 254 nm (reference at 500 nm, 40 nm bandwith). Mass spectrometry was performed with an electrospray ionization (ESI) source in either positive or negative mode with the following parameters: detection in the 50-2000 m/z range with alternating MS/MS, capillary voltage ± 3500 V, drying gas temperature 365 °C, nebulizer pressure 50 psi, drying gas flow 10 L min^{-1}. All other tuning parameters were optimized with the standard tuning mix provided by Bruker for a generic detection in the above mass range.

The chemical structure of organic compounds adsorbed on the used TiO_2 surface was analyzed by using a Jasco 4200 FTIR, accessorized with an ATR module.

Photocatalytic results

The different tested AOPs present very different efficiencies in terms of mineralization degree at the end of the degradation tests, as shown by numerical values reported in Tab. 5.2 (first three rows). The mineralization percentages were calculated in the same way as for methylene blue degradation (see eq. 5.1).

Process	$[4\text{-CP}]_0$ (mM)	COD_{in} ($mg_{O_2}\ L^{-1}$)	COD_{fin} ($mg_{O_2}\ L^{-1}$)	mineralization %
Photocatalytic ozonation	0.2	1.3	0	100
	0.3	151	21	86
	0.4	186	56	70
Ozonation*	0.3	151	127	16
Photocatalysis	0.3	151	123	19

Table 5.2. Mineralization data of separate and combined tests after 180 min (* t_{fin} = 90 min) for different initial 4-CP concentrations. Combined treatments involve 90 min of initial O_3 equilibration step and 90 min of photocatalytic ozonation.

Ozonation leads to a 16% mineralization after 90 min of treatment. Photocatalysis is by far less efficient since it requires a 2.5 longer time to obtain a comparable mineralization (18% of mineralization after 240 min instead than 90 min). These results are in agreement with the literature concerning the degradation of other EDCs.[32]

Combining photocatalysis and ozonation leads to a much higher mineralization. Before testing the combined process, the solution was treated with O_3 for 90 min to allow a complete ozone solubilization. An 86 % mineralization was achieved at the end of the combined test (including 16 % mineralization during the initial ozonation step and 70 % of the degradation during 90 min of photocatalytic ozonation)for the intermediate concentration ($[4\text{-CP}]_0$ equal to 0.3 mM).

At varying the initial 4-CP concentration, a relevant final mineralization was achieved in all cases (100, 86, 70 % for $c_{(4\text{-CP})0}$ = 0.2, 0.3, 0.4 mM, respectively), showing that no accumulation of stable intermediates takes place even at high 4-CP concentrations. When $[4\text{-CP}]_0$ is equal to 0.2 mM, a complete mineralization is achieved after less than 90 min of the combined treatment. Analogously, fig. 5.4 reports the disappearance of the 4-CP along with the proceeding of the reaction.

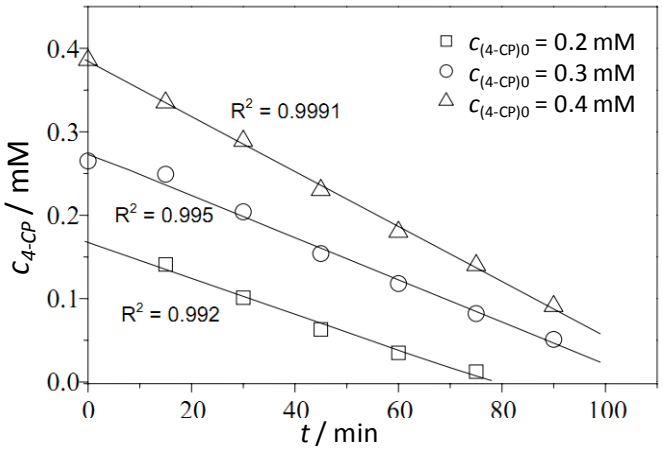

Figure 5.4. 4-CP removal as a function of the irradiation time during photocatalytic ozonation tests with different initial pollutant concentrations (initial 4-CP concentration 0.2-0.4 mM, ozone concentration 3 mg L-1, initial ozone equilibration step 90 min).

The disappearance of the pollutant as a function of time shows a good linear correlation for the three reported initial concentrations, as can be appreciated from Table 5.3. However, the slope varies with increasing 4-CP content, suggesting the occurrence of a complex kinetic pattern, which necessarily implies surface reaction steps.

Process	$[4\text{-CP}]_0$ (mM)	COD_{in} (mg_{O_2} L^{-1})	COD_{fin} (mg_{O_2} L^{-1})
Ozonation	0.3	151	127
Photocatalysis*	0.3	151	123
Photocatalytic ozonation	0.2	103	0
	0.3	151	21
	0.4	186	56

Table 5.3. Mineralization data of separate and combined test (t_{fin}= 90 min; * t_{fin} = 240 min).

The high efficiency of photocatalytic ozonation can be related to highly synergistic effects occurring between ozonation and TiO_2 photocatalysis. Indeed, an initial ozone attack on 4-CP generates highly hydrophilic species, which can be more easily adsorbed onto the TiO_2 surface and mineralized. Furthermore, decomposition of O_3 at the TiO_2 surface leads to the formation

of $^{\bullet}OH$ and $^{\bullet}OOH$ species, which are active oxidizing species. Additionally, the electron transfer of photogenerated electrons from TiO_2 to O_3 is much faster than the corresponding process to O_2. This effect may enhance the quantum efficiency of the photocatalyst by slowing down the recombination of photogenerated electrons and holes at the TiO_2 surface.[6]

Complete degradation of CP to CO_2 is obtained after very short reaction times, at room temperature, by the combination of ozone and photocatalytic treatments. The success of the process is largely due to the presence of sandwiched TiO_2 layers deposited onto an Al lamina. The stable, purposely rough, TiO_2 surface offers a large number of adsorption sites for both the pollutant and ozone thus promoting synergistic, highly oxidizing reaction steps. The optimal mineralization, the simplicity of the process and, most of all, the absence of suspended solids or sludges, make the present process an excellent candidate for a CP degradation treatment plant.

Degradation mechanisms

Intermediate products of 4-CP oxidation during photocatalytic ozonation were identified by HPLC/MS determinations on 4-CP solutions (intermediate concentration, namely $[4\text{-CP}]_0$ = 0.3 mM) sampled at different reaction times and by ATR-FTIR analyses of the used catalyst at the end of the reaction. Related to these latter investigations, the FTIR spectrum of the titania film after photoreaction show no trace of the 4-CP characteristic peaks (Fig. 5.5a). On the contrary, the spectrum presents a peak at about 1700 cm^{-1} attributable to COOH/CHO moieties and a peak centered at 1550 cm^{-1} that can be attributed to double bonds.[33]

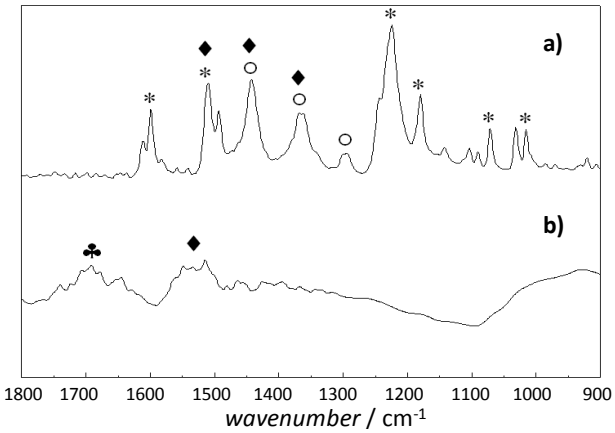

Figure 5.5. ATR-FTIR spectra of (a) pure 4-CP molecule, (b) TiO_2 sampled at the end of the O_3 + TiO_2 + UV run (0.3 mM starting 4-CP concentration, the curve of bare TiO_2 was subtracted). Peaks are labeled as follows: * aromatic ring, ° C–OH, ♦ alkenes, and ♣ CHO/COOH.

Fig. 5.6 presents a 4-CP degradation mechanism by photocatalytic ozonation that can be proposed on the grounds of the reaction intermediates identified by HPLC-MS and FTIR analyses.

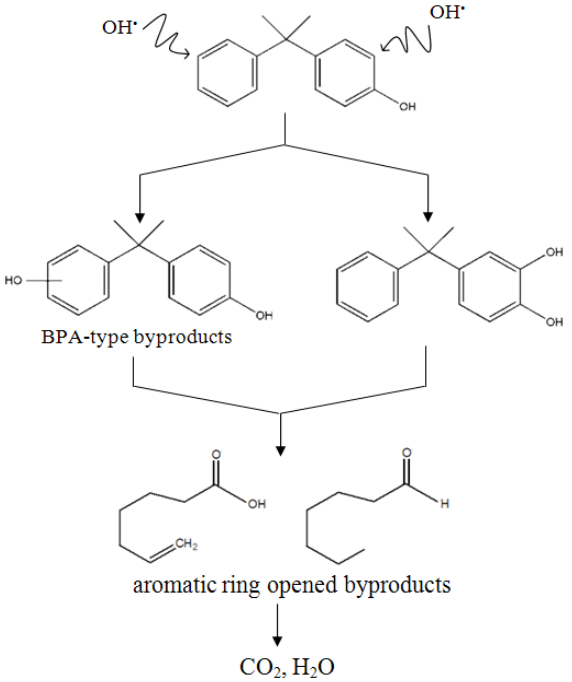

Figure 5.6. Proposed reaction pathway for the degradation of the 4-CP molecule.

In the HPLC/MS spectra (Fig. 5.7) the peak at the retention time of 5.6 min can be attributed to 4-CP by comparison with the pure 4-CP mass spectrum. The chromatographic peaks at a retention time of about 4.5 min certainly correspond to a mixture of oxidation products of 4-CP. Even when the polarity of the eluent was changed, it was not possible to obtain a better separation for the corresponding compounds. The attribution of the HPLC peaks at about 4.5 min was performed using the method of the internal calibration by addition of a known compound (bisphenol A). The peak at 4.6 min can be attributed to bisphenols bearing the second hydroxyl group on the non-phenolic aromatic ring, such as bisphenol A (BPA). The peak at 4.4 min can instead be attributed to isomers of BPA bearing the second hydroxyl group in orto or para positions with respect to the 4-CP hydroxyl group. This attribution is based on the proximity of this peak to the one of BPA-type compounds and on the grounds of spectrophotometric considerations. In both cases, the attribution of precise chemical structures was not feasible since several isomers might occur. In addition to the previously described degradation products, few minor chromatographic peaks were also observed. Because of the very low retention time, these compounds certainly corresponded to smaller and more polar molecules such as acids or aldehydes, as confirmed by FTIR analyses and in agreement with literature results on other ECDs.[34]

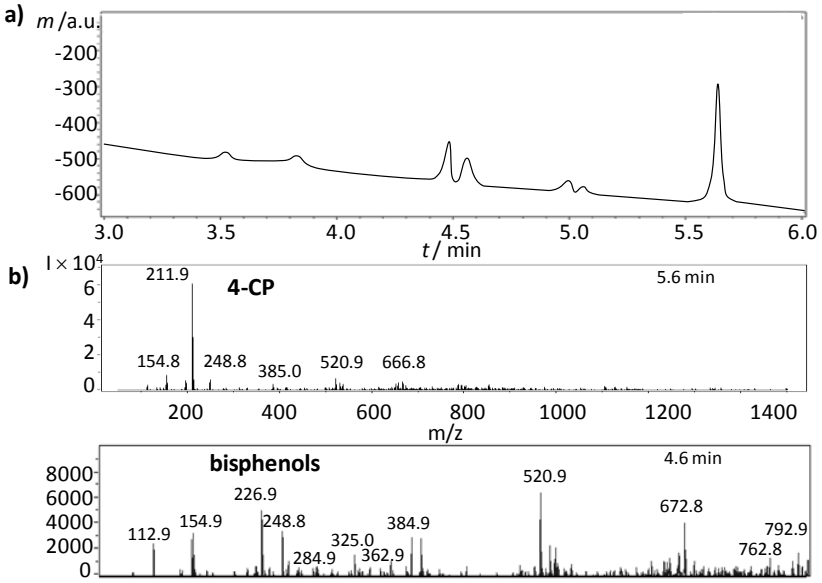

Figure 5.7. a) HPLC peaks for different retention times and **b**) relative mass spectra of 0.4 mM 4-CP solution at the end of the combined ozonation and photocatalysis.

The occurrence of bisphenols as reaction intermediates suggests a degradation mechanism starting with an initial attack of an hydroxyl radical on one of the aromatic rings. The possible attack of the hydroxyl radical on the phenolic ring may be favored by the presence of the former –OH group of the 4-CP molecule. The proximity of two hydroxyl groups may lead more easily to ring opening products. Two possible open ring intermediates are proposed in Fig. 5.6 on the grounds of both FTIR and HPLC/MS results.

5.2.2. Bisphenol A

The pollutant

Bisphenol A is a controversial organic compound since it exerts weak, but detectable, hormone-like properties, raising concerns about its presence in consumer products and foods contained in such products.

For this reason, it is said to be an endocrine disruptor, or, more appropriately, an endocrine modulator, as it does not show any reproducible evidence of adverse effects as a result of hormone-like properties.

Having two phenol functional groups, it is a key monomer in production of epoxy resins and in the most common form of polycarbonate plastic.[35] This means it is used primarily to make plastics in a wide variety of commercial products; some of these include digital media (*e.g.*, CDs, DVDs), electrical and electronic equipment, automobiles, airplanes, construction material, sporting goods, food and drink can liners, dental sealants, and so on. Products using bisphenol A-based plastics have been in commercial use since 1957. At least 3.6 million tonnes (about 8 billion pounds) of BPA are used by manufacturers yearly.

Several governments questioned its safety, prompting some retailers to withdraw polycarbonate products, especially from 2008. A 2010 report from the United States Food and Drug Administration (FDA) raised further concerns regarding exposure to fetuses, infants, and young children.[36]

Endocrine disruptors or modulators such as bisphenols, alkylphenols, and phthalates are pollutants that have raised great concern not only because of their their potential health effects but also for their high resistance to traditional wastewater treatments.

Since conventional water and wastewater treatment plants may be inadequate for substantially removing many organic contaminants like the

above mentioned ones, a type of advanced oxidation process, namely the combination of ozonation and photocatalysis by TiO_2 for the degradation and final mineralization of BPA, has been adopted in this thesis work.

The aim of this work is to degrade BPA producing its best mineralization to CO_2 since intermediate products might be as toxic as the starting compound or even more hazardous. It will be shown in the following that the combination of ozonation and photocatalysis by nano-TiO_2 does not require any filtration or separation of the oxide slurry and it leads to the complete pollutant mineralization in short reaction time (90 min).

The photocatalyst

Thin TiO_2 films made of P25 (Evonik) nanoparticles were employed as in the case of 4-cumylphenol. The same deposition procedure was adopted.

Photocatalytic set up

BPA degradation was carried out at atmospheric pressure and 25 °C in a 600 mL cylindrical jacketed glass reactor. Different initial BPA concentrations were tested, namely 1.5, 0.8, 0.6, 0.3, 0,1 mM; 0.3 mM initial BPA concentration was employed for further mechanistic studies. The ozone feed was produced from pure oxygen using an ozone generator (Ozono Elettronica Internazionale S.r.l.). Before testing the combined processes, the solution was treated with O_3 for 90 min to allow a complete ozone solubilization. The ozone flow rate (30 L h^{-1}), determined analytically *ex situ* as reported by Oyama *et al.*,[37] was maintained throughout the duration of the degradation test in order to keep a constant dissolved ozone concentration of 3 mg L^{-1}. Photon sources were provided by two UV lamps (see the Appendix for details) symmetrically placed with respect to the Al/TiO_2 lamina (see the sketch of the experimental setup in Fig. 5.8). The emission of the lamp was checked by measuring its actual intensity inside the Pyrex jacketed glass reactor thermostatted at room temperature by water recirculation so that both the glass and the water filter effects were also taken into account.

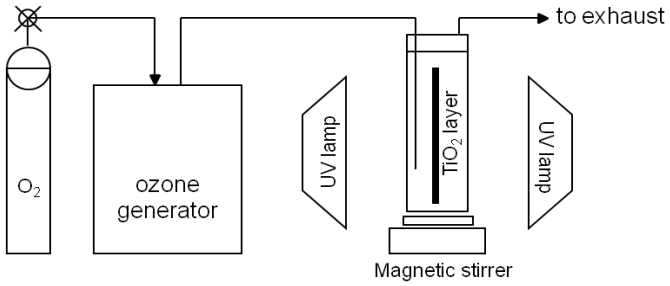

Figure 5.8. Experimental O_3/photocatalytic setup.

The initial concentration of BPA solution (spontaneous pH) was varied in the range 0.1-1.5 mM and pH was maintained between 4 and 5 by the addition of diluted HN O_3 and KOH. Degradation tests were performed with the lowest BPA concentrations, which are commonly utilized in the literature, while the highest concentrations were selected in order to more readily identify the reaction intermediates. These latter are typically higher than those found in natural water. However, industrial effluent discharges and landfill leachates can be much more concentrated: concentrations as high as 17200 μg L^{-1} have been reported.[38]

The mineralization degree of BPA was determined by total organic carbon (TOC) analyses (TOC 5000 A Shimadzu carbon analyzer).

Possible intermediate oxidation products were identified by HPLC/MS and FTIR, using the same instrumental equipment as reported for the study on 4-CP.

Photocatalytic results

Different AOPs (UV photolysis, TiO_2 photocatalysis (TiO_2 + UV), and ozonation) were tested independently to study the BPA degradation. Numerical results are summarized in Tab. 5.4.

Test		% mineralization	*S*
Single experiments	UV	<3	-
	TiO_2 + UV	6	-
	O_3	6	-
Combined experiments	O_3 + UV	13	1.2
	O_3 + TiO_2	15	1.5
	O_3 + TiO_2 + UV	55	4.1

Table 5.4. Mineralization percentage of the separate and combined tests. UV = photolysis; TiO_2 + UV = photocatalysis (TiO_2); O_3 = ozonation.

Considering that no appreciable BPA stripping by the ozone flux was observed, in agreement with the low Henry's constant of the pollutant, the sole treatment by O_3 produces a 6 % BPA removal after 90 min. The mineralization is not as efficient since only about one half of the degraded molecules is actually mineralized. TiO_2 photocatalysis leads to an equal BPA removal but, in this case, all the degraded molecules are actually mineralized. Instead the sole irradiation by UV-A seems not to be effective in the adopted conditions (<3 % removal). In Tab. 5.5, the percentages of BPA removal and mineralization are separately shown for an initial BPA concentration of 0.3 mM.

Test (t_{fin} = 90 min)	**% BPA removal**	**% BPA mineralization**
photolysis	2	-
photocatalysis	6	6
ozonation	12	6

Table 5.5. % BPA removal and % mineralization of the separate tests. $c_{(BPA)0}$ = 0.3 mM.

During ozonation treatments, ozone is transferred from the gas to the liquid phase. Several aspects concur to the actual activity of ozone: its dissolved and saturated concentration and its self-decomposition.[39]

Three different types of combined experiments were then performed and compared: O_3 + TiO_2 in the dark, O_3 + UV irradiation, and O_3 + TiO_2 + UV irradiation. In all these combined tests, a simple ozonation step of 90 min was initially performed to allow a complete ozone solubilization. After this "pre-treatment", 90 min combined treatment was applied. The pollutant mineralization achieved with the combined methods is higher (in the case of 0.3 mM bisphenol A) than those obtained by individual treatments, since photolytic ozonation and catalytic ozonation lead to 13 % and 15 % removal, respectively. Fig. 5.9a reports the results for the three different experiments. Results of degradation experiments for several initial BPA concentrations, in the range 0.1–1.5 mM are reported in Fig. 5.9b. In the case of initial BPA concentration equal to 0.1 mM, an almost complete mineralization is achieved after only 90 min of the combined treatment (ozonation coupled with photocatalysis by TiO_2); even for the higher tested concentration, the mineralization is still appreciable after such a short reaction time. However, a far more promising mineralization degree is obtained with the "O_3 + TiO_2 +

UV" process (55 %) in the case of an initial BPA concentration equal to 0.3 mM.

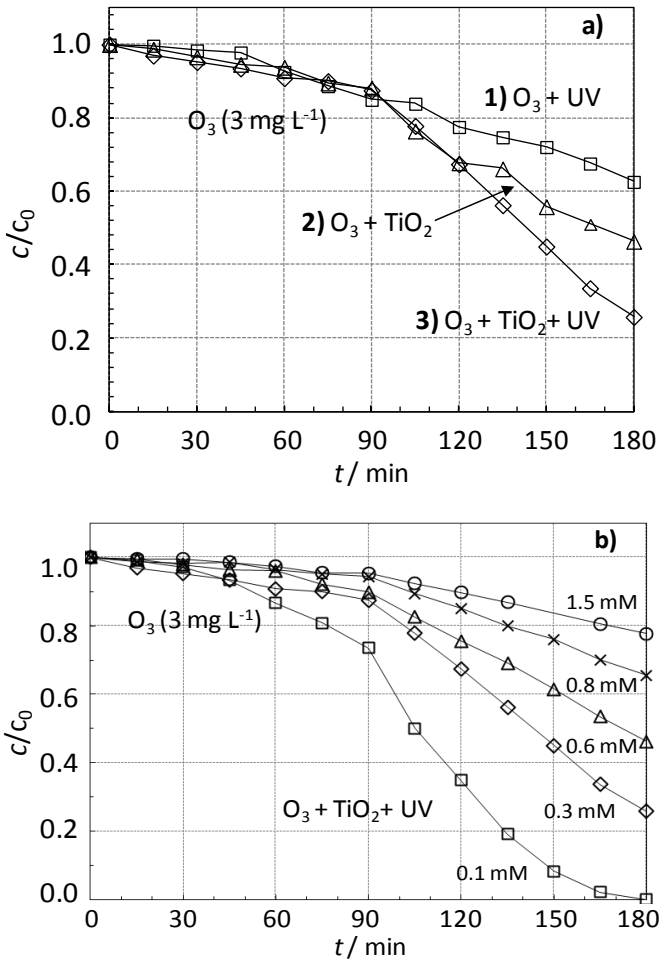

Figure 5.9. Disappearance of BPA molecule in the case of combination of ozone (first 90 min) with **1)** UV light (photolysis)**, 2)** TiO_2 powders (dark experiment) and **3)** TiO_2 + UV (photocatalysis). $[BPA]_0$ = 0.3 mM, $[O_3]$ = 3 mgL^{-1} **(a)**; case **3)** is considered for increasing starting BPA concentration **(b)**.

This finding is explained by the occurrence of highly synergistic effects, evaluated by the following parameter (Table 5.4, 4th column), on the grounds of what reported by Torres *et al.*:[40]

$$S = \frac{\%min_{combined}}{\sum \%min_{independent}} = \frac{\%min_{combined}}{\%min_{UV} + \%min_{ozone} + \%min_{photocatal}} \quad \text{(eq. 5.2)}$$

where % $min_{combined}$ represents the mineralization percentage or total organic carbon removed, for a combined process - subtracting the initial mineralization due to the sole ozonation, 6 % - while % min_{UV}, % min_{ozone}, and % $min_{photocatal}$ correspond to the total organic carbon removed by the independent photolysis, ozonation, and photocatalysis, respectively. If *S* is equal to 1, additive effects take place, but *S* values higher or lower than 1 indicate synergistic or antagonistic effects, respectively, among the combined processes. In our case, an *S* value of 4.1 is obtained for the combination of ozone and TiO_2 photocatalysis, indicating the occurrence of synergistic effects much higher than those occurring with the other combined techniques investigated.

This achievement can be related to the interactions between ozone and the nanosized titania surface. Decomposition of O_3 at the TiO_2 surface should lead to the formation of $^{\bullet}OH$ and $^{\bullet}OOH$ species, which are active oxidizing species able to promote BPA degradation. Furthermore, ozone may act as an electron scavenger for photogenerated electrons from TiO_2. Such effect may slow down the recombination between photo-generated electrons and holes at the TiO_2 surface, thus promoting the oxidation of BPA and of its intermediates. Specifically, the electron transfer from TiO_2 to O_3 generates one hydroxyl radical for each trapped electron through the formation of ozonide radicals.[6,41] Previous results by Rivas *et al.*[42] showed a synergistic effect of the combined UV light and ozone treatment, but in that case, a powerful UV-C source was employed. Indeed, at wavelength lower than 300 nm, ozone is photolyzed to highly reactive O (1D) species, which in turn generate $^{\bullet}OH$ radicals, thus increasing the process efficiency. On the other hand, when near UV irradiation is employed, O_3 photolysis generates the much less active H_2O_2.[6]

Reaction kinetics

During the sole ozone treatment, at constant O_3 flux, the rate of BPA degradation is best represented by a zero order reaction. This can be the result, on one side, of the high initial concentration of BPA accompanied by low degradation, and, on the other side, of the invariant ozone content in the reacting mixture due to the continuous O_3 fluxing. Instead, The rate of the homogeneous reaction of BPA disappearance is observed to increase with the ozone concentration. These results are in agreement with data by Lee *et al.*,[43]

who found that the rate of BPA degradation was sensitive and proportional to the ozone feed rate, but insensitive to pH and the concentration of BPA.

In the case of the sole photocatalytic degradation of BPA several authors adopted the Langmuir-Hinshelwood (LH) model to interpret the rate of the process.[44] This equation applies in all cases in which heterogeneous catalytic processes control the kinetics of the reaction:

$$r = -\frac{dC}{dt} = \frac{\kappa KC}{1+KC} \quad \text{(eq. 5.3)}$$

where r represents the rate of reaction proceeding in time (t), κ the degradation rate constant, and K the adsorption equilibrium constant. When $KC \ll 1$ the equation turns into a pseudo-first order decay kinetics where $\kappa_{app} = \kappa K$.

During the present combined O_3 + TiO_2 photocatalytic treatment, the heterogeneous degradation process may involve reactions between the organic solute adsorbed onto the TiO_2 surface and the semiconductor holes, O_3 and $^{\bullet}OH$ radicals. At the same time, also O_3 itself may provoke reactions onto the adsorbed molecules.

In agreement with most part of literature results, the best empirical equation for the present lower initial BPA concentrations was actually found to follow a pseudo-first order kinetics, according to the LH model. At higher concentrations a reaction order of 0 was found. This is still consistent with the mechanism implied by eq. 5.3, *i.e.*, a decomposition governed by a surface reaction between the adsorbed reagent and O_3/OH; with increasing BPA concentrations KC becomes in the order of unity and the dependence of the rate on BPA is better represented by a reaction order 0. In other words, it can be said that the active sites for the degradation reaction remain the same for all BPA concentrations. Almost no inhibition of the catalyst occurs[45] when the BPA initial concentration is low. However, as the BPA initial concentration increases, more and more BPA molecules (and their by-products) are adsorbed on the surface of TiO_2 film. The accumulation of BPA molecules at the titania surface may result in adsorption competition for the active sites between BPA molecules. The surface area of the photocatalyst becomes the rate limiting parameter for the reaction leading to an apparent zero order rate with respect to the BPA concentration (Tab. 5.6).

Test		κ_{app} x 10^6 ($M\ s^{-1}$)
Single experiments	UV	-
	TiO_2 + UV	2.6 ± 0.2
	O_3	8.5 ± 0.9
Combined experiments	O_3 + UV	10.5 ± 0.6
	O_3 + TiO_2	8.7 ± 0.8
	O_3 + TiO_2 + UV	36.7 ± 0.4

Table 5.6. "Apparent" kinetic constants for the separate and combined tests. UV = photolysis; TiO_2 + UV = photocatalysis (TiO_2); O_3 = ozonation.

Degradation mechanisms

The mechanisms of BPA degradation during ozonation and photocatalysis, as separate treatments, have already been widely investigated in the literature. The principal pathway of BPA oxidation by ozone is reported to be its direct reaction with the contaminant.[32,46] In particular, ozone can act as a direct oxidant or decompose to $^{\bullet}OH$ radicals, especially in alkaline conditions. A large fraction of these radicals, which are much less selective and much more reactive than ozone, are scavenged by the water matrix.[32] Due to its electrophilic character, ozone commonly reacts with aromatic rings by electrophilic substitution.[34]

In the case of the sole TiO_2 photocatalytic treatment, Watanabe *et al.*[47] showed that the reaction pathway, followed an initial attack of $^{\bullet}OH$ and $^{\bullet}OOH$ radicals on the two methyl groups and the subsequent cleavage of the methyl moieties to produce simple aldehydes, acids and carbon dioxide.

HPLC-MS measurements were performed at the end of the present combined O_3 + TiO_2 + UV experiments, in order to assess the nature of the intermediates. Data relative to 1.5 mM BPA after 180 min (incomplete mineralization) are reported in Fig. 5.10. In addition to the most intense peak centered at 4.4 min, attributable to BPA molecule, several peaks at different retention times (from 2.6 to 4.0 min) can be observed. On the grounds of the mass values, the peaks at 4.0 and 2.6 min can be attributed to the compounds labelled as B_1 and B_2, respectively (Fig. 5.10).

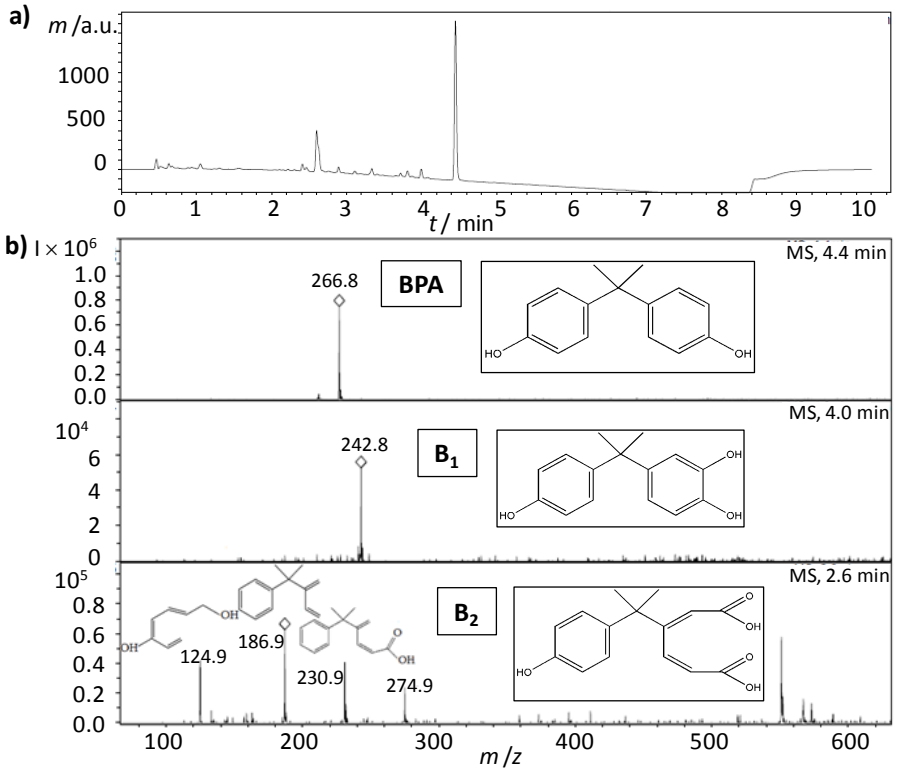

Figure 5.10. HPLC peaks for different retention times (**a**) and b relative mass spectra (**b**) of 1.5 mM bisphenol A (BPA) solution at the end of the combined ozonation and photocatalysis. The chemical structures of compounds corresponding to the attribution of fragmentation peaks for compound B_2 are also reported. The first step of the oxidation reaction leads to compound B_1 which further degrades to opened ring products (*e.g.*, B_2), and finally to CO_2 and water.

Thus, a possible BPA degradation route, starting with the •OH direct attack at the aromatic ring is proposed. The nature of the intermediate products observed by HPLC-MS support the first formation of compound B_1 as the result of the attack of •OH to the aromatic ring in orto position with respect to the former •OH group. The progressive oxidation of the intermediates may lead first to the progressive loss of CO_2 (B_2) and to the final formation of aromatic ring opening intermediates, as depicted in Fig. 5.11.

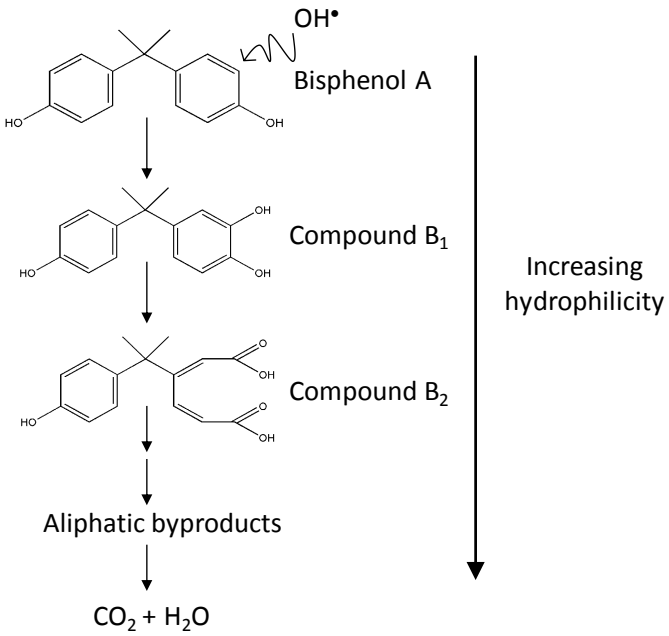

Figure 5.11. Proposed reaction pathway for the degradation of the BPA molecule.

FTIR determinations were performed in order to gain information on the nature of intermediate reaction species adsorbed onto the photocatalyst.[48,49] Fig. 5.12 reports vibrational modes of TiO_2 exhausted samples withdrawn from the reacting mixture at the end of the reaction. The blank curve relative to the pure oxide, was subtracted. The spectrum of the pure BPA (a) is also reported for the sake of comparison; two curves pertaining to different BPA concentrations (curve b: 1.5mM and curve c: 0.3 mM) are reported. Appreciable amounts of un-reacted BPA molecules are present in the case of the higher starting concentration; while for the 0.3 mM BPA the spectral region at about 1700 cm^{-1} shows the presence of possible adsorbed carbonylic species, which support the formation of compounds like B_2, as in the proposed mechanism.

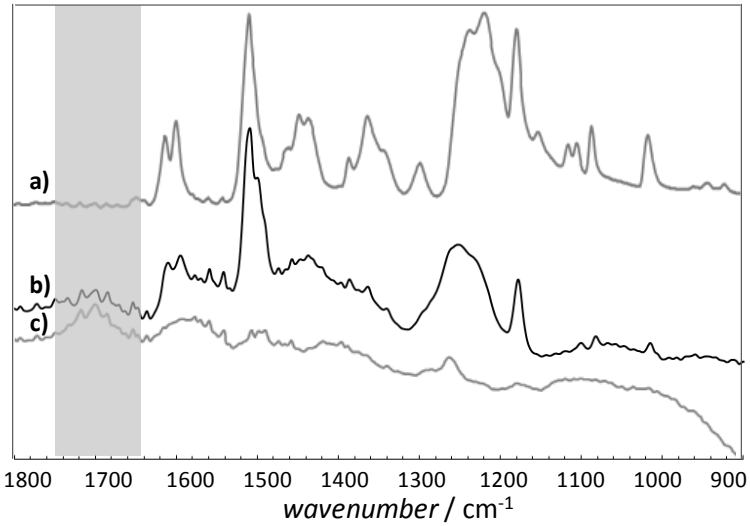

Figure 5.12. ATR-FTIR spectra of pure bisphenol A (BPA, **a**) molecule and P25 (Evonik) titania sampled at the end of the O_3 + TiO_2 + UV run in the case of 1.5 mM (**b**) and 0.3 mM (**c**) starting BPA concentrations. For each oxide, the curve of the relative bare TiO_2 was subtracted. The residual presence of carbonyl moieties can be appreciated in the case of the highest BPA concentration in the range 1650–1750 cm^{-1}.

5.3. Cr(III) and Cr(VI)

The pollutant

Unlike most organic pollutants, metals are particularly problematic for the environment since they are not biodegradable and can accumulate in living tissues, thus becoming concentrated throughout the food chain. While they are essential at low doses as micronutrients, in higher doses they can detrimentally affect the health of most living organisms.[50-52] As a consequence, the presence of heavy metals in wastewaters causes great environmental damages and human health problems.

Among hazardous metal ions, hexavalent chromium, widely used in several industrial processes (metal plating, leather tanning, paint making, *etc*.),[53-55] is one of the highly harmful pollutant due to its toxicity and easy migration. Moreover, it is a strong oxidizing agent that is carcinogenic and mutagenic and diffuses quickly through soil and aquatic environments. Since it does not form insoluble compounds in aqueous solutions, separation by precipitation is not feasible. However, Cr(III) cations are not as mobile and toxic for the environment as Cr(VI) oxyanions. Like many metal cations, Cr(III) forms

insoluble precipitates. Thus, reducing Cr(VI) to Cr(III) simplifies its removal from effluent and also reduces ts toxicity and mobility.

Therefore, the removal of Cr(VI) is a general concern not only for the problem of its removability, but also for its difficult analytical speciation and determination. Thus, the experimental work has been twofold, since both its determination and its removal are relevant debated issues.

Traditionally, spectroscopic measurements (FAAS, GF-AAS, ET-AAS and ICP-tandem), chromatographic systems (HPLC, GC and IC), chemiluminescence methods and mass spectrometry are the most commonly used techniques to monitor chromium species. Although such techniques provide low detection limits (at the ng L^{-1} or µg L^{-1} level), they are time consuming, need expensive equipments and laborious sample pretreatments.[56] Also electroanalytical determinations by DPAdSV (Differential Pulse Adsorptive Stripping Voltammetry) at the HMDE (Hanging Mercury Drop Electrode) are reported[57-59] as alternative methods to follow Cr(VI) species by using an electroactive probe, mostly pyrocatechol violet (PCV). Because of the several disadvantages of HMDE due to its toxicity, contamination and difficult handling, despite its good performances, in this work it has been replaced by a commercially available and environmentally friendly Bi-SPE (bismuth screen-printed electrode) in a square wave voltammetric determination. This method offers many advantages: besides being a mercury-free analytical technique performed without stripping, thus lowering analysis time, Bi-SPEs are portable - permitting *on-site* analysis - cheap and disposable, avoiding surface contamination and difficult polishing steps. The new analytical method also shows negligible matrix interferences and has proved to reach high sensitivity and low detection limits (in the range of µg L^{-1}, around 0.01 µM).

The two techniques are compared in the Cr(VI) determination by means of pyrocatechol violet using Square Wave Voltammetry (SWV) for the Bi-SPE case and Differential Pulse Adsorptive Stripping Voltammetry (DPAdSV) for the HMDE case.

From the chromium abatement point of view, conventional chemical methods to reduce Cr(VI) to Cr(III) lead to the precipitation of noxious hydroxide sludges that are difficult to handle and to remove.[60,61] Recently, many efforts

have been devoted to the development of alternative removal processes such as photocatalysis assisted by TiO_2 nanoparticles.[60,62-64] Besides the more simple photolysis and electrocatalytic removal, also photoelectrocatalytic tests have been recently reported in the literature.[65]

In this context, the photocatalytic performances of different titania films, obtained by electrophoretic deposition (EPD), towards the Cr(VI) reduction have been studied. Besides, an innovative and environmentally friendly electroanalytical determination of chromium species in solution has been adopted.

The photocatalyst

Three different types of titania powders were chosen for photocatalytic tests and deposited as films on Ti grids: two commercial samples, P25 (Evonik) and Hombikat UV 100 (Sachleben), and a home-made sample, labelled as "T" (see paragraph 2.1.1).

High purity Ti grids (10 mm × 50 mm × 1 mm) were sand blasted and etched in oxalic acid 10 % at 80 °C for 60 min, followed by immersion in an ultrasonic bath with acetone and rinsing with water. Electrophoretic deposition was used to deposit the thin TiO_2 layers starting from a suspension of the TiO_2 powder (3.5 g L^{-1}) in acetylacetone, for a fixed time (90 s). Two depositions at 20 V were performed followed by a final calcination (500 °C for the first layer in order to enhance the adhesion between the TiO_2 layers and the Ti supports, and 300 °C for the second layer to preserve the surface area of the particles).

SEM pictures of the grids, taken by LEO 1430, show that the morphology of the powders at nanoscale remained unaltered (Fig 5.13). The TiO_2 film thickness on the Ti grid is estimated to be about 10 µm.

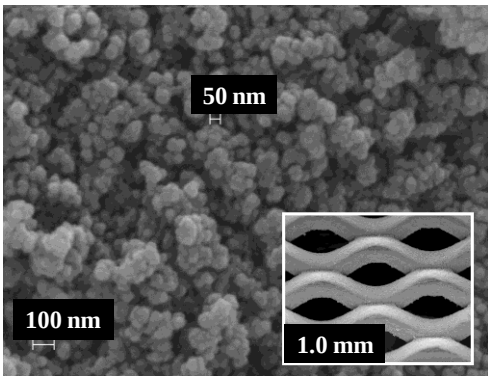

Figure 5.13. SEM image of the titania layer employed in Cr(VI) photo-reduction.

Photocatalytic tests

Materials

Cr(VI) solutions were prepared by dissolving the appropriate amount of potassium dichromate (Fluka ≥ 99.5 %) in water. Adequate quantities of chromium(III) nitrate nonahydrate were dissolved in water to obtain Cr(III) solutions. Pyrocatechol violet (PCV, Fluka) and N-(2-Hydroxyethyl)-ethylenediamine-N,N',N'-triacetic acid (HEDTA, Fluka ≥ 98.0 %) were used as chelating agents, dissolved in water. Acetate buffer (pH = 4.7) was obtained by dissolving acetic acid (Fluka >99.8 %) and sodium acetate (anhydrous, ≥99.0 %) in water. Potassium nitrate solution was prepared from potassium nitrate powder (J.T. Baker >99.0 %). 2-Propanol, nitric acid (Fluka 65 %) and acetylaceton ReagentPlus were employed for photocatalytic experiments.

The starting solutions were prepared by dissolving potassium dichromate (0.01 mM), isopropyl alcohol (50 mM) and nitric acid in ultrapure water, at a pH around 4. The isopropyl alcohol was chosen as scavenger in order to avoid the electrons-holes recombination. The photocatalytic reduction was conducted in a Pyrex jacket glass cylindrical reactor (V = 200 mL), thermostatted at (30 ± 1) °C by continuous water recirculation during the runs (reaction time = 90 min). The photon source was provided by a UV lamp (see the Appendix for details) fixing the distance from the reactor at 30 cm. At the end of the photodegradation tests, the used TiO_2 powders immobilized onto Ti grids were sonicated in ultrapure water in order to perform XPS analyses

Photocatalytic results

The whole work done in the group laboratories on this topic comprises both the photocatalytic reduction of Cr(VI) and its analytical estimation in solution. The analytical part allows the fine trace estimation of Cr(VI) during the photocatalytic degradation. In the following, the main focus will be kept on the photocatalytic part. Details and supplementary electrochemical experiments, such as those performed to test the possible interference by Cr(III) - the reduced species formed during the photocatalytic tests - can be found elsewhere.[66]

Once optimized the electroanalytical determination parameters, having reached a detection limit (calculated according to IUPAC rules) of 0.01 µM and excellent relative linearity behavior, photocatalytic experiments were performed on the electrodeposited commercial and home-made titania nanopowders. Since the reduction potential of Cr(VI) to Cr(III) is pH dependent and the thermodynamic driving force decreases with increasing pH, the reduction is favoured at very low pH, typically around 2.[61,64,65] Here, to meet environmental concerns, a slightly acidic condition (pH 4) was adopted. Provided that the addition of organic additives can act as hole scavengers to limit the electron-hole recombination,[53-55,67] in the present case 50 mM isopropyl alcohol (IPA) was used as sacrificial molecule.

Hombikat UV 100 commercial nanopowders in slurry and electrodeposited onto titanium grid by EPD definitely showed different performances towards Cr(VI) photoreduction. Fig. 5.14 shows the comparison between the obtained results, normalized by the weight of the photocatalyst. Surprisingly, the photoreduction in the case of immobilized titania particles is markedly greater than that of suspension powders, reaching the total removal of Cr(VI) in around 60 min. This result is not trivial, since opposite trends are present in the literature concerning the limited photocatalytic activity of titania deposited layers with respect to suspended particles. Many authors demonstrate that the resulting efficiency of the Cr(VI) photocatalytic reduction is substantially lower than that with a TiO_2 powder suspension, because of the relatively small surface area of thin film. Yoon *et al.*[68] reported that with an initial concentration of Cr(VI) as low as 2 mg L^{-1}, the complete

photoreduction of Cr(VI) to Cr(III) over TiO_2 nanotubes costed as long as 120 min.

Our TiO_2 films are deposited onto grids with a large exposed surface area, thus preserving the active adsorption sites of the nanopowders. Moreover, as reported in a previous work from the group,[69] strong adhesion is achieved by an optimized heat treatment: 500 °C for the first layer in order to enhance the adhesion between the TiO_2 layers and the Ti supports, and 300 °C for the second layer to preserve the surface area of the particles. As a consequence, the best degradation in the case of TiO_2 thin films can be explained on the grounds of the total absence of turbidity, which is a typical drawback of the slurries; in these conditions the actual irradiation power of the lamp is preserved.

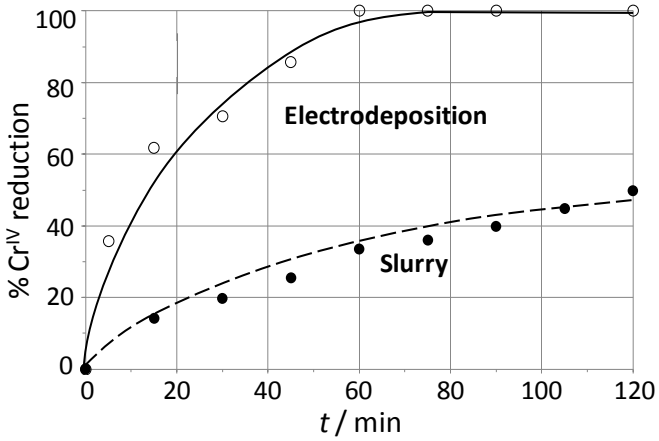

Figure 5.14. Comparison between the Cr(VI) reduction performances of Hombikat powders in slurry or electrodeposited on Ti grids. Inset: SEM image of the titania layer.

Additionally, the adhesion of the titania particles on the Ti grids is good. The stability of the film was verified by performing reused tests on the catalyst also by washing and UV-irradiating regeneration. The photodegradation loss of the used film was about 20 % and 30 % for the first and second run, respectively. The regeneration test slightly increased the final photocatalytic reduction (about 5 %) with respect to the used catalyst.

Fig. 5.15 displays the percentage of Cr(VI) disappearance as a function of the reaction time for the studied photocatalysts.

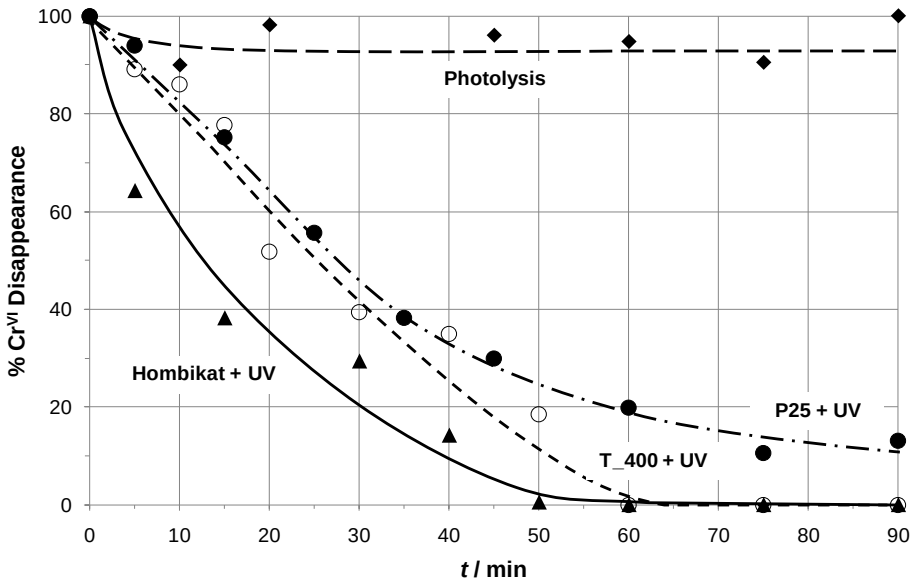

Figure 5.15. Results of the photocatalytic tests for photolysis, adsorption and photocatalysis of Hombikat, P25 and T.

The direct photolysis of Cr(VI), by using a UV-A lamp, is negligible (<10 %). In the absence of irradiation, the depletion by adsorption of Cr(VI) at the titania surface after 90 min reaction time reaches different values (see Table 5.7), proportionally to the specific surface area of the samples. All the tested samples, both commercial and home-made, show excellent photocatalytic behavior. The photoreduction sequence follows the relative adsorption features: the best performance is obtained in the case of the Hombikat, having the higher surface area, while a similar photoactivity occurs for P25 and T sample, even if after 60 min the home-made one achieves the total Cr(VI) reduction.

Sample	Adsorption (%) after 90 min
P25	25
T	31
Hombikat UV100	58

Table 5.7. Adsorption percentage of all tested electrodeposited samples after 90 min (dark tests).

Determination of chromium speciation

In order to evaluate the speciation of chromium at the end of the photocatalytic tests, the used TiO_2 powders, scratched by the metal grid and subsequently dried, were submitted to XPS analyses. High resolution scan of Cr 2p multipeaks (Cr $2p_{3/2}$ and $2p_{1/2}$) is shown in Fig. 5.16 for P25 as a representative sample. The best fit procedure yields the presence of three components for each doublet attributable to Cr (VI), Cr(III) and Cr(0).[70] The presence of metallic chromium, thermodynamically inexpiable on the basis of the relative TiO_2 and Cr(III)/Cr(0) potentials, can be justified only by the occurring of possible redox reaction between the scavenger radicals (2-propanol, in the present case, see Experimental Section) and Cr(III)[71] adsorbed at the TiO_2 surface.[64]

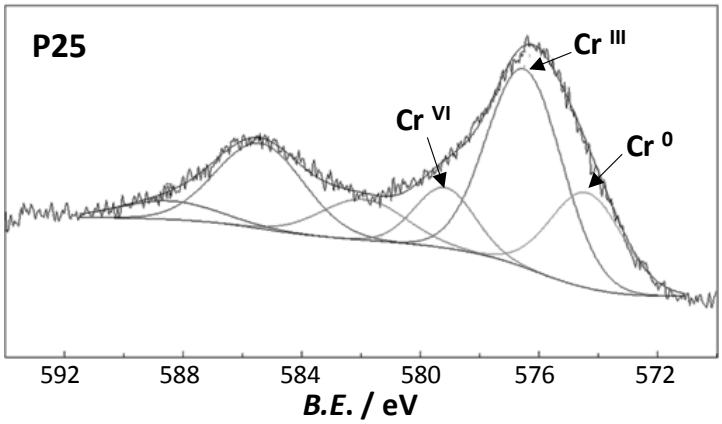

Figure 5.16. Cr $2p_{1/2}$ (BE >580 eV) and Cr $2p_{3/2}$ (BE <580 eV) XPS components in the case of P25 used sample at the end of the photocatalytic test (90 min).

Tab. 5.8 reports the binding energies of Cr(VI), Cr(III) and Cr(0), from the fitting elaboration of the Cr $2p_{3/2}$ peak, for the adopted samples; the atomic ratios between each component and the total chromium is also evaluated. The presence of a considerable amount of Cr(III) adsorbed at the titania particles confirms the efficient photoreduction process for all the samples, as above mentioned. Moreover, in the case of the two commercial powders Cr(0) is appreciable; this occurrence could be justified by the interplay between the scavenger radicals, produced by the photocatalysis and the different physico-chemical features of the nanosized powders during the photocatalytic tests.[64]

Sample	B. E. Cr $2p_{3/2}$ (eV)			Cr^{VI}/Cr	Cr^{III}/Cr	Cr^{0}/Cr
	Cr^{VI}	Cr^{III}	Cr^{0}			
P25	579.2	576.8	574.6	0.27	0.59	0.14
T	580.1	577.1	—	0.31	0.69	—
Hombikat UV100	579.4	576.5	574.2	0.28	0.55	0.17

Table 5.8. Binding energies and ratios of Cr(VI), Cr(III) and Cr(0) on Cr $2p_{3/2}$ fitting.

Reaction kinetic

To obtain the rate constant (*k*) values for the different catalysts (Tab. 5.9), concentration ratios in a logarithmic scale were plotted against time, with *k* values obtained by the linear slopes. All the graphs present good linearity and follow closely the photocatalytic sequence, previously discussed (P25 < T < Hombikat).

Fig. 5.17 reports the case of P25, as example. For all the samples the reaction kinetics can be described by a pseudo-first order rate equation. This finding is not in accordance with what reported by Kajitvichyanukul *et al.*[72] for TiO_2 deposited layers, since they statistically found reaction rates following a zero order kinetic model. When comparing Cr(VI) reduction using thin TiO_2 film and P25, they reported a first order kinetics for the powder. A detailed study on chromium(VI) photocatalytic reduction has been performed by Gimenz and coworkers using a continuous flow system.[73] In their work, the kinetics and the influence of catalyst concentration and pH on the reaction rate have been analyzed and supported by data from electronic microscopy and adsorption techniques. Kinetic results showed a half-order reaction at pH lower than 4, and a first-order reaction for pH above 4. In the latter case, deactivation of titania was found to occur, due to the fouling of titania caused by chromium hydroxides. Their proposed model for catalyst deactivation described the performance of the catalyst at the different experimental conditions tested.

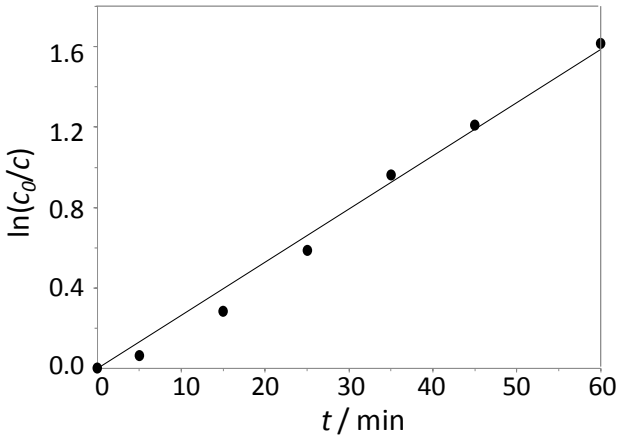

Figure 5.17. Logarithmic plot adopted to obtain the rate constant for P25 by applying a first-order rate equation.

Sample	$k \times 10^2$/ min^{-1}	R^2
P25	2.5 ± 0.2	0.97
T	3.0 ± 0.2	0.98
Hombikat UV100	4.8 ± 0.3	0.98

Table 5.9. Rate constants for P25, T, and Hombikat obtained by applying a first-order equation.

Then, in order to corroborate our results, the *k* values together with the adsorption percentage in the dark of Cr(VI) after 90 min are plotted as the function of the surface area (Fig. 5.18); unexpectedly a very similar behavior occurs, suggesting that, notwithstanding the use of immobilized catalysts, the adsorption mechanisms of Cr(VI) at the surface of the oxide during the photoreduction removal is the rate determining step of the process. This observation indicates that the present reaction is favoured by small crystallites and large surface area. Wang *et al.*[74] found that the photocatalytic reduction of Cr(VI) under UV irradiation and in the presence of titania dispersion, was dependent on both specific surface area and crystalline structure of TiO_2 in the absence of any organic compounds, but was dominated by the specific surface area of TiO_2 in the presence of organic compounds, acting as scavenger molecules.

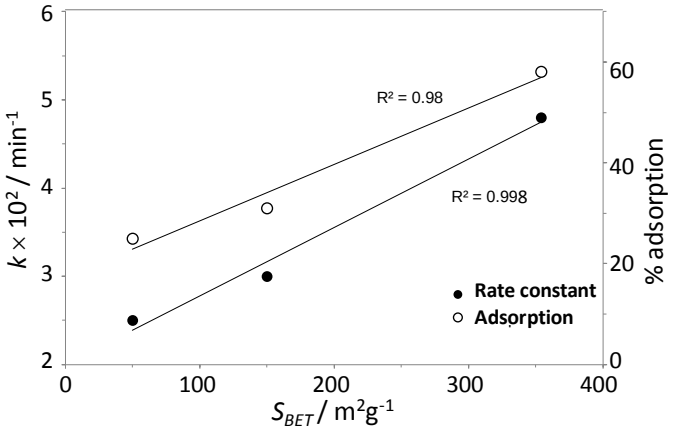

Figure 5.18. Linear trends of pseudo-first order kinetic constants and adsorption in the dark after 90 min as a function of surface area of the different TiO_2 samples.

Efficiency of HMDE and Bi-SPE in photocatalytic analyses

For the electroanalytical determination Cr(VI) in solution during the photocatalytic tests, the HMDE method was also employed for comparison, showing that bismuth screen-printed electrodes offer similar or even better results, being less affected by interferences of this complex matrix.

To compare the efficiency of both methods in a practical situation, analyses were performed on the same samples derived from T photocatalytic tests with HMDE and Bi-SPE. As Fig. 5.19 shows, HMDE and Bi-SPE results are in good accordance, but HMDE is affected by photocatalytic matrix interferences, giving scattered values. To the contrary, the complex matrix has not a great influence on the Bi-SPE.

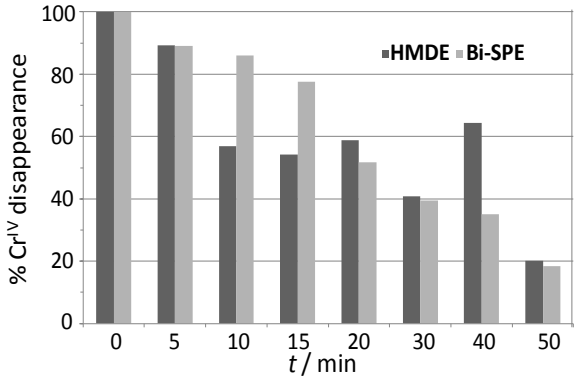

Figure 5.19. Cr(VI) disappearance in photocatalytic test with sample T monitored by HMDE and Bi-SPE.

5.4. Ethanol

The pollutant

Even if ethanol is one of the best tools we may have to fight air pollution from vehicles, it has been calculated that ethanol would end up dumping more ozone into atmosphere than gasoline does. Indeed, ethanol is an important atmospheric pollutant: it is a commonly used industrial solvent and a fuel additive, besides being produced by breweries and bakeries. Moreover, atmospheric concentrations of this pollutant are expected to rise in consequence of the use of ethanol as biofuel in the automotive sector (bioethanol). Even if ethanol itself has a limited toxicity, its main degradation intermediate, acetaldehyde, is far more toxic and plays a crucial role in photo-oxidative smog processes. Besides, acetaldehyde is an important indoor pollutant (acetaldehyde concentrations are very often higher indoors than outdoors), released by some building materials such as rigid polyurethane foams, and some consumer products such as cigarettes, adhesives, coatings, lubricants, inks, and nail polish remover.

The photocatalyst

In the following two types of photocatalytic tests will be exposed. The first one was performed in liquid media, employing N-TiO_2 photocatalysts in powdery form (as a slurry), and monitored by total organic carbon analysis. On the contrary, the second one involved Ag- and N,Ag-TiO_2 samples deposited on a glass substrate, and gas phase ethanol degradation was followed by gas chromatography.

N-TiO_2

Photocatalytic set up

To test the photoactivity of the N-doped samples, both as-prepared and after being stored several days in the dark, the degradation of ethanol in aqueous media was monitored at 308 K in a custom-made Pyrex glass batch reactor.

The initial concentration of ethanol was set at 1 mM, corresponding to a value of about 25 ppm of organic carbon as read by TOC analysis. Fresh ethanol solutions were prepared before each test. N-TiO_2 powders were finely ground in a mortar and used with a concentration of 1 g L^{-1} as slurry in 670 mL of the above mentioned ethanol solution. Photolysis experiments (in the absence of

photocatalyst) and dark tests were performed to evaluate the possible degradation of the organic molecule and the correspondent adsorption, respectively. Both types of experiments led to a 10 % of mineralization. The reproducibility of the results was checked by repeating the tests and was found to be within acceptable limits (5 %).

The proceeding of the reaction was followed by TOC analyses using a Shimadzu TOC-V CPN total organic carbon analyzer. FTIR (Fourier transform infrared) spectra on the powders before and after photocatalysis were recorded by a Jasco 4200 accessorized by attenuated total reflectance (ATR) module, in the region 1000–4000 cm^{-1}.

Photocatalytic results

Ethanol degradation tests under UV and visible irradiation were performed for all these N-doped samples. The concentration of this pollutant was quantitatively monitored in time using TOC. In the degradation curves, the experimental points were interpolated by linear regressions with high correlation coefficients (R^2 >0.984) to obtain the kinetic rate constants. From such results, ethanol breakdown seemed to follow a zero order kinetics. However, in the literature a first order reaction has also been reported for ethanol photocatalytic oxidation in the gas phase,[75] probably due to the competition in adsorption between ethanol and its main degradation intermediate, acetaldehyde.[76-79] This byproduct is supposed to deeply affect the rate determining step of the reaction. Since it strongly adsorbs to the titania surface, the catalyst poisoning could partially occur: it can't be excluded that acetaldehyde somehow saturates the active sites of the photocatalyst thus eventually inhibiting a faster proceeding of ethanol degradation. Moreover, TOC analysis merely evaluates organic carbon based on the number of C atoms in the molecule, not discriminating between ethanol and acetaldehyde. This could account for the decay of ethanol concentration following a trend which is not steep exponential. Indeed, as already stated, the ethanol concentration decreased steadily over the whole reaction time.

Dark test, photolysis and both UV and visible photocatalysis by using a freshly prepared selected sample (TN_NH_3) are compared in Fig. 5.20. It can be immediately observed that TN_NH_3 shows relatively poorer photocatalytic activity under visible light than under UV (about 23% and 57% after 6 h,

respectively), while adsorption and photolysis account for a very small part of ethanol mineralization. It should be noted that the final mineralization in the case of visible photolysis is slightly higher with respect to the UV case due to the higher effective power of the lamp (see the Appendix).

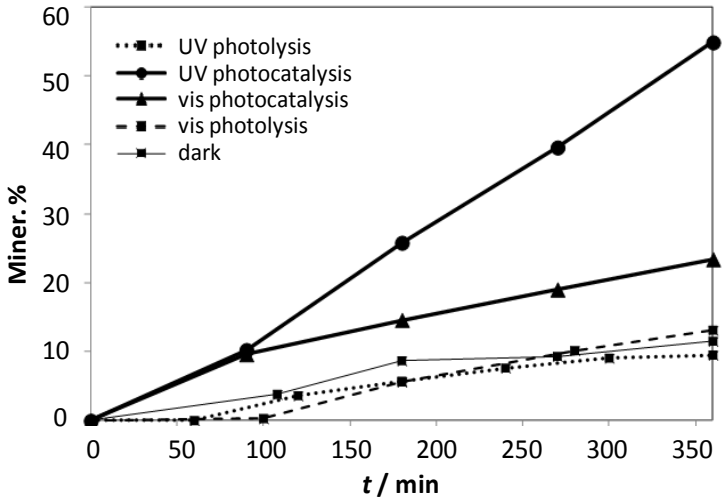

Figure 5.20. Ethanol mineralization curves indicating the performances of TN_NH_3 sample freshly prepared: photocatalysis under UV and visible light, photolysis under both types of illumination and dark experiment for comparison.

TN_NH_3 sample has been selected as a representative case of all our N-doped samples. It has to be underlined that the activity under visible light, though relatively low, is however not poor since the mineralization and not only the pollutant disappearance has been evaluated. In Table 5.10 the final ethanol mineralization percentages are reported for all "fresh" N-doped samples under either UV or visible irradiation.

Sample	% mineralization UV	% mineralization vis
TN_TEA	65	20
TN_urea	63	17
TN_NH_3	62	24

Table 5.10. Photocatalytic results expressed as ethanol mineralization percentage for all "fresh" N-doped samples under UV and visible irradiation.

Apparently, for each irradiation source all values are very similar and no appreciable differences can be noticed. Different nitrogen sources introduce relevant differences in the material features, but in our case do not lead to striking dissimilarities in the photocatalytic performance of the samples since, presumably, different factors tend to counterbalance each other. This is why all N-doped samples do not show a distinct final mineralization, converging more or less to the same values. Moreover, from the structural point of view, all N-doped titania samples show high tendency for crystallization, no increase in crystal size due to any specific dopant and a fairly equivalent predominance of the anatase polymorph, which is known to be more reactive in photocatalytic processes.[72,80] The chemical structure of the organic compounds adsorbed on the oxide surface was analyzed using FTIR in the attenuate reflectance mode. Yu and Chuang[79] found out that the adsorption of ethanol on the TiO_2 surface at room temperature forms both molecularly adsorbed and dissociatively adsorbed ethanol (adsorbed ethoxy), which they reported to exhibit similar bands of C–H stretching vibrations at 2971 and 2931 cm^{-1}, as well as a C–O stretching vibration at 1052 cm^{-1}. We could not clearly observe such bands in our spectra. However, the main peaks refer to adsorbed acetaldehyde and reaction intermediate species (acetic acid, formaldehyde and formic acid), as also reported by Yu and Chuang[79] and illustrated in Fig. 5.21 (a selected range of the spectrum obtained for TN_NH_3 by subtracting the curves of the as prepared samples from the spectra of the used catalyst is displayed). More specifically, adsorbed acetaldehyde gives rise to the presence of a peak at 1718 cm^{-1}. Also adsorbed acetic acid (CH_3COOH_{ad}) could be present, owing to the peak found at about 1684 cm^{-1}. The products of complete mineralization also give characteristic bands ($CO_{2,ad}$ at 2363 cm^{-1} and H_2O_{ad} at 1651 cm^{-1}). Other authors have also suggested that organic species may displace the adsorbed water from the catalyst surface.[76,77,79,81]

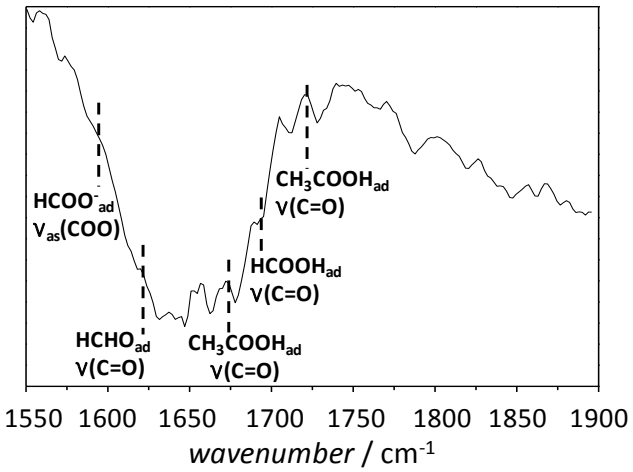

Figure 5.21. FTIR-ATR spectra of the same sample after the whole time of reaction (6 h) under UV light. The curve of the as prepared catalyst was subtracted.

Fig. 5.22 highlights the difference between the photocatalytic activity under UV for "fresh" and "old" samples, for all doped materials, as for the photocatalytic degradation of the organic compound ("Δ_{min}" values obtained as the difference in ethanol mineralization between "fresh" and "old" – two months – samples, at each time "t"). It can be clearly seen that the ammonia doped oxide exhibits the larger split between the "fresh" sample tested after 24 hours from the calcination and the same sample calcined about one or two months (40 up to 60 days) before.

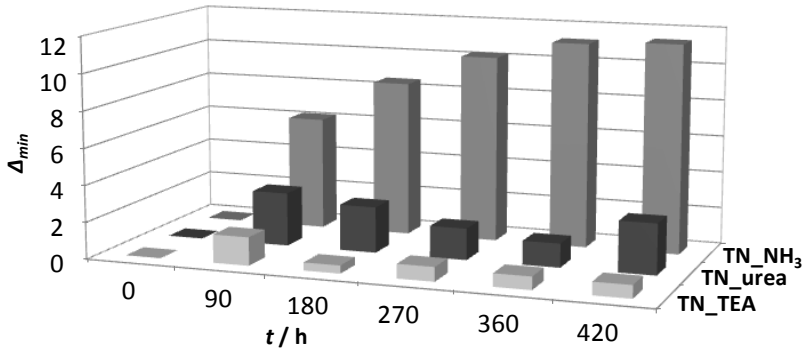

Figure 5.22. Difference between "fresh" and "old" sample performance in ethanol mineralization (Δ_{min}) for TN_urea, TN_NH_3 and TN_TEA under UV illumination.

The rate constants at room temperature in the UV case were calculated according to the zero order reaction law and listed in Table 5.11. It can be noticed that the main difference lies between "fresh" and "old" samples performances, while the rate constants of the three "fresh" doped oxides mainly level off to very similar values, in the range 32-36 $\times$ 10^{-3} mg L^{-1} min^{-1}.

Sample	$k \times 10^3$ (mg $L^{-1}min^{-1}$)
TN_urea	32
TN_urea_old	33
TN_NH_3	36
TN_ NH_3_old	27
TN_TEA	36
TN_TEA_old	31

Table 5.11. Kinetic constants of the same photocatalytic oxidation for all doped samples.

All the N-doped samples degraded about 50 % of the initial ethanol concentration in 6 hours. The freshly prepared TN_urea, which has the highest specific surface area among the N-doped samples, does not show the highest rate constant (Table 5.11), even though all values for the "fresh" samples are very similar to each other. On the other hand, the adsorption phenomena, evaluated in the dark on the same time scale as the photocatalytic tests for all these oxides, take place according to their specific surface areas.

When comparing Fig. 5.22 with the EPR intensity decay for "aged" samples, it should be noted that the photocatalytic tests remarkably follow the trend obtained by EPR for the concentration of the paramagnetic species, indicating a clear decay for TN_NH_3. This means that such sample contains a number of paramagnetic species which after about two months from the synthesis and calcinations is less than half the initial value. Also within a much shorter span of time the amount of paramagnetic centers is diminished with respect to that measured on the as-synthesized sample. Consequently, if the photocatalytic activity of N-doped titania is directly or indirectly related to the presence of paramagnetic species,[82,83] it should be expected not to be favoured in the case of our ammonia-doped sample tested after one or two months from the

synthesis. Indeed, Δ_{min} is much higher for TN_NH_3 than for TN_TEA and TN_urea. As for these other two N-doped samples, the former exhibits a very low intensity of the paramagnetic signal even immediately after the preparation, while the latter has the peculiarity of a nearly constant amount of paramagnetic species. Accordingly, TN_TEA and TN_urea samples do not display a pronounced photocatalytic advantage in using the "fresh" sample instead of the "aged" one (Fig. 5.22).

Curiously, TN_TEA, though presenting a much lower concentration of paramagnetic species –already as a "fresh" sample – and a lower surface area, is as active as TN_NH_3. This superior photocatalytic activity of TEA-doped titania has been reported elsewhere by our group[2] and other authors.[84,85] Kometani *et al.*[84] reported that the most efficient N-doping could be accomplished by the batch treatment with a small amount of TEA; the as-obtained catalyst showed the highest photocatalytic activity for both the reduction of Ag^+ ions and the degradation of methylene blue under visible light irradiation. This result is justified by the authors in view of the small bond dissociation energy of about 231 kJ mol^{-1} for TEA ($3 \times E_{C-N}$), which is far lower than that for ammonia (about 1.170 kJ mol^{-1}, $3 \times E_{N-H}$). Thus, the authors also affirm that the highest dissociation energy for ammonia leads to the lowest efficiency of nitrogen doping, though, in any case, the thermal energy required to generate N atom is considerably large, resulting in the low efficiency of nitrogen doping in general. By comparing titania systems doped with three different organic sources, Ananpattarachai and coworkers found out the mineralization ability towards 2-chlorophenol in the order diethanolamine > triethylamine > urea > undoped TiO_2.[85] Thus, once again TEA-doped titania turned out to be better performing than urea-doped, which the authors reported to be very homogeneous in particle size distribution (contrary to the case of TEA-TiO_2 powders which presented aggregates consisting of smaller – 100 nm – to larger – 500 nm – particles).

In our case, the above mentioned collapse of the total pore volume for TN_TEA and the hindered accessibility of the pores with smaller diameter owing to the adsorbed species in the micropores for TN_urea are different reasons which both limit the photocatalytic activity. It could be argued that the accessibility of the inner surfaces of these catalysts, doped with organic N sources, is mainly blocked.

TiO_2 synthesised with organic materials under air atmosphere at same temperature also provided no significant absorption in the visible light region. This information suggests that organic materials introduced the nitrogen to N-doped TiO_2 under the nitrogen atmosphere reaction and visible light absorption ability is mainly dependent on the type of nitrogen dopant. Among the three different nitrogen sources, the urea dopant definitely leads to the most active doped titania even after 2-month aging.

Ag-TiO_2 and N,Ag-TiO_2

Photocatalytic setup

28 mg of powdery oxide were suspended in 5 mL 2-propanol and sonicated for 15 min. Then, the suspension was drop-casted and dried onto a circular glass substrate.

The as-prepared TiO_2 film was positioned inside the jacketed reactor (a Pyrex® glass cylindrical reactor with a capacity of 7.5 L and a diameter of 22 cm). 5 µL of ethanol were injected with a (10 ± 0.1) µl syringe inside the reactor, which was kept at 40 °C during the photocatalytic tests. After 20 min of dark equilibration, a measurement cycle under illumination was started. Photocatalytic tests in controlled air were performed in batch conditions. The sample could receive light irradiation owing to a UV-transparent window on the top of the reactor, with the UV lamp positioned just over it, at about 50 cm from the sample. The photocatalytic reaction was followed for 1 h using an Agilent 7820A gas chromatograph, with a measurement every 7 min. The reactor was filled with the gaseous mixture from cylinder. Before every measurement dry gaseous mixture from cylinder was flown inside the reactor for about 30 minutes in order to substitute atmospheric air (this step was considered completed when the CO_2 peak measured by the gas chromatograph disappeared).

Photocatalytic results

The concentrations of ethanol, acetaldehyde and carbon dioxide were measured during the entire photocatalytic test. No other peaks were detected. Indeed, acetaldehyde has widely been acknowledged as the main gaseous intermediate in ethanol degradation. Several authors found lower concentrations of other products, such as acetic acid and formaldehyde.

However, acetic acid and formic acid are scarcely detectable by the gas chromatographic technique, as they are less volatile than acetaldehyde and tend to adsorb onto the catalyst surface. For this reason, they are more easily detectable analyzing the catalyst surface using FT-IR or with a solid-liquid extraction of the used catalyst. Carbon dioxide and water are invariably the final products of the oxidation over TiO_2. Accordingly, the final plateau in the CO_2 curve shows that the reaction went to completion.

A typical photocatalytic test gives the curves shown in Fig. 5.23. Difference can be noted between Fig. 5.23a and Fig. 5.23b, relative to TNAg_0.01 and TNAg_0.05, respectively: in the latter case ethanol total degradation is reached at longer times than for the former sample, CO_2 production rate is slower, and acetaldehyde saturates without disappearing at the end of the reaction. This finding will be rediscussed in the following.

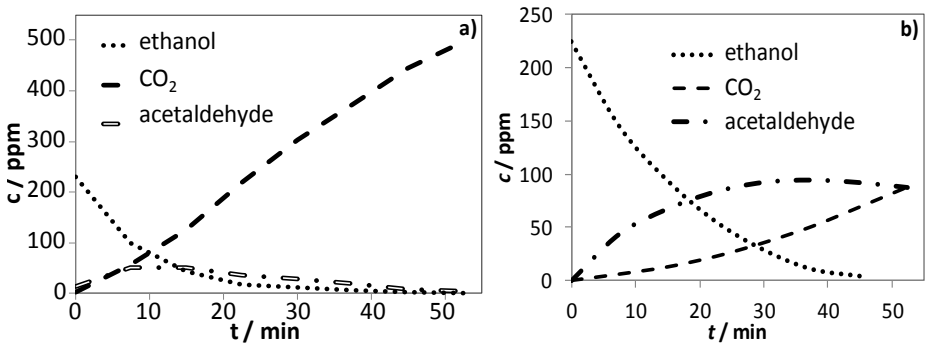

Figure 5.23. Species detected by gas chromatographic analysis during the photocatalytic oxidation of ethanol over TiO_2 as a function of time: the disappearance of ethanol was followed along with the formation of carbon dioxide as final product (total mineralization) and acetaldehyde as reaction intermediate. Samples TNAg_0.01 (**a**) and TNAg_0.05 (**b**).

However, the curves reported in Fig. 5.23a show that the reaction goes to completion. Indeed, the acetaldehyde concentration decreases under the detection limit and the CO_2 concentration is compatible with a complete mineralization of acetaldehyde.

Ethanol degradation shows a good linear $\ln(c_0/c)$ *vs* t correlation for all samples (see Fig. 5.24 for a representative sample, TNAg_0.01), which usually indicates a pseudo-first order kinetics. However, in some cases (samples TN, Tag_0.05, and TNAg_0.05), linearity gets lost after the first 20-30 min of

reaction proceeding. Since an initial dark period was spent for equilibration of the system (the initial gas-phase ethanol concentration was lower than the nominal introduced concentration due to adsorption phenomena), the initial points of the 'concentration *vs* time' curve were considered for the determination of the rate constant of ethanol degradation (see Fig. 5.24).

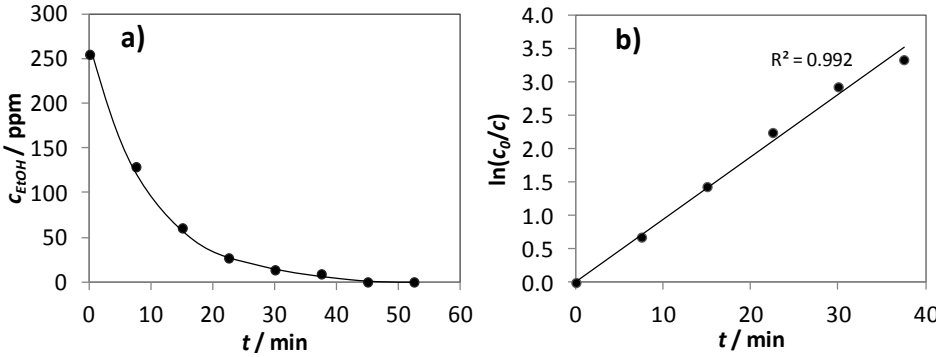

Figure 5.24. Ethanol degradation expressed as concentration *vs* time and $\ln(c_0/c)$ *vs* time to evaluate the kinetic constant (sample TNAg_0.01 as representative for all doped and codoped titania, at least in the first 15-30 min of reaction proceeding).

Experiments with different initial concentration of the pollutant would be needed if one aims at confirming or excluding a first order kinetics or to assess if the reaction actually follows a Langmuir-Hinshelwood kinetics (linear correlation in a $k_{t=0}$ *vs* $1/C_0$ graph). This consideration is related to the issue of a possible competition for adsorption among ethanol, acetaldehyde and other reaction intermediates and products. Results herein reported can be interpreted as deriving from a competitive adsorption of several species on the titania surface.

As a matter of fact, different catalysts have different adsorption properties, resulting in diverse initial amounts of ethanol adsorbed, and different mineralization percentage (see Table 5.12). Note that ethanol degradation is reported "after 15 min" because at the end of the reaction all samples produce a 100 % ethanol degradation. On the contrary, CO_2 production is reported "after 45 min". Hereafter (Table 5.12, 3rd column) the kinetic constants for ethanol photo-oxidation over tested samples are also reported. It appears that they follow quite closely the trend of ethanol degradation percentages.

Sample	EtOH degrad. % (after 15 min)	k_{30} (mg $L^{-1}min^{-1}$)	CO_2 production % (after 45 min)
T	60	0.039	34
TN	68	0.042	47
TAg_0.01	73	0.078	70
TAg_0.01_R	76	0.100	79
TAg_0.05	49	0.044	11
TAg_0.05_R	57	0.080	36
TNAg_0.01	77	0.097	87
TNAg_0.01_R	78	0.106	88
TNAg_0.05	53	0.050	13
TNAg_0.05_R	62	0.101	21

Table 5.12. Ethanol degradation after 15 min, CO_2 production after 45 min, and kinetic rate constants for ethanol degradation – evaluated after 30 min of reaction – for (N,)Ag-doped titania samples.

The highest photocatalytic performance was reached by TNAg_0.01_R, that is a codoped sample with chemical reduction treatment. Samples with a higher Ag percentage (Ag/Ti molar ratio equal to 5 %) lead to a lower photocatalytic activity than the reference TN (TiO_2 doped with only nitrogen deriving from urea source). However, also in this series, the beneficial effect of both the presence of codopants and the chemical reduction are appreciable. Nonetheless, oxides with Ag/Ti = 0.05, although degrading all ethanol amount at the end of the experiment, show limitations towards acetaldehyde evolution (which reaches a plateau) and mineralization (slower rate of CO_2 production).

Furthermore, the photocatalytic efficiency depends on the nominal oxidation state of the metal dopant, *i.e.*, allegedly metallic Ag seems to give a higher performance with respect to the oxidized Ag(I) specie.[86]

It has to be noted that TNAg_0.01 performed better than TAg_0.01, even though the latter has a higher surface area (see Tab. 3.16). This means that codoping leads to a slightly improvement in the photocatalytic activity despite the decrease in surface area. Such a result implies that the gain in photocatalysis cannot only be attributed to the increase in the interfacial charge transfer rate and efficiency due to the specific surface area increase.

He *et al.*, studying Ag-doped titania towards the degradation of methylene blue in aqueous media, invoked electronic effects:[87] as the Fermi level of TiO_2 is higher than that of Ag, electrons would transfer from TiO_2 film to metallic Ag particles spreading on the TiO_2 film resulting in a space charge layer at the boundaries between Ag and TiO_2, which enhance the photogenerated electron-hole pair separation and inhibits their recombination. Unfortunately, photocurrent measurements to evaluate recombination rate have proved to be problematic and highly challenging on titania promoted with silver, as reported in chapter 4. Thus, future work will be devoted to elucidate these aspects.

As evident from Tab. 5.12, codoping does not *a priori* lead to a high performance, but it seems to induce a synergistic effect with the Ag dopant. Indeed, N,Ag codoped samples do not show the highest photocatalytic activity among all samples, but both TNAg_0.05 and TNAg_0.01 exhibit better results than the correspondent Tag_0.05 and TAg_0.01. Literature evidences[88] pointed out that high dopant concentrations favor segregation phenomena of the dopant itself to the thin film surface, both of which is stated to be detrimental to the photocatalytic activity.

Photocatalytic tests with selected (N,)Ag-doped titania photocatalysts were also performed upon visible-light irradiation (see the Appendix for details about the lamp utilized), keeping unvaried all other experimental conditions. It should be noted, however, that in this way ethanol degradation takes place much more slowly. Thus, the total reaction time has been set to 210 min, instead of the 45 min considered for UV experiments. Preliminary results are reported in Tab. 5.13. It is immediately clear that kinetic constants, evaluated after 90 min of reaction, are lower than those obtained upon UV-light irradiation. It is here underlined that the effective power of the visible-light lamp is considerably lower than that of the UV-light lamp at the same working distance (9 and 64 mW cm^{-2}, respectively, see the plot in the Appendix). Moreover, the trend of the four samples reported in Tab. 5.13 is not the same as that found under UV light, with TAg_0.01 resulting the best photocatalyst when operating under visible light. TN and TAg_0.01, the two best performing samples, also show a nearly 100 % ethanol degradation (Table 3.12, 2nd column), while TNAg_0.01 only reaches 53 %. Degradation percentages after 90 min of reactions (not reported in the Table) are 65, 74, 62, 36 for TN,

TAg_0.01, TAg_0.01_R, and TNAg_0.01, respectively. As for carbon dioxide production at the end of the reaction, TNAg_0.01 does not exhibit even 10 % mineralization, whereas the other single doped samples lead to a final mineralization percentage in the range 10-16 (Table 5.13, 4th column).

Sample	EtOH degrad. %	$k_{90} \times 10^{-2}$ (mg $L^{-1}min^{-1}$)	CO_2 production %
TN	99	1.18	16
TAg_0.01	99	1.87	13
TAg_0.01_R	91	1.10	10
TNAg_0.01	53	0.52	4

Table 5.13. Ethanol degradation, CO_2 production (both considered at the end of the test, namely after 210 min), and kinetic rate constants for ethanol degradation – evaluated after 90 min of reaction – for selected (N,Ag)-doped titania samples.

Photocatalytic ethanol degradation in batch reactors has been investigated by several authors. Then, some studies explored in details the influence of experimental conditions on the breakdown mechanism and kinetics. However, no general agreement on the reaction mechanism and the related kinetic description has been reached yet. Sauer and Ollis can be annoverated among the first authors carrying out a study on ethanol photodegradation.[89] They proposed that ethanol reacts to acetaldehyde, which then forms CO_2 both directly and through a formaldehyde intermediate. To provide closure on the carbon mass balance, they hypothesized the presence of other intermediates, namely acetic acid and formic acid, which desorb from the illuminated portions of the catalyst and reversibly collect on the dark TiO_2. The authors suggested that acetic acid and formic acid react quickly on illuminated TiO_2 and therefore are present only in low concentrations for a fully illuminated reactor. They developed a kinetic model for the ethanol photocatalytic oxidation assuming a single-state Langmuir Hinshelwood rate equation, where the oxidation intermediates compete with ethanol for adsorption. Then, some authors employed a complex mechanism of ethanol degradation,[90] whereas some others proposed two step mechanism.[91,92] As already mentioned above for photocatalytic tests on ethanol in aqueous medium, Muggli and co-workers hypothesized a mechanism based on the presence of two types of

ethanol adsorption sites with weak and strong adsorption,[77] as confirmed later on by other authors.[93]

However, to draw a possible photocatalytic reaction mechanism is outside the scope of this work.

Several literature studies point out that the exact reaction pathway and kinetics may be influenced by a series of parameters, such as sample characteristics, like surface acidity,[78] surface hydration[79] and the presence of dopants. As for this latter case, literature examples of Ag-doped TiO_2 photocatalysis are not abundant. Zhang *et al.* reported about freshly prepared silver-coated TiO_2 with a 20 % higher photocatalytic activity than uncoated TiO_2.[94] However, the photocatalytic performance decreased with an increase in UV exposure time and the deactivated sample changed into brownish-gray color. The authors suggested that deactivated silver-coated TiO_2 photocatalyst can be easily reactivated by ambient light illumination. The process converts Ag^0 to Ag(I) in the form of Ag_2O. When the activated catalyst is used in photocatalysis, Ag(I) would be eventually reduced to Ag^0 forming fresh non-aggregated silver nanoparticles on TiO_2. The Ag^+ ions can definitely oxidize the partially degraded species adsorbed on the catalyst during the photocatalytic process and help to regenerate a clean surface. Yuan *et al.* prepared Ag,N-codoped TiO_2 with antibacterial properties.[95] Among all their samples, a 1% Ag-N-TiO_2 (which presents the same dopant concentration as the best performing sample presented in this work) had the highest antibacterial activity under fluorescent light irradiation. Finally, Wan and coworkers tested the photoelectrocatalytic performance of Ag/$TiO_{2-x}N_x$ nanotubes obtaining encouraging results under both UV and visible light.[96]

5.5. References

1. F. Spadavecchia "Visible-active second generation photocatalysts. TiO_2 nanoparticles promoted with nitrogen.", Master Thesis.
2. F. Spadavecchia, G. Cappelletti, S. Ardizzone, C. L. Bianchi, S. Cappelli, C. Oliva, P. Scardi, M. Leoni, P. Fermo *Appl. Catal. B: Environ*. 96 (**2010**) 314.
3. Y. Iwasawa, M. Soma, T. Onishi, K. Tamaru *J. Chem. Soc., Faraday Trans. 1* 68 (**1972**)1697.
4. L. M. Dorfman and G. E. Adams, Reactivity of the Hydroxyl Radical, National Bureau of Standards, Report No. NSRDS-NBS-46, 1973.
5. W. H. Glaze, J. W. Kang, D. H. Chapin *Ozone Sci. Eng*. 9 (**1987**) 335.
6. V. Augugliaro, M . Litter, L. Palmisano, J. Soria *J. Photochem. Photobiol., C* 7 (**2006**) 127.
7. R. R. Giri, H. Ozaki, T. Ishida, R. Takanami, S. Taniguchi *Chemosphere* 66 (**2007**) 1610.
8. G. Marcì, E. Garia-Lopez, L. Palmisano *J. Appl. Electrochem*. 38 (**2008**) 1029.
9. T. Oppenlander, Photochemical purification of water and air, Wiley-VCH Verlag, Weinheim, Germany, 2003.
10. S. Malato, J. Blanco, A. Vidal, C. Richter *Appl. Catal. B: Environ*. 37 (**2002**) 1.
11. A. Alum, Y. Yoon, P. Westerhoff, M. Abbaszadegan *Environ. Toxicol*. 19 (**2004**) 257.
12. W. Giger, P.-H. Brunner, C. Schaffner *Science* 225 (**1984**) 623.
13. W . J. Biggers and H. Laufer *Biol. Bull*. 206 (**2004**) 13.
14. T. Shioda and M. Wakabayashi *Chemosphere* 40 (**2000**) 39.
15. C.-E. Purdom, P.-A. Hardiman, V.-J. Bye, N.-C. Eno, C.-R. Tyler, J.-P. Sumpter *Chem. Ecol*. 275 (**1944**) 275.
16. N.-E. Skakkebaek, R.-D. Meyts, E, N. Jorgensen, E. Carlsen, P.-M. Ptersen, A. Giwercman, A.-G. Andersen, T.-K. Jensen, A.-M. Andersson, J. Muller *APMIS* 106 (**1998**) 3.
17. Illinois EPA Endocrine Disruptors Strategy, EPA, Illinois, USA, 1997.
18. U. S. Environmental Protection Agency. High Production Volume (HPV) Challenge Program. Robust summaries: p-cumylphenol. 2005.
19. C. Alves, C. Pio, A. Duarte *Atmos. Environ*. 35 (**2001**) 5485.
20. J. Lopez-Darias, V. Pino, J. H. Ayala, V. Gonzalez, A. M. Afonso *Anal. Bioanal. Chem*. 391 (**2008**) 735.
21. R. J. Hunt, M. Borchardt, K. D. Richards, S. K. Spencer *Environ. Sci. Technol*. 44 (**2010**) 7956.

22. R. C. Hale, C. L. Smith, P. O. De Fur, E. Harvey, E. O. Bush, M. J. La Guardia, G. G. Vadas *Environ. Toxicol. Chem*. 19 (**2000**) 946.
23. A. Matsushima, T. Teramoto, H. Okada, X. Liu, T. Tokunaga, Y. Kakuta, Y. Shimohigashi Biochem. *Biophys. Res. Commun*. 373 (**2008**) 408.
24. M. Terasaki, F. Shiraishi, T. Nishikawa, J. S. Edmonds, M. Morita, M. Makino *Environ. Sci. Technol*. 39 (**2005**) 3703.
25. T. Nakazawa, K. Kasahara, S. Ikezaki, Y. Yamaguchi, H. Fedamoto, N. Nishimura, M. Yahata, K. Tamura, E. Kamata, M. Ema, R. Hasegawa J. *Toxicol. Pathol*. 22 (**2009**) 125.
26. B. L. L. Tan, D. W. Hawker, J. F. Müller, F. D. L. Leusch, L. A. Tremblay, H. F. Chapman *Chemosphere* 69 (**2007**) 644.
27. B. L. L. Tan, D. W. Hawker, J. F. Müller, L. A. Tremblay, H. F. Chapman *Water Res*. 42 (**2008**) 404.
28. E. Stathatos, T. Petrova, P. Lianos *Langmuir* 17 (**2001**) 5025.
29. Y. Liu, X. L. Wang, F. Yang, X. R. Yang *Microp. Mesop. Mater*. 114 (**2008**) 431.
30. I. M. Arabatzis, T. Stergiopoulos, M. C. Bernard, D. Labou, S. G. Neophytides, P. Falaras *Appl. Catal. B: Environ.* 42 (**2003**) 187.
31. H. Bai, Z. Liu and D. D. Sun *Chem. Commun*. 46 (**2010**) 6542.
32. I. Gultekin and N. H. Ince *J. Environ. Manage*. 85 (**2007**) 816.
33. http://webbook.nist.gov/chemistry/vib-ser.html.
34. M. Deborde, S. Rabouan, P. Mazellier, J.-P. Duguet, B. Legube *Water Res*. 42 (**2008**) 4299.
35. *Phenol Derivatives*. Ullmann's Encyclopedia of Industrial Chemistry Weinheim: Wiley-VCH; 2002.
36. U.S. Food and Drug Administration. Update on Bisphenol A for Use in Food Contact Applications: January 2010; 15 January 2010.
37. T. Oyama, I. Yanagisawa, M. Takeuchi, T. Koike, N. Serpone, H. Hidaka *Appl. Catal. B: Environ*. 91 (**2009**) 242.
38. T. Yamamoto and A. Yasuhara *Chemosphere* 46 (**2002**) 1215.
39. J. Staehelin and J. Higne *Environ. Sci. Technol*. 16 (**1982**) 676.
40. R. A. Torres, J. I. Nieto, E. Combet, C. Petrier, C. Pulgarin *Appl. Catal. B: Environ*. 80 (**2008**) 168.
41. M. Addamo, V. Augugliaro, E. G. Lopez, V. Loddo, G. Marci, L. Palmisano *Catal .Today* 108 (**2005**) 612.
42. F. J. Rivas, A. Encinas, B. Acedo, F. J. Beltran *J. Chem. Technol. Biotechnol*. 54 (**2009**) 589.
43. J. Lee, H. Park, J. Yoon *Environ. Technol*. 24 (**2003**) 241.
44. W. T. Tsai, M. K. Lee, T. Y. Su, Y. M. Chang *J. Hazard. Mater*. 168 (**2009**) 269.
45. R. Wang, D. Ren, S. Xia, Y. Zhang, J. Zhao *J. Hazard. Mater*. 169 (**2009**)

926.
46. U. von Gunten *Water Res*. 37 (**2003**) 1443.
47. N. Watanabe, S. Horikoshi, H. Kawabe, Y. Sugie, J. Zhao, H. Hidaka *Chemosphere* 52 (**2003**) 851.
48. B. Fei, C. Chen, H. Wu, S. W. Peng, X.Y. Wang, L.S. Dong *Europ. Polym. J.* 39 (**2003**) 1939.
49. S. Ardizzone, C. L. Bianchi, G. Cappelletti, A. Naldoni, C. Pirola *Environ. Sci. Technol.* 42 (**2008**) 6671.
50. R. Shrivastava, R. K. Upreti, U. C. Chaturvedi FEMS *Immun. Med. Microbiol*. 38 (**200**3) 65.
51. M. Yemane, B. S. Chandravanshi, T. Wondimu *Food Chem*. 107 (**2008**) 1236.
52. E. Pécou, A. Maass, D. Remenik, J. Briche, M. Gonzalez *Mathem. Biosci*. 203 (**2006**) 222.
53. S. Goeringer, C. R. Chenthamarakshan, K. Rajeshwar *Electrochem. Commun*. 3 (**2004**) 290.
54. J.-K. Yang, S. M. Lee *Chemosphere* 63 (**2006**) 1677.
55. J. M. Meichtry, M. Brusa, G. Mailhot, M. A. Grela, M. I. Litter *Appl. Catal. B: Environ*. 71 (**2007**) 101.
56. D. T. Pierce and J. X. Zhao, Trace Analysis with Nanomaterials, Wiley-VCH, Weinheim, 2010.
57. D. V. Vukomanovic, G. W. vanLoon, K. Nakatsu, D. E. Zoutman *Microchem. J*. 57 (**1997**) 86.
58. O. Domínguez and M.J. Arcos *Electroanal*. 12 (**2000**) 449.
59. O. Domínguez and M.J. Arcos *Anal. Chim. Acta* 470 (**2002**) 241.
60. Y. Ku and I. L. Jung *Water Res.* 35 (**2001**) 135.
61. X. Wang, S. O. Pehkonen, A. K. Ray *Ind. Eng. Chem. Res*. 43 (**2004**) 1665.
62. Y. Cho, H. Kyung, W. Choi *Appl. Catal. B: Environ*. 52 (**2004**) 23.
63. J. J. Testa, M. A. Grela, M. I. Litter *Environ. Sci. Tech*. 38 (**2004**) 1589.
64. G. Cappelletti, C. L. Bianchi, S. Ardizzone *Appl. Catal. B: Environ*. 78 (**2008**) 193.
65. Q. Wang, J. Shang, T. Zhu, F. Zhao *J. Mol. Cat. A: Chem*. 335 (**2011**) 242.
66. V. Pifferi, F. Spadavecchia, G. Cappelletti, E. A. Paoli, C. L. Bianchi, L. Falciola *Catal. Tod*. (**2012**) in press.
67. S. M. Lee, I.-H. Cho, Y.-Y. Chang, J.-K. Yang *J. Environ. Sci. Health A Tox. Hazard Subst. Environ. Eng*. 42 (**2007**) 543.
68. J. Yoon, E. Shim, S. Bae, H. Joo *J. Hazard. Mater*. 161 (**2009**) 1069.
69. E. Paoli, G. Cappelletti, L. Falciola *Electrochem. Commun*. 12 (**2010**) 1013.
70. J. F. Moulder, W. F. Stickle, K. D. Bomben, Handbook of X-ray Photoelectron Spectroscopy, Perkin Elmer: Eden Praire, 1992.

71. N. Serpone, I. Texier, A. V. Emeline, P. Pichat, H. Hidaka, J. Zhao *J. Photochem. Photobiol. A: Chem*. 136 (**2000**) 145.
72. P. Kajitvichyanukul, J. Ananpattarachai, S. Pongpom *Sci. Tech. Adv. Mater.* 6 (**2005**) 352.
73. J. Gimenz, M. A. Aguado, S. Cervera-March *J. Mol. Catal. A: Chem*. 105 (**1996**) 67.
74. L. Wang, N. Wang, L. Zhu, H. Yu, H. Tang *J. Hazard. Mater*. 152 (**2008**) 93.
75. D. Meroni, S. Ardizzone, G. Cappelletti, C. Oliva, M. Ceotto, D. Poelman, H. Poelman *Catal. Today* 161 (**2011**) 169.
76. D. S. Muggli, J. T. McCue, J. L. Falconer *J. Catal*. 173 (**1998**) 470.
77. D. S. Muggli, K. H. Lowery, J. L. Falconer *J. Catal*. 180 (**1998**) 111.
78. D. V. Kozlov, E. A. Paukshtis, E. N. Savinov *Appl. Catal. B: Environ*. 24 (**2000**) L7.
79. Z. Yu, S. S. C. Chuang *J. Catal*. 246 (**2007**) 118.
80. P. Kajitvichyanukul, P. Amornchat *Sci. Technol. Adv. Mater*. 6 (**2005**) 344.
81. E. Piera, J. A. Ayllón, X. Doménech, J. Peral *Catal. Today* 76 (**2002**) 259.
82. X. Zhou, F. Peng, H. Wang, H. Yu, J. Yang *J. Solid State Chem*. 184 (**2011**) 134.
83. S. Hoang, S. P. Berglund, N. T. Hahn, A. J. Bard, C. B. Mullins *J. Am. Chem. Soc*. 134 (**2012**) 3659.
84. N. Kometani, A. Fujita, Y. Yonezawa *J. Mater. Sci*. 43 (**2008**) 2492.
85. J. Ananpattarachai, P. Kajitvichyanukul, S. Seraphin *J. Hazard. Mater*. 168 (**2009**) 253.
86. L. Zhang and J. C. Yu *Catal. Commun*. 6 (**2005**) 684.
87. C. He, Y. Yu, X. Hu, A. Larbot *Appl. Surf. Sci.* 200 (**2002**) 239.
88. U. G. Akpan and B. H. Hameed *Appl. Catal. A: Gen.* 375 (**2010**) 1.
89. M. L. Sauer and D. F. Ollis *J. Catal*. 158 (**1996**) 570.
90. M. R. Nimlos, E. J. Wolfrum, M. L. Brewer, J. A. Fennell, G. Bintner *Environ. Sci. Tech*. 30 (**1996**) 3102.
91. A. V. Vorontsov, E. N. Savinov, G. B. Barannik, V. N. Troitsky, V. N. Parmon *Catal. Tod*. 39 (**1997**) 207.
92. A. V. Vorontsov, V.P. Dubovitskaya *J. Catal*. 221 (**2004**) 102.
93. J. M. Coronado, S. Kataoka, I. Tejedor-Tejedor, M. A. Anderson *J. Catal*. 219 (**2003**) 219.
94. L. Z. Zhang, J. C. Yu, H. Y. Yip, Q. Li, K. W. Kwong, A. W. Xu, P. K. Wong *Langmuir* 19 (**2003**) 10372.
95. Y. Yuan, J. Ding, J.S. Xu, J. Deng, J.B. Guo *J. Nanosci. Nanotech*. 10 (**2010**) 4868.

96. B. Wan, M.-B. Chen, X.-Y. Zhou, W. Wang, W.-G. Li *J. Inorg. Mater.* 25 (**2010**) 285.

6.
Solar Cells

Dye-sensitized solar cells (DCSs) can be considered as photoelectrochemical systems where dye molecules are chemisorbed (attached) to a wide-band-gap mesoporous metal oxide (*i.e.*, TiO_2) film. Photon absorption leads to excitation of the dye (photoactive component), followed by electron injection from the dye into the conduction band of the metal oxide, leaving the dye in the oxidized state. This latter has to be reduced by the electrolyte in order to start a new cycle. After charge separation has occurred, electron transport takes place. This is the typical case of n-type behavior of the inorganic semiconductor, which preferentially implies that holes are injected into the electrolyte. Within this picture, electrons have to reach the back contact and flow through an outer electric circuit in order to get the effective current out of the solar cell.

In the search for low-cost photovoltaic (PV) devices, DSCs surely are considered promising, even though much research has still to be conducted to optimize their efficiency. Indeed, the estimated and actual manufacturing costs for DSCs are minor to the projected costs of other PV technologies. Significant progress has been made in the transition from glass substrates to plastic foils and from batch to continuous processing. Important improvements reached by using solid state electrolytes or hole conductor layers make new types of DCSs on the verge of commercialization.[1,2]

6.1 Solar cells' characterization

The key parameters used to characterize a DSC are the open circuit voltage (V_{OC}), the short circuit current density (J_{SC}), the fill factor (FF) and the efficiency (η), which ultimately indicates the electrical output power of the solar cell. They are all measured under a set of standard conditions,[3] which essentially specify that the temperature of the cell should be 25 °C and the solar radiation incident on the cell should have a total power density of 1000 W m^{-2}, with a spectral power distribution characterized as AM 1.5. Air mass 1.5 global (AM 1.5G) illumination is part of the standard test conditions for PV cells and indicates the intensity of incoming light equivalent to the sun shining through the atmosphere to sea level, with oxygen and nitrogen absorption, at an oblique angle 48.2 deg from the zenith.

The open circuit voltage represents the voltage that can be generated in such device and depends on the difference of the redox potential of the electrolyte and the quasi-Fermi level of TiO_2. However, the V_{OC} was found to depend also on the recombination rates, to the sensitizer and its adsorption mode. Indeed, the sensitizers adsorption geometry induces substantial downshift of the conduction band energy of the metal oxide thereby reducing the V_{OC}.[4] Moreover, the necessity of a thermodynamic driving force to achieve charge separation reduces the maximum voltage that can be generated.[5]

The short-circuit current is the current through the solar cell when the voltage across the solar cell is zero (*i.e.*, when the solar cell is short circuited). To remove the dependence of the solar cell area, it is more common to list the short-circuit current density (J_{SC}) rather than the short-circuit current (I_{SC}). In this thesis it will be done this way since the active area of the solar cells is always smaller than 1 cm^2. Such parameter is due to the generation and collection of light-generated carriers. For an ideal solar cell at most moderate resistive loss mechanisms, the short-circuit current and the light-generated current are identical. Therefore, the short-circuit current is the largest current which may be drawn from the solar cell. It is closely linked to the absorption spectrum of the dye and to how finely this matches the solar spectrum; then, in order to have a good light harvesting, a high TiO_2 surface area is needed so that the dye can more easily adsorb and also charge separation can be facilitated. The short-circuit current is also affected by other factors such as the number of photons (*i.e.*, the power of the incident light source – direct dependence), the optical properties (absorption and reflection) of the solar cell, and its collection probability, which, in turn, depends chiefly on the surface passivation and the minority carrier lifetime. Indeed, when comparing solar cells of the same type of material, diffusion length and surface passivation represent the most critical material parameters. In a cell with a perfectly passivated surface and uniform generation of charge carriers, the short-circuit current depends strongly on the generation rate and the diffusion length. As excitons need to be transferred to the vicinity of an interface to be charged-separated, the exciton diffusion length (L_{XD}) – see definition in paragraph 6.2 – can be a limiting factor to device performance.

The fill factor of the solar cell is a measure of decrease in photocurrent with increase in photovoltage and could be qualitatively determined by the "squareness" of the I–V curve. Ideally, the power generated within the cell

should dissipate at the external circuit. Parallel current paths, like charge recombination and electron back transfer within the device are possible causes of poor fill factor.

The conversion efficiency of the solar cell (η), is defined as the ratio of the maximum power output (P_{max}) to the power input (P_{in}) to the cell, defined as the total radiant energy incident on the surface of the cell:

$$\eta = \frac{P_{max}}{P_{in}} = \frac{J_{SC} V_{OC} FF}{P_{in}} \quad \text{(eq. 6.1)}$$

i.e., higher J_{SC}, V_{OC}, and FF for lower solar irradiance are the key for increased η.

Maximum efficiency is obtained when power delivered to the load is P_{max}. Incident optical power is normally specified as the solar power on the surface of the earth which is approximately 1 mW mm^{-2}. J_{SC} is directly proportional to the incident optical power Pin; but V_{OC} also increases logarithmically with the incident power. So the overall efficiency of the solar cell is expected to increase logarithmically with the incident power. However, at high sunlight concentration thermal effects and electrical losses in the series resistance of the solar cell limit the efficiency enhancement that can be achieved. As a result, the efficiency of practical solar cells peaks at some finite concentration level.

The mesoporous metal oxide network directly influences all the above mentioned parameters. Thus reducing the losses in the inorganic semiconductor network, improvements in the efficiency of the solar cell could be achieved.

As shown in Figure 6.1, solar cell efficiencies vary from 6 % for amorphous silicon-based solar cells to 40.7 % with multiple-junction research lab cells and 42.8 % with multiple dies assembled into a hybrid package.[6]

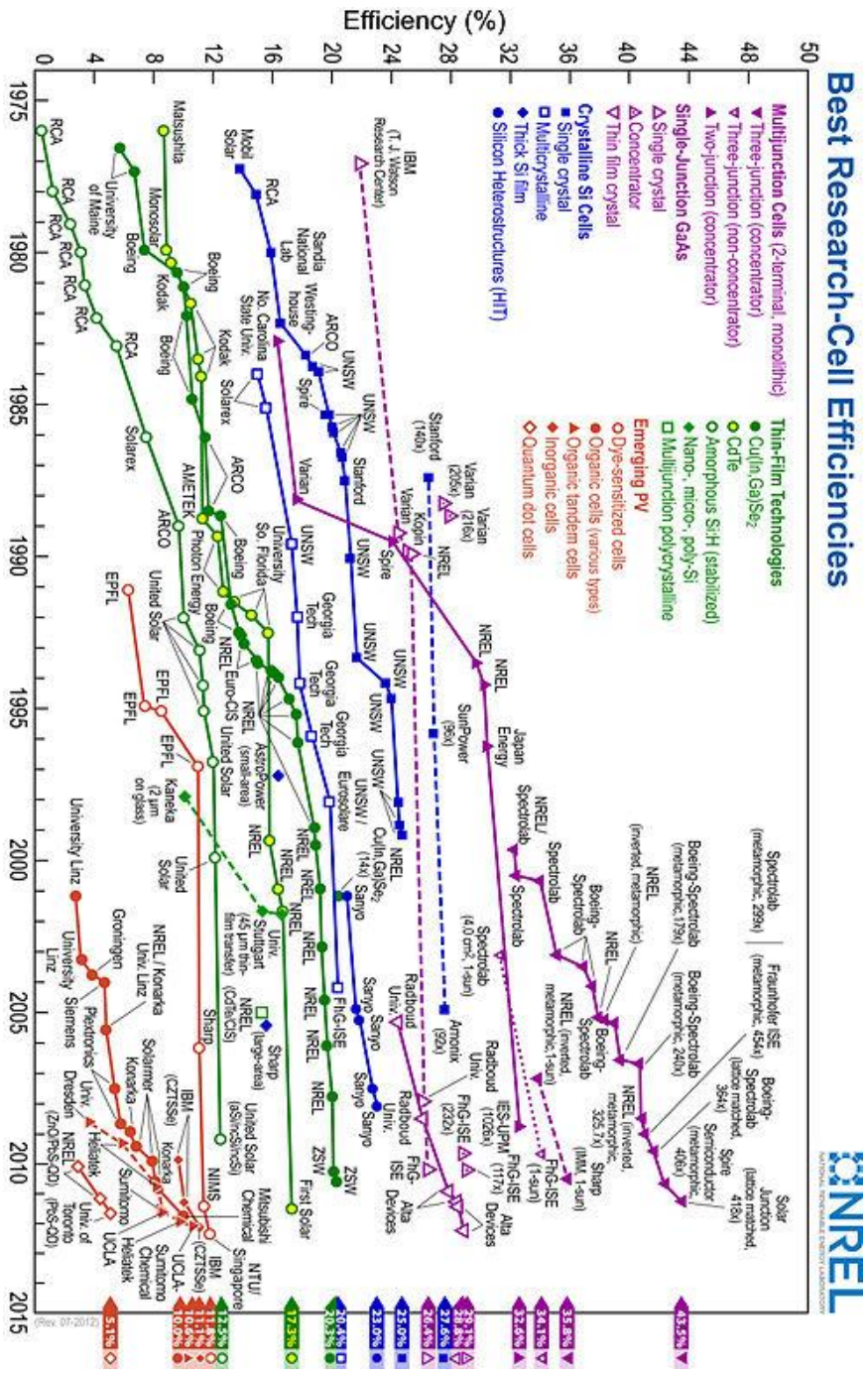

Figure 6.1. Reported timeline of solar cells energy conversion efficiency (from National Renewable Energy Laboratory, USA).

A solar cell may be represented by the equivalent circuit model shown in Figure 6.2, which consists of a light-induced current source (I_L), a diode that generates a saturation current, a series resistance (R_s), and a shunt resistance (R_{sh}). The series resistance is due to the resistance of the metal contacts, ohmic drops in the front surface of the cell, impurity concentrations, and junction depth. The main impact of series resistance is to reduce the fill factor, although excessively high values may also reduce the short-circuit current. Ideally, the series resistance should be zero; thus, it should be minimized. The shunt resistance represents the loss due to surface leakage along the edge of the cell or to crystal defects. It should be ideally infinite and thus maximized in a real device.

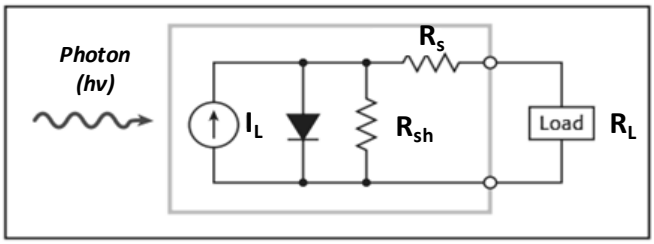

Figure 6.2. Idealized equivalent circuit of a photovoltaic cell.

A variety of measurements are used to characterize solar cells performance, including its output and its efficiency. This electrical characterization is performed as part of research and development of photovoltaic cells and materials, as well as during the manufacturing process.
Among the techniques mainly used to characterize DSCs in this thesis work, photoelectric current (I–V) measurements and incident photon to conversion efficiency (IPCE) have been used.

Current-voltage measurements and incident photon to current conversion efficiency (IPCE) measurements

Typical voltage-current characteristics, known as the I-V (or J-V, according to the density of current considered instead of the current intensity) curve of a diode without illumination is shown in Fig. 6.3. Without illumination, no current flows through the diode unless there is an external potential applied. With incident sunlight, the I-V curve shifts up and indicates that there is an external current flowing from the solar cell to a passive load.

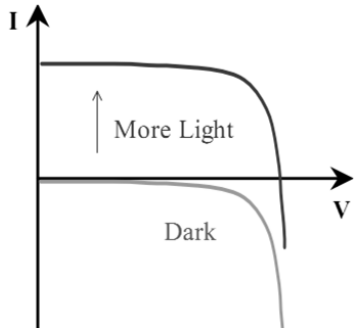

Figure 6.3. The progression of the solar cell I-V curve as the incident light increases.

Short circuit current, I_{SC}, flows with zero external resistance (V=0) and is the maximum current delivered by the solar cell at any illumination level. Similarly, the open circuit voltage, V_{OC}, is the potential which is developed across the terminals of the solar cell when the resistance is very large. Note that no power is generated when open circuit voltage or short circuit current is measured. Thus, the power delivered to the load is zero at both extremes and reaches a maximum (P_{max}) at a finite load resistance value. In Fig. 6.4, P_{max} is shown as the area of the shaded rectangle (which is the largest one under the I-V curve).

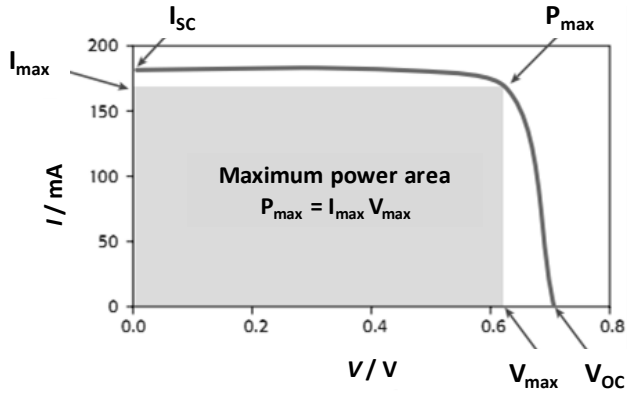

Figure 6.4. Typical forward bias I-V characteristics of a PV cell.

The overall light-to-electricity conversion efficiency (η), fill factor (FF), open-circuit voltage (V_{OC}), and short-circuit current density (J_{sc}) were obtained through the current-voltage characteristics of a solar cell at room temperature and in ambient atmosphere. Measurements were performed using a Keithley 2400 source-meter and a Newport solar simulator (model 91160) giving light

with AM 1.5G spectral distribution, which was calibrated using a certified reference solar cell (Fraunhofer ISE) to an intensity 1000 W m^{-2}.
Incident photon to current conversion efficiency (IPCE) - also known as external quantum efficiency (EQE) - spectra were recorded using a computer-controlled setup consisting of a xenon light source (Spectral Products ASB-XE-175), a monochromator (AB301-T), and a Keithley 2007 multimeter.
It has to be underlined that it is not correct to assume linearity for current measured and light intensity. If not otherwise stated, J-V and IPCE are recorded with a different light intensity (*i.e.*, 1000 W m^{-2} and 100 W m^{-2}, respectively) in standard conditions.
Photovoltaic performance was measured by using a black mask which was 1 mm wider than the active area of the cell to avoid significant additional contribution from light falling on the device outside the active area. During characterization, the solar cell devices were pressed together with clamps. Data listed in the following represent the average values of best cells for each type studied.
In an illuminated solar cell under equilibrium open-circuit conditions, charge carrier separation rate at the hetero-interface equals the recombination rate. When switching off the illumination source a new equilibrium involving the recombination of charge carriers will be established. This process can be monitored following the decay of the open circuit voltage. Thus, open-circuit photovoltage (V_{OC}) decay measurements were carried out on a computer controlled white LED in combination with a DAQ multi-meter used to read out the voltage decay of a solar cell device after turning off the illumination source.

Light absorption and charge separation

The fraction of light absorbed by the active component(s) is the light harvesting efficiency (LHE). The internal quantum efficiency (IQE) includes all the processes that lead to the generation of separated charge carriers. The product of LHE and IQE is referred to as the external quantum efficiency (EQE or IPCE, incident photon-to-current conversion efficiency), which is the fraction of photons incident on the device that are converted into electrons flowing in an external circuit. As the EQE is commonly determined under short-circuit conditions, the integrated EQE spectra should correspond to J_{SC}.

The IPCE is a wavelength-dependent parameter which is used to describe the conversion efficiency from incident photons to electrons, and it can be obtained by the current density generated by a solar cell under monochromatic irradiation P_{spec} (spectral photon flux Φ_{spec}) according to the following equation:

$$IPCE\ (\lambda) = \frac{Jsc(\lambda)}{\Phi_{spec}(\lambda)} = \frac{hc}{e} = \frac{Jsc(\lambda)}{\lambda\, P_{spec}(\lambda)} = \frac{1240\, Jsc(\lambda)}{\lambda\, P_{spec}\lambda} \quad \text{(eq. 6.2)}$$

Along with the working principles of the DSC (chapter 1.3.1), the IPCE can be also expressed as the product of the light harvesting efficiency (LHE), the charge injection efficiency (η_{inj}), the charge collection efficiency (η_{coll}) and the regeneration efficiency (η_{reg}), which is summarized in equation 6.3:

$$IPCE = LHE \cdot\ \eta_{inj} \cdot \eta_{coll} \cdot \eta_{reg} \quad \text{(eq. 6.3)}$$

The IPCE is often measured at short circuit by recording the current generated by the solar cell during monochromatic irradiation. In dye sensitized solar cells the IPCE spectrum should resemble the absorption spectrum of the employed sensitizer dye.

Recombination of charge carriers: losses in DSCs

Losses due to charge recombination between the electrons in the semiconductor and the oxidized species in the redox electrolyte limit the DSC efficiency by lowering the charge-collection efficiency and, therefore, the photocurrent. In a paper published in 2010, Snaith reviewed the electrical and optical losses in the dye-sensitized system.[7] He specifically highlighted the main losses in potential from the conversion of an absorbed photon at the optical bandgap of the sensitizer to the open-circuit voltage generated by the solar cell. For the best performing DSCs with current technology, the ‘‘loss-in-potential’’ from the optical bandgap to the open-circuit voltage is around 0.75 eV, which leads to a maximum power-conversion efficiency of 13.4 % with an optical bandgap of 1.48 eV (840 nm absorption onset). Means by which the loss-in-potential could be reduced to 0.4 eV are discussed; a maximum efficiency of 20.25 % with an optical bandgap of 1.31 eV (940 nm) is possible if this is achieved.

For a photovoltaic device with minimal losses, the ideal optical bandgap for maximizing the solar-to-electrical power conversion efficiency is 1.1 eV.[8]

However, dye-sensitized solar cells (DSCs) do not have negligible electronic losses and the system is considerably different from a p–n junction solar cell. Nevertheless, as the loss-in-potential is reduced, the optimum optical bandgap moves to lower energies, and with losses reduced to 0.2 eV a maximum power conversion efficiency of 26 % is achievable with an optical bandgap of around 1.1 eV. Due to disorder and heterogeneous charge generation processes in dye-sensitized solar cells, there can be a tradeoff between open-circuit voltage and photocurrent generation.[9] All these calculations are for single junction devices, and further increases inefficiency, which are not addressed here, can be expected by incorporating more advanced, tandem, unconverting, or down-converting concepts. It should also be possible to recuperate at least 0.3 eV loss from the hole regeneration, by moving from a multistep dye-regeneration mechanism to a single hole-transfer process, possibly by replacing the iodide/triiodide redox couple with a hole transporter.[7]

6.2 Hybrid solar cells

The type of solar cells mostly investigated in this thesis can be generally classified as hybrid solar cells (HSCs). This definition encompasses a wide range of solar cell devices with different assembling materials and architectures which have been established as a new and challenging research area.

HSCs are conceptually related to both organic solar cells and dye-sensitized solar cells, and, as the latter, combine inorganic and organic semiconducting materials.[10] The inorganic component, namely TiO_2, is involved in the interfacial charge separation and charge transport but does not contribute significantly to the light harvesting efficiency. In analogy with organic solar cells, photons are often harvested in the bulk of an organic component leading to the formation of strongly-bound excitons. Charge separation requires a built-in asymmetry in the whole devices that drives electrons and holes in opposite directions. In the dark, solar cells exhibit the characteristic current density-voltage (J-V) curve of a diode, as shown in Fig. 6.3. Solar cells can be operatively described by the Schockley equation, which expresses the

current density J extracted from the cell as a function of the applied potential V_a:

$$J(V_a) = \frac{1}{1+\frac{R_S}{R_{sh}}}\left\{J_{ph} - j_0\left[\exp\left(\frac{V_a+JR_SA}{\frac{nk_BT}{e}}\right)-1\right]-\frac{V_a}{R_{sh}A}\right\} \quad \text{(eq. 6.4)}$$

where *A* is the area of the device, *e* the elementary charge, k_B the Boltzmann constant and *T* the temperature. R_s and R_{sh} are the series resistance and the shunt resistance, respectively. The dark saturation current density j_0 is the leakage current through the diode in the absence of illumination. The ideality factor *n* is related to the type of recombination processes in the device. It is thought to be related to both exciton and charge carrier recombination in organic and dye-sensitized solar cells.[11]

Under illumination, the whole J-V curve is shifted by the amount of photogenerated current density.

Analysis of the dark J-V behavior of solar cells, as well as of the analogous photoresponse, gives important information for optimization of each component of the complete device.

Bilayer HSCs are the simplest devices of this type and, for such reason, are usefully used to explore new material combinations and to evaluate specific parameters which characterize the device. Efficiencies for bilayer HSCs are typically in the range 0.1-0.6 %.[12-14]

While HSCs often employ polymers as the organic compounds, also small molecular semiconductors such as merocyanines and porphyrins are sometimes used. Among the latter, a triphenylamine (TPA) based compound has been adopted to build the solar cells investigated in this thesis. It basically plays the role of a bulk-light harvesting material. The TPA unit, a common functionality in hole transporting materials in opto-electronic devices,[15-16] introduces a peculiar 3D geometry that only allows some specific molecular organizations. A long-range order in bulk light absorbing materials can results in anisotropic exciton and charge transport.[16] High hole mobility has been measured in some of these compounds.[17]

Eventually, the devices investigated herein can be considered solid state dye-sensitized solar cells with the traditional “transparent” hole conductor such as spiro-MeOTAD replaced by a hole transporting dye. Thus, all the types of devices built and analyzed in this thesis can be generically - but not incorrectly - referred to as “dye-sensitized solar cells”.

Energy transfer: exciton diffusion

Exciton diffusion can be considered an energy transfer process of vibrationally relaxed excited dye molecules transferring their excitations energy to nearby molecules. It is assumed as the fundamental mechanism for energy transfer in this type of hybrid devices. Thus, a valuable parameter to take into account for such excitonic solar cells is the exciton diffusion length (L_{XD}), which is defined as the distance *D* over which an exciton can diffuse during its lifetime τ_x:

$$L_{XD} = (D\tau_x)^{\frac{1}{2}} \quad \text{(eq. 6.5)}$$

Very often exciton diffusion to a charge-separating interface represents a limiting factor for energy conversion in excitonic solar cells. Molecular compounds without long-range order typically have an LXD in the order of 10 nm.[18] In the simplest configuration of bilayer solar cells, the exciton diffusion length can be evaluated with varying thickness of the light harvesting component on the quenching substrate, as it has been done for devices considered in this thesis. The absorption coefficient used in the equation was determined from dye layer thickness measured by DekTak profilometry. Thus, the L_{XD} evaluation was affected by the uncertainty on such measurements. L_{XD} determined from the analysis of the IPCE at 380 nm using $\alpha_{(380nm)} = 1.7 \times 10^7$ m^{-1}.

When dealing with exciton diffusion, the first step to be considered is light absorption, which results in exciton formation for the devices considered herein. The absorption coefficient of a solid samples, α(λ), reflects the probability for an electronic transition to occur at a particular wavelength in the material considered. Such parameter allows the determination of the thickness of a light harvesting material (*e.g.*, a dye) from the sample assorbance and is also needed to model the exciton diffusion length. *Viceversa*, the absorption coefficient can be derived by the above mentioned parameters, if known. A property directly related to α is the light penetration depth (α^{-1}), which is the thickness of the material where approximately 67 % of the incident light has been absorbed. Electronic transitions occur between discrete energy levels in dye molecules, giving rise to an absorption spectrum with maxima and minima (*e.g*, the one reported in Fig. 6.5).

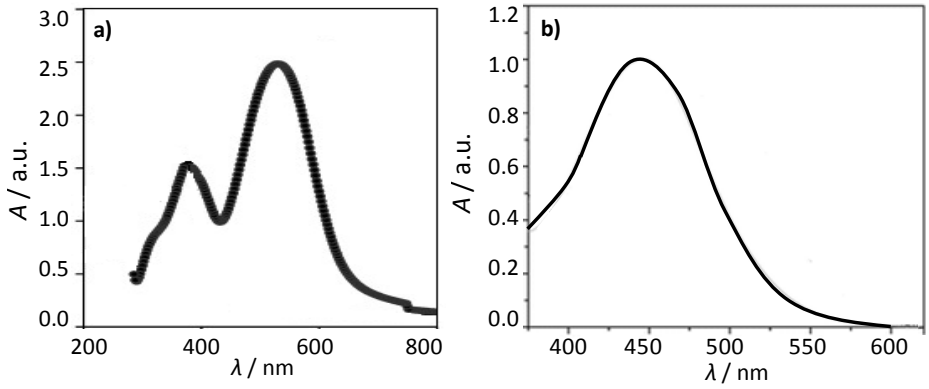

Figure 6.5. Absorption spectra of **a**) dyes **TDCV-TPA**, ([tris(dicyano-vinyl-2-thienyl)phenyl]amine, and **b**) **D35** ((E)-3-(5-(4-(Bis(20,40-dibutoxybiphenyl-4-yl)amino)phenyl)thiophen-2-yl)-2-cyanoacrylic acid.

Organic semiconductors possess larger absorption coefficients than inorganic semiconductors, such as silicon, thus requiring less material to achieve the same light harvesting efficiency. However, Frenkel-type excitons are generated following light absorption in organic semiconductors: since they have a stronger binding energy, an energetic offset is needed to obtain charge separation.

6.3. Comparison of spray-pyrolyzed and spin-coated TiO_2 for hybrid solar cells

Aim of the work

The motivation for thoroughly characterizing two types of thin TiO_2 films prepared by two different deposition procedures has arisen from a striking difference noticed in the IPCE (incident photon-to-current efficiency) spectra of solar cells built with spray pyrolyzed or spin-casted TiO_2 underlayer. This finding is displayed in Fig. 6.6.

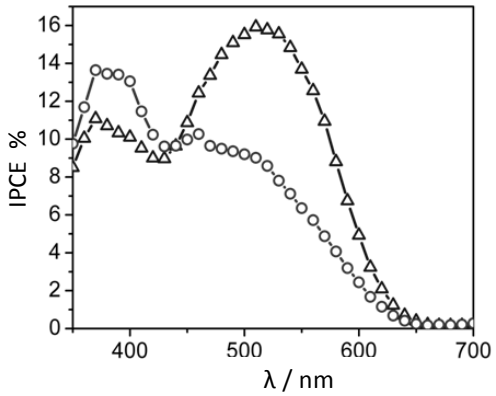

Figure 6.6. IPCE spectra of solar cell devices built with spin-TiO_2 (triangle) and spray-TiO_2 (circle), respectively.

The devices prepared with the spray-TiO_2 substrates exhibited a similar shape to those previously reported for this compound for thick dye layers,[19] whereas the spin-TiO_2 samples gave a response more resembling the absorbance spectrum of the dye indicating that these devices are less limited by exciton diffusion. Distinct differences in the spectral response of the EQE and in device performance could have been explained by either a difference in the conduction band or a different morphology, mainly at the nanometer scale, of the prepared titania layers.

Thus, various experimental methods (SEM, AFM, XRD, XPS, UV-Vis spectroscopy with an integrating sphere, linear scanning voltammetry and Mott-Schottky measurements) have been employed to characterize titania films prepared using the two different preparation routes and to highlight the differences between them.

First, optical and electronic properties of the titania film are presented. Secondly, structural and morphological features of the films investigated by XRD, SEM and AFM will be compared. In the last section solar cell devices were built to characterize the photovoltaic performance of the titania substrates obtained by the two alternative preparation routes as acceptor layer in hybrid solar cells.

Deposition procedure

Thin layers of titania on conducting fluorine doped tin oxide (FTO) glass substrates (TEC15, Pilkington, substrate thickness 2.3 mm) were prepared by either spray pyrolysis[12] or spin-coating.[12,19]

Spray-pyrolysis

A TiO_2 precursor was prepared under nitrogen by adding drop-wise 2.4 mL of Ti(IV)-tetraisopropoxalate to 3.6 mL acetylacetone (Fluka) resulting in a bright yellow liquid containing diisopropoxy-Ti(IV)-bis(acetoacetonate) which could be stored in a sealed flask at 8 °C until further use. Prior to deposition the precursor was diluted 1:9 with ethanol to give a ca 1.2 M solution. FTO glass substrates were heated to 450°C on a high temperature Titan hotplate (PZ 28-3 TD temperature controller, Harry Gerstigkeit GmbH) covered by a Robax glass plate to avoid direct deposition of TiO_2 onto the hotplate. The aerosol deposition was carried out in 12 spray cycles (one cycle consisting in a single movement of the spray nozzle over the substrate) with a commercial hand-held air brush (distance ~6 cm, speed ~5 cm s^{-1}) using nitrogen as a carrier gas (1.5 bar).[19]

TiO_2 formation occurs by reaction of the organo-titanate with atmospheric oxygen at the hot substrate surface. By this deposition method the metal oxide film grows about 10 nm per spray cycle.

Spin-coating

Alternatively, the spin-cast TiO_2 layers were prepared according to the route described by Goh *et al.*:[12] 1.4 ml of titanium-tetraisopropoxide was stirred for 15 minutes with 8 ml of an ethanol blend containing small quantities of deionized water and hydrochloric acid. Then, 20 µl cm^{-2} of the sol-gel solution were spin-cast onto FTO substrates at 2000 rpm for 30 s, left to condense at 120 °C overnight and calcined at 450 °C on a hotplate (PZ 28-3 TD temperature controller, Harry Gerstigkeit GmbH).

TiO_2 formation takes place during the blending of the precursor and storage at 120 °C. In this step, $Ti(OH)_x$ crystallites are formed through hydrolysis of the Ti precursor followed by water and alkoxide condensation reactions.

Device fabrication

The small molecular semiconducting dye [tris(dicyano-vinyl-2-thienyl)phenyl]amine (TDCV-TPA, structure shown in Fig. 6.7) was purchased from Aldrich and used as received. It was developed by the group of Jean Roncali in Angers, France, and it is now commercially available. It was spin-cast at 4000 rpm for 30 s (after 3 s at 2000 rpm) from methylene-chloride solution. The conducting polymer poly(3,4-ethylenedioxy-thiophene):poly-

(styrene-sulfonate) (PEDOT:PSS, Aldrich) was spin-cast at 4000 rpm for 20 s (after 3 s at 2000 rpm). To remove solvent residues, the samples were first heated to 120°C and then evacuated (10^{-5} mbar, 30 min). A piece of double-sided self-adhesive foam tape (Tesa, mounting tape) with a round hole (standard hole punch, hole diameter of 5.5 mm) was attached to the sample. Electrical contact was established by compressed graphite powder, and electric contact was finally established with a second piece of conducting glass.[20] The active area of the test devices was 0.19 cm^2.

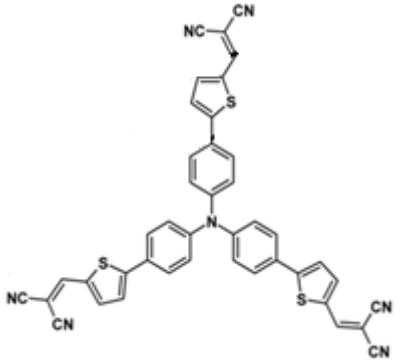

Figure 6.7. Chemical structures of dye TDCV-TPA.

6.3.1. Optical and electronic properties

Mott-Schottky plot and linear sweep voltammetries

To estimate the conduction band position of the prepared titania the flatband potential, V_{fb}, of both types of TiO_2 thin films was evaluated by measuring the capacitance, C, at the TiO_2/Na_2SO_4(aq) interface in dependency of the applied potential, V_a. Mott-Schottky plots for the measurements of spray-TiO_2 (solid), spin-TiO_2 (dashed) and FTO (dotted) are displayed in Fig. 6.8 and are based on equation 4.5. Herein also the geometric area, A, of the substrate (1 cm^2) and the roughness factor, R, of the substrate were taken into account.

The response of the FTO alone has been shown as a reference along with the curves of both types of titania films, each deposited on FTO. The junction capacitance of the semiconductor/electrolyte was derived from the the real Z' and imaginary part Z'' of the impedance measured in aqueous solution at 1 kHz.[21]

The spray-pyrolyzed TiO_2 film exhibits a characteristic behaviour for a low-doped semiconductor film with C^{-2} saturating at positive applied potentials

when the space charge region extends throughout the film to the conducting back contact.[22] Extrapolating the steep part of the curves to the potential axis, the flatband-potential V_{fb} and doping densities N_D were determined and are summarized in Table 6.1, 2nd and 3rd column, respectively. For the spray-TiO_2 a V_{fb} value of -0.27 V *vs* NHE was determined which is in close agreement with other values found in literature at pH 3.[22] Assuming a nernstian shift of 0.059 V per pH unit,[23] this value corresponds to -0.5 V *vs* NHE at pH 7.

The TiO_2 films prepared by spin-casting were found not to be blocking charge transfer with the underlying FTO substrate in electrochemical measurements using a ferrocene containing electrolyte (inset of Fig. 6.8, triangles). Therefore it was not possible to determine the V_{fb} and doping densities N_D for these films as the Mott-Schottky relation does not apply.[24] Instead, the data can be rationalized in terms of an FTO substrate which is covered with a porous titania layer.[25] Since for highly doped films, such as FTO, the Helmholtz capacitance has to be taken into account in the determination of the flatband potential,[24] a value of 10 µF cm^{-2} was used.[26] When analyzing in more details the behavior of the spray-pyrolyzed film, it can be noticed that a transition in the Mott-Schottky plot at V_{tr} (indicated in Fig. 6.8) occurs when the width of the space charge region in the TiO_2 film extends through the FTO back contact. At more positive applied potentials the TiO_2 layer acts as a dielectric layer with the capacitance C_d[25] which is a function of the film thickness t and interfacial roughness R:[27]

$$C_d = \frac{AR\varepsilon_0\varepsilon_r}{t} \quad \text{(eq. 6.6)}$$

From the capacitance at V_{tr} the roughness R of the TiO_2 substrate can be estimated from equation 6.6 using the thickness t of the spray-pyrolyzed TiO_2 film determined from the SEM cross section measurements shown in Fig. 6.12 and a relative dielectric constant $\varepsilon_{r,TiO2}$ of 54[28] for TiO_2. The surface roughness factor R for the spray-pyrolyzed TiO_2 substrates was determined to be 2.9. From the slope in the Mott-Schottky plot, the N_D of spray-pyrolyzed TiO_2 was determined to be 1.2×10^{17} cm^{-3}.

Apparently, the slopes associated with the capacitance of FTO between the uncovered FTO and the spray-pyrolyzed FTO differ by a factor of $(1.7)^2$ which is similar to the difference found in the R_{rms} by AFM measurements for these two substrates (Table 6.1). The different slopes are therefore ascribed to a change in surface roughness upon deposition of the TiO_2 layer. The roughness

factor for the uncoated FTO substrate should be accordingly 4.9. Using a dielectric constant for FTO of 9,[25] the N_D is determined to be 4.1×10^{19} cm^{-3}. This is comparable to values found for FTO substrates by Cameron *et al.*[26] who took *R* into account, but it is lower than values obtained when *R* was not accounted for.[25]

The inset of Fig. 6.8 shows Tafel plots of linear sweep voltammetry measurements for spray-TiO_2, spin-TiO_2 and FTO with a ferrocene containing redox couple. Unlike the spray-TiO_2, the spin-cast TiO_2 layer on FTO film was found not to be a blocking layer for the oxidation of ferrocene as exchange current densities were in the same order of magnitude as the FTO substrate. Hence, the deposited TiO_2 film does not act as a barrier and the V_{fb} cannot be determined reliably from Mott-Schottky plot (corresponding values are however reported in italic in Table 6.1, but have to be taken with care).

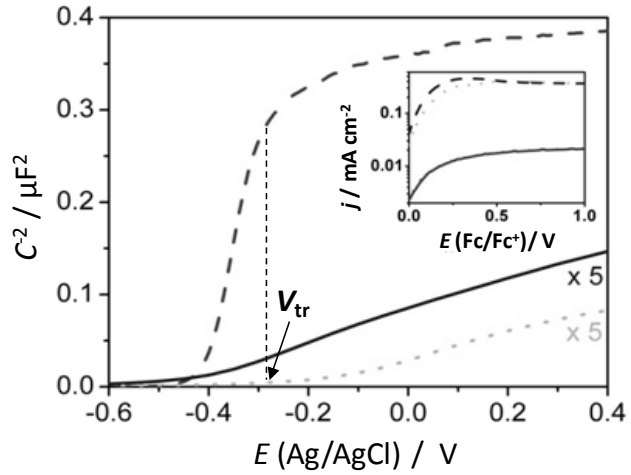

Figure 6.8. Mott-Schottky plot of spray-TiO_2 (circles), spin-TiO_2 (triangles) and FTO (squares) in Na_2SO_4 (1 kHz, pH 3). For the spray-pyrolyzed titania film a transition at V_{tr} a transition of the TiO_2 from a space charge capacitance to a dielectric capacitance occurs. Inset: Tafel-plot of linear sweep voltammetry (10 mM ferrocene, 0.1 M $TBAPF_6$, in acetonitrile).

DRS

In Fig. 6.9a the optical transmittance *T* and reflectance *R* of the spray-pyrolyzed (solid) and spin-cast (dashed) titania films are compared with the FTO substrate (dotted). Because of the high refractive index and the thickness of doped tin oxide coatings, it is not surprising that the absorption spectrum –

taken with the light beam perpendicular to the surface – exhibits an interference pattern. The different interference of the films could be rationalized with a different titania layer thickness and porosity of the films. The indirect bandgap E_g of spray-TiO_2 and spin-TiO_2 was determined by plotting $(\alpha h\upsilon)^{1/2}$ versus $h\upsilon$ (Fig. 6.9b). The as-obtained values are summarized in Table 6.1 (6th column) and are slightly larger than bulk TiO_2 (3.2 eV). They are found to be similar for the spin-cast and spray-pyrolyzed samples and also to values previously found for nano-sized titania films.

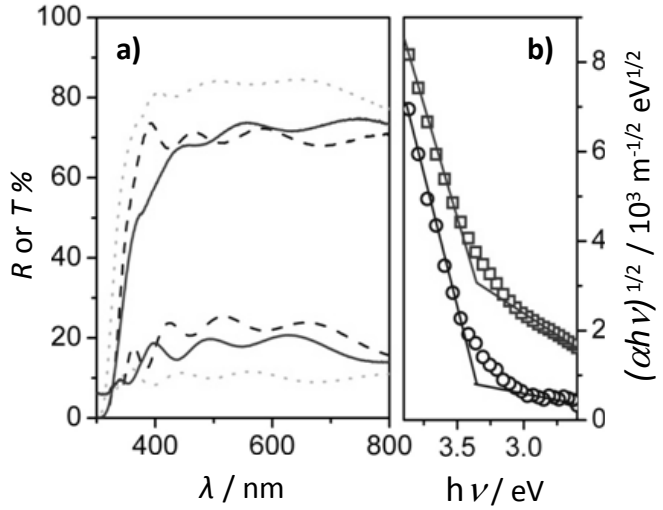

Figure 6.9. a) Transmittance *T* and Reflectance *R* of spray-pyrolyzed TiO_2 (solid), spin-coated TiO_2 (dashed) and FTO substrate (dotted). **b)** Indirect bandgap of spray-pyrolyzed (squares) and spin-cast (circles) TiO_2 films**.**

XPS

To investigate the valence band and bandgap states of the titania films, XPS measurements using synchrotron radiation were performed at MAX-lab, Lund University. The valence band edge for the two samples may be approximated using a linear fit of the valence band and the extension of this line to the baseline. The valence band edge E_{VB} *vs* the Fermi level E_F in TiO_2 was found to be similar for the two titania samples (Table 6.1, 5th column). At binding energies lower than the valence band edge, in the band gap of the two samples, it is possible to observe a finite density of states for both samples. States in this binding energy region are often referred to as bandgap

states, since they are located between the valence and conduction band edges. As shown in Fig. 6.10, the samples exhibited slight differences in the density of bandgap states which can be due to a difference in the defect structure or amount of surface-adsorbed species. Comparing the bandgap states, which are generally considered to originate from Ti atoms with a strong Ti 3d character, some small differences were noticeable between the two films. The detailed explanation of the bandgap states of TiO_2 have been investigated previously.[29-31] More bandgap states lay at higher binding energies for the spray-pyrolyzed TiO_2 compared to the spin-cast TiO_2, whereas a higher density of bandgap states is located at lower binding energies for the spin-cast TiO_2 compared to the spray-pyrolyzed TiO_2. As a consequence, differences in the defect structure or in the amount of surface adsorbed species exist for these samples. Although these differences are small, they may partly be a reason for the slightly different optical properties of these films.

Assuming a density of states N_C of 10^{19} cm^{-3} the conduction band E_{CB} can be estimated to be 112 mV more negative than the flatband potential V_{fb} using:

$$E_{CB} = eV_{fb} + k_B T \left(\frac{N_D}{N_C}\right) \quad \text{(eq. 6.7)}$$

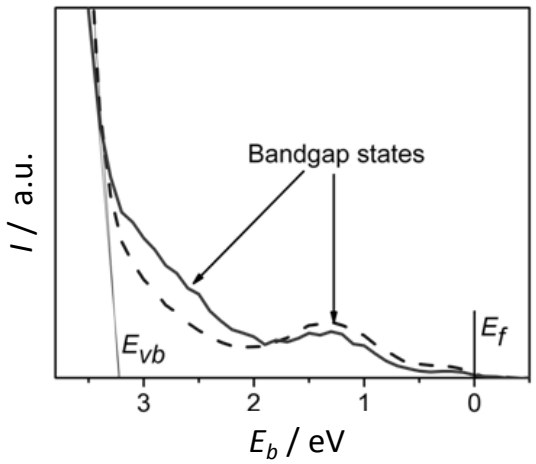

Fig. 6.10. Photoelectron spectroscopy signal intensity *versus* binding energy (E_b) of spray-pyrolyzed (solid) and spin-cast (dashed) titanium dioxide on FTO.

Sample	V_{fb} (V *vs* NHE)	N_D (cm^{-3})	*R*	E_{VB} (eV)	E_g (eV)
spray-TiO_2	-0.26	1.3×10^{17}	1.7	3.2	3.35
spin-TiO_2	-0.25	1.8×10^{19}	-	3.2	3.40

Table 6.1. Electronic and optical properties of TiO_2 films: flatband potential V_{fb}, doping density N_D and roughness factor *R* determined from Mott-Schottky plot at pH 3, valence band energy E_{vb} *vs* Fermi level E_f in TiO_2 (XPS analysis), band-gap E_g from optical measurements.

6.3.2. Morphological and structural properties

SEM

Top-view SEM images displayed in Fig 7.11 represent a first tool to show the difference in film morphology. The spray-pyrolyzed TiO_2 gives rise to a surface morphology that seems to consist of bigger grains. This is probably due to preferential growth on certain crystal surfaces of the underlying FTO substrate during the spray deposition. The TiO_2 substrate prepared by spin-coating appears more “even”; at higher magnification crystallites are visible.

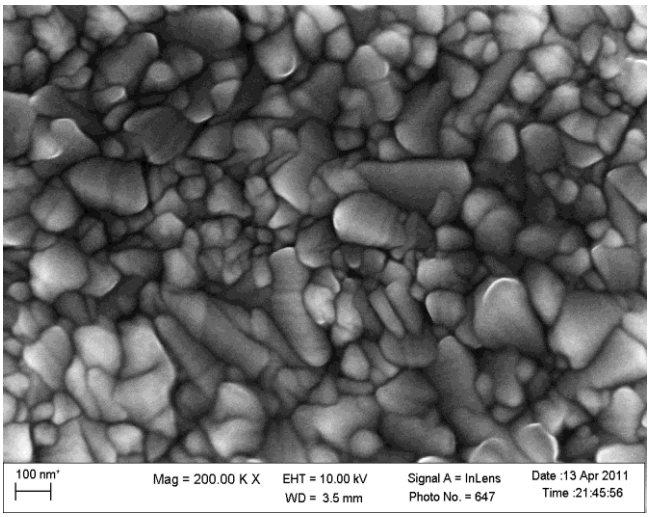

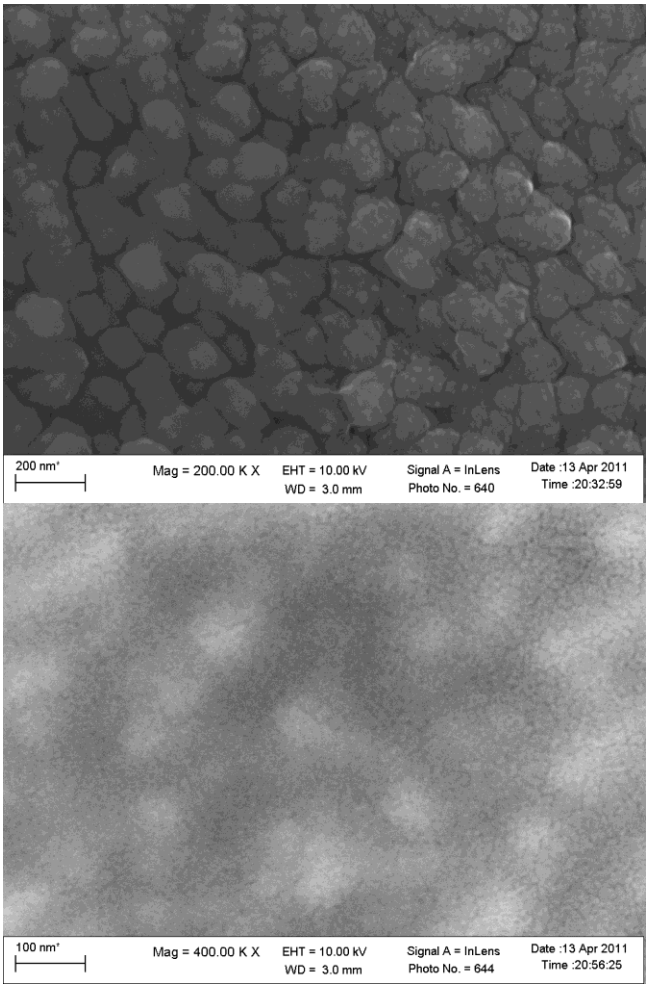

Figure 6.11. Top-view SEM images of the surface of the bare FTO (top - previous page - 200k magnification), spray-TiO_2 (center, 200k magnification), and spin-cast TiO_2 (bottom, 400k magnification).

However, not fairly clarifying information can be obtain by this sort of analysis.

Figure 6.12 compares the cross-section SEM images of the spray-pyrolyzed TiO_2 (a) and spin-cast TiO_2 (b), witnessing that the spray-pyrolyzed and spin-cast TiO_2 films have a rather dissimilar appearance. The spray-pyrolyzed TiO_2 film (slightly darker shade of grey in Figure 6.12a) seems to have grown on top and intimately connected to the underlying FTO. The TiO_2 film seems to be rounding off the sharp edges of the FTO surface but adapting to the surface

topography of the FTO layer. In contrast, the spin-cast TiO_2 film (Fig. 6.12b) appears more like a separate layer lying on top of the FTO and the sharp edges of the surface of the FTO substrate are visible. As expected from the quite obscure top-view SEM image, the spin-TiO_2 film is composed of smaller particles forming a relatively even layer on top of the FTO substrate. The thickness of the deposited TiO_2 layers was determined from these SEM cross-section images and are summarized in Table 6.2 (2nd column). The surface of the spin-cast TiO_2 film, as revealed by the cross-section image, is more smooth compared to the spray-pyrolyzed TiO_2 film and less affected by the underlying FTO substrate.

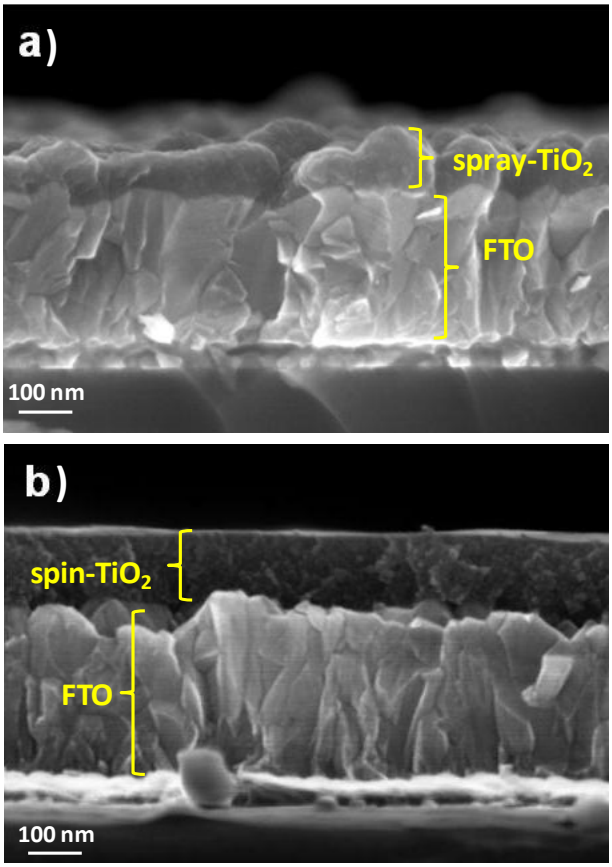

Figure 6.12. Cross-section scanning electron microscopy (SEM) images of spray-pyrolyzed TiO_2 (a) on FTO and spin-coated sol-gel TiO_2 (b) on FTO.

AFM

The two different types of TiO_2 films were also analyzed using atomic force microscopy. The AFM images are compared in Figure 6.13. The underlying FTO crystals appear as larger domains in the order of 150 to 300 nm (Fig. 6.13a). From the analysis of the AFM images the average height h_{av} and root-mean square surface roughness (R_{rms}) of the titania films were determined and are included in Table 6.2, 3rd and 4th column, respectively. In comparison to the R_{rms} of the FTO substrate, the TiO_2 layer deposited by spray-pyrolysis decreases the surface roughness by a factor of 1.7. TiO_2 films prepared by the spin-casting route have a lower R_{rms} and have, as also apparent in the SEM cross-section images (Fig. 6.13b), a more smooth surface.

While AFM analysis gives valuable information on the surface topography of a sample, it does not provide any interesting insight into the sample porosity. However, what can be firmly concluded by the help of the used microscopies is that both for the spin-cast and spray-pyrolyzed TiO_2 films small particles in the order of 20 nm are distinguishable both in the AFM and SEM image.

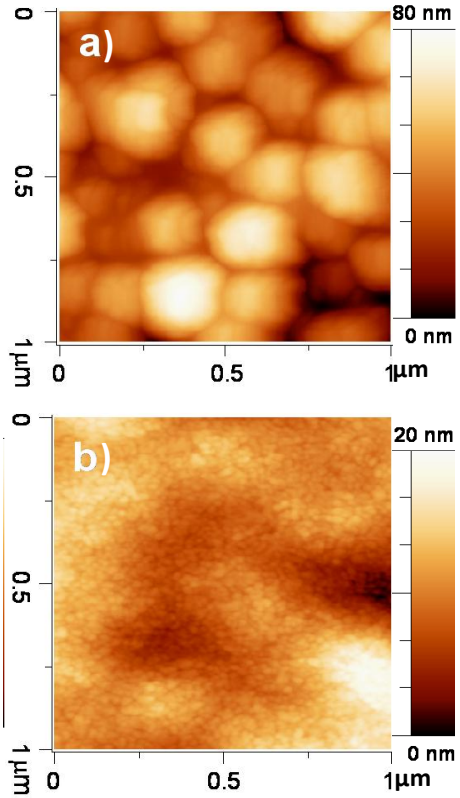

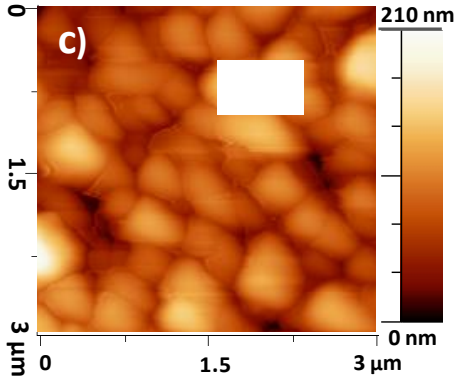

Figure 6.13. Atomic force micrographs of the surface morphology of spray-pyrolyzed (a) and spin-coated (b) TiO_2 on FTO glass substrates (c). Note the difference in magnitude for the z-scales and also for the x-y coordinates relative to the FTO sample.

XRD

In Fig. 6.14 the X-ray diffraction spectra of the spin-TiO_2 (trace a) and spray-TiO_2 (trace b) layers on FTO (trace c) substrates are shown. Compared to the FTO two additional peaks at 2ϑ of *ca* 25° and 48° can be distinguished for the TiO_2 samples. These can be assigned to the anatase (101) and (200) peaks showing that the prepared TiO_2 films are crystalline and predominantly anatase. As the (101) peak is partly obscured by the underlying FTO, the (200) peak was used to determine the crystallite size *B* of the TiO_2 films using the Scherrer equation:

$$B = \frac{K\lambda}{L\,cos\theta} \quad \text{(eq. 6.8)}$$

Assuming spherical particles, a value of the 0.9 was used for the shape factor *K*. *L* is the full width at half maximum of the (200) peak, θ the Bragg angle and λ the X-ray wavelength of the Cu K_α radiation used for the measurements. The determined crystallite sizes are summarized in Table 6.2 (5th column).

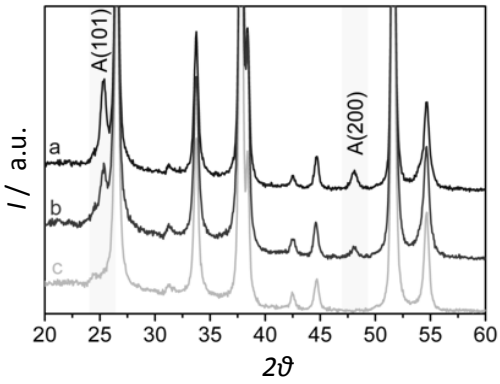

Figure 6.14. X-ray diffraction patterns of spray-pyrolyzed (a) and spin-cast (b) titanium dioxide on FTO (c).

Sample	t (nm)	h_{av} (nm)	R_{rms} (nm)	d_A^{200} (nm)
spray-TiO_2	85 (± 20)	54	16	26
spin-TiO_2	130 (± 20)	11	4	25
FTO	330 (± 20)	79	29	-

Table 6.2. Morphological and structural data of TiO_2 films and of the substrate (FTO): crystallite size determined from XRD (200) peak, film thickness determined from cross-section SEM (such a low thickness did not allow to properly measure with the DekTak profilometer and compare the results obtained with the two techniques), root-mean-surface roughness and average height determined from AFM surface analysis.

From the XRD analysis, both types of TiO_2 were found to contain crystallites in the order of 25 nm. AFM and SEM images suggest that for the spray-pyrolyzed TiO_2 films these crystallites built up the titania films in a densely fused manner, while for the spin-cast TiO_2 films the crystallites are more loosely connected. It can be inferred that these films may exhibit a nanoporosity.

The differences in the TiO_2 film morphology is a consequence of the different conditions in the preparation routes employed. As for what they look like, titania samples prepared by spray-pyrolysis in 12 spray cycles had an even, faint yellowish colour due to interference effects for titania films with thickness in the order of 100 nm on FTO. Spin-casting gave rise to films with even colouring throughout most of the film.

Then, spray-pyrolysis deposition results in compact TiO_2 films grown layer by layer adapting to the surface morphology. In particular, droplets produced at the end of the jet possess a wide size distribution. The droplets vaporize partially or entirely during their way to the substrate (heated at 450 °C) relieving the stress in the films and depressing the shrinkage. Partially dried droplets having a variable shape become flat droplets when they impact the substrate. If one spray cycle could lead to poor connection among particles, the following ones definitely improved connections among particles/aggregates, as depicted in Fig. 6.15.

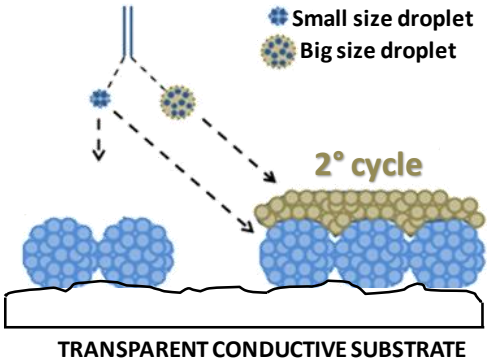

Figure 6.15. Spray-pyrolysis deposition of a colloidal metal oxide suspension on a substrate.

In the spin-casting preparation route titania crystallites are likely to form during storage at 120 °C during which the TiO_2 alkoxide hydrolyzes. Small TiO_x crystallites form which are subsequently fused together during sintering at 450 °C. The resulting titania films consist of TiO_2 nanocrystallites forming a nanoporous structure, whereas in the spray-pyrolyzed samples the TiO_2 particles are intimately fused together.

In Table 6.2 the morphological and structural properties of the films are summarized and compared. The spin-casting route leads to films that were slightly thicker compared to the spray-TiO_2. The surface appears to be less rough as it seems less affected by the morphology of the underlying FTO. These data only provide information on the surface morphology and not strictly on the porosity of the prepared films. Nevertheless, from SEM analysis the spin-cast TiO_2 films appear more porous and less dense than the spray-pyrolyzed films.

6.3.3. Dye deposition

The thickness *d* of the small molecular semiconducting dye (TDCV-TPA) layer was varied by spin-casting the dye from solution of different concentrations. The amount of deposited dye can be estimated from absorption measurements. Fig. 6.16 shows the absorption *A* at absorption maximum of the dye of deposited dye layer in dependency of the dye solution concentration. For concentrations *c* <5 mM the amount of deposited dye on spray-pyrolyzed TiO_2 substrates (Fig. 6.16, red circles) linearly correlates with the solution concentration. TDCV-TPA deposited on spin-coated substrates

(Fig. 6.16, blue triangles) resulted in higher sample absorbance, almost twice the value relative to spray-TiO_2 for the same solution concentration. The relatively larger amount of TDCV-TPA deposited on spin-cast TiO_2 substrates can be interpreted as a "soak-in" effect: the small-molecular semiconductor infiltrates the nanoporous spin-cast TiO_2 films. Moreover, the sample absorbance *A* was correlated to the effective dye layer thickness *d* via profilometry measurements of reference samples on microscope glass slides (inset of Fig. 6.16). A linear correlation factor of $\alpha' = 0.0146\ nm^{-1}$ between *A* and *d* was found. The absorption coefficient α of TDCV-TPA at 520 nm was determined to be $(3.2 \pm 0.2) \times 10^7\ m^{-1}$ which is slightly lower than previously reported by the Hagfeldt group[19] but larger than the value mentioned elsewhere.[32]

SEM-cross section images were acquired for samples prepared with both types of substrates and a dye layer, deposited from a 20 mM solution of TDCV-TPA in dichloromethane. In comparison with the absorbance of these samples the thickness of the dye layer found for the spray-pyrolyzed TiO_2 substrates were in the same order as the dye layer visible in the SEM cross section. For the spin-cast TiO_2 layer the thickness of the overstanding TDCV-TPA layer was found to be about 17 nm thinner than expected from the sample absorbance. This is another indication that the dye infiltrates the porous TiO_2 films prepared by spin-casting.

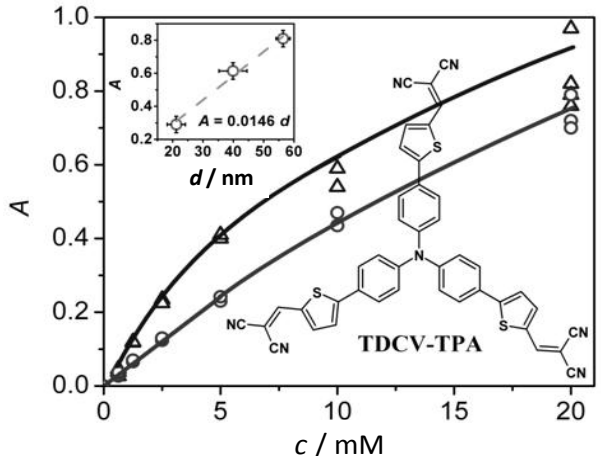

Figure 6.16. Sample absorbance *A* at 520 nm in dependency of the solution concentration *c* of TDCV-TPA on spray-TiO_2 (circles) and spin-TiO_2 (triangles) substrates. Inset: absorption *A vs* dye layer thickness *d*. Trend-lines were added as a guide to the eye.

6.3.4. Dark characteristics of bilayer solar cell samples

To analyze the diode properties of the solar cell devices, the dark current density, J_D, was measured as a function of applied potential, V_a. Figure 6.17 shows plots of $\ln(|J_D|)$ *vs* V_a for devices built with both types of TiO_2 substrates for various dye layer thicknesses and reference diodes where the TiO_2 layer was directly contacted with PEDOT:PSS (d = 0 nm). The dark diode properties of the solar cell devices were analyzed using the Shockley equation (6.4) in its logarithmic form taking into account both the series R_s and shunt resistance R_{sh} of the solar cell devices:[33]

$$\ln(|J_D|) = ln\left(\frac{R_{sh}}{R_{sh}+R_s}\right) + ln\left\{j_0\left[\exp\left(\frac{V_a - IR_s}{\frac{nk_BT}{q}}\right) - 1\right] + \frac{V_a}{R_{sh}}\right\} \quad \text{(eq. 6.9)}$$

Spray-pyrolyzed titania substrates directly contacted with PEDOT:PSS exhibit R_{sh} in the order of $10^4\ \Omega\ cm^2$ which increases by one order of magnitude when a dye layer is added. The junction formed between the spin-cast titania substrates and PEDOT:PSS exhibits R_{sh} in the order of $10^3\ \Omega\ cm^2$ and no rectification. This can be rationalized with short circuits as the TiO_2 films prepared by spin-casting are not pin-hole free. These films are thus not suitable to be used as blocking layers in electrochemical and solid state solar cell devices.

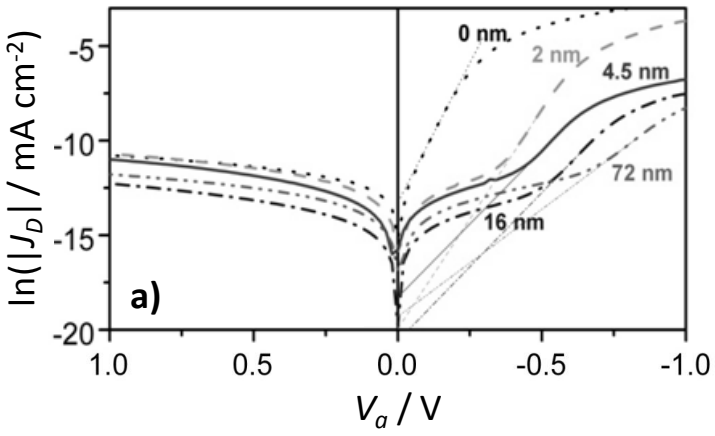

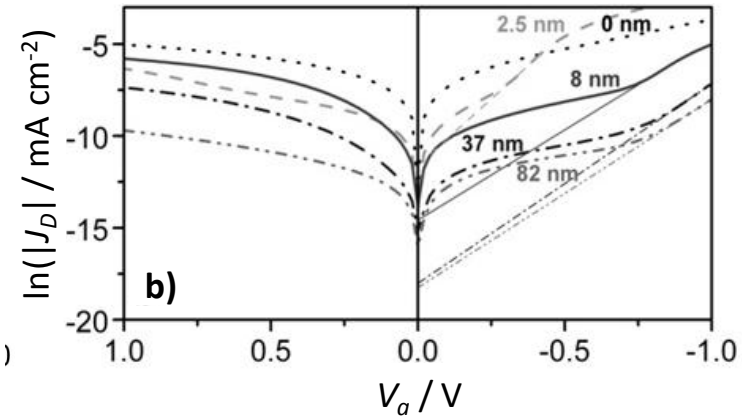

Figure 6.17. Tafel plots of dark current-density *vs* voltage of solar cell devices with varying dye layer thickness (indicated in Figure) for spray-pyrolyzed (a) and spin-cast (b) titanium dioxide electrodes.

The term $I \cdot R_S$ in the logarithmic form of Shockley equation has the dimensions of a potential and can be interpreted as a constant potential offset at regimes where a small, constant current flows through the device. This parameter affects both the dark exchange current density and the shunt resistance of the devices. Furthermore the dye layer thickness *d* influences the ideality factor of the devices.

In Fig. 6.18 n, j_0, and R_{sh} parameters from the analysis of the dark J-V curves are shown for devices built with spray-pyrolyzed (circles) and spin-cast (triangles) titania substrates as a function of the dye layer thickness.

The exchange current density and ideality factor were determined from the extrapolated linear part of the $\ln|J_D|$ plot at negative V_a.

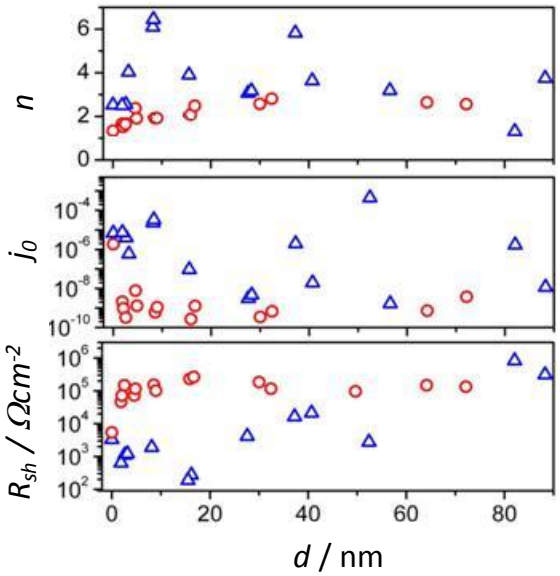

Figure 6.18. Ideality factors *n*, dark current density j_0 and shunt resistance R_{sh} derived from the dark current-voltage measurements for devices built with spray-pyrolyzed titania (circles) and spin-cast titania substrates (triangles).

The comparison illustrates that the spray-pyrolyzed TiO_2 substrate acts as sufficient blocking layers and rectifying contacts. The spin-cast TiO_2 layers exhibit an increase in R_{sh} and decrease in j_0 with increasing *d* (namely with the amount of spray cycles for spray-TiO_2), which means that the dye layer itself can act as an insulating layer between the electron and hole selective contacts and functioning solar cell diodes can be achieved once the dye layer is thick enough to prevent electrical shorts. The spray-pyrolyzed TiO_2 layers give hybrid solar cell devices with more consistent characteristics while there is much more spread in the values attained for the spin-cast TiO_2 layers. The larger variation in these latter experimental values shows that spin-cast TiO_2 films probably exhibit differences in blocking ability and pinholes among individual samples. Due to their apparently lower adhesion to the underlying FTO substrates these films might also be more prone to partial destruction during sample preparation.

Mott-Schottky on bilayer solar cells

Mott-Shottky measurements (in the dark) on the bilayer devices built with spin-cast titania samples led to results reported in Fig. 6.19. The flatband

potential, or built-in potential, correlates well with the V_{OC} attained for the devices. One might be able to determine the relative dielectric constant ε_r for dye TDCV-TPA by plotting the measured capacitance as a function of the reciprocal dye layer thickness and taking the slope into account (inset of Fig. 6.19). It came out a value of 1.29, which is reasonable for an organic material.

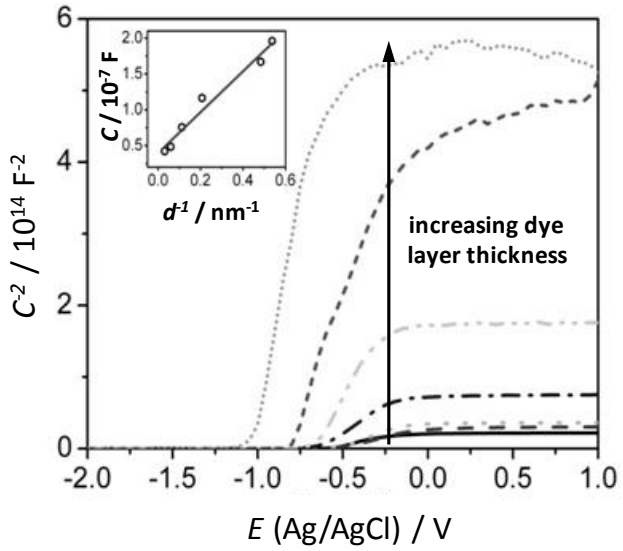

Figure 6.19. Mott-Schottky plot derived from measurements on the assembled solar cells built with spin-TiO_2 at varying dye layer thickness. Inset: capacitance values as a function of the reciprocal of dye layer thickness.

6.3.5. Hybrid solar cells under illumination

Cameron and Peter[26] had a very similar aim about TiO_2 blocking layers for solar cells and found out that titania prepared by spray pyrolysis are n-doped but are not degenerately doped like the FTO substrate. The electron density at the TiO_2-electrolyte interface will depend on doping density and on the band bending in the TiO_2 film, which is controlled by the photovoltage in the DSC. Under strong illumination at open circuit or on load, the TiO_2 blocking film is driven toward the flatband condition, so that electron transfer to the electrolyte becomes possible and the films can no longer be described as "blocking". Their complete DSCs were comprised of a spray-pyrolyzed TiO_2 layer with a thickness in the range 56-118 nm (measured by spectroscopic ellipsometry) acting as blocking layer and a nanocrystalline TiO_2 layer of about 4-5 μm.

In the present work, current density - voltage (*J*-*V*) measurements under simulated AM1.5 illumination (1000 W m^{-2}) were performed to compare the solar energy conversion efficiency η of the two different types of titania substrates. Selected *J* – *V* curves are shown in Figure 6.20a for spray-pyrolyzed (circles) and spin-cast (triangles) titania substrates for devices comprising a TDCV-TPA layer of approximately 8 nm and 80 nm thickness, respectively. In Figure 6.20b the corresponding IPCE of these devices is shown.

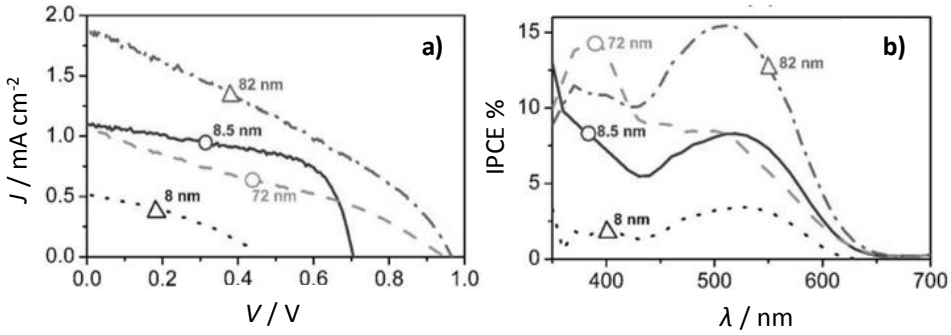

Figure 6.20. Current-density *vs* voltage (a) and IPCE spectra (b) of devices with dye layer thickness around 80 nm and 8 nm (as indicated in Figure) for spin-TiO_2 (triangle) and spray-TiO_2 (circle), respectively.

Bilayer solar cell devices comprising TDCV-TPA and spray-pyrolyzed TiO_2 (spray-TiO_2) substrates exhibit similar trends as previously reported[19] but the overall conversion efficiencies obtained herein are higher, reaching 0.47 %. This difference could be also ascribed to the different dye batches employed. Solar cell devices prepared using the spin-cast TiO_2 substrates often exhibited short-circuits or low performance for devices comprising dye layer thicknesses d < 20 nm. The efficiency of a sample comprising ~10 nm TDCV-TPA (Fig. 6.20, dotted) was low (<0.1 %) compared to the device built with spray-TiO_2 of comparable d (Fig. 6.20, solid). For thicker d the spin-cast TiO_2 devices outperformed the spray-TiO_2 devices with η up to 0.6 % (Fig. 6.20, dash-dot). The asymmetric shape of the *EQE* can be explained with a more efficiency harvesting of higher energy excitons in this device geometry.[19]

The spectral response of the solar cell devices appears significantly different for devices comprising spin-cast and spray-pyrolyzed TiO_2 substrates for thick TDCV-TPA layers (Fig. 6.20b). The mismatch between the *EQE* of TDCV-TPA and the corresponding light harvesting efficiency, *LHE*, of the device has been

observed previously and is due to a more efficient exciton harvesting for the higher energy excitons in TDCV-TPA created at 380 nm.[19] This effect is only apparent if the dye layer thickness exceeds the exciton diffusion length, L_{XD}, for the lower energy transition. The lack of the distortion of the *EQE* spectrum for devices built with the spin-cast TiO_2 substrates indicates that excitons are generated within the L_{XD} of the lower energy excitons. This indicates that the nanoporosity of the spin-cast TiO_2 films is on the same length scale or smaller than the L_{XD} of TDCV-TPA.

In Figure 6.21 the *d*-dependency of the *EQE*, the open circuit voltage, V_{OC}, and fill factor, *FF*, is compared for all devices investigated in this study. From the *d*-dependency of the *EQE* the exciton diffusion length, L_{XD}, can be determined.

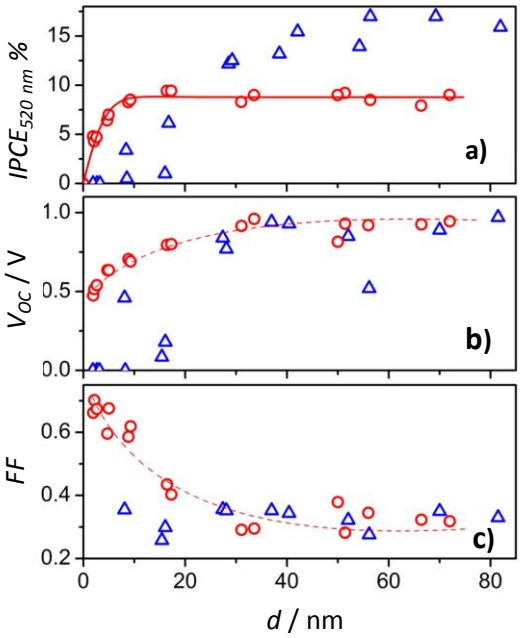

Figure 6.21. Comparison of **a**) the *IPCE* at absorption maximum of dye TDCV-TPA (520 nm), **b**) open circuit voltage V_{OC} and **c**) fill factor *FF* in dependency of the dye layer thickness *d* for hybrid solar cells prepared with spray-pyrolyzed (circles) and spin-cast (triangles) TiO_2. Trend-lines in the *d*-dependence of V_{OC} (**b**) and *FF* (**c**) were added as a guide to the eye. For the spray-pyrolyzed TiO_2 substrates, the *IPCE* dependency on *d* could be fit to an exciton diffusion model.

It has to be underlined that the exciton diffusion models employed herein assume planar interfaces which is not necessarily given in bilayer devices, as

already shown. However, the exciton diffusion length of TDCV-TPA was determined to be 6.5 nm for an interfacial charge transfer efficiency, η_{CT}, of 52 % assuming a non-quenching PEDOT:PSS interface and planar interfaces.[18,19] Assuming a quenching PEDOT:PSS contact and allowing for η_{CT} = 100 % the L_{XD} was determined to be 3.3 nm. This is slightly higher than reported previously,[19] which is partly due to the different absorption coefficient used in this study but also to the higher overall performance of the devices. This finding illustrates that experimentally determined exciton diffusion lengths are often dependent on the conditions under which they were determined[34] and the commonly-made assumption of planar interfaces might be invalid for most experimental devices. For the spin-cast TiO_2 no systematic dependence of the *IPCE* on the dye layer thickness *d* was found as devices with thin *d* were not functional.

The V_{OC} exhibited a similar *d*-dependency for the devices built with spray-pyrolyzed TiO_2 substrates as reported previously.[19] The shift in the V_{OC} and voltage onset in the dark can be rationalized with TDCV-TPA acting as a dielectric layer between the two electric contacts. The spin-cast electrodes exhibit short circuits for thin dye layers. At thicker *d* the V_{OC} appears to reach a limiting value of 0.95 V for both types of substrates. As in organic solar cells, the V_{OC} in hybrid solar cell devices is expected to be limited by the difference in the quasi-Fermi level for electrons in the n-type TiO_2 and the quasi Fermi level for holes in TDCV-TPA. For thin dye layers, however, the V_{OC} is influenced by the contact between TiO_2 and PEDOT:PSS and the limiting V_{OC} can only be established for dye layers thick enough to efficiently prevent a direct contact between TiO_2 and PEDOT:PSS. At low dye coverage the flatband potential / quasi-Fermi level in TiO_2 might also be influenced by the acidity of PEDOT:PSS.[35] The similar limiting V_{OC} for both types of TiO_2 substrates supports the hypothesis that the V_{fb} of the titania films is similar for both types of substrates.

The fill factor for the spray-pyrolyzed TiO_2 substrates was found to decrease from about 0.7 to about 0.3 with increasing *d*. This was previously rationalized with a limitation in the hole transport through the TDCV-TPA layer with increasing *d*.[19] For the spin-cast TiO_2 layers the *FF* is around 0.3 even for small *d*. This can be ascribed to higher recombination losses which is also apparent in the low shunt resistance (R_{sh}) and dark saturation current density (j_0) observed in the dark *J-V* measurements (Fig. 6.18).

Photovoltage (V_{OC}) decay measurements were carried out to gain insight into the recombination processes in the solar cell devices. After illumination for 10 s with an LED with an approximate light intensity of 1 sun, the light source was switched off and the voltage decay recorded over time. Figure 6.22 displays the V_{OC} decays for devices built with the spin-cast TiO_2 (a) and spray-pyrolyzed TiO_2 (b). The former samples exhibit a much faster voltage decay (note the difference in time-scales) and the recombination kinetics becomes slower with increasing dye layer thickness. Devices built with spray-pyrolyzed TiO_2 substrates initially show a progressively slow V_{OC} decay with increasing dye layer thickness. However, for dye layers exceeding 40 nm the V_{OC} decays faster (see the curved arrow in Fig. 6.22). For a better understanding of the results, V_{OC} decays of samples with TiO_2 layers of different thicknesses are shown in a semi-logarithmic plot in Figure 6.22c.

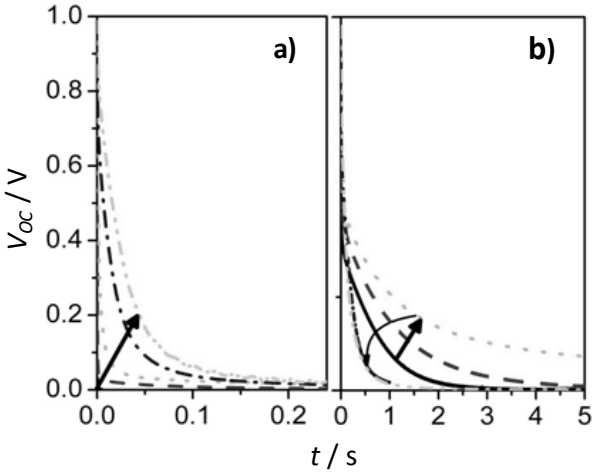

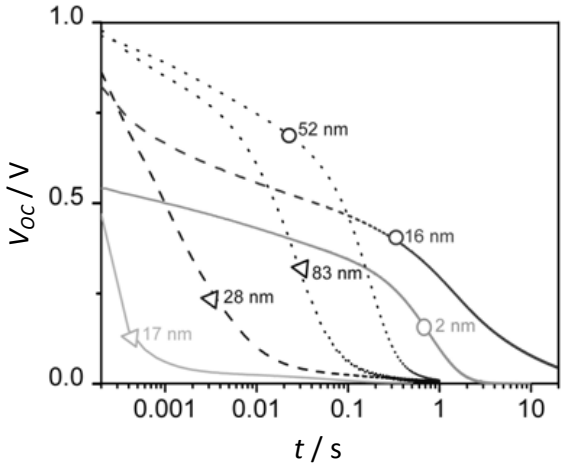

Figure 6.22. Top (previous page): photovoltage decay (V_{OC}) for a) spin-coated TiO_2 and b) spray-pyrolyzed TiO_2 solar cell devices with increasing dye layer thickness (solid *ca*. 2 nm, dashed ca. 8 nm, dotted *ca*. 20 nm, dash-dot *ca*. 40 nm and dash-dot-dot *ca*. 80 nm). Bottom: Semi-logarithmic plot decays for bilayer solar cells built with spin-cast TiO_2 (triangles) and spray-pyrolyzed TiO_2 (circles) films of different thicknesses (indicated in figure).

The voltage decay was found to be multi-exponential, and this can be rationalize considering the charge carrier behavior at the interfaces. In the devices investigated herein up to four recombination pathways have to be considered, as indicated in the energy level diagram (Fig. 6.23). Process (1) is the recombination of electrons in TiO_2 with holes in the dye layer and (2) the recombination of electrons in TiO_2 with holes in PEDOT:PSS. If the titania layer is not sufficiently blocking the FTO, pathways (3) and (4), which represent recombination processes via interfaces of either the dye or PEDOT:PSS with the FTO substrate, have to be considered.

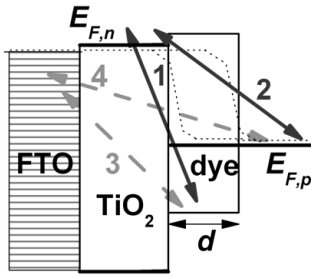

Figure 6.23. Illustration of recombination pathways at the different interfaces in the solar cell device.

As already noticed, devices built with spin-cast TiO_2 substrates exhibit faster V_{OC} decays on shorter time scales compared to devices built with spray-pyrolyzed TiO_2 substrates. For thin *d* no considerable device voltage was measurable as all charges were lost rapidly through recombination. With increasing *d* the recombination kinetics of the spin-cast titania devices becomes slower. This is another indication that the dye layer acts as a barrier between the FTO and PEDOT:PSS interfaces. For thicker dye layers we could therefore build functioning solar cell devices with the spin-cast titania even exceeding the performance of devices built with spray-pyrolyzed TiO_2.
On the contrary, for bilayer solar cells built with spray-pyrolyzed TiO_2 the V_{OC} decay occurred on a longer time scale. In these devices recombination pathways to the FTO (paths 3,4 of Fig. 6.22) can be neglected. Increasing the dye thickness from thin layers to about 20 nm, the V_{OC} decay becomes slower indicating that recombination events become less frequent with increasing dye layer thickness. The faster V_{OC} decay for *d* >40 nm may be due to a less sufficient extraction of photogenerated holes from the TDCV-TPA layer.

Considering the more porous appearance of the spin-cast TiO_2 substrates in SEM and AFM analyses and the soak-in effect observed for the dye deposition (Fig. 6.16), the higher photocurrent can be interpreted to be a consequence of a larger interfacial area for charge separation. From SEM cross-section of spin-cast TiO_2 samples with deposited TDCV-TPA (fig. 6.24), the visible overstanding dye layer was about 17 nm thinner than expected from the sample absorbance. This corresponds to about 72 % of the light harvested in the interpenetrated dye/TiO_2 region. As the distance to the nearest TiO_2 interface can be expected to be small, excitons are harvested very efficiently.

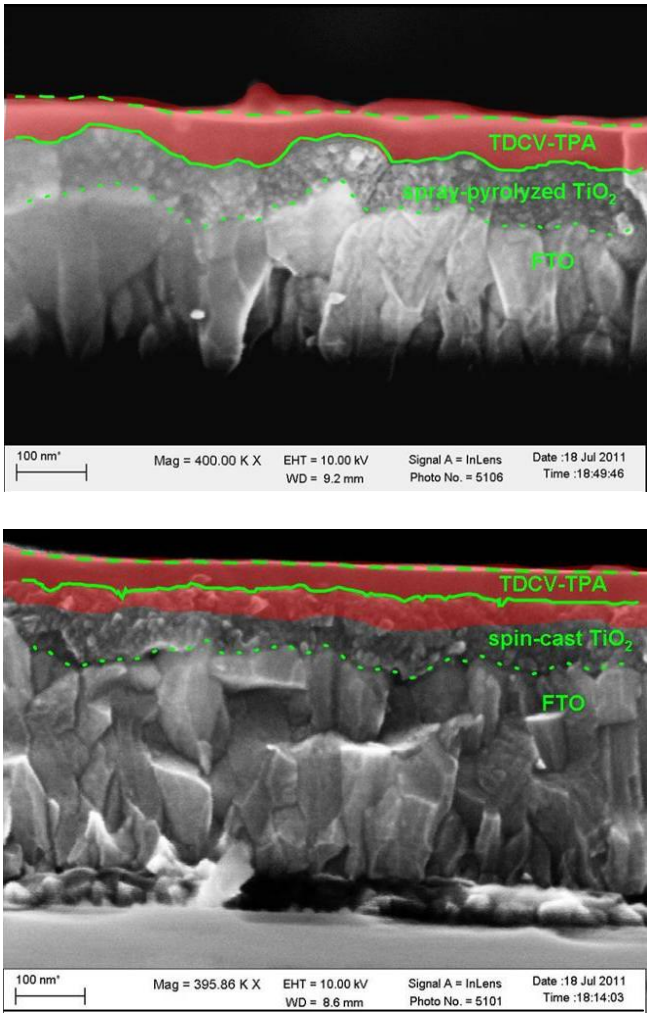

Figure 6.24. SEM cross-section of spray-pyrolyzed (top) and spin-cast (bottom) TiO_2 films with a layer of TDCV-TPA deposited from a 20 mM dye solution. For the spray-TiO_2 film the layer of TDCV-TPA is marked in red. For the spin-TiO_2 the red band the dye layer infiltrates into the porous TiO_2 layer.

The effect of the preparation route of the titania might be negligible in comparable HSC devices comprised of polymers[12,36] but to the author's best knowledge a systematic comparison of TiO_2 substrates prepared using different preparation routes has not been reported.

The efficiencies for the bilayer devices comprising TDCV-TPA and spin-cast TiO_2 films reported herein compare favourably with bilayer HSCs using TiO_2

films prepared in a similar manner in combination with the well-known poly-3-hexylthiophene (P3HT).[12] Thus, TDCV-TPA is an interesting compound to be used in hybrid solar cell devices and the smaller molecular dimensions might prove to be beneficial when realizing nanostructured hybrid solar cells as the dimensions of the organic compound affect the infiltration into the scaffold of a porous inorganic acceptor.[37]

The second part of this chapter deals with the fabrication and test of dye-sensitized solar cell devices with a main focus of the effectiveness of titania pastes.

Three different types of solar cells were studied with home-made nanostructured TiO_2: hybrid solar cells (HSCs), solid-state dye-sensitized solar cells (SS-DSCs) and dye-sensitized solar cells with a liquid electrolyte (DSCs). All of these are made of different components, as depicted in Fig. 7.1 and explained much in details in the following paragraphs. The counter electrodes range from graphite (for HSCs) to silver (for SS-DSCs) to platinum (for DSCs). Whereas dye for HSCs is the same used for HSCs studied in the previous chapter (TDCV-TPA), dye D35 ((E)-3-(5-(4-(Bis(20,40-dibutoxybiphenyl-4-yl)amino)phenyl)thiophen-2-yl)-2-cyanoacrylic acid), quite commonly adopted in literature, has been used for both SS-DSCs and DSCs with a liquid electrolyte. This latter component consists in the previously mentioned PEDOT:PSS or in the well-known spiro-OMeTAD ((2,2',7,7',-tetrakis(N,N-di-p-methoxyphenyl-amine)-9,9',-spirofluorene) for HSCs and SS-DSCs, respectively. Then, titanium dioxide, as the mainly investigated component, is present as both a compact "blocking layer" on top of the underlying FTO substrate and purposely nanostructured. A blocking layer is particularly required for both types of devices made with a solid-state electrolyte, while in the third type of solar cells (traditional DSCs) other expedients are adopted to build a functioning device, with the use of different TiO_2 layers (see Fig. 6.25).

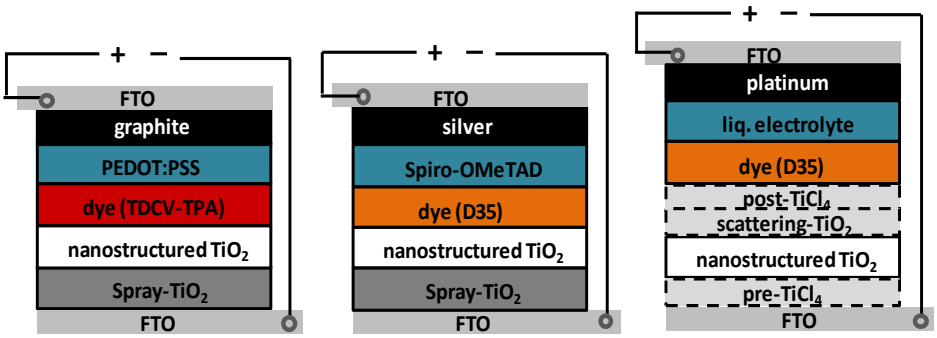

Figure 6.25. Schematic picture of the main components of solar cell devices presented in this chapter: hybrid solar cells (left), solid-state dye-sensitized solar cells (middle), dye-sensitized solar cells with a liquid electrolyte (right), namely a cobalt bipyridyl redox complex compared with the traditional triiodide/iodide.

6.4. TiO_2 pastes

Design and refinement of TiO_2 pastes has presented challenges also to several authors in the literature, as witnessed by the abundant papers on the topic. The importance of "knowing what you have" cannot be stressed enough. As a matter of fact, both preliminary and optimization studies require a synergistic combination of several types of characterization techniques.

For synthetic improvements one needs to know the average particle size, degree of dispersion, surface chemistry as well as the combination of these properties that lead to desirable features for the entire device. Scanning electron microscopy is the formidable technique that has mostly helped throughout all the work on the topic. It proved useful in the main stages of paste optimization for monitoring important effects such as particles aggregation and size, complete coverage of the support and homogeneity of the final porosity. In contrast to SEM, TEM cannot probe surface morphology and could, at times, be misleading because the largest particles in an ensemble are most easily imaged and can be overrepresented in "typical" images. However, both these electron microscopy techniques are limited in terms of truly revealing the entire three-dimensional geometry of a single particle and do not statistically rely on a significant number of particles.

At a first stage, the most simple and at the same time effective way to deposit TiO_2 layers by spin-coater on top of the FTO substrate was thought to be the following. Starting from commercial or home-made titania nanopowders, they

were suspended in 2-propanol, sonicated and spin-coated (taking the surnatant suspension in case a conspicuous powdery amount was left on the bottom of the beaker).

However, SEM analyses showed a disappointing TiO_2 coverage of the underlying substrate, thus negating the initial conjecture. Even the addition of acetylacetone (acac) and/or α-terpineol to the suspension did not improve substantially the deposition: in Figure 6.26, a representative titania deposition of Degussa (Evonik) P25 powder at two different magnification is reported. The spin-coated suspension consisted in TiO_2 and 2-PrOH, terpineol, acac (ca. 10:10:1 v/v). It is evident that the nanoparticles do not form unfavourable aggregates but succeed in covering less than half of the FTO surface, even though two TiO_2 depositions were performed on the same substrate. The same happens for "T" powder when suspended in 2-propanol, even at the optimized amount (see Fig. 6.27). Although a fine nanoporous nanoparticolate system is obtained, in the film finally consists of big aggregates not homogenously deposited on the substrate, leaving it pretty extensively uncovered.

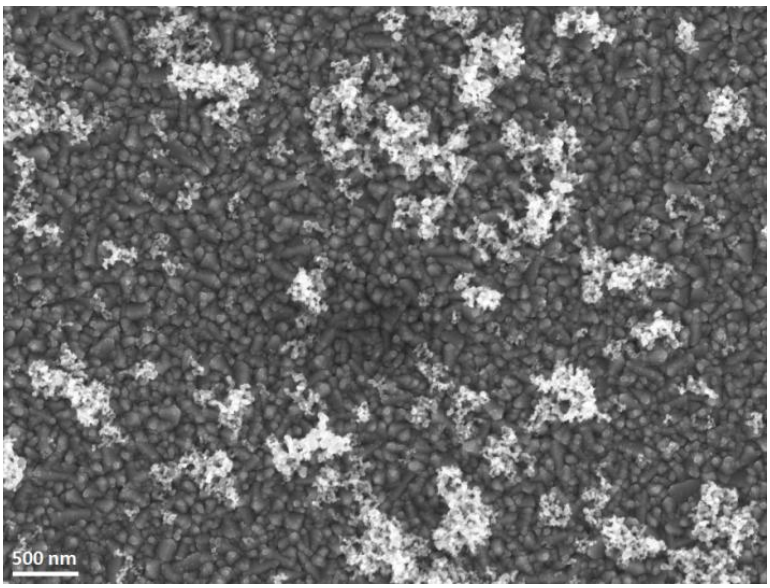

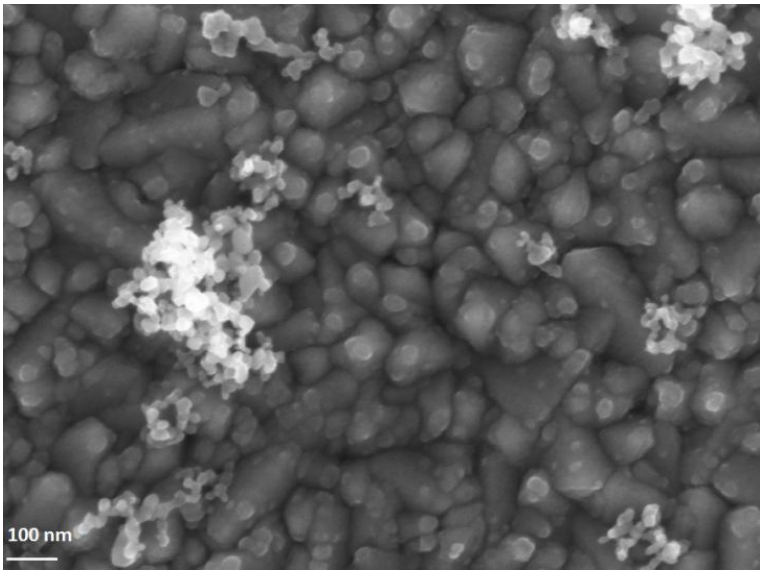

Figure 6.26. SEM images of a dispersion of Degussa (Evonik) P25 deposited on the substrate for hybrid solar cells at two different magnifications. Both TiO_2 nanoparticles (white spots) and the uncovered substrate (spray-pyrolyzed TiO_2 on top of FTO) are visible.

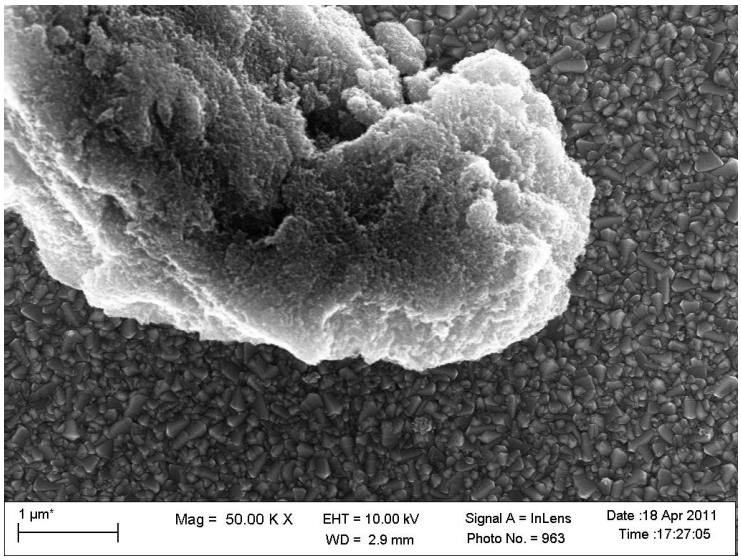

Figure 6.27. SEM images of a dispersion of Degussa (Evonik) P25 deposited on the substrate for hybrid solar cells at two different magnifications. Both TiO_2 nanoparticles (white spots) and the uncovered substrate (spray-pyrolyzed TiO_2 on top of FTO) are visible.

Reached the awareness that such a simple route to disperse TiO_2 nanoparticles starting from a powdery habit was not effective in the context of DSCs, different procedures to obtained home-made titania slurries/pastes have been adopted from the literature or *ex novo* designed and optimized starting from either TiO_2 powders or sols.

A commercial world-wide used TiO_2 paste (Dyesol, DSL 18NR-T) was used at different dilutions with α-terpineol as reference for hybrid solar cells.

Hereafter the experimental procedures of selected titania materials employed in HSCs are reported. All of them were deposited by spin-coater on an FTO substrate. It is underlined that, when using home-madeTiO_2 as powdery raw material, it is highly important to grind well using pestle and mortar for several minutes.

All surfactants were purchased by BASF Company (USA) or obtained by their courtesy.

- According to the pioneering procedure reported more than 20 years ago by O'Regan and coworkers,[38] TiO_2 colloid solutions were prepared by hydrolysis of titanium(IV) isopropoxide (62.5 mL) in 2-propanol (10 mL) with 375 mL of water under vigorous stirring. Within 10 min of the alkoxide addition, 2.85 mL of 65 % nitric acid was added to the hydrolysis mixture, which subsequently was stirred for 8 h at 80 °C. The 2-propanol (and some water) was allowed to evaporate during this time. The sol was even more concentrated at the rotary evaporator (about 20 min). Crystallization occurred during the refluxing, the initial TO_2 precipitate being amorphous.

  The as-prepared sol was named "**O'Regan_sol**". The titania morphology at the nanoscale can be appreciated in Fig. 6.28.

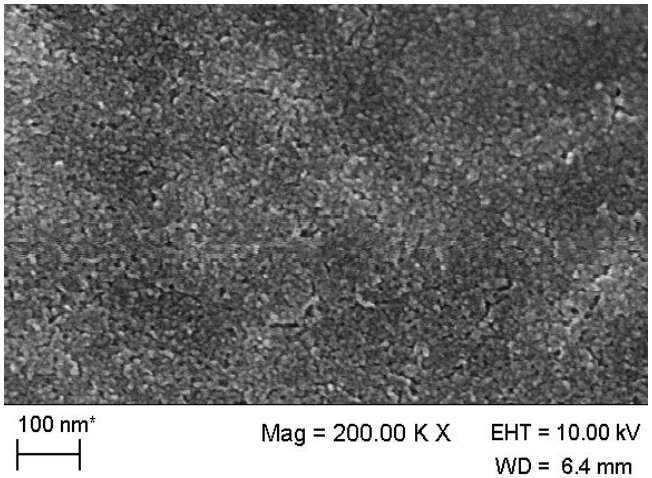

Figure 6.28. SEM image of the titania layer deriving from "O'Regan sol" deposited for hybrid solar cells.

- A procedure adapted from Ahn *et al.*[39] consisted in the following: 3.75 g P123 [poly(ethyleneoxide)20-poly(propyleneoxide)70-poly(ethyleneoxide)20] was dissolved in 10 g of acetylacetone (acac)by stirring for 90 min. Then, 4.7 g of titanium(IV) isopropoxide mixed with 5 g of acac was added with vigorous stirring. Finally, the sol solution was stirred at room temperature for 90 min until a uniform bright yellow TiO_2 sol was obtained.
  The as-prepared sol was named "**Ahn_sol**". The titania morphology at the nanoscale can be appreciated in Fig. 6.29.

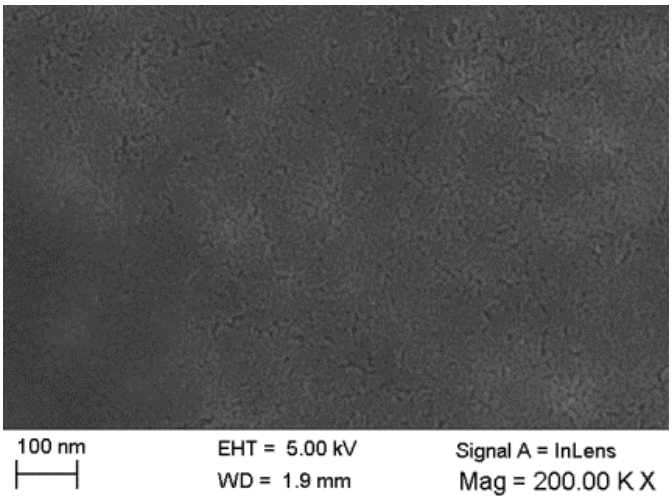

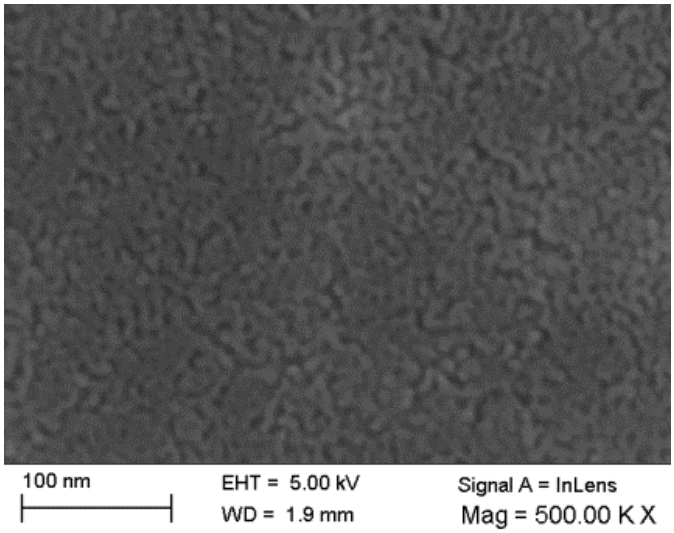

Figure 6.29. SEM image of the titania layer deriving from "Ahn sol" deposited for hybrid solar cells at two different magnifications.

- Using surfactant a Pluronic surfactant, a template TiO_2 sol was obtained. The Pluronic PE type surfactant are low-foaming, nonionic surfactants. They are triblock copolymers in which the central polypropylene glycol group is flanked by two polyethylene glycol groups. They conform to the following structural formula reported in Fig. 6.30, with x,y,z standing for the numbers of PEO, PPO and again PEO units (PEO = polyethylene oxide and PPO = polypropylene oxide).

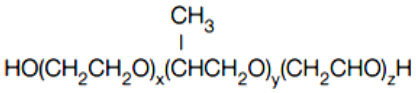

Figure 6.30. Chemical formula of Pluronic PE surfactants.

A solution of 0.1 mol of $Ti(OC_3H7)_4$ in 38 mL of 2-propanol was stirred for 10 min at 300 rpm at 25 °C. Then, 180 mL of water was added, dropwise, fast, to the alkoxide solution, to obtain a water/alkoxide molar ratio of 100 and a water/2-propanol molar ratio of 20. The slurry was stirred for 90 min to complete the hydrolysis. Subsequently, hydrochloric acid (HCl 37 %) was added to peptize the hydroxide precipitate to obtain a homogeneous milky suspension. The

mixture was maintained under reflux at 80 °C for 5 h. Then, Pluronic PE10400 surfactant was added to the sol after being liquefied in 2-propanol (as it is a white waxy solid at room temperature) in such an amount that the optimized ratio between the number of ethoxy units and the number of titanium moles (EO/Ti) was equal to 0.5. The mixture was maintained under stirring for 3 h at 50 °C. This modified template synthesis allows to control the morphology of the colloidal titania: the sol-gel synthesis leads to TiO_2 aggregates; the use of HCl enables smaller particles to be obtained; Pluronic PE 10400 induces self-assembly with titania nanoparticles and its removal by a thermal treatment (when the sol deposited on the FTO glasses is placed for 2 hours on the hotplate at 450 °C) allows the formation of mesopores in the titania structure.

The as-obtained TiO_2 sol was named "**PE10400_sol**". For SS-DSCs, such sol was further concentrated at the rotary evaporator in order to obtain a more dense sol with the aim of depositing a thicker TiO_2 layer.

Different magnifications of SEM images reported in Fig. 6.31 allow to discuss different aspects of the paste resulting from template TiO_2 sol. From the first image of the group represented in Fig. 6.31, it is pretty evident that the titania layer is still smeared with unburnt surfactant. This is, in principle, an inconvenient issue, which could lead to obstruction of the pores of the inorganic TiO_2 scaffold. However, the second image does not confirm such a pessimistic hypothesis, showing a nanometer scale homogeneous porosity. The other two images grouped in Fig. 6.31 highlight the same issue (*i.e.*, the coverage of the substrate) at two different magnification levels: it is clearly visible from the former (third image of Fig. 6.31) that the substrate is partially covered by big TiO_2 aggregates and partially not. The latter image lets appreciate that some small TiO_2 nanoparticles are spread here and there over the underlying bigger grains of the spray-pyrolyzed TiO_2 layer covering the FTO.

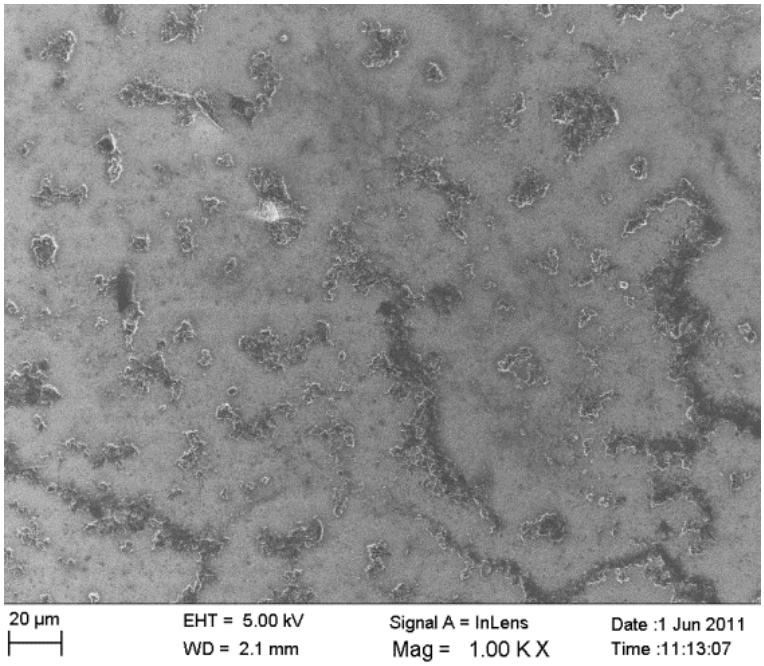
20 µm
EHT = 5.00 kV
WD = 2.1 mm
Signal A = InLens
Mag = 1.00 K X
Date :1 Jun 2011
Time :11:13:07

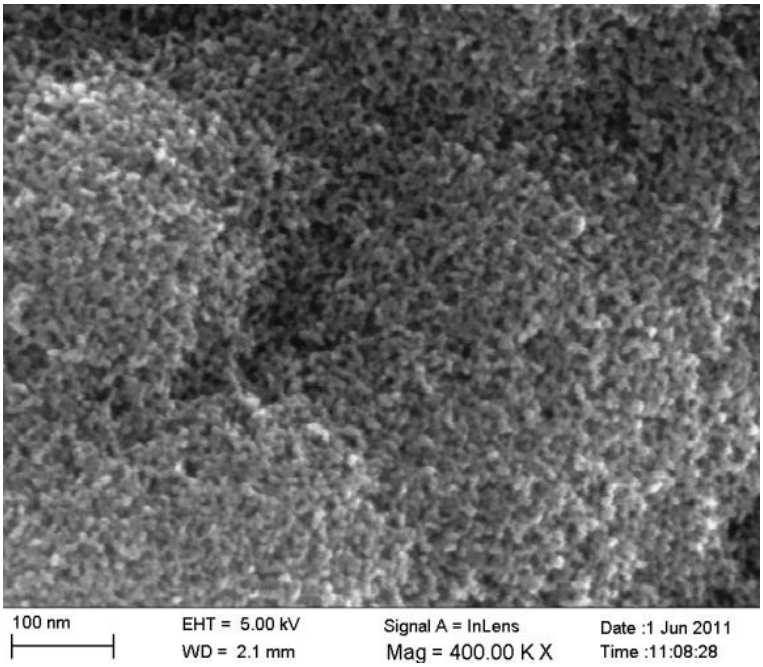
100 nm
EHT = 5.00 kV
WD = 2.1 mm
Signal A = InLens
Mag = 400.00 K X
Date :1 Jun 2011
Time :11:08:28

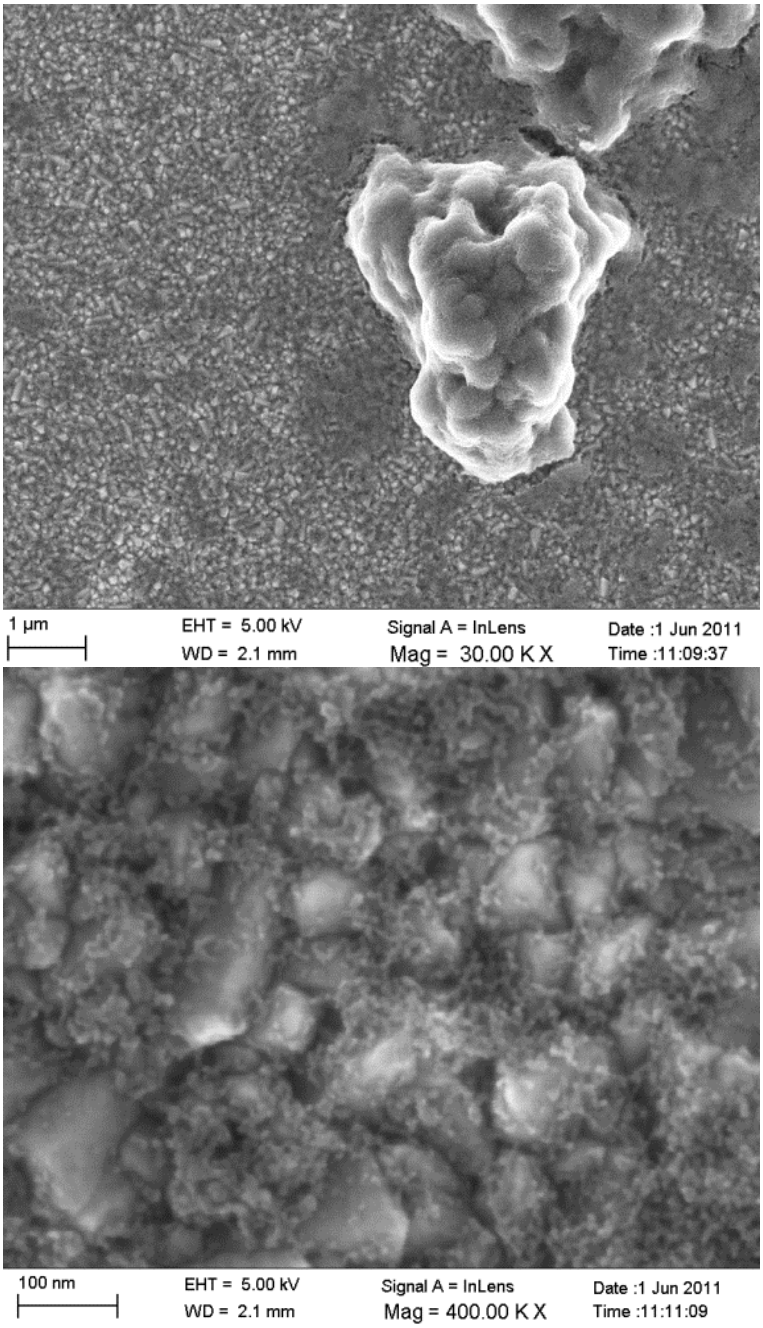

Figure 6.31. SEM images of the nanoporous titania layer deposited from "PE10400 sol" paste to be used for hybrid solar cells. Four different magnifications are reported to illustrate several aspects (see the main text).

- Two different titania pastes were formulated starting from either Degussa (Evonik) P25 powder or the home-made "T" powder (see paragraph 2.1.1 for the synthetic route) adopting the procedure described by Ito *et al.*[40] 2 g of TiO_2 nanopowder were stirred in diluted nitric acid (0.3 mL of 65 % HNO_3 in 40 mL of H_2O) under heating at 80 °C for 8 h and dried in a rotary evaporator to reach a powdery aspect of the dispersion. Thus, HNO_3 resulted adsorbed on the TiO_2 surface (TiO_2/NO_3^-). Nitric acid plays the role of enhancing dispersion of TiO_2 particles and also to increase surface area and porosity of the resulting TiO_2 film. The titania paste was prepared by Ito and coworkers mixing 0.8 g of TiO_2/NO_3^-, 4 mL of H_2O, 0.25 g of polyethylene glycol (a porosity-increasing material) and 0.08 g of ethyl cellulose (as a thickener). Instead of this procedure, different materials in different amount have been finally used, after having tested that literature recipe. The optimized route consisted in the use of $P25/NO_3^-$, α-terpineol, 2-propanol, and acetylacetone (1:28:15:4 w/w). The beaker containing the whole mixture was sonicated and then heated on a hotplate at *ca*. 100 °C for about 1h letting most of the solvent evaporate.

  The as-prepared TiO_2 pastes were named "**$P25/NO_3^-$**" and "**T/NO_3^-**". The titania morphology at the nanoscale can be appreciated in Fig. 6.32.

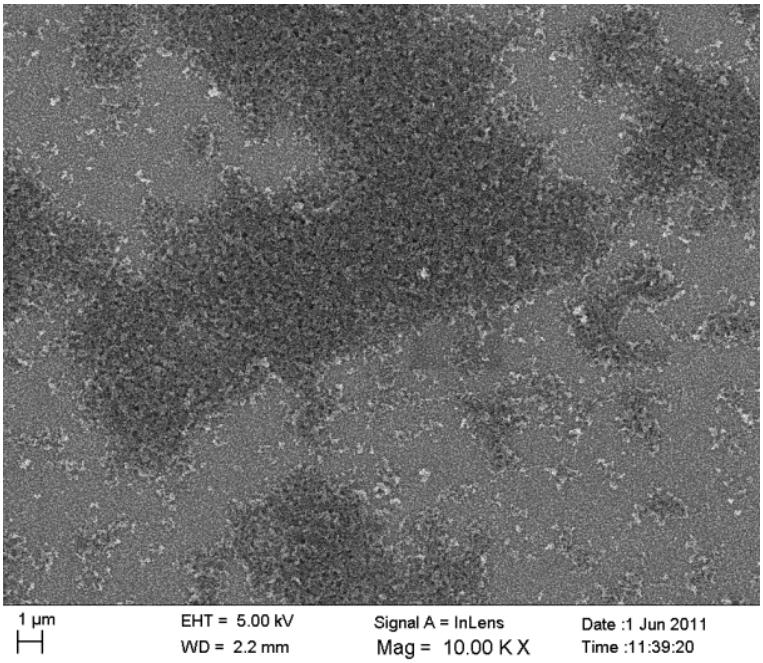
1 µm
EHT = 5.00 kV
WD = 2.2 mm
Signal A = InLens
Mag = 10.00 K X
Date :1 Jun 2011
Time :11:39:20

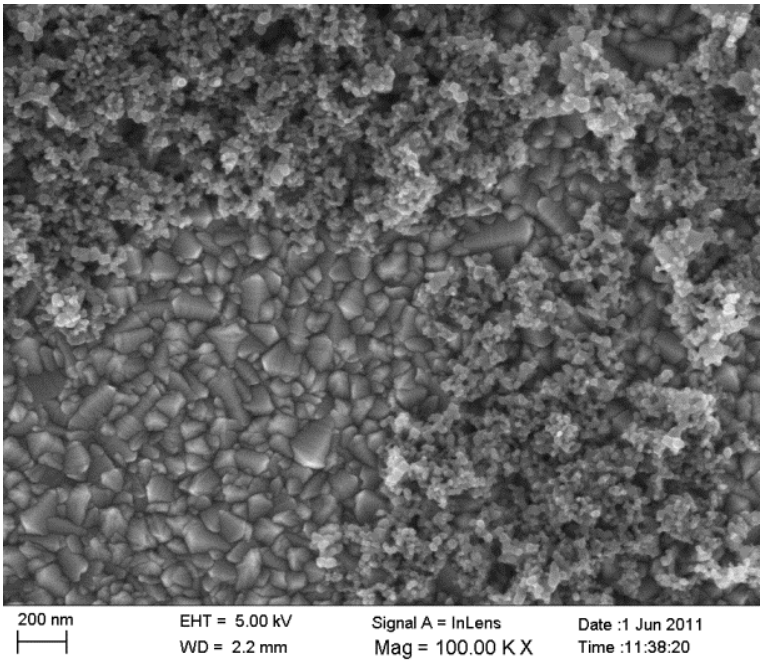
200 nm
EHT = 5.00 kV
WD = 2.2 mm
Signal A = InLens
Mag = 100.00 K X
Date :1 Jun 2011
Time :11:38:20

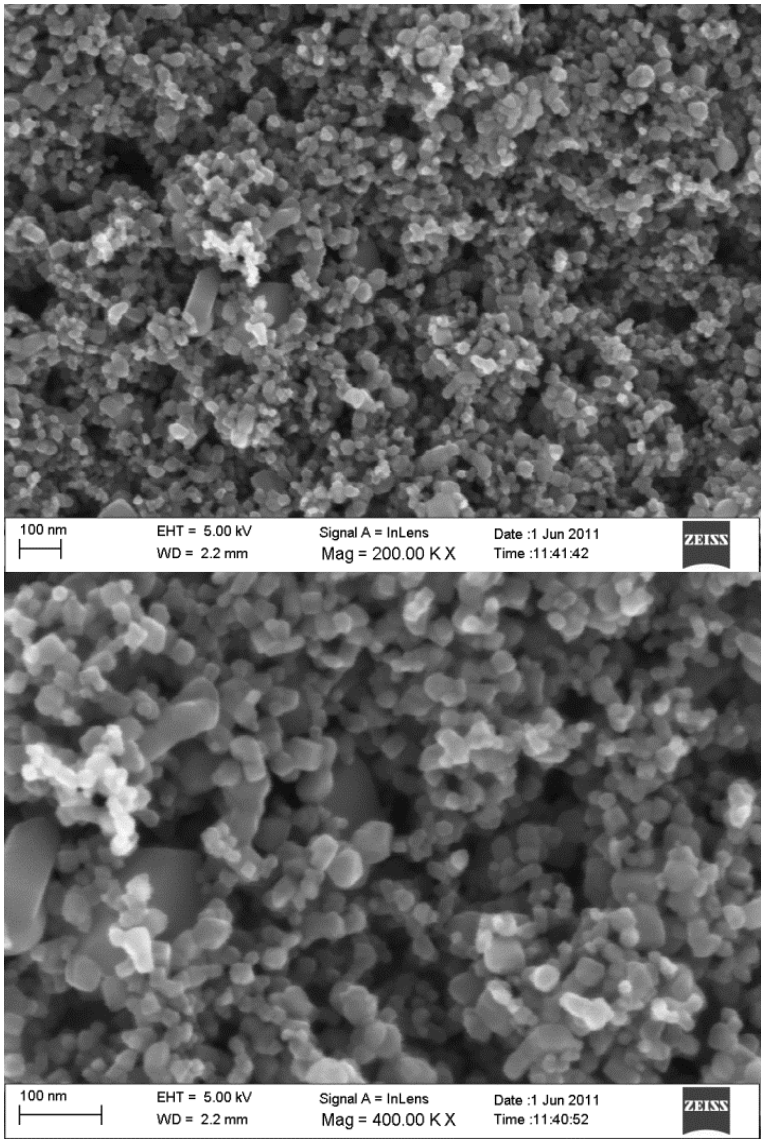

Figure 6.32. SEM images of the nanocrystalline titania layer deposited from the optimized "P25/NO_3^-" paste to be used for hybrid solar cells. Four different magnifications are reported to illustrate several aspects (see the text).

- One among all the doped-TiO_2 powders reported in chapter x has been used in another different procedure to obtained a suitable TiO_2 material for deposition on FTO. The titania slurries were consisted of

0.25 g of nitrogen-doped titania (the not calcined powder was used), 2 g of 2-propanol, 0.4 mL of acetylacetone, 3 ml of α-terpineol.
The as-prepared TiO_2 pastes was named "**TN_TEA_pre**". The titania morphology at the nanoscale can be appreciated in Fig. 6.33.

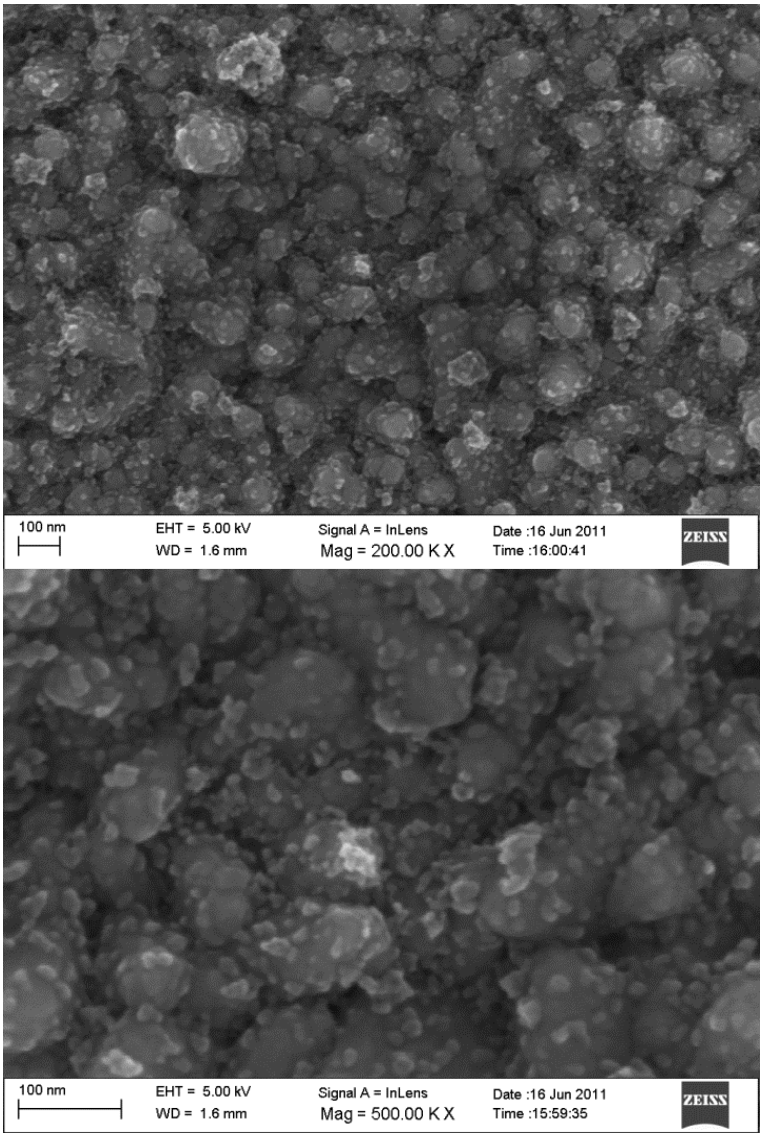

Figure 6.33. SEM images of the "TN_TEA_pre" titania deposited to be used for hybrid solar cells at two different magnifications. In both images the underlying substrate (spray-pyrolyzed TiO_2 on top of FTO) is visible as bigger grains.

- The procedure reported by Karthikeyan *et al.*[41] was adapted to obtained a quite viscous titania paste. First, 1 g of home-made T powder was sonicated in ethanol for 30 min. Then, 4 mL of the supernatant system containing fine titania was taken and 0.1 g of 4-hydroxy benzoic acid and 8 g of ethanol were slowly added during mixing. The mixture was stirred until a homogeneous paste was obtained (about 50 min). Ethanol was left to evaporate yielding a compact powder. 3.5 g of 5 % ethyl cellulose in α-terpineol was added to the compact powder and allowed to mix well. After obtaining a homogeneous system, 4 g of α-terpineol was added to the dispersion and mixing was continued until a homogenous paste was obtained.
  As shown in Figure 6.34, the nanoscale morphology of the starting material has been preserved (see the right-handed image), but the problem of not covering homogenously the underlying FTO has not been overcome (see the left-handed image).
  The as-prepared TiO_2 pastes was named "**T_Karthik**".

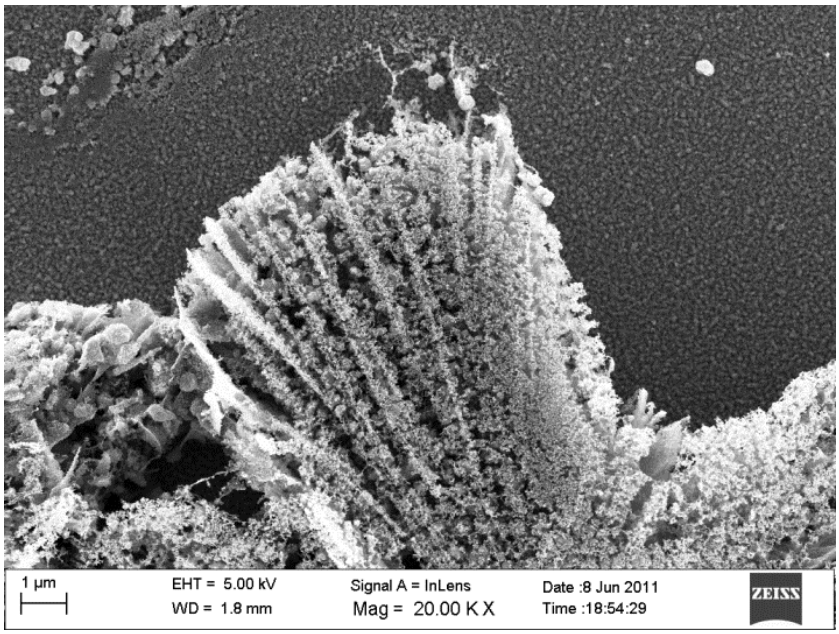

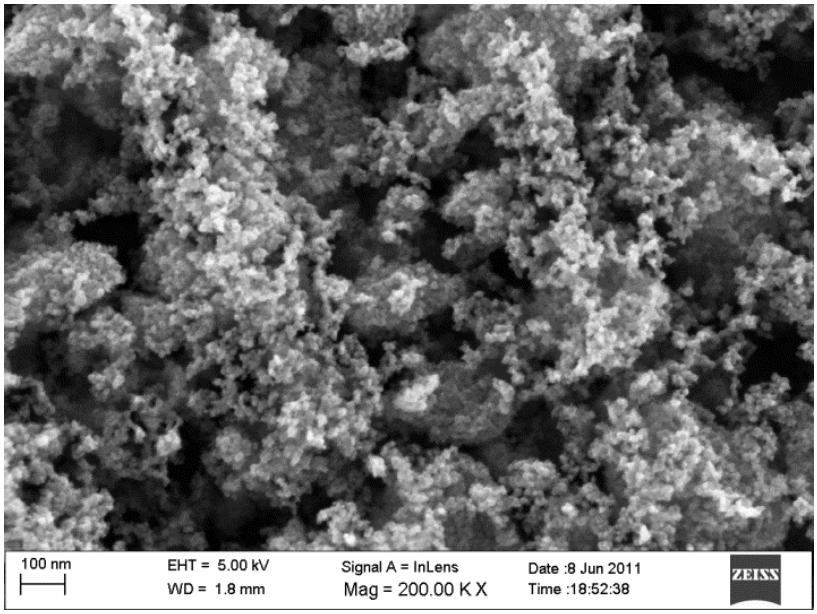

Figure 6.34. SEM images of the porous titania nanocrystalline film obtained from T_Karthik" paste at two different magnifications. At lower magnification (left-handed image), both TiO_2 and the uncovered substrate (FTO) are visible.

6.5. Device fabrication and materials used

HSC

After cleaning the FTO substrates (TEC15, Pilkington, 2.3 mm thickness, 15 Ω/square sheet-resistance), a dense TiO_2 blocking layer is deposited onto the conductive glass to constitute the working electrode. Such blocking layer should prevent a direct contact between the hole conductor and the FTO, otherwise short-circuiting the cell.

Mesoporous layers of TiO_2 on FTO glass substrates were prepared by spin-casting a paste of titania nanoparticles (commercial or home-made). Different pastes were tested (O'Regan_sol, Ahn_sol, PE10400_sol, P25/NO_3^-, T/NO_3^-, TN_TEA_pre) and presented in details in paragraph 6.4. Samples were sintered using a standard sintering procedure (180 °C, 10 min; 320 °C, 10 min; 390 °C, 10 min; 500 °C, 30 min).

The small molecular semiconducting dye [tris(dicyano-vinyl-2-thienyl)phenyl]amine (TDCV-TPA, structure shown in Fig. 6.7) was spin-cast (30 s, 4000 rpm) from a methylene-chloride solution with varying concentrations (0.1-30 mM).

The conducting polymer poly(3,4-ethylenedioxy-thiophene):poly-(styrenesulfonate) (PEDOT:PSS) was applied by spin-coating. Solvent residues were removed in vacuum (2.5 10-5 mbar). Ideally, during spin-coating, the solution fills the TiO_2 pores and the solvent is allowed to evaporate, thus enabling the hole conductor (as it also happens in the case of spiro-MeOTAD, see the following) to be in contact with the metal oxide both within the pores and on top of it, as a further layer.

A square hole (punch, Fisher, 0.19 cm^2) or round hole (one-hole punch, 0.24 cm^2) was punched out of a piece of double-sided tape (Stokvistapes, Clas Olson) and mounted onto the sample.

The back contact was finally established by compressed graphite powder and a second conducting glass slide (schematically shown in Figure 6.25). Silver tape was applied to establish contact points to the solar cell. The active area of the devices was 0.19 cm^2.

As for all the other types of solar cell devices, two samples of each configuration were prepared, exhibiting reproducible results.

SS-DSC

All devices were assembled on FTO (TEC 15, Pilkington). A dense layer of titanium dioxide was deposited on these substrates by spray pyrolysis, while a thicker mesoporous TiO_2 layer was spin-coated at 2500 rpm for 30 s and subsequently sintered at 450 °C for 45 min. Different pastes were tested; two of them (PE10400_sol, and T_Karthik) were selected and presented in details in paragraph 6.4. Then, the electrodes were soaked for 30 min in an aqueous solution of 40 mM $TiCl_4$ at 70 °C and heated again at 450 °C for 45 min. Dye D35 (see the structure in Fig. 6.35) adsorption onto the TiO_2 working electrodes was carried out by dipping the warm(∼100 °C) substrates into a 3×10^{-4} M ethanolic solution of the dye. The choice to operate at that temperature sprang from the need to minimize adsorption of impurities from moisture in the ambient air. The substrates were stored in the dye solution for 16 h and were rinsed with EtOH before use, to remove non-chemically attached dye molecules. For complete solar cell devices a fresh solution of spiro-OMeTAD (2,2',7,7',-tetrakis(N,N-di-p-methoxyphenyl-amine)-9,9',-spirofluorene, Merck KGaA, as received) was used as hole-conductor. Specifically, a solution of 120 mM spiro-OMeTAD, 60 mM 4-tertbutylpyridine and 15 mM $LiN(CF_3SO_2)_2$ in chlorobenzene was applied to the films, let

penetrate into the films for 1 min and then spin-coated for 30 s at 2000 rpm with an initial step of 3 s at 1500 rpm.

On top, a 100 nm silver layer was deposited by thermal evaporation in a vacuum chamber (Leica EM MED020) with a base pressure of about 10^{-5} mbar. The active area of the device was equal to 0.20 cm^2.

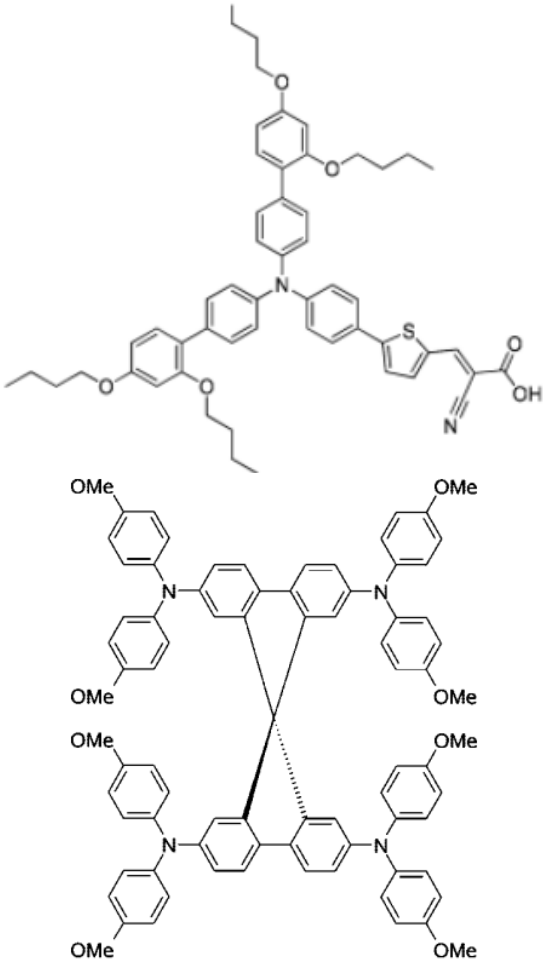

Figure 6.35. Chemical structures of dye D35 (top) and of the hole conductor spiro-MeOTAD (bottom).

Liquid electrolyte DSC

The working electrode was prepared according to the following procedure. First of all, FTO glasses were deterged in an ultrasonic bath for 15 min, and then rinsed with water and ethanol. An ozone treatment was applied for 18

min and followed, for selected samples, by immersion in a 40 mM aqueous $TiCl_4$ solution at 70 °C for 30 min and then washed with water. After rinsing again with water and ethanol, TiO_2 paste was screen printed and dried on the hot plate at 125 °C for 6 min. This step was repeated three times in order to get an optimal film thickness in the order of 10 µm. The electrodes were then heated under airflow to 325 °C (5 min), 450 °C (15 min) and up to 500 °C (15 min). Furthermore, one layer of a TiO_2 paste made of 400 nm particles (JEC PST-400C) was applied to selected electrodes. A "post-treatment" with $TiCl_4$ in water was also applied to selected samples. Three different final thicknesses of the TiO_2 layers were obtained, namely 6, 14, and 19 µm. The electrodes were finally heated again at 500 °C for 30 min before use. After cooling to 80 °C, the TiO_2 electrodes were immersed in a dye bath containing 0.2 mM D35 in ethanol at room temperature for at least 12 h. After washing with ethanol to remove the excess dye and drying under an air flow, the sensitized titania electrodes were assembled with thermally platinized counter electrodes (prepared starting from a 4.8 mM H_2PtCl_6 solution in ethanol) using a thin thermoplastic frame (Surlyn). The liquid electrolyte was composed of 0.8 M 1-methyl-3-propylimidazolium iodide, 0.5 M 1-methylbenzimidazole, 0.1 M guanidium thiocyanate and 0.03 M I_2 in acetonitrile. For comparison, DSCs were also prepared using bis(2,2'-bipyridine) cobalt hexafluorophosphate as the redox couple, that is 0.22 M $Co(bpy)_3(PF_6)_2$, 0.033 M $Co(bpy)_3(PF_6)_3$ (see the structure of the redox complex in Fig. 6.36), and additionally 0.1 M $LiClO_4$, 0.2 M 4-*tert*-butylpyridine (TBP) in acetonitrile. The electrolyte was introduced under vacuum through a prefabricated drilled hole in the CEs. The hole was sealed with a 50 mm thermoplastic frame and a glass plate. The active area of the cells was 0.25 cm^2.

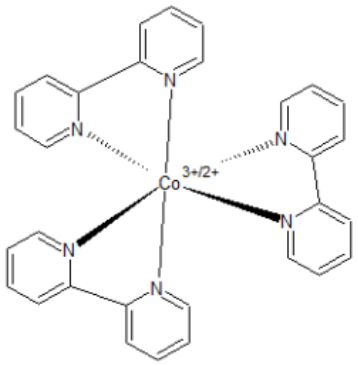

Figure 6.36. The chemical structure of cobalt bipyridyl redox complex.

6.6. Hybrid solar cells' results

For all hybrid solar cell devices, the dye TDCV-TPA - not properly soluble in chlorobenzene - was dissolved in acetonitrile. Actually, this was not the best solvent for dye deposition because of its very high evaporation rate. Such feature played a crucial role during the deposition of the dye by spin-coating onto the underlying TiO_2. Instead, a slightly higher time should probably have given to let the dye penetrate into the inorganic semiconductor.

The concentration of the dye was already optimized by Prof. Hagfeldt's research group, paying attention not to work at high dilutions, in order to avoid an insufficient infiltration in TiO_2 pores.
A drawback of TDCV-TPA was found to be a low efficiency in regeneration of the dye (injection process).
Generally speaking, by increasing the interfacial area for charge separation, hybrid solar cell performance can be theoretically increased. A direct way to dispose of a higher interfacial area is the use of nanostructured metal oxides. Indeed, their morphology affects the exciton harvesting efficiency, the charge collection efficiency and the charge recombination.
Titania surface area and pore size are concepts strictly related. However, pore volume and shape distributions have to be carefully taken into account since small/large pores and cylindrical/spherical/bottle-neck pores have a very different and peculiar influence on the device performance. Indeed, this latter is deeply affect by the pore filling fraction, which very often represents a limiting factor to high efficiency of the cell.[42,43] Actually, a high pore filling fraction can facilitate the separation of geminate electron-hole pairs.[43]

Different V_{OC} and J_{SC} values were obtained depending on the TiO_2 paste (Table 6.3).
It seems that the commercial Dyesol paste and titania pastes made from sols adapted from two literature works (as mentioned in the experimental procedure of the paste) give rise to a slightly higher short circuit current. However, also TN_TEA_pre presents a similar values. As a matter of fact, the J_{SC} increases as the amount of dye increases. In turn, the amount of dye-loading is mainly affected by the surface area of TiO_2 films. This means that

the amount of "working dye" adsorbed onto TiO_2 electrodes of the above-cited cells is slightly higher with respect to other samples. This finding is not in contrast with all reported SEM images, which show a TiO_2 layer covering the all substrate surface only in the cases corresponding to cells with higher J_{SC}.
Exceptionally high V_{OC} and best performing devices were obtained when titania pastes "O'Regan sol" and "TN_TEA_pre" were employed. Dyesol cell efficiency is the highest of all, though not at all a highly out-of-range value.
The device containing the "PE10400 sol" titania paste showed intermediate values of J_{SC}, V_{OC}, FF, and η. The quite low FF value (Table 6.3, to be compared with the other values) is consistent with what stated above: it could be due to the bigger unwanted aggregates that can retard the transport of electrons and result in higher recombination rate.

Working electrode	V_{OC} (V)	J_{SC} (mA cm^{-2})	FF	η (%)	IPCE (%)
Dyesol (1:9 terp.)	0.850	1.02	0.424	0.37	14
O'Regan sol	0.960	1.11	0.450	0.45	13
Ahn sol	0.848	1.11	0.315	0.30	11
PE10400 sol	0.870	0.72	0.516	0.32	9
P25/NO_3^-	0.740	0.54	0.430	0.20	9
T400/NO_3^-	0.825	0.74	0.322	0.20	9
TN_TEA_pre	0.870	0.91	0.630	0.50	11

Table 6.3. Current-voltage characteristics and IPCE values for solar cells devices sensitized with the small-molecular semiconducting dye TDCV-TPA employing the conducting polymer PEDOT:PSS and graphite powder.

Unfortunately, with a high pore volume titanium dioxide, it might be possible that the middle of the pore would not contribute to the light absorption by the dye. This could be valid for almost all the titania pastes presented herein. Morphology control is an essential aspect of optimization of solar cell devices. It is highly important to achieve a pore size of the inorganic scaffold in order to properly interpenetrate organic and inorganic phases. The pore size should be in the order of the exciton diffusion length, and, at the same time, it is desirable to get efficient charge carrier transport in the respective phase.
Samples "P25/NO_3^-" and "T/NO_3^-", both derived from HNO_3 treatment of the bare TiO_2 powders, exhibited the lowest J_{SC} and FF. It seems that the apparently beneficial effect of nitric acid was washed out. This is in contrast

with literature results: Park and coworkers, who also studied the effects of HNO_3 treatment of TiO_2 nanoparticles on the photovoltaic properties of DSCs, found an increased adsorption amount of the dye and consequently increased short circuit current and efficiency of the devices. Moreover, the authors reported that XPS analysis attested an increase of the Ti^{3+} content in the material (Ti 2p peak shifted at higher binding energies).[44]

In the present situation, as in a general case, a low J_{SC} could depend on a low concentration of dye in TiO_2 layer, or directly to a low quality TiO_2 layer. Alternatively, it may be due to degraded dye molecules or to the presence of water adsorbed on the TiO_2 layer or in the electrolyte. Last but not least, a poorly sealed cell or defective construction (shorts, electrolyte coverage, and leaks) could be the culprit of low J_{SC} values.

Notwithstanding the low performance, SEM analysis of the P25/NO_3^- electrode was very promising high magnification, as can be appreciate in Fig. 6.37. The home-made P25 dispersion after HNO_3 treatment looks very similar in size and shape to the Dyesol nanoparticulate electrode. The major problem resides in the highly inhomogeneous coverage of the substrate (see Fig. 6.32).

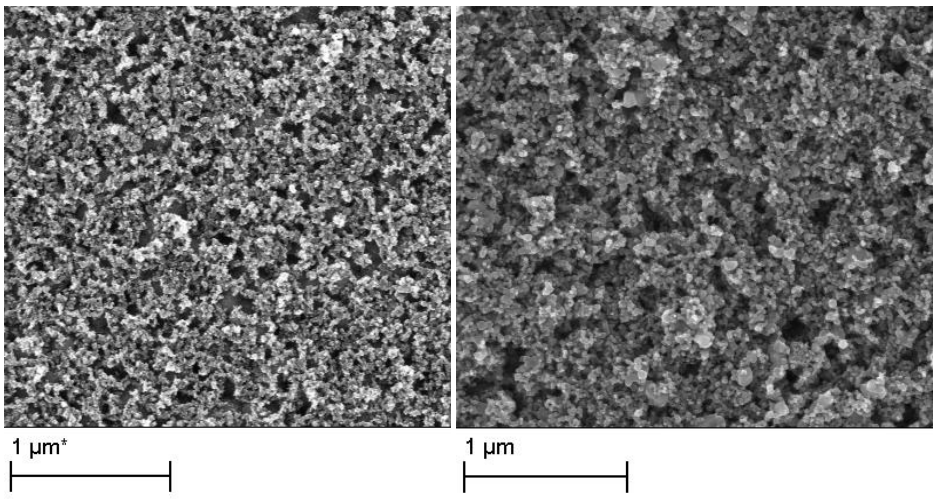

Figure 6.37. SEM images of two different titania electrodes: comparison between the commercial Dyesol paste and the home-made nanoporous titania layer deriving from an optimized paste (P25/NO_3^-, terpineol, 2-PrOH, acac 1:28:15:4 w/w).

As displayed in Fig. 6.38, the driving force for electron injection from the dye LUMO to the TiO_2 conduction band is comparatively low.[19] In principle this can lead to a slow injection from the dye to TiO_2. The scenario is, however, more

complex as indirect effects may play a role in the energetic of the system. Indeed, besides light harvesting, the dye could influence cell performance by altering the surface recombination kinetics and band edge energetics of the TiO_2 film.[45] Such a shift of the conduction band edge increases V_{OC} and reduces the driving force for electron injection (-ΔG) associated with a decreased TiO_2 density of states (because it should be considered that the density of states in the TiO_2 conduction band increases with energy.). This is not always valid: Jang *et al.* found no evidence that the organic dye contributed to the high voltage by shifting the band edges to more negative electrode potentials.[46] Nevertheless, on the grounds of DFT calculations, they claimed that steric shielding of the electrons in the TiO_2 by the organic dye was important in reducing recombination.

Nevertheless, a quite large variation in V_{OC} values could be partially ascribed to some sort of slight modification of the TiO_2 conduction band position.

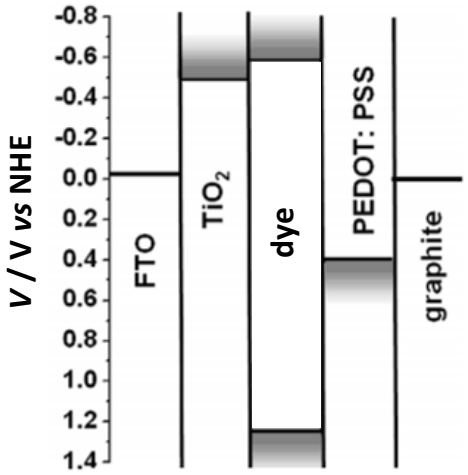

Figure 6.38. Energy level diagram of the bilayer hybrid solar cell devices derived from electrochemical and spectroscopic data for all the components.

N-doped TiO_2 based HSC

In the context of this thesis, a separate discussion is worth for the solar cell device based on N-doped TiO_2.

When dealing with the TiO_2 conduction band position, in the case of the titania nanopowder doped with triethylamine, proper measurements have been performed to evaluate both the flatband potential and the quasi-Fermi level (paragraph 4.4.1). The result was a not significant variation of the

conduction band edge position. However, no doubts that TN_TEA_pre is a highly defective sample. Surface states cannot be a priori excluded and the abundance presence of oxygen vacancies has been attested by more than one method (see chapter 3). Thus, electrons in the increased surface states (charge trap sites) experienced more trapping/detrapping events, causing the increase of residence time in the trap sites. On the other hand, photocurrent measurements on the bare N-doped titania electrode (*i.e.*, not assembled in the whole cell) have shown a lower electron-hole recombination rate (paragraph 4.7.1), that, of course, has a beneficial effect also in the solar cell device.

Unlike the countless literature works both on nitrogen-doped titania and on dye-sensitized solar cells, DSCs based on the N-TiO_2 electrodes are not frequently studied.

In the following, a brief review of the main papers focusing on such joint topic will be given.

Starting from one of the most relevant and recent works, Guo *et al.*[47] investigated the effect of varying amounts of N dopant (aqueous ammonia) on the performance of DSCs based on N-TiO_2. The use of high energy ball milling was introduced to overcome the problem of a poor adhesion between the TiO_2 film and FTO, which initially led to low J_{SC} and efficiency, at the expense of the collapse of nanochannels and meso-macroporous structures. As suggested by Su *et al.* and Shao *et al.*,[48,49] such a hierarchical structure of uniform macrochannels with mesoporous walls of nanoparticles would have been formed by self-assembly during the synergistic packing of the nanoparticles and rapid release of alkanol molecules. At increasing N amount, the short-circuit current and efficiency of the devices increased, with a top efficiency of 7.95 %, which is much higher than that of undoped TiO_2-based DSCs, namely 4.80 %. The optimal N dopant amount for the N-doped TiO_2 electrodes was 0.40 %, on the basis of the XPS results. That amount exactly coincides with the value provided by elemental analysis (CHN) for the N-TiO_2 powder characterized in paragraphs 3.4, 4.4.1, 4.7.1 and used for the paste of the tested solar cell device and It is here recalled that that sample was doped with triethylamine using a nominal N/Ti molar ratio of 0.1. Instead, survey XPS analysis on that sample provided a value of 0.022 N/Ti atomic ratio.

Comparing with undoped TiO_2, by adding different amounts of ammonia in N-TiO_2 photoelectrodes, the authors speculated that the pH-dependent ζ

potential and thereby the isoelectric points of N-doped TiO_2 changed. The isoelectric points of TiO_2 have an effect on the dye-loading; as for instance, surfaces with higher isoelectric points are preferable for the attachment of dye with acidic carboxyl groups.[50,51] Moreover, the hydrolysis of TTIP in deionized water formed the aggregations of the undoped TiO_2 nanoparticles, which also decreased the dye-loading amount of undoped TiO_2 films. In previous papers, Guo *et al.*[52,53] reported that the faster electron transport in the N-doped DSCs contributed to the enhanced J_{SC}. Thus, they concluded that the synergistic effect of higher dye uptake, N dopant amount, and faster electron transport contributed to the enhanced J_{SC} of N-doped DSCs. The N dopant amount apparently affected both the charge transfer resistance and electron lifetime.

In a very recent work, Tian and coworkers[54] dealt with the preparation of N,B-codoped TiO_2 electrodes for dye-sensitized solar cells by a facial modified sol–gel method. Impedance spectra showed that the enhanced electron lifetime could be attributed to the formation of an O–Ti–B–N bond in the oxide, which retards electron recombination at the photoelectrode/electrolyte interface. The authors reported a high efficiency of 8.4 % under 0.2 sun illumination, probably ascribable to the ideal combination of retarded electron recombination and superior energy band structure from the unique N,B–TiO_2 particle structure.

In a previous paper, Tian *et al.*[55] noticed that doping TiO_2 with nitrogen successfully retarded charge recombination at the TiO_2/electrolyte interface. If, on one hand, the increase of titania crystallite size affected the N719 dye adsorption, with a decreased J_{SC}, on the other hand back electron transfer was found to be suppressed, retarding the dark current and improving V_{OC} and FF. The introduction of N replaced the O deficiency in the titania crystal lattice, with an O-Ti-N structure that could be the reason of the enhanced electron lifetime and retarded dye degradation. A negative point was the weakening of the driving force for the photoelectron injecting ensuing from a shift of the flat-band potential to the negative direction, but overall the devices built with N-TiO_2 showed higher stability (1 sun light soaking, 70 °C, more than 1000 h) than those consisting of undoped TiO_2.

On the contrary, Zhang *et al.*[56] found out N-TiO_2 to have a lower conduction band edge than TiO_2, which is helpful for electron injection. Moreover, by N

doping, the growth of particle size was inhibited, and the best match of components was achieved with N719/P3HT, giving η = 2.34 %).
Single-cycle dip-deposited N,S-TiO_2 thin films (with thiourea as precursor for codoping) were obtained by Prabakar *et al.* as visible light harvesters as well as blocking layers for DSCs (η = 5.88 %).[57]
An efficiency slightly lower (η = 4.86 %) was reported by Kang and coworkers,[58] owing to the increase of light absorption in the near-vis and partially to the morphological characteristics of the N-TiO_2 film. However, a lower electron diffusion coefficient was ascribed to trap states and disorder in the lattice.

6.7. Solid state dye-sensitized solar cells'results

Dye D35 ((E)-3-(5-(4-(Bis(20,40-dibutoxybiphenyl-4-yl)amino)phenyl)thiophen-2-yl)-2-cyanoacrylic acid) was prepared by researchers of the Department of Organic Chemistry at KTH University (Stockholm) according to the published procedure.[59] D35 is an organic sensitizer based on triphenylamine (TPA) donors.[60] The chemical structure is shown in Figure 6.35. The dye D35 shows a great performance when combined with the cobalt redox couple. This dye, however, cannot absorb any light beyond 620 nm. Nowadays, a co-sensitization method[61,62] is often carried out to optimize the light absorption on the working electrode in order to improve significantly the current density, and, consequently, the efficiency of the device.

Since the presence of hole transporting materials in ss-DSCs involves hole hopping among molecules, several essential conditions must be met:[63] (i) a compatible energy level layout with the dye-TiO_2 functioning as a typical p–n junction for dye regeneration through hole transfer; (ii) efficient deposition within the mesoporous TiO_2 film, good pore filling ability, and stable interfacial contact with the dye-TiO_2; (iii) sufficient hole mobility; (iv) thermal and photochemical stability; and (v) no strong absorption in the visible spectrum to avoid competition with dye molecules. The first two requirements directly deal with the TiO_2 component; thus, they have to be taken more seriously into consideration.

Solar cells were assembled using the well-established spiro-OMeTAD hole-conductor instead of the promising Poly-(3-hexylt hiophene-2,5-diyl) (P3HT) because photo-induced absorption measurements performed by the Hagfeldt group in a recent work[64] suggested that the regeneration of the same dye and the polymer infiltration are not complete using P3HT, while spiro-OMeTAD regenerates the dyes efficiently. However, the TiO_2/D35/P3HT system showed rather high energy conversion efficiency and electrochemical oxidation of the dyes on TiO_2 indicates that D35 have an efficient dye to dye hole conduction. Therefore, the dye hole conduction was considered to be of significant importance for optimizing the energy conversion in such hybrid TiO_2/dye/polymer systems.

The highest efficiency (η = 0.85 %) was obtained for the PE10400conc sample.

In general, a negative effect could be induced by a too high concentration of the spiro-OMeTAD solution and by the too few amount of dye loaded, according to UV-vis absorbance measurements, which is presumably due to too thin TiO_2 films. Indeed they were below the optimal thickness of 2 µm. However, concentrating the sol rich in surfactant in order to increase the thickness of the metal oxide layer, then there would be probably too much surfactant, not easy to remove by the simple sintering step.

An interesting case is that reported by Jiang *et al.* who fabricated a TiO_2 film from a binder-free nanoparticle-TiO_2 paste at room temperature:[65] they found that an increase of the TiO_2 film thickness from 0.35-0.55 to 0.9-1.1 µm led to the decrease of J_{SC} from 4.74 to 3.45 mA cm^{-2} and FF from 0.65 to 0.48, and the resulted IPCE decreased from 2.60 % to 1.40 %.

Actually, a thin TiO_2 layer configuration was purposely sought in the present study because of the difficulty in completely filling the pores of the TiO_2 films with spiro-MeOTAD[66] and the relatively fast recombination kinetics,[67] SSDSSCs are limited to thinner dye-covered films[68,69] that often lead to poor light-harvesting properties.[70] Then, it should not be forgot that, to achieve high SS-DSSC performance with TiO_2 films thinner than those for DSCs, dyes with high absorption coefficient are a necessity.

Low IPCE values (see Table 6.4) with increasing redox potential of the redox mediator may be the result of slow regeneration kinetics. Note that the redox potential of the I_3^-/I^- couple in the liquid electrolyte is about 0.4 V (vs NHE), whereas the one-electron oxidation potential of spiro-$MeOTAD^+$/spiro-MeOTAD couple is about 0.82 V (vs NHE).[71]

Working electrode	V_{OC} (V)	J_{CS} (mA cm^{-2})	FF	η (%)	IPCE (%)
T_Karthik	0.703	0.64	0.45	0.19	10
PE10400_sol_conc	0.790	1.7	0.55	0.85	16

Table 6.4. Current-voltage characteristics and IPCE values for two types of solar cells devices with different TiO_2 pastes sensitized with D35 using spiro-OMeTAD as hole transporting material and silver as counter electrode.

The low performance of both types of devices reported in Table 6.4 could be generally due to the high oxidation potential of the redox shuttle which is perhaps too close to the oxidation potential of the dye resulting in slow dye regeneration; therefore, low current was obtained, especially under full sun. This finding is quite surprising but not confirmed by the literature. Nevertheless, even a small difference in oxidation potential can result in a drastically lower device performance,[72] pointing towards the conclusion that a driving force of less than 100 mV for dye regeneration can be insufficient.
A direct contact between the FCO and Spiro-OMeTAD will result in carriers lost since holes can also move towards and inject into the cathode. This fact contributes to lower both J_{SC} and V_{OC} values. Such a situation could be valid for T_Karthik, since the substrate is partially uncovered, as revealed by SEM images (Fig. 6.34).

6.8. Liquid electrolyte dye-sensitized solar cells'results

Liquid electrolytes: iodide/triiodide versus Co-based redox mediators

Since transparent conductive oxide (TCO) substrates, such as FTO, exhibit insufficient electron transfer kinetics for I_3^-reduction, a thin layer of Platinum (Pt) is coated onto the TCO substrate (platinized cathode) and is used to catalyze the cathodic reduction of I_3^- ions, *i.e.*, redox couple regeneration.[73] However both these components of DSCs suffer from their inability in long-term reliability. The I_3^-/I^- based electrolyte is corrosive, yellow in color and dissipative towards light absorption, while platinized cathode is subject to corrosion, sensitive to side products formation, and liable to become inactivated with ageing, apart from being uneconomical. These are major attributes which may limit the use of I_3^-/I^- based electrolytes and Pt in some

cases. Nevertheless, hardly any electron outer-sphere redox couples have shown a power conversion efficiency comparable to the I_3^-/I^- based redox couples, to complement its use. This occurred until the very last years. Indeed, after the seminal work on the use of cobalt electrolytes in DSCs,[74] much attention has been given to polypyridyl cobalt redox complexes in recent times.[60,75-77] In early 2010, Feldt *et al*.[60] published a paper reporting a DSC with an efficiency of 6.7 % under full sun illumination with a cobalt tris-bipyridine redox shuttle combined with an organic dye. This breakthrough report demonstrated the feasibility of using outer-sphere redox couples to produce high efficiency DSCs through combined optimization of dye and redox couple. A recent review was published in 2011 by Hamann and Wondersma.[78]

The attempts to replace the I_3^-/I^- redox shuttle by cobalt polypyridine complexes was not only limited to their low visible light absorption but also due to their higher redox potential and noncorrosive nature towards cathode. Moreover, the V_{OC} of a iodide/triiodide system solar cell is restricted by the large driving force in the dye regeneration process. On the contrary, the cobalt redox couple needs a smaller driving force in the dye regeneration process, thereby generating a larger V_{OC} compared with iodide/triiodide.

For many one-electron, outer-sphere redox couples, faster recombination and shorter electron lifetimes have been measured compared to devices incorporating iodide/triiodide, and this is thought to be the main limitation to these alternative redox systems.[60,79-81] Another significant drawback of the relatively bulky cobalt complexes (compared to I_3^-/I^-) is the slow mass transport through the mesoporous electrode.[82-84] At full sun (AM 1.5 GM) the performance of cobalt complexes as redox shuttles is diffusion limited and also a faster back reaction of photo-injected electrons with the oxidized species is expected. Thus, an additional asset is the overall good reversibility of oxidation of such redox shuttle.

However, in two of their papers, Tsao and coworkers have also demonstrated a device efficiency of 10 % with dye Y123 and $[Co^{III}(bpy)_3](B(CN)_4)_3/[Co^{II}(bpy)_3](B(CN)_4)_2$ redox couple.[85,86]

If the usage of Co-based redox mediators has led to the partial overcome of electrolyte diffusion limitations, and the overpotential for dye regeneration has been reduced, further improvements can lead to increased photocurrent densities and/or photovoltages.[87] One issue that needs to be addressed, however, is the stability of these redox shuttles. For example, a 10–15 %

decrease in the efficiency was reported following 220 h of exposure to full sunlight at 30 °C.[88] While this decay was attributed to loss of the volatile acetonitrile solvent, the stability of the cobalt complex electrolyte was not established. To the best of the author's knowledge, no long term stability studies have been carried out, which will certainly be necessary if these redox shuttles are to serve as real replacements for I_3^-/I^-.

Counter electrode: the use of platinum

Concerns over platinum's cost and stability have led to a plethora of studies, primarily with the iodine-based mediator, examining alternative catalysts such as CoS,[89] polymers,[90] and carbon nanomaterials including carbon black,[91,92] carbon nanotubes,[93,94] and reduced graphene oxide.[95-97] The floppy carbon layer can increase the active surface area of the counter electrode, thereby reducing the charge transfer resistance of the counter electrode. However, up to date, there have been no reports of an alternative catalyst to platinum that can match − or exceed − this precious metal's performance with multiple redox couples.

Devices with home-made TiO_2 pastes

A quite unsuitable dark J-V behavior was found for almost all the DSCs built with the cobalt redox couple at high voltage values, as shown in Fig. 6.39: beyond 0.5 V the current stops rising and reaches a plateau. This finding could be ascribed to either inhomogeneity of the counter electrode or to dye dissolution. However, in the range of high voltage no particular significance should be addressed to the reaction rate at the counter electrode. Thus, a third possible explanation could refer to the concentration of the redox mediator. Indeed, $Co(bpy)3(PF6)^{2+}/^{3+}$ occasionally shows diffusion problems, as a typical issue of Co complexes in general. In the present case where more than one semiconductor layer is involved, more difficulties in mass transport could arise.

Perhaps the situation could have been even more extreme and complicated if additional specific blocking layers had been added (even though the "pre" treatment with $TiCl_4$ is thought to block the contact with FTO and inhibit recombination, enhancing the performance of the colloidal film as a dye-sensitized photoanode is improved by deposition of TiO_2 from aqueous $TiCl_4$ solution.[98] Indeed, to avoid the problem of faster recombination and shorter

electron lifetimes of outer-sphere redox couples, a number of groups have applied thin, insulating blocking layers to the TiO_2 surface.[99-101] While this had been shown to reduce the charge recombination and increase the photovoltage obtained, the electron injection kinetics may be affected, leading to a reduction in photocurrent. Klahr and Hamann demonstrated that although a blocking layer does not significantly affect the photovoltaic performance of DSSCs containing some redox shuttles (*e.g.*, $[Co(t\text{-}Bu_2bpy)_3]^{3+/2+}$ and I_3^-/I^-), it is crucial for others (*e.g.*, $[Co(Me_2bpy)^3]^{3+/2+}$ and $[Co(bpy)_3]^{3+/2+}$) and should be employed when new redox couples are investigated.[102]

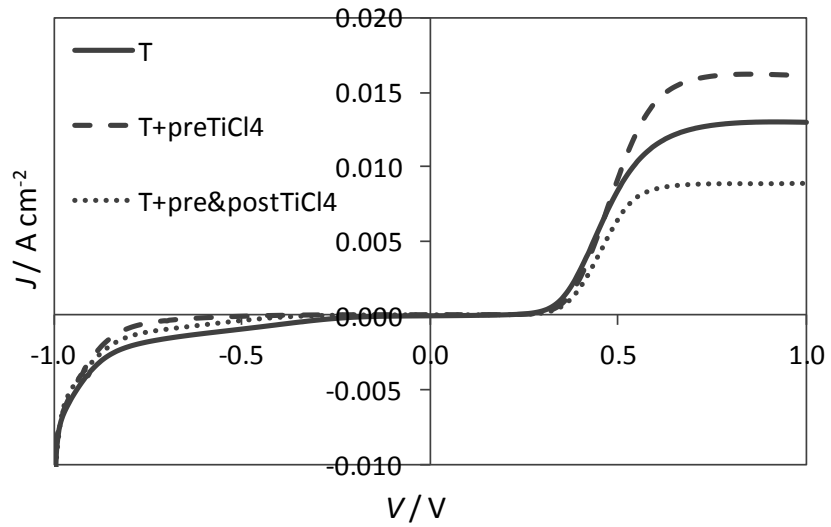

Figure 6.39. Dark current density *vs* applied potential curves for DSCs sensitized with D35 employing a $Co(bpy)_3(PF_6)^{3+/2+}$ based electrolyte. Comparison among three different configurations of TiO_2 layers.

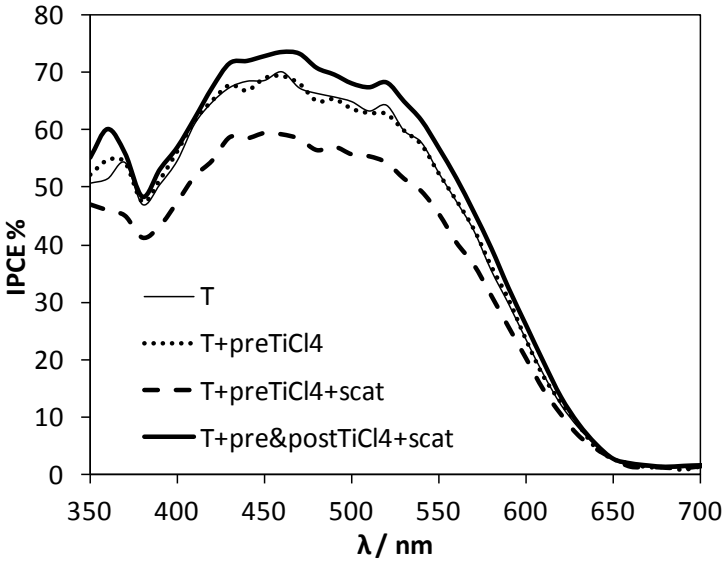

Figure 6.40. Spectra of incident photon to current efficiency (IPCE) for DSCs sensitized with D35 employing I_3^-/I^- as redox mediator and a platinized counter electrode. Different configurations concerning the TiO_2 layers are compared (see the text for labels).

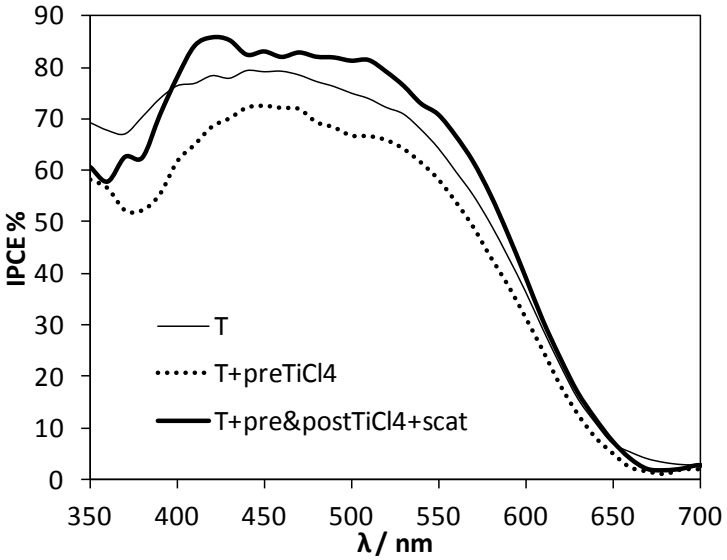

Figure 6.41. Spectra of incident photon to current efficiency (IPCE) for DSCs sensitized with D35 employing $Co(bpy)^3(PF^6)^{3+}/^{2+}$ as redox mediator and a platinized counter electrode. Different configurations concerning the TiO_2 layers are compared (see the text for labels).

The DSCs with liquid electrolyte presented in this thesis consisted of materials similar to those used in the landmark paper by Feldt et al. on codesigning the dye and cobalt redox couple,[60] which can be considered the complementary components of DSCs with respect to TiO_2 as the one mainly studied herein.

As fast recombination between the conduction band of TiO_2 and cobalt mediators has limited DSSC performance for devices using traditional dyes such as N719, a dye with bulky side chains (D35) was used in this study. Butoxyl chains on D35 sterically hinder the interaction of cobalt complexes with TiO_2, reducing the recombination .

Results obtained for two types of liquid electrolytes, iodide/triiodide and cobalt based, are reported in Tables 6.5 and 6.6, respectively. In turn, for each of these two categories, four types of different devices were built. Based on a home-made "T_400" nanopowder paste, cells "T" were prepared as the simplest ones; then, some electrodes were pretreated by immersion in an aqueous $TiCl_4$ solution ("T+preTiCl4"), some others were also covered by a light-scattering TiO_2 layer on top of the mesoporous TiO_2 film ("T+preTiCl4+scat"), and the "most complete" cells ("T+pre&postTiCl4+scat") comprised a second "post" treatment by $TiCl_4$ solution too. It has to be underlined that since the home-made mesoporous TiO_2 films showed themselves a quite scattering behavior, solar cells both with and without a scattering layer were built, as mentioned in the device preparation procedure. The need of a scattering oxide layer has been demonstrated by optimization studies.[103-105] Even if the scattering layer itself did not bring a sharp advantage in the present case, among the iodide/triiodide based devices the one with both the light-scattering layer and "pre" and "post" $TiCl_4$ treatment showed the highest efficiency. Likewise, Feldt *et al*.[60] found that the best efficiency was still obtained for quite thick films because of the increased light-harvesting efficiency, *i.e.*, two layers of TiO_2 and one light-scattering layer giving a total thickness of 15 µm (12 + 3 µm). Contrary to these results for Co-based electrolyte and although mass transport problems were shown to be avoided in the DSCs employing $[Co(bpy)_3]^{3+/2+}$, the highest efficiency was obtained for cells without any additional "pre" or "post" $TiCl_4$ treatment, nor scattering TiO_2 layer. This point will be discussed in the following.

Working electrode	V_{OC} (V)	J_{SC} (mA cm^{-2})	FF	η (%)	IPCE (%)
T	0.775	7.0	0.74	4.0	63
T+preTiCl4	0.798	6.7	0.75	4.0	57
T+preTiCl4+scat	0.783	6.6	0.75	3.9	53
T+pre&postTiCl4+scat	0.785	7.1	0.74	4.1	74

Table 6.5. Current-voltage characteristics and IPCE values for solar cells devices with different configurations of TiO_2 layers sensitized with D35 employing I_3^-/I^- as redox mediator and a platinized counter electrode.

Working electrode	V_{OC} (V)	J_{SC} (mA cm^{-2})	FF	η (%)	IPCE (%)
T	0.885	8.5	0.61	4.6	81
T+preTiCl4	0.865	7.8	0.63	4.3	72
T+preTiCl4+scat	-	-	-	-	-
T+pre&postTiCl4+scat	0.850	7.7	0.55	3.8	84

Table 6.6. Current-voltage characteristics and IPCE values for solar cells devices with different configurations of TiO_2 layers sensitized with D35 employing $Co(bpy)3(PF6)^{3+/2+}$ as redox mediator and a platinized counter electrode.

Actually, the scattering layer is supposed to increase J_{SC} and give a gain especially in the high-wavelength part of the IPCE spectrum.

As illustrated in Figures 6.40 and 6.41, the fabricated cells exhibit broad incident photon-to-current conversion efficiencies (IPCE) almost plateau-like from 450 to 550 nm with high IPCE maxima up to 84 % (for cells with Co-based redox shuttle) and slightly lower for cells with I_3^-/I^- (74 %, in the best case). The highest profile is shown by the most complete devices, namely the ones with the addition of "pre" and "post" $TiCl_4$ treatment, and a scattering TiO_2 layer; the lowest values are reached by the cells with the addition of a scattering layer without post-$TiCl_4$ treatment, whereas cells without any additional treatment and those with just a pre-$TiCl_4$ treatment lie in between, either overlapping or the latter resulting slightly lower (Fig. 6.40). With an IPCE approaching 100 %, light harvesting efficiency and injection efficiency can be theoretically close to unity (which is actually possible for D35-sensitized solar cells).

As a matter of fact, Co-based mediator stained the titania films with an enhanced photocurrent response, which, according to the literature[60] [Feldt JACS] should be a response centered in the spectral range 390–470 nm

compared to the I_3^-/I^- based system due to lower absorption coefficients in the blue region, and reasonably gave rise to higher V_{OC}, IPCE, and, consequently, higher efficiency.

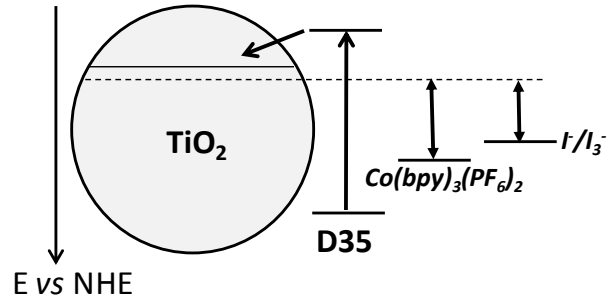

Figure 6.42. Schematic energy diagram for a nanostructured TiO_2 electrode sensitized with D35 employing either $[Co(bpy)^3]^{3+/2+}$ or I_3^-/I^- based electrolytes. Re-drawn from ref [106].

The only failure concerns the fill factors, which unaccountably fell in the range 0.55-0.61. Actually, the fill factor is influenced by many factors. If we assume a bias-independent charge-generation efficiency,[9] then the non-ideality of the fill factor can be due to recombination losses under electrical bias[70] or simply resistive losses in the device and external circuit. In an optimized DSC typical fill factors of 0.7–0.75 are obtained,[107,108] occasionally higher.

For the present devices containing I_3^-/I^-, lower V_{OC} values have been found. Besides the intrinsic limitation due to the redox potential of I_3^-/I^-, which is less positive than that of $[Co(bpy)_3]^{3+/2+}$ (0.4 V *vs* 0.56 V - E_0(D35) = 1.1 V, see Fig. 6.42), a possible reason for a low V_{OC} could be that the electrolyte can infiltrate the cathode film including pores which are too small for the cobalt redox couple to access. This would shift the electrolyte concentration in the active part of the solar cell and could influence the electrolyte redox potential, and eventually V_{OC} of the device.

A low J_{SC} could be due, at least in part, to a not negligible light absorption by the mediator.

In order to estimate the driving forces for dye regeneration in a real device, the difference between the redox potential of the redox couple in solution and the dye absorbed onto a TiO_2 film must be known. Feldt *et al.*[106] determined the regeneration halftimes, regeneration efficiencies and driving

forces - calculated as the difference between E_0(redox) and E_0(dye) - for D35-sensitized DSCs employing either iodide/triiodide or $[Co(bpy)_3]^{n+}$ as redox couple. In the former case the parameters resulted: 0.79 eV, 15 μs, 0.95; whereas for the latter mediator: 0.55 eV, 19 μs, 0.94.

Interestingly, for DSSCs using an iodine-based electrolyte, solar cell performance improved markedly over the first day, as found by Roy-Mayhew and coworkers.[109] Components of the electrolyte such as 4-tertbutylpyridine (TBP) and iodine may be adsorbing to the porous electrodes during this time.[110] Likewise, it may take time for the electrolyte to fully infiltrate the film, so that, over time, more surface area would be accessible to catalyze the reduction of triiodide.

However, most of the devices of all sorts presented in this thesis showed the highest activity shortly after fabrication (when IPCE and I-V measurements have been resorted to).

The best PV performance using the Co-based mediator showed a short circuit photocurrent density of 8.5 mA cm^{-2}, an open circuit potential of 0.885 V and a fill factor of 0.61 resulting in 4.6 % power conversion efficiency at standard global AM 1.5 solar irradiation (Table 6.6), which is also the highest value among all those reported herein. Surprisingly, this was obtained for cells without any additional “pre” or “post” $TiCl_4$ treatment, nor scattering TiO_2 layer. On the basis of these results, since a scattering layer usually doubles the current, it can be concluded that the present TiO_2 pastes (indicated as “T”) possess some sort of scattering features themselves, maybe owing to particle aggregates in the range of 200-400 nm - actually confirmed by granulometric analysis on the pristine titania nanopowder. On the other hand, resistivity generally increases as the number of scattering interactions of charge carriers increase, and is greatest in the thinner films.[111] In other words, resistivity will be higher as long as the ratio of film thickness to the mean free path of conductors (*e.g.*, electrons) is not large. This is a reminder to the minimum TiO_2 thickness - around 5 μm - for such DSCs with liquid electrolyte.

Under the same conditions adopted for DSC with Co-based electrolyte, the cell with paste “T” and the iodide/triiodide redox couple under-performed: the efficiency dropped to 4.0, which is however not too low if compared to the results given by the other cells, in the range 3.9-4.1 %, as reported in Tab. 6.5. Efficiencies for the cells with $[Co(bpy)_3]^{3+/2+}$ lie in a broader range: 3.8-4.6 % (see Tab. 6.6).

The lower performance exhibited in the current work compared to that of Feldt *et al*.[106] is likely due to the use of TiO_2 with a smaller primary particle size, on one side. This explanation is consistent with the finding by Yella *et al*. that smaller pores impede the transport of the relatively large cobalt complexes and decrease device efficiency.[88] On the other side, poor adhesion of TiO_2 with the underlying FTO or a not complete coverage of the substrate could have had a deep negative impact on the overall performance of the cells.

Although V_{OC} is reasonably high, FF and J_{SC} are quite low, probably owing to a high charge transfer resistance (which, indeed, is true in the case of platinum counter electrodes).

Here it is confirmed what affirmed by Feldt and coworkers:[60] dye D35 efficiently suppresses recombination when used with a cobalt redox couple that possesses a more positive redox potential than the iodide/triiodide one. However, contrary to the present results, Feldt et al. reported that the short-circuit photocurrent in the DSCs decreased with increasing redox potential of the complexes, owing to the slow regeneration kinetics, fast recombination kinetics and/or diffusion limitations. In contrast, DeVries *et al*.[112] did not find a clear correlation between photocurrent and redox potential in their study, but it should be noted that they obtained only low photocurrents of about 0.2 mA cm^{-2}.

The regeneration efficiency could also be affected by the different counterions used; for instance, Pelet *et al*. observed faster dye regeneration for iodide/triiodide using cations in the electrolyte that adsorbed to the TiO_2 surface.[113]

An application of photocurrent transient measurements (see chapter 4) is found just in this context. The effect of mass transport in DSCs can be investigated by monitoring photocurrent transients using a large modulation (on/off) of the incident light, as Feldt and coworkers shown in their work.[106] The observed decrease in photocurrent with time was a result of slow diffusion of Co(III) to the counter electrode.

The diffusion of the oxidized form of the redox couple to the counter electrode completes the circuit and this mass transport flux is in series with other charge transport processes. the decay at early times is attributed to diffusion limited photocurrent densities.[82,84] The diffusion limiting current density is proportional to the film porosity, the diffusion coefficient, the

concentration of the oxidized form of the redox shuttle, [Co^{3+}], and inversely proportional to the electrolyte diffusion distance.[114]

6.9. General remarks

Of course with the proper choice of the dye and the redox couple the above-mentioned device performance can be improved. Indeed, an excellent performance should also be due to a perfect match between the oxidation potential of the dye and the redox shuttle.

However, this section of the thesis - as in its whole meaning - is mainly aimed at studying TiO_2 system.

When focusing on the study and optimization of one component (TiO_2) of the whole device (solar cell), one ends up in acquiring knowledge of the other components and on how some parameters are unavoidably affected by more than one sole chemical entity.

As for instance, electron lifetimes in DSCs usually only reflect the electron recombination between TiO_2 and the oxidized form of the redox species in the electrolyte, but in case of slow regeneration of the oxidized dye, also the effect of electron recombination to the oxidized dye will affect the measured lifetime, thus involving TiO_2, the dye and the electrolyte.

The electron transfer rate is also expected to depend on the structure of both the dye and the redox mediator, since the size of the donor and acceptor should affect the reorganization energy and electronic coupling.[106]

Then, as another example, the V_{OC} does not depend on the dye, as a first order approximation, whereas the maximum current is directly dependent on dye, which, in turn, is deposited onto the inorganic semiconductor according to specific features of TiO_2 itself. If this appears to be a general statement, then a plethora or specific cases of parameter-dependent effects contribute to make the picture highly complex and challenging and intriguing at the same time.

As a general note, it has been observed that a few samples performed significantly worse than the rest of the data set; thus, to prevent skewing of data with outliers, they have not been included in the average tabulation.

The results presented are indicative of what we can be achieved as a mere preliminary study. Although there is no certainty why a minority of cells behaved poorly, it could be due to variations in the processing of the film.

6.10. References

1. A. Hagfeldt, G. Boschloo, L. Sun, L. Kloo, H. Pattersson *Chem. Rev*. 110 (**2010**) 6595.
2. M. Grätzel *J. Photochem. Photobiol. C: Photochem. Rev.* 4 (**2003**) 145.
3. X. Mathew, H. Takakura *Sol. Energy Mater. Sol. Cells* 92 (**2008**) 371.
4. F. De Angelis, S. Fantacci, A. Selloni, M. Grätzel, M. K. Nazeeruddin *Nano Lett*. 7 (**2007**) 3189.
5. T. M. Clarke and J. R. Durrant *Chem. Rev*. 110 (**2010**) 6736.
6. "UD-led team sets solar cell record, joins DuPont on $100 million project". *udel.edu/PR/UDaily*. 2007-07-24. Retrieved 2007-07-24.
7. H. J. Snaith *Adv. Funct. Mater*. 20 (**2010**) 13.
8. W. Shockley and H. J. Queisser *J. Appl. Phys*. 32 (**1961**) 510.
9. S. Koops, B. O'Regan, P. R. F. Barnes, J. R. Durrant *J. Am. Chem. Soc*. 131 (**2009**) 4808.
10. E. Arici, N. S. Sariciftci, D. Meissner *Encyclopedia of Nanoscience and Nanotechnology* 3 (**2004**) 929.
11. B. Kippelen and J.-L. Brédas *Energy Environ*. Sci. 2 (**2009**) 251.
12. C. Goh, S. R. Scully, M. D. McGehee *J. Appl. Phys*. 101 (**2007**) 114503.
13. A. Huijser, B. M. J. M. Suijkerbuijk, R. J. M. Klein Gebbink, T. J. Savenije, L. D. A. Siebbeles *J. Am. Chem. Soc*. 130 (**2008**) 2485.
14. J. A. Ayllon and M. Lira-Cantu *Appl. Phys*. A 95 (**2009**) 249.
15. M. Thelakkat *Macromol. Mater. Eng*. 287 (**2002**) 442.
16. J. Roncali, P. Leriche, A. Cravino *Adv. Mat*. 19 (**2007**) 2045.
17. H. Ohishi, M. Tanaka, H. Kageyama, Y. Shirota *Chem. Lett*. 33 (**2004**) 1266.
18. J. E. Kroeze, T. J. Savenije, M. J. W. Vermeulen, J. M. Warman *J. Phys. Chem. B* 107 (**2003**) 7696.
19. E. L. Unger, E. Ripaud, P. Leriche, A. Cravino, J. Roncali, E. M. J. Johansson, A. Hagfeldt, G. Boschloo *J. Phys. Chem. C* 114 (**2010**) 11659.
20. G. P. Smestad, S. Spiekermann, J. Kowalik, C. D. Grant, A. M. Schwartzberg, J. Zhang, L. M. Tolbert, E. Moons *Sol. Energy Mater. Sol. Cells* 76 **(2003**) 85.
21. T. J. Savenije, E. Moons, G. K. Boschloo, A. Goossens, T. J. Schaafsma *Phys. Rev. B* 55 (**1997**) 9685.
22. G. K. Boschloo, A. Goossens, J. Schoonman *J. Electrochem. Soc.* 144 (**1997**) 1311.
23. F. Spadavecchia, G. Cappelletti, S. Ardizzone, M. Ceotto, L. Falciola *J. Phys. Chem. C* 115 (**2011**) 6381.
24. F. Cardon, W. P. Gomes *J. Phys. D: Appl. Phys.* 11 (**1978**) L63.

25. F. Fabregat-Santiago, G. Garcia-Belmonte, J. Bisquert, P. Bogdanoff, A. Zaban *J. Electrochem. Soc.* 150 (**2003**) E293.
26. P. J. Cameron and L. M. Peter *J. Phys Chem B* 107 (**2003**) 14394.
27. M. E. Özsan, D. R. Johnson, M. Sadeghi, D. Sivapathasundaram, G. Goodlet, M. J. Furlong, L. M. Peter, A. A. Shingleton *J. Mater. Sci. Mater. Electronics* 7 (**1996**) 119.
28. R. Van de Krol, A. Goossens, J. Schoonman *J. Electrochem. Soc.* 144 (**1997**) 1723.
29. S. Wendt, P. T. Sprunger, E. Lira, G. K. H. Madsen, Z. Li, J. Ø. Hansen, J. Matthiesen, A. Blekinge-Rasmussen, E. Laegsgaard, B. r. Hammer, F. Besenbacher *Science* 320 (**2008**) 1755.
30. Y. He, O. Dulub, H. Cheng, A. Selloni, U. Diebold *Phys. Rev. Lett.* 102 (**2009**) 106105.
31. C. M. Yim, C. L. Pang, G. Thornton *Phys. Rev. Lett.* 104 (**2010**) 036806.
32. K. Sulaiman, M. S. Fakir *Thin Solid Films* 519 (**2011**) 5219.
33. W. U. Huynh, J. J. Dittmer, N. Teclemariam, D. J. Milliron, A. P. Alivisatos, K. W. J. Barnham *Phys. Rev. B* 67 (**2003**) 115326.
34. S. R. Scully and M. D. McGehee *J. Appl. Phys.* 100 (**2006**) 034907.
35. D. F. Watson, A. Marton, A. M. Stux, G. J. Meyer *J. Phys. Chem. B* 107 (**2003**) 10971.
36. A. C. Arango, L. R. Johnson, V. N. Bliznyuk, Z. Schlesinger, S. A. Carter, H. H. Hörhold *Adv. Mater.* 12 (**2000**) 1689.
37. E. M. J. Johansson, S. Pradhan, E. Wang, E. L. Unger, A. Hagfeldt, M. R. Andersson *Chem. Phys. Lett.* 502 (**2011**) 225.
38. B. O'Regan, J. Moser, M. Anderson, M. Grätzel *J. Phys. Chem*. 94 (**1990**) 8720.
39. K.-S. Ahn, M.-S. Kang, J.-W. Lee, Y. S. Kang *J. Appl. Phys*. 101 (**2007**) 084312.
40. S. Ito T. Kitamurab, Y. Wadab, S. Yanagida *Sol. Energ. Mat. Sol. Cells* 76 (**2003**) 3.
41. C. S. Karthikeyan, M. Thelakkat, M. Willert-Porada *Thin Solid Films* 511–512 (**2006**) 187.
42. U. B. Cappel, E. A. Gibson, A. Hagfeldt, G. Boschloo *J. Phys. Chem. C* 113 (**2009**) 6275.
43. J. Melas-Kyriazi, I. K. Ding, A. Marchioro, A. Punzi, B. E. Hardin, G. F. Burkhard, N. Tetreault, M. Grätzel, J.-E. Moser, M. D. McGehee *Adv. Energy Mat*. 1 (**2011**) 407.
44. K.-H. Park, E. M. Jin, H. B. Gu, S. E. Shim, C. K. Hong *Mater. Lett*. 63 (**2009**) 2208.
45. P. Chen, J. H. Yum, F. De Angelis, E. Mosconi, S. Fantacci, S. J. Moon, R. H. Baker, J. Ko, M. K. Nazeeruddin, M. Grätzel *Nano Lett*. 9 (**2009**) 2487.

46. S.-R. Jang, K. Zhu, M. J. Ko, K. Kim, C. Kim, N.-G. Park, A. J. Frank *ACS Nano* 5 (**2011**) 8267.
47. W. Guo, Y. Shen, L. Wu, Y. Gao, T. Ma *J. Phys. Chem. C* 115 (**2011**) 21494.
48. B.-L. Su, A. Vantomme, L. Surahy, R. Pirard, J.-P. Pirard *Chem. Mater*. 19 (**2007**) 3325.
49. G.-S. Shao, X.-J. Zhang, Z.-Y. Yuan *Appl. Catal. B: Environ.* 82 (**2008**) 208.
50. A. Kay and M. Grätzel *Chem. Mater*. 14 (**2002**) 2930.
51. E. Ramasamy and J. Lee *Energy Environ. Sci*. 4 (**2011**) 2529.
52. W. Guo, L. Wu, Z. Chen, G. Boschloo, A. Hagfeldt, T. Ma *J. Photochem. Photobiol. A* 219 (**2011**) 180.
53. W. Guo, Y. Shen, G. Boschloo, A. Hagfeldt, T. Ma *Electrochimica Acta* 56 (**2011**) 4611.
54. H. Tian, L. Hu, C. Zhang, L. Mo, W. Li, J. Sheng, S. Dai J. *Mater. Chem*. 22 (**2012**) 9123.
55. H. Tian, L. Hu, C. Zhang, W. Liu, Y. Huang, L. Mo, L. Guo, J. Sheng *J. Phys. Chem. C* 114 (**2010**) 1627.
56. J. Zhang, X. Zheng, X. Yang, W. Cao *J. Inorg. Organomet. Polym*. 21 (**2011**) 150.
57. K. Prabakar, M.-K. Son, D. Ludeman, H.-J. Kim *Thin Solid Films* 519 (**2010**) 894.
58. S.-H. Kang, H. S. Kim, J.-Y. Kim, Y.-E. Sung *Mater. Chem. Phys*. 124 (**2010**) 422.
59. D. P. Hagberg, X. Jiang, E. Gabrielsson, M. Linder, T. Marinado, T. Brinck, A. Hagfeldt, L. Sun *J. Mater. Chem*. 19 (**2009**) 7232.
60. S. Feldt, E. Gibson, E. Gabrielsson, L. Sun, G. Boschloo, A. Hagfeldt *J. Am. Chem. Soc*. 132 (**2010**) 16714.
61. G. Lingamallu, K. Ravi Kumar, V. Veerapandian *Chem. Rec*. 12 (**2012**) 306.
62. D. Colonna, V. Capogna, A. Lembo, T. M. Brown, A. Reale, A. Di Carlo *Appl. Phys. Expr*. 5 (**2012**) 022303.
63. C.-Y. Hsu, Y.-C. Chen, R. Y.-Y. Lin, Kuo-Chuan Ho, J. T. Lin *Phys. Chem. Chem. Phys*. 14 (**2012**) 14099.
64. L. Yang, U. B. Cappel, E. L. Unger, M. Karlsson, K. M. Karlsson, E. Gabrielsson, L. Sun, G. Boschloo, A. Hagfeldt, E. M. J. Johansson *Phys. Chem. Chem. Phys.* 14 (**2012**) 779.
65. C. Y. Jiang, W. L. Koh, M. Y. Leung, S. Y. Chiam, J. S. Wu, J. Zhang *Appl. Phys. Lett*. 100 (**2012**) 113901.
66. I. K. Ding, N. Tetreault, J. Brillet, B. E. Hardin, E. H. Smith, S. J. Rosenthal, F. Sauvage, M. Grätzel, M. D. McGehee *Adv. Funct. Mater*. 19 (**2009**) 2431.

67. F. Fabregat-Santiago, J. Bisquert, L. Cevey, P. Chen, M. K. Wang, S. M. Zakeeruddin, M. Grätzel *J. Am. Chem. Soc*. 131 (**2009**) 558.
68. L. Schmidt-Mende, S. M. Zakeeruddin, M. Grätzel *Appl. Phys. Lett*. 86 (**2005**) 13504.
69. L. Schmidt-Mende and M. Grätzel *Thin Solid Films* 500 (**2006**) 296.
70. H. J. Snaith, R. Humphry-Baker, P. Chen, I. Cesar, S. M. Zakeeruddin, M. Grätzel *Nanotechnology* 19 (**2008**) 424003.
71. U. Bach, Solid-State Dye-Sensitized Mesoporous TiO_2 Solar Cells. Ph.D. Dissertation, Ecole Polytechnique Fédérale de Lausanne, Lausanne, Switzerland, 2000.
72. S. Ahmad , T. Bessho , F. Kessler, E. Baranoff , J. Frey , C. Yi , M. Grätzel, M. K. Nazeeruddin *Phys. Chem. Chem. Phys*. 14 (**2012**) 10631.
73. N. Papageorgiou *Coord. Chem. Rev*. 248 (**2004**) 1421.
74. H. Nusbaumer, J.-E. Moser, S. M. Zakeeruddin, M. K. Nazeeruddin, M. Grätzel *J. Phys. Chem. B* 105 (**2001**) 10461.
75. S. A. Sapp, C. M. Elliott, C. Contado, S. Caramori, C. A. Bignozzi *J. Am. Chem. Soc.* 124 (**2002**) 11215.
76. H. Nusbaumer, S. M. Zakeeruddin, J. E. Moser, M. Grätzel *Chem.–Eur. J.* 9 (**2003**) 3756.
77. H. X. Wang, P. G. Nicholson, L. Peter, S. M. Zakeeruddin, M. Grätzel *J. Phys. Chem. C* 114 (**2010**) 14300.
78. T. W. Hamann and J. Wondersma *Energy Environ. Sci*. 4 (**2011**) 370.
79. B. A. Gregg, F. Pichot, S. Ferrere, C. L. Fields *J. Phys. Chem. B* 105 (**2001**) 1422.
80. S. Hattori, Y. Wada, S. Yanagida, S. Fukuzumi *J. Am. Chem. Soc*. 127 (**2005**) 9648.
81. Z. Zhang, P. Chen, T. N. Murakami, S. M. Zakeeruddin, M. Grätzel *Adv. Funct. Mater*. 18 (**2008**) 341.
82. B. M. Klahr and T. W. Hamann *J. Phys. Chem. C* 113 (**2009**) 14040.
83. P. J. Cameron, L. M. Peter, S. M. Zakeeruddin, M. Grätzel *Coord. Chem. Rev.* 248 (**2004**) 1447.
84. J. J. Nelson, T. J. Amick, C. M. Elliott *J. Phys. Chem. C* 112 (**2008**) 18255.
85. H. N. Tsao, C. Yi, T. Moehl, J.-H. Yum, S. M. Zakeeruddin, M. K. Nazeeruddin, M. Grätzel *Chem. Sus. Chem*. 4 (**2011**) 591.
86. H. N. Tsao, J. Burschka, C. Yi, F. Kessler, M. K. Nazeeruddin, M. Grätzel *Energy Environ. Sci*. 4 (**2011**) 4921.
87. W. T. Hamann *Dalton Trans*. 41 (**2012**) 3111.
88. A. Yella, H.-W. Lee, H. N. Tsao, C. Yi, A. K. Chandiran, M. K. Nazeeruddin, E. W.-G. Diau, C.-Y. Yeh, S. M. Zakeeruddin, M. Grätzel *Science* 334 (**2011**) 629.
89. M. Wang, A. M. Anghel, B. Marsan, N.-L. Ha Cevey, N. Pootrakulchote,

S. M. Zakeeruddin, M. Grätzel *J. Am. Chem. Soc*. 131 (**2009**) 15976.
90. S. Ahmad, J.-H. Yum, H.-J. Butt, M. K. Nazeeruddin, M. Grätzel *Chem. Phys. Chem*. 11 (**2010**) 2814.
91. A. Kay and M. Grätzel *Sol. Energy Mater. Sol. Cells* 44 (**1996**) 99.
92. T. N. Murakami, S. Ito, Q. Wang, M. K. Nazeeruddin, T. Bessho, I. Cesar, P. Liska, R. Humphry-Baker, P. Comte, P. Pechy, M. Grätzel *J. Electrochem. Soc.* 153 (**2006**) A2255.
93. J. G. Nam, Y. J. Park, B. S. Kim, J. S. Lee *Scr. Mater*. 62 (**2010**) 148.
94. J. E. Trancik, S. C. Barton, J. Hone *Nano Lett*. 8 (**2008**) 982.
95. J. D. Roy-Mayhew, D. J. Bozym, C. Punckt, I. A. Aksay *ACS Nano* 4 (**2010**) 6203.
96. D. W. Zhang, X. D. Li, H. B. Li, S. Chen, Z. Sun, X. J. Yin, S. M. Huang *Carbon* 49 (**2011**) 5382.
97. P. Hasin, M. A. Alpuche-Aviles, Y. Wu *J. Phys. Chem. C* 114 (**2010**) 15857.
98. M. K. Nazeeruddin, A. Kay, I. Rodicio, R. Humphry-Baker, E. Müller, P. Liska, N. Vlachopoulos, M. Grätzel *J. Am. Chem. Soc*. 115 (**1993**) 6382.
99. E. Palomares, J. N. Clifford, S. A. Haque, T. Lutz, J. R. Durrant *J. Am. Chem. Soc*. 125 (**2002**) 475.
100. T. W. Hamann, O. K. Farha, J. T. Hupp *J. Phys. Chem. C* 112 (**2008**) 19756.
101. J. W. Ondersma and T. W. Hamann *J. Phys. Chem. C* 114 (**2009**) 638.
102. B. M. Klahr and T. W. Hamann *J. Phys. Chem. C* 113 (**2009**) 14040.
103. G. Dai, L. Zhao, S. Wang, J. Hu, B. Dong, H. Lu, J. Li *J. Alloys. Comp*. 539 (**2012**) 264.
104. J. Song, H. B. Yang, X. Wang, S. Y. Khoo, C. C. Wong, X.-W. Liu, C. M. Li *Appl. Mater. Interfaces* 4 (**2012**) 3712.
105. K. S. Lee, J. Kwon, J. H. Im, C. R. Lee, N.-G. Park, J. H. Park *Appl. Mater. Interfaces* 4 (**2012**) 4164.
106. S. M. Feldt, G. Wang, G. Boschloo, A. Hagfeldt *J. Phys. Chem. C* 115 (**2011**) 21500.
107. M. K. Nazeeruddin, F. De Angelis, S. Fantacci, A. Selloni, G. Viscardi, P. Liska, S. Ito, B. Takeru, M. Grätzel *J. Am. Chem. Soc*. 127 (**2005**) 16835.
108. H. J. Snaith, S. M. Zakeeruddin, L. Schmidt-Mende, C. Klein, M. Grätzel *Angew. Chem, Int. Ed*. 44 (**2005**) 6413.
109. J. D. Roy-Mayhew, G. Boschloo, A. Hagfeldt, I. A. Aksay *Appl. Mater. Inter.* 4 (**2012**) 2794.
110. H. Hu, B.-L- Chen, C.-H. Bu, Q.-D. Tai, F. Guo, S. Xu, J.-H. Xu, X.-Z. Zhao *Electrochimica Acta* 56 (**2011**) 8463.
111. J. L. Anderson and N. Winograd, Film Electrodes in "Laboratory Techniques in Electroanalytical Chemistry", Second Edition, Revised

and Expanded, Peter T. Kissinger and William R. Heineman. Marcel Dekker, Inc.; New York – Basel.
112. M. J. DeVries, M. J. Pellin, J. T. Hupp *Langmuir* 26 (**2010**) 9082.
113. S. Pelet, J.-E. Moser, M. Grätzel *J. Phys. Chem. B* 104 (**2000**) 1791.
114. N. Papageorgiou, M. Grätzel, P. P. Infelta *Sol. Energy Mater. Sol. Cells* 44 (**1996**) 405.

Conclusions

Several aspects of pristine and doped nano-titania are logically gathered in this thesis and analyzed from different points of view. The main emphasis has been placed on electronic and structural characterizations of the metal oxide.

Three different synthetic routes have been adopted to obtain nanostructured and mesoporous titania with tailored physico-chemical characteristics. A classical sol-gel synthesis has been integrated on one side by doping with both metal and non-metal heteroatoms and on the other side by a hydrothermal growth step using monomeric (DPC) or dimeric gemini-like (GS3) surfactants as template directing agents. Furthermore, a microemulsion-mediated route has been employed to accurately control the synthesis of bare titanium dioxide nanocrystals grown in nanoreactors by the confinement in aqueous droplets. Starting from these three different synthetic paths, crystalline TiO_2 nanopowders with high specific surface areas (up to 196 m^2g^{-1}) and small crystallite sizes (approximately in the range 7-40 nm) were obtained.

N-doped TiO_2 has been the mostly investigated material, being a many-sided topic. Different nitrogen sources, namely urea, ammonia, and triethylamine, have been employed to obtain photocatalysts characterized by visible-light absorption. The role of the aging time after the calcinations of the powders (from “freshly prepared” to “old” samples) both on the intensity of the optical features and on the bulk paramagnetic nitrogen concentration (as measured by EPR) was considered for all N-doped samples. Among the three different nitrogen sources, the urea dopant led to the most active doped titania even after 2-month aging. Apparently, the lifetime of the induced defects (Ti^{3+} and/or oxygen vacancies) at room temperature and ambient pressure depends on the specific structure and chemical environment of the defect itself.

Even though titanium dioxide is one of the most commonly adopted semiconductors in photocatalysis, univocal conclusions on the Fermi energy levels and related charge transfer processes versus dopant concentration were still missing. In this thesis, the electronic effects induced by the presence of N or Pr impurities in the TiO_2 nanocrystals were investigated. Both photovoltage and impedance experiments in conjunction with theoretical DFT calculations allowed us to outline a comprehensive picture of the electronic structure of N-doped nanoparticles. From both photovoltage and impedance measurements, one can appreciate that, in the present case, quasi-Fermi energy levels and flatband potentials are invariant under N-doping and slightly

pointing towards negative values for Pr-TiO_2. These findings are rationalized by assuming that, in the N-TiO_2 case, the position of the conduction band is not affected by the doping, and these considerations can be extended to the Fermi energy level. Then, comparisons with theoretical calculations allowed to assert that vacancies are more numerous than N doping centers in the home-made samples and that the electron transfer from Ti^{3+} 3d orbitals occurs only in part, keeping the Fermi energy pinned at the bottom of the conduction band. At least, this is the case for the synthetic route adopted here.

Therefore, the introduction of a dopant leads to final material with different features with respect to the undoped oxide, and, even though both Pr and N concur in extending the absorption to the visible region, they induce a different effect on the (quasi-)Fermi energy location.

Moreover, a joint EXAFS and DFT analysis has unequivocally identified the substitutional N locations at low dopant concentrations and clearly proved the generation of oxygen vacancies by N doping. Interestingly, the presented procedure can be used for the characterization of many doped materials.

Analogously, experimental and theoretical investigations enabled a conclusive evaluation of the nature of the Pr-dopant inclusion in bulk titania. Indeed, the generated midgap levels in Pr-TiO_2 are found to be 4f states by DFT calculations, and electron transitions from the valence band or shallow d Pr orbitals to the f Pr empty orbitals (just below the conduction band) could easily happen, causing the absorption peaks in the visible region detected by the optical measurements of diffuse reflectance.

In addition, both these Pr-TiO_2 samples and N-doped ones have proved to suffer from charge carriers recombination much less than undoped titania. This finding was achieved by means of optimized electrochemical analyses based on chronoamperometry with chopped light. Actually, the use of photocurrent measurements for the characterization of semiconductor thin film electrodes was not straightforward due to the lack of a widely accepted experimental procedure and the several parameters involved in this type of analysis (layer reproducibility, choice of extrapolation time range, photoanode modification during analysis, *etc.*). For this reason, an optimization of experimental parameters was performed to achieve a reliable insight into the relation between the type/concentration of a dopant and charge carriers recombination rate under either visible or UV illumination. Since no literature examples exist with this specific aim, such a tool can be proposed as a helpful

prescreen of semiconductor oxides both in powdery form and deposited as a film.

Then, on one hand photocatalytic experiments were performed to merely test selected home-made powders and judge their performance towards a certain pollutant. In this context, ethanol was employed in both aqueous and gaseous media, whereas methylene blue was successfully degraded directly on the "dry" TiO_2 film. On the other hand, specific environmentally hazardous compounds were chosen as targets for photocatalytic application of TiO_2 films deposited on proper substrates. With this aim, a combination of two advanced oxidation processes, ozonation and photocatalysis by nano-TiO_2, was successfully applied to the degradation and final mineralization of bisphenol A and 4-cumylphenol. The use of TiO_2 immobilized in thin films is of paramount importance for the plant-scale applicability of the process, especially if a low intensity irradiation source, such as solar light, is to be exploited. The coupling of ozonation and photocatalysis has led to pronounced synergistic effects, which might arise from interactions between ozone and the oxide surface. To this end, the oxide layer morphology/roughness may play a key role due to the large number of reactive surface sites.

Good photocatalytic performances of titania layers have been achieved in the reduction of the highly toxic Cr(VI), which constitutes a general environmental concern. Total Cr(VI) disappearance was obtained by means of both commercial and home-made TiO_2 nanoparticles deposited on Ti supports by an electrophoretic deposition method. During the photoreductive removal, the rate determining step of the process is the Cr(VI) adsorption at the oxide surface, indicating that the reduction is favored by small crystallites and large surface area. Furthermore, the monitoring of the photocatalytic process following the Cr(VI) disappearance from the solution was efficiently performed by a novel, environmentally friendly, ad hoc voltammetric technique, employing innovative bismuth screen-printed electrodes, instead of mercury ones.

Moving from photocatalytic to photovoltaic applications of TiO_2, different types of dye-sensitized solar cells (DSCs) were explored at two levels of research. Firstly, two different routes for the preparation of flat titanium dioxide layers as "blocking layers" in hybrid (dye-sensitized) solar cells were widely investigated. In this field the issue of charge recombination comes

again as a serious drawback of TiO_2-based systems. Such titania films prepared by either spray-pyrolysis or spin-coating exhibited marked differences in morphology, and electrochemical measurements proved that spin-coated TiO_2 films were not dense. The small-molecule semiconductor dye employed in the tested devices infiltrated the spin-coated TiO_2 layers, which led to the conclusion that the spin-coating preparation route results in nanoporous TiO_2 films. These observations were found to bear a more general meaning not restricted to the specific case of bilayer hybrid solar cells. Then, different types of both solid-state dye-sensitized solar cells and DSCs with a liquid electrolyte were tested making use of the above-mentioned spray-pyrolyzed TiO_2 as “blocking layer” and optimizing home-made nanostructured titania pastes. As conspicuous studies are devoted to optimization of both the dye and the redox mediator components and new strategies of co-sensitization and conjugation are continuously coming out at the stage of academic research, future efforts could be, instead, devoted to the improvement of the inorganic semiconductor component of DSC devices.

Appendix

Instruments, methods and accessories

Illumination sources

The illumination sources employed in this thesis have been two distinctive ones, because of the aim of irradiating the samples either in the UV (mainly UVA) or in the visible region of the electromagnetic spectrum. UV light and visible light were generated by a 500-W UV halogen lamp (Jelosil HG 500, iron halides) and by a LOT-Oriel lamp (Lamp Housing LSH302) emitting in the range 315-400 nm and 400-950 nm, as shown in the following Figure.

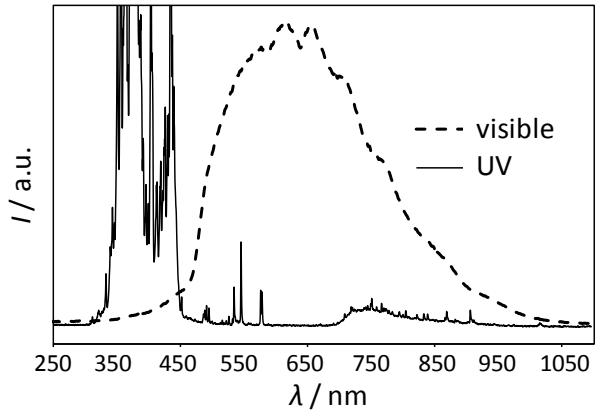

Emission spectra of the two lamps employed for both photocatalytic experiments and electrochemical characterizations.

The effective power (measured by Thorlabs S314C, see the following) was evaluated at different distances *d* from the source, as reported in the Figures below.

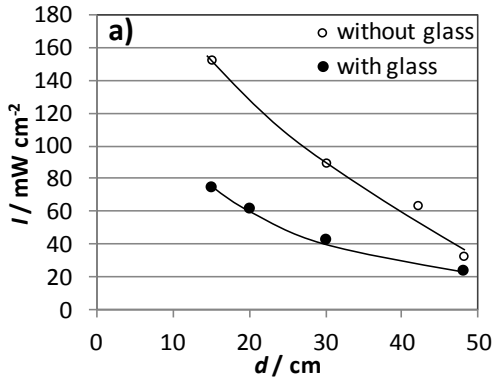

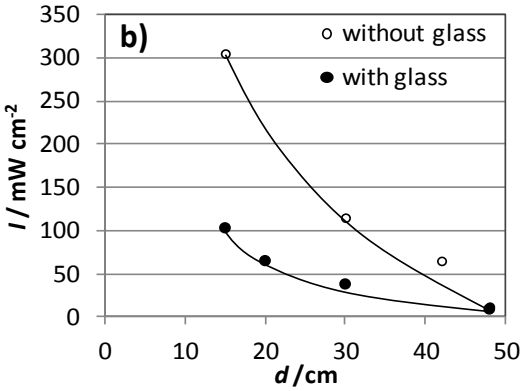

Effective power of the utilized UV (**a**) and visible (**b**) lamps as measured by Thorlabs S314C at different distances *d* from the source both directly ("without glass") and with the presence of a Pyrex glass placed between the lamp and the power-meter, to simulate the conditions of experimental measurements under illumination.

Exceptions are the illumination sources employed for solar cell characterizations: current-voltage (J-V) curves were recorded using a solar simulator (Newport model 91160), whereas IPCE measurements were performed with a xenon light source (ASB-XE-175).

Light source power measurements

The PM100A Handheld Optical Power Meter is designed to measure the optical power of laser light or other light sources. It has been used to determine the effective power at different distances from the source (see the above Figure) of the two lamps employed for characterization purposes and photocatalytic tests. Ambient light, with or without artificial indoor illumination, was detected to be about 250 mW cm^{-2}. Numerical values reported in the Figure were obtained by dividing the output value (in mW) by the active geometrical area of the power-meter (2 cm^{-2}).

When measuring very small power levels, dark current of photodiode sensors or zero voltage on thermal sensors will have an influence on the measurement result and must be compensated by the zero adjustment. Photodiode sensors emit small current levels, even when no photons hit the active area – the so called dark current, that is temperature dependent and in the region of some nA for silicon and InGaAs sensors and up to some µA for germanium sensors.

To perform an accurate measurement it is necessary to enter the operating wavelength of the light to measure so that the power-meter can calculate the

light source power from the measured photocurrent and the right response value from the wavelength calibration table.

Chapter 3

BET-BJH analyses

Specific surface areas were determined by multipoint BET method using the adsorption data in the relative pressure (p/p_0) range of 0.05–0.3. Data were acquired from Coulter SA 3100 apparatus. Desorption isotherms were used to determine the pore size distribution using the Barret–Joyner–Halander (BJH) method with cylindrical pore size.

SEM measurements

Scanning electron microscopy (SEM) photographs were acquired by a LEO 1430 with energy-dispersive X-ray spectroscopy (EDX) which enabled the possibility of a semi-quantitative elemental analysis.

HR-TEM measurements

HR-TEM investigations were carried out employing a JEOL 3010-UHR instrument (300 kV acceleration potential; LaB_6 filament) equipped with an Oxford INCA X-ray energy dispersive spectrometer (EDS) with a Pentafet Si(Li) detector. Samples were ‘‘dry” dispersed on lacey carbon Cu grids.

DRS measurements

Optical measurements in the UV-visible range were performed using a Perkin-Elmer, Lambda 35 spectrophotometer, equipped with a Labsphere RSA-PE-20 diffuse reflectance accessory. A TiO_2 thin film was placed in the sample holder on integrated sphere for the reflectance measurements. A “total white” Perkin-Elmer reference material was used as the reference.

XRPD analyses

- **Template TiO_2, microemulsion-mediate TiO_2, and (N,)Ag-TiO_2 samples.** Room-temperature X-ray powder diffraction (XRPD) patterns were collected with a Siemens D500 diffractometer over the 2θ range 10°–80°, with a step scan of D2θ = 0.02°, and a Cu Ka radiation. Rietveld refinement has been performed using the GSAS software

suite and its graphical interface EXPGUI.[1,2] The broadening due to the instrumental contributions was taken into account by means of a calibration performed with a standard Si powder. Components of peak broadening due to strain were not varied in the fitting procedure. The backgrounds have been subtracted using a shifted Chebyshev polynomial. The diffraction peak's profile has been fitted with a pseudo-Voigt profile function. Site occupancies and the overall isotropic thermal factors have been varied. The average diameter of the crystallites was estimated from the most intense reflection of the anatase (101) and rutile (110), when present, TiO_2 phases using the Scherrer equation.

- **N-TiO_2 samples.** High-resolution XRPD data were collected on the ID31 beamline at the ESRF, Grenoble, from 2° to 75° 2θ at 2° 2θ min^{-1} in Debye-Scherrer capillary geometry using a wavelength of 0.3999284 Å and a multi-detector system.[3] Wavelength was calibrated using the NIST SRM 640b Si standard, while the instrumental resolution function was parameterized on the pattern of the NIST SRM 660a LaB_6 powder. Phase identification was done with the X'Pert Highscore 2.2 software (PANAlytical b.v., Almelo, The Netherlands) and phase quantification via the Rietveld method as implemented in the TOPAS 4.2 software (Bruker AXS, Karlsruhe, Germany). The PM2K software[4] implementing the WPPM was used for the microstructural analysis.
- **Pr-TiO_2 samples.** X-ray powder diffraction (XRPD) experiments were performed on the freshly prepared nanostructured TiO_2 samples to evaluate the amount of their brookite content and possible changes in the lattice parameters, crystallite size and lattice strain as a function of the doping extent. The diffraction profiles were recorded at room temperature by a Philips PW 3710 Bragg-Brentano goniometer equipped with a scintillation counter and 1° divergence slit, 0.2 mm receiving slit and 0.04° soller slit systems. A graphite-monochromated Cu K_α radiation at 40 kV x 40 mA nominal X-rays power was employed. The same data collection strategy was applied to all the specimens. More in detail, θ:2θ scans between 20° to 90° with step size 0.08° wide was performed for a total counting time of 4 hours. A microcrystalline Si-powdered sample was used as a standard to

correct for instrumental line broadening effects. The XRPD patterns were analyzed with the Rietveld method as implemented in the GSAS-EXPGUI program suite. The background was described by power series in $Q^{2n}/n!$ and $n!/Q^{2n}$ and a surface roughness correction for microabsorption effects was also applied.[5] Line profiles were fitted using a pseudo-Voigt function.[6] Preferred orientation of crystallites was taken into account by a spherical harmonic model.[7,8] In the last cycles of the refinement, scale coefficient(s), cell parameters, positional coordinates and thermal factors were allowed to vary, as well as background and profile coefficients. All the attempts made to exactly locate the Pr ions in the unit cell from the experimental XRPD patterns were unsuccessful, probably because the low doping extent and the inherently disordered nature of the dopant ions.

XPS analyses

XPS measurements were taken in an M-probe apparatus (Surface Science Instruments). The source was monochromatic AlK radiation (1486.6 eV). A spot size of 200 mm $\times$ 750 mm and a pass energy of 25 eV were used. The energy scale was calibrated with reference to the $4f_{7/2}$ level of a freshly evaporated gold sample, at (84.00 ± 0.1) eV, and with reference to the $2p_{3/2}$ and 3s levels of copper at (932.47 ± 0.1) and (122.39 ± 0.15) eV, respectively. The binding energies (BE) were corrected for specimen charging by referencing the C 1s peak to 284.6 eV, and the background was subtracted using Shirley's method. The accuracy of the reported BE can be estimated to be ± 0.2 eV. The C region was fitted into two or three peaks, depending on the tail shape. The deconvolution was performed using only Gaussian line shapes. The peaks were fitted without BE or full width at half maximum (FWHM) constraints.

The same experimental setup was used for determination of chromium speciation on TiO_2 films by XPS analysis (results reported in *chapter 5*).

EPR measurements

Electron paramagnetic resonance spectra have been collected at room temperature by means of a Bruker Elexsys spectrometer at the working frequency of about 9.4GHz. The magnetic field intensity has been accurately tested by an ER035M Bruker Teslameter accessory and the microwave

frequency has been measured by the HP 5340A frequency counter. The spectral simulations were obtained by the Bruker SimFonia program.

X-ray absorption spectroscopy (XAS) and extended X-ray absorption fine structure (EXAFS)

Ti K-edge XANES and EXAFS data were collected at room temperature in transmission mode at the BM01B beamline of ESRF (European Synchrotron Radiation Facility, Grenoble, France). A Si (111)-monochromated beam was employed to probe the nanostructured samples in the 4.9-5.4 (pristine TiO_2) and 4.9-5.8 keV (N-doped TiO_2) energy ranges. To avoid thickness effects, sample tablets suitable for recording XAS spectra were prepared by carefully diluting the too absorbing titania with $CaCO_3$. The Horae suite of programs,[10] based on the IFEFFIT library[11] was used throughout for data processing and fitting. As samples contained a variable non-negligible fraction of brookite, backscattering paths belonging to both anatase and brookite crystal structures were explicitly took into account. In regard to the anatase phase, three Δr parameters were independently refined corresponding, respectively, to the Ti-O first-shell equatorial, Ti-O first-shell axial, and Ti-outer shell distances. To maintain the total number of parameters below the upper limit set by the Nyquist theorem (N free $=2\Delta k\Delta r/\pi + 1$), back-scattering paths involving bulk N atoms were never introduced explicitly. Rather, the effect of dopant N atoms was indirectly inferred from the distortions of the average axial and equatorial Ti-O bond distances in the Ti first coordination shell.

More details on the EXAFS data refinement, namely statistics and agreement factor *s*, together with the statistical assessment of the fitting model employed to interpret experimental data, can be found in the Supplementary Materials of ref [12].

Chapters 6 & 7

Spin-coater

A Chemat Technology KW-4A spin-coater was used for any type of compound (TiO_2, dye, PEDOT:PSS) to be spun for characterization or preparation of solar cell devices. In all other cases, a Spin150 spin-coater (SPS, ATP GmbH) was employed to deposit titania films.

Profilometry

The Sloan DekTak 150 profilometer was used to measure the height of mesoporous TiO_2 films above a thickness of 500 nm. Typically, a cantilever was scanned across the surface of a sample registering height differences.

XRD

Room temperature X-ray diffraction was measured on a Siemens Diffraktometer D5000.

SEM

SEM images were recorded on a Zeiss Leo 1550 scanning electron microscope located in the clean-room facility of the Ångström laboratory at Uppsala University. Top view and cross section images were acquired on titania samples on FTO glass. For the latter type of measurements the samples were scribed with a diamond-tip from the glass-slide and cracked prior to SEM-imaging in a 90° sample holder. To some extent also the infiltration of organic compounds into a porous inorganic material can be investigated in this manner.

AFM

Atomic force microscopy measurements were performed in tapping mode with a NanoScope III (Physics department, Ångström laboratory at Uppsala University) using a silicon cantilever which has a tip radius better than 10 nm. Image analysis was carried out using Nanotec WSxM 5.0 software.[13]

Absorbance, transmittance, and reflectance measurements

The transmittance and reflectance of the prepared titania films were measured on a Cary 5000 spectrometer equipped with an integrating sphere. Instead, an Ocean Optics, HR2000 fiberoptic spectrometer was used to measure the sample absorbance (before and after dye deposition) and consequently estimate the dye layer thickness, using the TiO_2 coated substrates without the dye as reference. The dye was spin-cast onto the TiO_2-covered FTO substrates from dichloromethane with varying solution concentrations.

XPS

Analysis on bare titanium dioxide for dye-sensitized solar cells were performed using synchrotron light at the undulator based BL I411 at the Swedish national laboratory MAX in Lund.[14]

The take-off angle used was 70° and the angle between polarization and photoelectron direction was 0°. The photon energy used in the PES experiments was 100 eV.

Electrochemical measurements

Electrochemical measurements were carried out on a CH-Instruments 660 potentiostat. Titania films on the fluorine-doped tin oxide (FTO) were used as the working electrode (area: 1 cm^2). Flatband potentials V_{fb} and doping densities N_D were determined from Mott-Schottky plots derived from impedance-voltage measurements at 1000 Hz in aqueous 0.1 M Na_2SO_4 (Merck) acidified to pH 3 with H_2SO_4. A Pt-wire was used as the counter electrode and Ag/AgCl as reference electrode. The potential was varied between +0.6 and –0.6 V (*vs* Ag/AgCl). To evaluate whether the prepared TiO_2 layers act as blocking layer preventing any contact between the conducting FTO and electron acceptors linear sweep voltammetry was carried between –0.6 and +0.6 V at a scan-rate of 0.01 V s^{-1} on substrates in contact with 0.01 M ferrocene and 0.1 M tetrabutylammonium hexafluoro-phosphate ($TBAPF_6$) as supporting electrolyte in acetonitrile.

For IPCE (EQE) and J-V measurements recorded on all types of solar cell devices, see chapter 6 (paragraph 6.1).

References

1. A. C. Larson and R. B. Von Dreele, GSAS: General Structural Analysis System. Laboratory Report LAUR 86-748, Los Alamos National Laboratory, Los Alamos, NM, USA, **1994**.
2. B. H. Toby *J. Appl. Crystallogr*. 34 (**2001**) 210.
3. J.-L. Hodeau, P. Bordet, M. Anne, A. Prat, A. N. Fitch, E. Dooryhee, G. Vaughan, A. Freund *Proc. SPIE* 353 (**1998**) 3448.
4. M. Leoni, M.; Confente, T.; Scardi, P. *Z. Kristall. Suppl.* **2006**, 23, 249.
5. W. Pitschke, H. Hermann, N. Mattern *Powder Diffraction* 8 (**1993**) 74.
6. P. Thompson, D. E. Cox, J. B. Hastings *J. Appl. Crist*. 20 (**1987**) 79.
7. H. J. Bunge Texture analysis in materials science. Butterworth-Heinemann, Oxford, **1983**.
8. B. Von Dreele *J. Appl. Cryst*. 30 (**1997**) 517.
9. D. Shirley *Phys. Rev*. B 5 (**1972**) 4709.
10. B. Ravel and M. Newville *J. Synchrotron Rad.* 12 (**2005**) 537.
11. M. Newville *J. Synchrotron Rad.* 8 (**2001**) 322.
12. M. Ceotto, L. Lo Presti, G. Cappelletti, D. Meroni, F. Spadavecchia, R. Zecca, M. Leoni, P. Scardi, C. L. Bianchi, S. Ardizzone *J. Phys. Chem. C* 116 (**2012**) 1764.
13. I. Horcas, R. Fernandez, J. M. Gomez-Rodriguez, J. Colchero, J. Colchero, J. Gomez-Herrero, A. M. Baro *Rev. Sci. Instrum*. 78 (**2007**) 013705.
14. S. Svensson, J. O. Forsell, H. Siegbahn, A. Ausmees, G. Bray, S. Södergren, S. Sundin, S. J. Osborne, S. Aksela, E. Nõmmiste, J. Jauhiainen, M. Jurvansuu, J. Karvonen, P. Barta, W. R. Salaneck, A. Evaldsson, M. Lögdlund, A. Fahlman *Rev. Sci. Instrum*. 67 (**1996**) 2149.

List of papers

The research activity of this thesis led to the following publications, which are hereafter ordered chronologically for simplicity.

F. Spadavecchia, S. Ardizzone, C.L. Bianchi, G. Cappelletti*, S. Cappelli, C. Oliva, P. Scardi, M. Leoni, P. Fermo.
Solar photoactivity of nano-N-TiO_2 from tertiary amine: role of defects and paramagnetic species.
Applied Catalysis B: Environmental, 96 (**2010**) 314–322. – DOI: 10.1016/j.apcatb.2010.02.027

G. Cappelletti*, S. Ardizzone, **F. Spadavecchia**, D. Meroni and I. Biraghi
Mesoporous Titania Nanocrystals by Hydrothermal Template Growth.
J. Nanomater., 2011 (**2011**) 597954/1–597954/9. – DOI**:** 10.1155/2011/597954

S. Ardizzone, G. Cappelletti*, D. Meroni and **F. Spadavecchia**
Tailored TiO_2 layers for the photocatalytic ozonation of cumylphenol, a refractory pollutant exerting hormonal activity.
Chem. Commun., 47 (**2011**) 2640–2642. – DOI: 10.1039/c0cc05134a

F. Spadavecchia*, G. Cappelletti, S. Ardizzone, M. Ceotto, L. Falciola
Electronic Structure of Pure and N-Doped TiO_2 Nanocrystals by Electrochemical Experiments and First Principles Calculations.
J. Phys. Chem. C, 115 (**2011**) 6381–6391. – DOI: 10.1021/jp2003968

M. Ceotto*, L. Lo Presti, G. Cappelletti, D. Meroni, **F. Spadavecchia**, R. Zecca, M. Leoni, P. Scardi, C.L. Bianchi, S. Ardizzone
About the Nitrogen Location in Nanocrystalline N-Doped TiO_2: Combined DFT and EXAFS Approach.
J. Phys. Chem. C, 116 (**2012**) 1764–1771. – DOI: 10.1021/jp2097636

A. Colombo, G. Cappelletti*, S. Ardizzone, I. Biraghi, C.L. Bianchi, D. Meroni, C. Pirola, **F. Spadavecchia**
Bisphenol A endocrine disruptor complete degradation using TiO_2 photocatalysis with ozone.
Environ. Chem. Lett, 10 (**2012**) 55–60. – DOI :10.1007/s10311-011-0328-0

S. Ardizzone, I. Biraghi, G. Cappelletti, D. Meroni, **F. Spadavecchia**
Physico-chemical tailoring of material surface properties.
In: *Surface tailoring of inorganic materials for biomedical applications.* I session: Surface tailoring technologies. 2012, 3-42. Lia Rimondini, Claudia Bianchi and Enrica Vernè, (Eds) Bentham Science Publishers

F. Spadavecchia*, S. Ardizzone, G. Cappelletti, L. Falciola, M. Ceotto, D. Lotti
Investigation and optimization of photocurrent transient measurements on nano-TiO_2
J. Appl. Electrochem. 14 (**2012**) 14:1301/1–1301/42. – DOI: 10.1007/s10800-012-0485-2

F. Spadavecchia*, G. Cappelletti, S. Ardizzone, M. Ceotto, M.S. Azzola, L. Lo Presti, G. Cerrato, L. Falciola
The role of Pr on the electron-hole recombination in nano-TiO_2: An experimental and theoretical study
J. Phys. Chem. C, 116 (**2012**) 23083−23093. – DOI: 10.1021/jp307303n

V. Pifferi*, **F. Spadavecchia**, G. Cappelletti, E.A. Paoli, C.L. Bianchi and L. Falciola
Electrodeposited nano-titania films for photocatalytic Cr(VI) reduction
Catal. Today, (**2012**) in press – DOI: 10.1016/j.cattod.2012.08.031

E.L. Unger, **F. Spadavecchia**, K. Nonomura, P. Palmgren, G. Cappelletti, A. Hagfeldt, E.M.J. Johansson, G. Boschloo*
Effect of the Preparation Procedure on the Morphology of Thin TiO_2 Films and their Device Performance in Small-Molecular Bilayer Hybrid Solar Cells
Appl. Mater. Inter., 4 (**2012**) 5997–6004. – DOI: /10.1021/am301604x

F. Spadavecchia*, S. Ardizzone, G. Cappelletti, C. Oliva, S. Cappelli
Time effects on the stability of the induced defects in TiO_2 nanoparticles doped by different nitrogen sources.
J. Nanopart. Res., 14 (**2012**) 1301/1–1301/12 – DOI: 10.1007/s11051-012-1301-y

Acknowledgments

I could reserve an entire thesis chapter or book to properly acknowledge everyone. I won't do that, of course.
With a bit of reflection and love, I will try to express my gratitude and congratulations in my turn.

My very first thanks go to the professor who held our group, Prof. Silvia Ardizzone, and to my formal supervisor, Dr. Giuseppe Cappelletti. They have given me the opportunity to conduct this research and to have decisive discussions on the results. Since I have known them for more than five years, I luckily had the possibility to enter not only in a work relationship but also in a friendly one.
Iole, who always knew how to deal with EVERYONE and EVERYTHING, starting from administrative tasks, all kinds of bureaucracy, technical stuff, practical issues and also one of the best people to confide something to. Daniela, the only one who has had the same evolution of studies and work as me, sharing the office and the "fate". Valentina, who arrived in the group for her Master Thesis, and, luckily, still gives us a lot of cheerfulness and positivity daily.
I owe my sincere thanks to Dr. Michele Ceotto and Dr. Luigi Falciola for being excellent collaborators and guides. To them my professional and human appreciation.
I also would like to thank all other colleagues of Università degli Studi di Milano, especially the ones of the NIG and ELAN group and Dr. Leonardo Lo Presti, including those who have come and gone over the years, for the nice working atmosphere. In this respect, I want to mention Stefano, Davide, Sara, Silvia, Michele, Chiara, Tommaso, Giulia, Matteo as well as Giulia, Guido, Maria Vittoria. I appreciated a lot all the thoughtfulness they showed to me when I appeared alone in a bad mood and I thank their precious all year–round work. In some cases it means precious cooperation to parts of this Thesis, and in some others it reveals in the deep sympathy I feel with them.

Of course the whole work would not have been what it is now without the assistance and support of many other people, also because results were obtained in the framework of collaborations and research abroad. Thanks to Prof. Giuseppina Cerrato (Università degli Studi di Torino), Dr. Roberto

Comparelli (CNR-IPCF, Istituto per i Processi Chimici e Fisici, Sez. Bari), Prof. Cesare Oliva and Dr. Serena Cappelli (Università degli Studi di Milano).

Here comes the special mention for all people I encountered in my 4-month wonderful winter/spring/summer in Uppsala, from the laboratory mates to the (beach-)volleyball ones. Prof. Hagfeldt and Dr. Boschloo (Ångström laboratories) welcomed me in a multicultural wonderful atmosphere. Critical questions, discussions of science and much more else now make me nostalgic of the past days, full of awesome memories. First and foremost I offer my sincerest gratitude to Anders, Gerrit, Erik, Eva, Kazu, Alex, Joe, Mahmoud (and Narges), Nick, Leif, Ute, Lei, Susanna, Peter, Martin, Kristofer, Shixin, Gang, Erik, Jojo, and, last but not least, Hanna, as a new-entry and Swedish/Italian friend. I will always remember their kindness and all the different personalities. I also want to thank Dr. Pål Palmgren for getting me started on the atomic force microscopy measurements and helping to interpret the first data.

I would like to thank my good friends and fellow chemistry students Simona, Elena, Erica, who are now moving away or are successfully employed somewhere else, and all other "laboratory–mates", with a mention for Miriam, Beatrice, and Marco.

With the feeling that I might have forgot someone, I would like to thank everyone who helped along with my project, lending their assistance where my own capabilities came short.

Special thanks is then given to all my friends with particular regards to those who are now living (very) far and gave me a new prospect and perception of life. Volleyball and artistic gymnastics mates, and all the others without a specific "membership" are acknowledged for their irreplaceable role in my life.

High gratitude goes to my parents and sister: they have ensured me the best ever "environment", warm and serene, where to live and work. I am then grateful to all my "enlarged family", which means to my closest relatives.

My deepest thank, once again, to Benny, for having shared all of this and even much more.